Tailoring the Surface Chemistry of Metal Oxides for Applications in Sustainable Catalysis

Dissertation

for the obtainment of the academic degree of

Doctor of Natural Sciences (*Dr. rer. nat.*)

Submitted to the Faculty of Mathematics, Informatics and Natural Sciences

Institute of Inorganic and Applied Chemistry

Department of Chemistry

University of Hamburg

Filippo Colombo

Hamburg, April 2025

The results presented in this dissertation were obtained from October 2020 to April 2025 in the working groups of Prof. Dr. Simone Mascotto and of Prof. Dr. Michael Fröba at the Institute of Inorganic and Applied Chemistry of the University of Hamburg.

First reviewer: Prof. Dr. Michael Fröba
Second reviewer: Prof. Dr. Alf Mews

Thesis defense committee:

Prof. Dr. Dorota Koziej, Prof. Dr. Simone Mascotto, Prof. Dr. Michael Steiger

Date of submission: 25th April 2025
Date of thesis defense: 13th June 2025

Table of Contents

List of Publications

1. Oh, D.*; Colombo, F.*; Nodari, L.; Kim, J. H.; Kim, J. K.; Lee, S.; Kim, S.; Kim, S.; Lim, D.K.; Seo, J.; Ahn, S.; Mascotto, S.; Jung, W. Rocking Chair-like Movement of Ex-Solved Nanoparticles on the Ni-Co Doped $La_{0.6}Ca_{0.4}FeO_{3-\delta}$ Oxygen Carrier during Chemical Looping Reforming Coupled with CO_2 Splitting. *Applied Catalysis B. Environmental* **2023**, *332*, 122745. https://doi.org/10.1016/j.apcatb.2023.122745. (*co-first authors)

2. Colombo, F.; Oh, D.; Tsiotsias, A.; Charisiou, N.D., Nodari, L.; Goula, M.; Jung, W.; Mascotto, S. Design of Bimetallic Nanoparticles with Switchable Catalytic Selectivity.
(to be submitted)

Oral Presentations

1. **Bimetallic Exsolution of Ni–Fe Nanoparticles from Perovskite Oxides: Insights into Mechanistic Aspects through *in-Situ* Synchrotron Measurements**
Advanced Inorganic Materials: Green and Unconventional Approaches and Functional Assessment
23rd–24th June 2022, Bari (Italy)

2. **Bimetallic Exsolution of Ni–Fe Nanoparticles from Perovskite Oxides: Insights into Mechanistic Aspects through *in-Situ* Synchrotron Measurements for Tailoring Catalytic Selectivity**
Nanotage 2022
24th–26th August 2022, Hamburg (Germany)

3. **Bimetallic Exsolution of Ni–Fe Nanoparticles from Perovskite Oxides: Insights into Mechanistic Aspects through *in-Situ* Synchrotron Measurements for Tailoring Catalytic Selectivity**
   "Power of Interfaces" International School & Workshop
   5th–7th October 2022, Palma de Mallorca (Spain)

4. **Exsolved bimetallic Ni–Fe Heterogeneous Catalysts for CO$_2$ Conversion Applications**
   Nanotage 2023
   5th–8th September 2023, Dresden (Germany)

Poster Presentations

1. **Bimetallic Exsolution of Ni–Fe Nanoparticles from Perovskite Oxides: Insights into Mechanistic Aspects for Tailoring Catalytic Selectivity**
   Desy User Meeting 2023
   25th–27th January 2023, Hamburg (Germany)

2. **Investigation of the Interactions between Water and Mesoporous Functional Metal Oxides**
   European Materials Research Society (EMRS) Spring Meeting
   29th May–June 2nd 2023, Strasbourg (France)

3. **Exsolved bimetallic Ni–Fe Heterogeneous Catalysts for CO$_2$ Conversion Applications**
   European Materials Research Society (EMRS) 2023 Spring Meeting
   29th May–June 2nd 2023, Strasbourg (France)

List of Abbreviations

ATR	Attenuated Total Reflectance
BCC	Body-Centered Cubic
BF	Bright Field
CCU	Carbon Capture and Utilization
CCUS	Carbon Capture, Utilization and Storage
CLR	Chemical Looping Reforming
CVD	Chemical Vapor Deposition
DF	Dark Field
DFT	Density Functional Theory
DRIFTS	Diffuse Reflectance Infrared Fourier Transform Spectroscopy
DER	Dry Ethane Reforming
DMR	Dry Methane Reforming
DVS	Dynamic Vapor Sorption
EDXS	Energy-Dispersive X-ray Spectroscopy
ECBM	Enhanced Coal Bed Methane
EOR	Enhanced Oil Recovery
EXAFS	Extended X-ray Absorption Fine Structure
FCC	Face-Centered Cubic
FT-IR	Fourier-Transform Infrared
FWHM	Full Width at Half Maximum
HAADF	High-Angle Annular Dark Field
HR-TEM	High-Resolution Transmission Electron Microscopy
IUPAC	International Union of Pure and Applied Chemistry
KAIST	Korea Advanced Institute of Science and Technology
LSTFN2	$La_{0.4}Sr_{0.6-\alpha}Ti_{0.6}Fe_{0.35}Ni_{0.05}O_{3-\delta}$
LCFO	$La_{0.6}Ca_{0.4}FeO_{3-\delta}$

LCF	Linear Combination Fitting
MTPR	Methane Temperature Programmed Reduction
NAP-XPS	Near-Ambient Pressure X-Ray Photoelectron Spectroscopy
OSC	Oxygen Storage Capacity
ODH	Oxidative Dehydrogenation of ethane
OSC	Oxygen Storage Capacity
pO$_2$	Oxygen Partial Pressure
PSD	Pore Size Distribution
PLD	Pulsed Laser Deposition
RH	Relative Humidity
ROS	Reverse Oxygen Spillover
STEM	Scanning Transmission Electron Microscopy
SAED	Selected Area Electron Diffraction
SSA	Specific Surface Area
SMSI	Strong Metal-Support Interaction
STO	Strontium Titanate
TEM	Transmission Electron Microscopy
UV-Vis	Ultraviolet-Visible
VOCs	Volatile Organic Compounds
XANES	X-ray Absorption Near-Edge Structure
XAS	X-ray Absorption Spectroscopy
XRD	X-ray Diffraction

Zusammenfassung

Im Rahmen der vorliegenden Dissertation wurde die Oberflächenchemie verschiedener Metalloxide gezielt modifiziert, um deren funktionale Eigenschaften für nachhaltige katalytische Anwendungen anzupassen.

Zunächst lag der Schwerpunkt auf dem Oberflächendesign von Perowskitoxiden für Anwendungen in Technologien zur Kohlenstoffabscheidung und -nutzung (Carbon Capture and Utilization, CCU). Der Mechanismus der bimetallischen Exsolution von FeNi-Nanopartikeln aus $La_{0.4}Sr_{0.4}Ti_{0.60}Fe_{0.35}Ni_{0.05}O_3$ (LSTFN2) wurde mittels *in-situ* XANES-Spektroskopie und Synchrotron-XRD untersucht, um die Reduktion der Fe- und Ni-Kationen sowie das Wachstum der FeNi-Partikel zu analysieren. Die *in-situ* XANES-Spektroskopie zeigte, dass die Kinetik der Ni-Reduktion der geschwindigkeitsbestimmende Schritt im bimetallischen Exsolutionsprozess darstellt und den Verlauf der Fe-Reduktion steuert, wobei diese unabhängig von der Behandlungstemperatur ist. Die endgültigen Mengen an metallischem Ni und Fe, die im Gleichgewicht beobachtet wurden, sind bei allen Temperaturen identisch und werden durch die Stöchiometrie (d. h. die Zusammensetzung) des Perowskitmaterials festgelegt. Darüber hinaus wurde bei allen analysierten Temperaturen eine Restmenge an Fe^{2+}-Spezies am Ende des Prozesses nachgewiesen. Die Reduktionskinetik von Ni beeinflusste maßgeblich die Zusammensetzung der abgeschiedenen γ-FeNi-Legierungsnanopartikel, wie durch *in-situ* Synchrotron-XRD belegt wurde. Höhere Temperaturen begünstigten die Keimbildung und das Wachstum von Ni-reicheren Legierungen, während niedrigere Temperaturen eine stärkere Fe-Einlagerung förderten.

Diese Ergebnisse zeigen die Möglichkeit, die Zusammensetzung von FeNi-Legierungsnanopartikeln durch Anpassung der Exsolutionstemperatur gezielt zu steuern und ebnen den Weg für den Einsatz des $La_{0.4}Sr_{0.4}Ti_{0.60}Fe_{0.35}Ni_{0.05}O_3$-Systems als heterogener Katalysator für die CO_2-unterstützte oxidative Dehydrierung von

Ethan (ODH) sowie die trockene Ethanreforming (Dry Ethane Reforming, DER); beide Prozesse wurden im Rahmen einer Kooperation mit dem *Korea Advanced Institute of Science and Technology* (KAIST), der Universität Westmakedonien und der Universität Padua untersucht. Die Ergebnisse dieser Studien zeigten, dass die bei hohen Exsolutionstemperaturen (850 °C) gebildeten Nanopartikel eine Kern-Schale-Struktur mit einem Fe_3Ni-Kern, einer Ni-Hülle und einer äußeren kristallinen Fe_yO_x-Schale aufweisen, dessen Bildung im Einklang mit dem Auftreten von Fe^{2+}-Spezies steht, die das *in-situ* XANES-Spektrum anzeigte. Die Ausbildung der kristallinen Kern-Schale-Morphologie wurde auf den Prozess des „Reverse Oxygen Spillover" (ROS) zurückgeführt; dies ist ein Mechanismus, bei dem Sauerstoffspezies von einem sauerstoffarmen Substrat zur Oberfläche der Metallnanopartikel wandern und dort eine Oxidschicht ausbilden.

Katalytische Tests der dem Exsolutionsprozess unterzogenen Perowskitmaterialien zeigten deren hohe thermische Stabilität und belegten, dass durch die Einstellung der Exsolutionstemperatur des LSTFN2-Ausgangsoxids die Reaktionsselektivität präzise kontrolliert werden kann. Insbesondere kann durch diese Anpassung die Reaktion entweder in Richtung Ethan-Dehydrierung mit Ni-reichen Nanopartikeln (R400) oder in Richtung Reforming mit Kern-Schale-Nanopartikeln (R850) gelenkt werden, was eine steuerbare Selektivität ermöglicht. Die Schlüsselergebnisse dieser Arbeit unterstreichen die Möglichkeit, die katalytische Selektivität durch Redoxzyklen zu schalten, wobei die einzigartige Eigenschaft der Perowskite genutzt wird, ihre ursprüngliche Struktur nach Reoxidation wiederherzustellen sowie die Redoxchemie des Eisens ausgenutzt wird. Die Re-Inkorporation der als Metall abgeschiedenen Ionen während der Regeneration war elementspezifisch: Für Nickel konnte eine vollständige Wiederherstellung des perowskitähnlichen chemischen Umfelds festgestellt werden, während für Eisen Restmengen an metallischer Phase detektiert und eine gestörte Koordinationssymmetrie nachgewiesen wurde, was auf die Bildung ungeordneter Eisenoxidspezies zurückgeführt wurde. Nach erneuter Exsolution blieb die Kern-Schale-Struktur der Nanopartikel erhalten, wobei die Oxidphasen der Schale je nach Reduktionsbedingungen entweder aus kristallinen oder amorphen Fe_yO_x-

Phasen bestanden. Die katalytische Leistungsfähigkeit und Selektivität wurden durch die Effektivität der Reoxidationsbehandlung zur Wiederherstellung der ursprünglichen Perowskitstruktur beeinflusst. Der Katalysator zeigte eine bemerkenswerte Beständigkeit gegenüber Kohlenstoffablagerungen und eine überlegene Stabilität im Vergleich zu einem kommerziellen Ni/Al_2O_3-Katalysator.

Das Konzept der Reversibilität bei der multimetallischen Exsolution wurde anschließend auf ein weiteres Fe-basiertes Perowskitsystem übertragen, welches wiederum für den Einsatz als regenerierbarer heterogener Katalysator in einer weiteren CCU-Technologie dienen sollte und im Rahmen einer Kooperation mit KAIST untersucht wurde. Das System $La_{0.6}Ca_{0.4}Fe_{0.95}M_{0.05}O_{3-\delta}$ (M = Ni, Co oder NiCo) wurde als Metalloxid-Sauerstoffträgerkatalysator für das Chemical Loop Reforming (CLR) von Methan in Kombination mit CO_2-Spaltung entwickelt. Für das co-dotierte Material wurde die Exsolution von trimetallischen FeCoNi-Legierungsnanopartikeln unter reduzierenden CH_4-Bedingungen beobachtet, während unter oxidierenden CO_2-Atmosphären NiCo-bimetallische Nanopartikel gebildet wurden. Ein „Rocking-Chair"-Verhalten der Fe-Kationen ermöglichte deren Hin- und Herbewegung zwischen der Perowskitmatrix und die teilweise Reinkorporation in ihren ursprünglichen Oxidationszustand und ihre ursprüngliche Koordinationsumgebung, wie durch die Charakterisierung mittels mehrerer unabhängigen Methoden (u. a. Röntgendiffraktometrie, XANES- und Mößbauerspektroskopie) gezeigt werden konnte.

Im letzten Teil der Dissertation wurde die Oberflächenmodifikation mesoporöser Titandioxid-Pulver durch verschiedene Methoden untersucht, darunter elektro- und photothermische Behandlungen sowie Dotierung mit aliovalenten Übergangsmetallen. Mittels Wasserdampf-Physisorption und IR-Spektroskopie wurde deren Einfluss auf die Oberflächen-Wasser-Wechselwirkungen analysiert, um das Potential als Katalysatoren für die photokatalytische Wasserspaltung zu evaluieren. Die Brønsted-Acidität der Oberfläche mesoporöser TiO_2-Pulver, die von der Konzentration an der Oberfläche befindlicher Hydroxylgruppen, die Wasserstoffbrücken mit Wasser eingehen können, abhängt, wurde maßgeblich durch

eine Erhöhung der spezifischen Oberfläche (SSA) beeinflusst, was ihre Hydrophilie verstärkt. Zudem wurde die Konzentration oberflächlicher Sauerstoffleerstellen durch elektro- und photothermische Behandlung sowie extrinsische Dotierung mit Fe und Nb gezielt verändert. In allen Fällen förderte die Bildung von Sauerstoffleerstellen in Kombination mit hoher Porosität die Ausbildung größerer Mengen an Hydroxylgruppen auf der Titandioxidoberfläche. Während die Oberflächenmodifikation erfolgreich war, erwies sich die Wasserdampf-Physisorption jedoch als nicht sensitiv genug, um signifikante Änderungen in der Wechselwirkung zwischen Wasser und mesoporösem Titandioxid zu detektieren. Weitere Untersuchungen dieses Systems mit ergänzenden Charakterisierungsmethoden wie Diffuse-Reflexions-Infrarot-Fourier-Transformationsspektroskopie (DRIFTS) und *Near Ambient Pressure X-ray Photoelectron*-Spektroskopie (NAP-XPS) könnten zukünftig weitere Einblicke in TiO_2-Wasser-Wechselwirkungen liefern.

Insgesamt zeigen die Ergebnisse dieser Dissertation, dass durch die Nutzung der Fe-Redoxchemie und die Modulation der Konzentration oberflächlicher Sauerstoffleerstellen exsolvierte Perowskitmaterialien mit einstellbaren funktionalen Eigenschaften und schaltbarer katalytischer Selektivität entwickelt werden können. Darüber hinaus wurden die Ausbildung oberflächlicher Hydroxylgruppen, getrieben durch Sauerstoffleerstellen, sowie erhöhte spezifische Oberflächen als Schlüsselfaktoren für die Oberflächenwechselwirkung von Wasser mit mesoporösem Titandioxid identifiziert.

Abstract

In the present dissertation, the surface chemistry of different metal oxides was modified for the purpose of tailoring their functional properties for sustainable catalytic applications.

First, the focus was put on the surface design of perovskite oxides for applications in Carbon Capture and Utilization (CCU) technologies. The mechanism of bimetallic exsolution of FeNi nanoparticles from $La_{0.4}Sr_{0.4}Ti_{0.60}Fe_{0.35}Ni_{0.05}O_3$ (LSTFN2) parent oxides was investigated with the means of *in-situ* XANES and synchrotron XRD, for studying the reduction of Fe and Ni cations and the growth of FeNi particles, respectively. *In-situ* XANES spectroscopy revealed that the kinetics of Ni reduction acts as the rate-determining step in the bimetallic exsolution process, driving the progression of Fe reduction, which is independent from the temperature of the treatment. The final amounts of metallic Ni and Fe observed at equilibrium are the same at all temperatures and are set by the stoichiometry (i.e. the composition) of the perovskite material. Moreover, a residual amount of Fe^{2+} species was observed at the end of the process for all of the analyzed temperatures. The reduction kinetics of Ni was shown to significantly influence the composition of the exsolved γ-FeNi alloy nanoparticles, as pointed out by *in-situ* synchrotron XRD. Higher temperatures favored the nucleation and growth of Ni-richer alloys, whereas lower temperatures were shown to promote larger Fe incorporation.

These results demonstrated the ability to control the composition of FeNi alloy nanoparticles by adjusting the exsolution temperature, and paved the way for the application of the $La_{0.4}Sr_{0.4}Ti_{0.60}Fe_{0.35}Ni_{0.05}O_3$ system as heterogeneous catalyst for CO_2-assisted Oxidative Dehydrogenation of ethane (ODH) and Dry Ethane Reforming (DER), as part of a study conducted with collaborators from the Korea Advanced Institute of Science and Technology (KAIST), the University of West Macedonia and the University of Padua.

The findings of this study revealed that, at high exsolution temperatures (850 °C), the grown nanoparticles exhibit a core-shell structure comprising a Fe_3Ni core, a Ni skin, and an external crystalline Fe_yO_x shell, whose formation is consistent with the presence of Fe^{2+} species identified through *in-situ* XANES spectroscopy. The formation of the crystalline core-shell morphology was attributed to reverse oxygen spillover (ROS), a mechanism where oxygen species migrate from an oxygen-deficient substrate to the surface of supported metal nanoparticles, forming an oxide layer around them. Catalytic testing of the exsolved perovskite materials revealed their high thermal stability and demonstrated that adjusting the exsolution temperature of the LSTFN2 parent oxide enables precise control over selectivity. Specifically, this adjustment directs the reaction toward ethane dehydrogenation with Ni-rich nanoparticles (R400) or reforming pathways with core-shell nanoparticles (R850), enabling tunable catalytic properties. The key findings of this study highlight the ability to switch catalytic selectivity through redox cycling, utilizing the unique property of perovskites to restore their original structure upon re-oxidation and by exploiting the redox chemistry of iron. The re-incorporation of exsolved ions during regeneration was species-dependent: nickel fully regained its perovskite-like chemical environment, while iron retained residual metallic phases and exhibited a disrupted coordination symmetry, attributed to the formation of disordered iron oxide species. Upon re-exsolution, the core-shell structure of the nanoparticles remained intact, with the shell oxide phases transitioning between crystalline and amorphous Fe_yO_x depending on the reduction conditions. The catalytic performance and selectivity were influenced by the effectiveness of the re-oxidation treatment in restoring the original perovskite oxide structure. The catalyst retained remarkable resistance to carbon deposition and superior stability compared to a commercial Ni/Al_2O_3 catalyst.

The concept of reversibility in multimetallic exsolution was subsequently extended to another Fe-based perovskite system, again for its application as regenerable heterogeneous catalyst for another CCU technique, as part of a collaboration with KAIST. The $La_{0.6}Ca_{0.4}Fe_{0.95}M_{0.05}O_{3-\delta}$ (M = Ni, Co, or NiCo) system was designed as

a metal oxide oxygen carrier catalyst for Chemical Loop Reforming (CLR) of methane coupled with CO_2-splitting. For the co-doped material, the exsolution of trimetallic FeCoNi alloy nanoparticles under reducing CH_4 conditions was observed, switching to NiCo bimetallic nanoparticles under oxidizing CO_2 atmospheres. A rocking-chair behavior of Fe cations was obtained, enabling them to move back and forth between the perovskite matrix and partially reincorporate into their original oxidation state and coordination environment, as demonstrated through a multi-technique bulk characterization approach, including X-ray diffraction, XANES spectroscopy, and Mössbauer spectroscopy.

Finally, the last part of this dissertation investigated the surface modification of mesoporous titania powders through various methods, including electro- and photo-thermal treatments and doping with aliovalent transition metals, by utilizing water vapor physisorption and IR-spectroscopy measurements to analyze their impact on surface-water interactions, with the perspective of evaluating their potential use as catalysts in photocatalytic water splitting. The surface Brønsted acidity of mesoporous TiO_2 powders, determined by the concentration of surface hydroxyl groups capable of hydrogen bonding with water, was significantly influenced by an increase in specific surface area (SSA), which determines enhanced hydrophilicity. Moreover, the concentration of surface oxygen vacancies was modified through electro- and photo-thermal treatments and extrinsic doping with Fe and Nb. In all these cases, the formation of oxygen vacancies, combined with high porosity, were key to inducing the formation of higher amounts of surface hydroxyl groups on titania's surface. However, while surface modifications were proved to be successful, water vapor physisorption was not sensitive enough in detecting significant changes in the interaction between water and mesoporous titanium dioxide. A further study of this system with complementary characterization techniques such as Diffuse Reflectance Infrared Fourier Transform Spectroscopy (DRIFTS) and Near Ambient Pressure X-ray Photoelectron Spectroscopy (NAP-XPS) could lead to further insights on TiO_2-water interactions in the future.

Overall, the results of this dissertation showed that leveraging Fe redox chemistry and modulating surface oxygen vacancy concentrations enables the development of exsolved perovskite materials with tunable functional properties and switchable catalytic selectivity. Furthermore, the formation of surface hydroxyl groups, driven by oxygen vacancies, along with increased specific surface areas, were identified as key factors influencing the surface interaction of water with mesoporous titanium dioxide.

Chapter 1

Introduction

Over the last 50 years, global energy demand has risen significantly. Since the 1970s, primary energy consumption has more than doubled, rising from approximately 6,101 million tons of oil equivalent (Mtoe) in 1973 to nearly 14,000 Mtoe by 2023[1]. This growth has been primarily driven by factors such as the rise of the global population, which grew from 3.68 billion in 1970 to 8.06 billion in 2023[2], also due to the demographic increase of developing nations, with subsequent expanding industrialization and global rise in the use of energy-consuming appliances.

Moreover, experts widely agree that the global energy consumption is expected to rise further in the short to medium term, with a rate of growth influenced by factors such as economic dynamics, population changes, and policy decisions. Projections suggest that the total energy demand could grow by 20–30% by 2050, depending on the level of commitment countries make toward enhancing energy efficiency and reducing carbon emissions[3].

Within this scenario, the production of energy through the combustion of fossil fuels, such as coal, oil, and natural gas, has dominated global energy consumption for decades. Even in recent years, non-renewable energy sources accounted for approximately 81.5% of worldwide primary energy use in 2023[4] (505.5 EJ, **Figure 1**). Although clean energy sources achieved a record high, accounting for approximately 14.6% of global primary energy consumption in the same year, the data highlight that the global energy mix still relies predominantly on hydrocarbons[5].
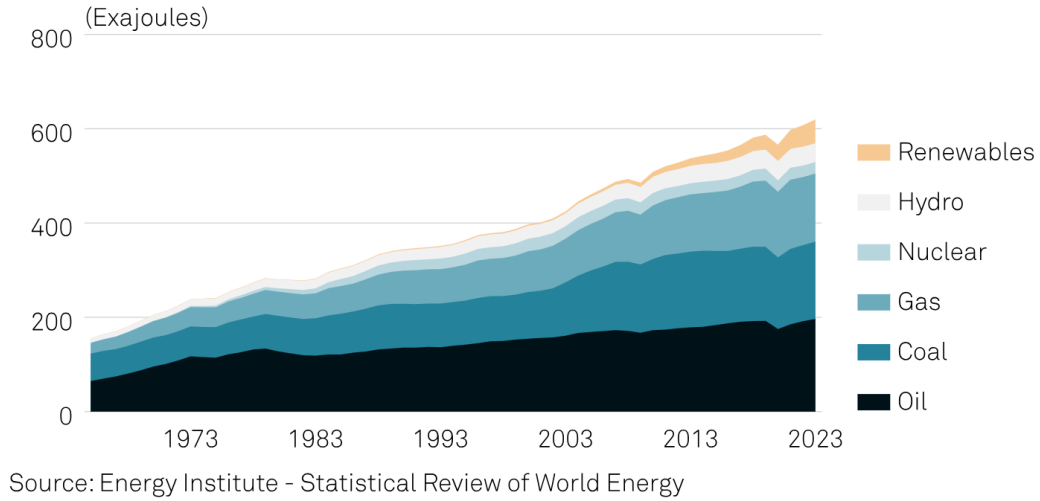
Figure 1. World energy consumption by source. Reported from S&P Global[4].

Among fossil fuels, natural gas is often regarded as a transitional energy source towards greater adoption of renewables. Conventional arguments in favor of its use emphasize its reliability in advancing the clean energy transition and its ability to compensate for declining coal and oil reserves, although questions remain about how its utilization can be ensured in both the short and long term[6].

Included within this broader discussion are the so-called CCUS, an acronym for "Carbon Capture, Utilization and Storage" processes. These refer to technologies designed to capture carbon dioxide (CO_2) emissions from sources such as power plants and industrial activities, preventing them from being released into the atmosphere. These technologies represent a valuable strategy for a more gradual transition to greater utilization of renewable energy sources. Their role is significant for several reasons, including their ability to support the advancement of renewables by offering low-carbon backup power for intermittent renewable sources and reducing emissions from existing CO_2-producing power plants through carbon re-utilization[7]. The initial key step in CCUS processes involves capturing CO_2 from emission streams using methods such as pre-combustion[8], post-combustion[9], and oxy-fuel combustion[10]. After capture, CO_2 can either be sequestered underground or reutilized for conversion into products like synthetic fuels, chemicals, and construction materials. Furthermore, CO_2 capture systems could eventually be combined with

hydrogen to produce hydrocarbons[11]. However, the impact of CCUS technologies remains limited, primarily because their adoption, though growing, is not yet sufficiently widespread, partly due to the absence of efficient catalysts to make it economically viable. For context, as of 2023, CCUS technologies captured only about 0.1% of global CO_2 emissions, equivalent to approximately 45 million metric tons annually[12]. Projections indicate that by 2050 energy-related CO_2 capture for the production of fuels such as ammonia and hydrogen could reach 1.25 Gigatons[13]. However, although these processes can help reduce emissions from energy production, improving their impact will require better efficiency and more effective catalyst designs. From a materials science perspective, this challenge involves designing heterogeneous catalysts that are more affordable, better performing, and use active phase metals with a lower environmental impact.

Alongside CCU processes (i.e. those considering only Carbon Capture and Utilization technologies), another promising solution for sustainable energy applications is the integration of renewables in the transition from fossil fuels through hydrogen production from water splitting. This consists of the process of splitting water into hydrogen and oxygen using electricity, through either water electrolysis or photocatalytic techniques. Within this class of processes, of particular interest is the production of the so-called green hydrogen, which is typically industrially obtained by using renewable energy sources (such as wind, solar, or hydroelectric power), generating hydrogen gas (H_2) and oxygen gas (O_2) with zero emissions[14], and blue hydrogen, which utilizes CCU technologies to reduce the CO_2 emissions linked to traditional hydrogen production[15]. Green and blue hydrogen are typically produced through water electrolysis[16], but clean hydrogen can also be generated using photocatalytic water splitting, where metal oxides act as photocatalysts driven by sunlight or UV radiation. This method has attracted considerable attention due to its potential to produce hydrogen without relying on fossil fuels or generating carbon dioxide emissions[17]. Recent developments in this sense have aimed at enhancing the efficiency of photocatalytic water splitting, particularly through the design of mesoporous metal oxides like TiO_2, which serve as effective photocatalysts for this

process[18,19]. CCUS and photocatalytic water splitting share common features beyond their role in supporting energy sustainability and facilitating the transition from conventional to renewable energy sources, as both processes rely on catalysis and require heterogeneous catalysts to efficiently drive their respective reactions. The development of efficient, accessible, and durable metal oxides for heterogeneous catalysis in CCU has garnered significant attention in recent years. In 2022, the catalyst industry was valued at approximately USD 29.72 billion, with heterogeneous catalysts representing 71% of the market share[20]. Furthermore, as highlighted earlier, the increasing focus on green technologies and the rising energy demand have made catalysts essential in refining processes like reforming, (de-)hydrogenation, and olefins cracking, with perovskite oxides emerging as ideal candidates for these applications. Similarly, titanium dioxide stands out as the most widely utilized photocatalyst in the market for applications such as air purification and water treatment techniques[21].

This dissertation aims at investigating the mechanistic aspects underlying the design and tailoring of the surface of these two classes of metal oxides, perovskite oxides and titanium dioxide, which find use in sustainable heterogeneous catalytic processes. To provide context on the role of perovskite oxides in heterogeneous catalysis for CCU, it is crucial to consider the process of metal exsolution from them. This innovative approach allows for the design of sustainable catalyst materials with enhanced performance and regenerability. The process consists in reducing a doped perovskite oxide in an oxygen-deficient environment at elevated temperatures. Upon oxygen release from the lattice, transition metal dopants are reduced to the elemental state. Following spontaneous nucleation and growth, metal nanoparticles emerge directly from the oxide matrix, intrinsically creating supported metal catalysts[22,23]. Unlike the conventionally employed deposition methods for supported catalysts' preparation[24,25], in catalysts designed through exsolution the metal nanoparticles are embedded and strongly anchored in the oxide surface, enhancing the cohesion between the nanoparticles and the metal support[26]. This results in the formation of a uniformly distributed and highly stable catalytically active metallic phase on the

surface of the supporting oxide[27]. Within this context, the employment of iron as active phase in metal oxide catalysts has been of interest because of its abundance and lower toxicity compared to other metals[28–30]. In addition to that, the design of materials incorporating multimetallic nanoparticles has gained significant interest in recent years, as these systems demonstrate enhanced catalytic performance compared to monometallic exsolved catalysts. Their unique structural diversity and the synergistic functionalities arising from the presence of multiple metals as active phases enable precise tuning of stability, catalytic activity, and adsorption properties. This makes bimetallic catalysts a highly versatile, cheaper, and more environmentally-friendly alternative to conventional noble metal-based metal oxide catalysts[22,31–33]. This is particularly true for the exsolution of Fe-based multimetallic alloy nanoparticles, since the complex defect chemistry of iron, combined with the presence as co-dopants of metals having different chemical characteristics, makes them particularly versatile in adapting to different applications in heterogeneous catalysis. In light of this, a large share of this dissertation will consider the tailoring of the surface properties of Fe-based multimetallic exsolved perovskite oxides, for catalytic applications in CCU processes.

Understanding the mechanisms behind dopant diffusion and reduction, along with nanoparticle nucleation and growth, is a primary requirement for advancing in the design of bimetallic exsolved materials. Therefore, in **Chapter 5**, mechanistic studies on the exsolution process of FeNi bimetallic alloy nanoparticles from a Fe, Ni-doped strontium titanate perovskite oxide with a 20% A-site deficiency (referred to as LSTFN2) were conducted, using *in-situ* techniques, and particularly *in-situ* X-ray Absorption Near-Edge Structure (XANES) spectroscopy and synchrotron XRD. This was done to gain better understanding of the dynamics of the bimetallic exsolution process, and to acquire knowledge of the experimental process variables on which to act for tailoring the composition and microstructure of the exsolved nanoparticles. This showed how the exsolution temperature, and thus the different reduction kinetics of Ni and Fe during the reduction process, represents a key variable in

tailoring the composition of the exsolved bimetallic FeNi nanoparticles, and so their catalytic selectivity.

After that, the study was extended by taking advantage of a fundamental property of the exsolution process, namely its reversibility. Specifically, by subjecting the exsolved perovskite catalysts to an oxidative atmosphere, it is possible to induce the re-incorporation of the metal cations back into host perovskite matrix, setting the stage for a subsequent new exsolution of the material. Furthermore, unlike traditional metal-support catalysts, exsolved perovskite oxides can be regenerated through redox cycling without causing metal particle agglomeration, preserving an active phase with more stable and extended catalytic activity[34–36]. The reversibility of the exsolution process, together with the ability of influencing the composition of the FeNi alloy on the material's surface by changing temperature, opens up opportunities for the application of the $La_{0.4}Sr_{0.4}Ti_{0.60}Fe_{0.35}Ni_{0.05}O_3$ system as switchable heterogeneous catalyst for CO_2-assisted Oxidative Dehydrogenation of Ethane (ODH) and Dry Ethane Reforming (DER). This research was carried out in collaboration with Anastasios Tsiotsias of the University of Western Macedonia, DongHwan Oh of the Korea Advanced Institute of Science and Technology (KAIST), and Luca Nodari from the Institute of Condensed Matter Chemistry and Technologies for Energy (ICMATE) and the University of Padua. The outcome of this study is reported in **Chapter 6**, where the exsolution behavior of FeNi bimetallic nanoparticles from LSTFN2 was first studied as a function of the exsolution temperature using a number of complementary laboratory and synchrotron characterization methods. The restoring of the original perovskite structure through re-oxidation and the subsequent regeneration of the catalyst materials was also extensively studied, allowing to make use of the redox chemistry of iron for designing perovskite materials with switchable catalytic selectivity.

In light of this, the concept of reversibility through redox cycling in multimetallic exsolution was subsequently extended to another Fe-based perovskite system, again for its application as regenerable heterogeneous catalysts for another CCU technique such as Chemical Looping Reforming (CLR) coupled with CO_2 splitting. In this

study, which has been carried out with DongHwan Oh of KAIST and whose results are reported in **Chapter 7**, a lanthanum ferrite-based perovskite catalyst was designed and employed as a host oxygen carrier for the process. By tailoring the catalyst's surface, Fe ions were first observed to move from the bulk to the surface of the perovskite host material, forming FeCoNi trimetallic nanoparticles which act as active sites for CLR, while later being re-incorporated into the perovskite host phase when subjected to an oxidizing CO_2 atmosphere, leaving bimetallic CoNi particles on the surface. Such reversible composition and switchable catalytic behavior were observed for more than 50 redox cycles, emphasizing the structural flexibility and stable catalytic performance of these materials.

Finally, in the final chapter of this work (**Chapter 8**), the surface morphology and defect chemistry of mesoporous titanium dioxide powders, a widely used heterogeneous catalyst for photocatalytic water splitting, was modified with different techniques, ranging from aliovalent doping to the application of electric fields and UV radiation at high temperatures. This was aimed at investigating the surface interactions between titania and water through water vapor physisorption. The findings reported in the chapter highlighted the critical role of porosity and oxygen vacancy formation in the hydrophilicity of titanium dioxide surfaces.

Overall, this dissertation emphasizes how the design of materials for sustainable catalytic applications is possible by leveraging the redox chemistry of iron. By making use of the process of multimetallic exsolution and of the redox cycling of Fe-based perovskite oxides, it was possible to obtain metal oxides with tailorable selectivity and switchable catalytic performances. At the same time, the investigation of water-surface interactions in mesoporous anatase provides valuable insights into optimizing titanium dioxide for potential applications in photocatalytic water splitting, laying the groundwork for further investigation on the role of porosity and surface oxygen vacancy formation for its interactions with water.

Chapter 2

Theoretical Background

2.1 Perovskite oxides

The discovery of perovskite oxides dates back to 1839, when German mineralogist Gustav Rose identified calcium titanate ($CaTiO_3$) in the Ural Mountains of Russia and named it after Russian mineralogist Lev Aleksevich von Perovski[37]. Nearly a century later, in 1926, Victor Goldschmidt provided the first detailed description of the crystal structure of this class of compounds[38]. Perovskite oxides are generally represented by the formula ABO_3, where the A site is occupied by larger cations, typically rare earth or alkaline earth metals, and the B site hosts smaller cations, often transition metals. The fundamental structural unit of perovskites is the corner-shared BX_6 octahedron, formed by six oxygen anions coordinated around the smaller B site cation. The larger A site cations are positioned in the voids between the octahedral network, resulting in a twelve-fold coordination with oxygen (**Figure 2a**).
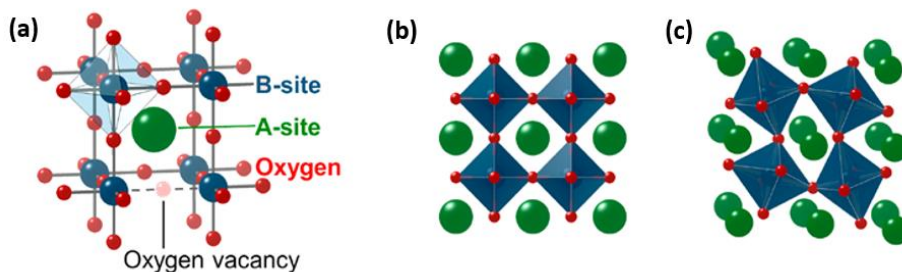

Figure 2. (a) Unit cell of the perovskite oxide. (b) Cubic and (c) distorted rhombohedral perovskite oxides.

The perovskite structure exhibits remarkable compositional flexibility, as it can accommodate substantial deviations from ideal stoichiometry without compromising its structural integrity. Additionally, variations in the sizes of A- and B-site cations are tolerated, allowing the crystal to maintain long-range order despite varying degrees of lattice distortions[39,40]. This enables approximately 90% of metallic elements from the periodic table to be incorporated without affecting its stability. This versatility arises from the wide range of possible cation valence states and from the requirement for charge balance based on the principle of electroneutrality (e.g., $A^IB^VO_3$, $A^{II}B^{IV}O_3$, $A^{III}B^{III}O_3$). The crystal symmetry of the perovskite structure can vary significantly depending on the radii of the cations involved. An empirical method for predicting the symmetry of perovskites is the tolerance factor t, also referred to as the Goldschmidt factor[38] (**Equation 1**):

$$t = \frac{r_A + r_O}{\sqrt{2}(r_B + r_O)} \tag{1}$$

where r_A and r_B are the radii of the respective cationic species and r_O corresponds to the anionic radius of oxygen.

In an ideal perovskite structure, the tolerance factor t equals 1, resulting in a cubic unit cell with the space group Pm-3m, as observed in $SrTiO_3$ (**Figure 2b**). For t values close to unity, within the range of $0.9 < t < 1.0$, the (pseudo)cubic symmetry is preserved. However, when the A-site cation is significantly smaller than the B-site cation ($0.71 < t < 0.9$), the BO_6 octahedra tilt, leading to a loss of symmetry. Equal out-of-phase tilting of the octahedral units along the a, b, and c axes of the ideal cubic perovskite structure results in rhombohedral symmetry, as illustrated in **Figure 2c**. In contrast, out-of-phase tilts restricted to the b and c axes lead to orthorhombic symmetry[41]. On the other hand, when t values exceed unity due to oversized A-site cations, hexagonal and tetragonal symmetries become stabilized.

The structural flexibility of perovskite oxides permits modifications to their crystal lattice, thereby enabling their deployment in a wide range of energy and environmental applications[42]. One effective approach for tailoring the chemical and physical properties of these materials is doping, which involves substituting ions at the A-site or B-site of the ABO_3 lattice with different heteroatoms. This strategy takes advantage of the ability of perovskite oxides to accommodate ions of varying sizes and charges while preserving phase stability[43,44]. In aliovalent doping, host cations in the perovskite lattice are replaced with heteroatoms of differing valence states, resulting in charge imbalances. These imbalances are compensated through oxygen vacancy formation or oxidation state adjustments, thereby improving ionic and/or electronic conductivity[43]. On the other hand, replacing lattice cations with heteroatoms having the same valence state affecting lattice distortions and structural properties without charge imbalance is referred as isovalent doping[45]. When introducing an atom into a host lattice, the Hume-Rothery rules provide the conditions under which an alloy or solid solution can form between two elements[46,47]. These rules can be summarized as follows:

- The atomic radii of the elements should differ by less than 15%;
- Both elements must share the same crystal structure, such as face-centered cubic (FCC) or body-centered cubic (BCC);
- The electronegativity difference between the elements should be less than 0.2 on the Pauling scale;
- The ratio of valence electrons per atom should be similar, typically within ±10%.

When the Hume-Rothery rules are followed, the substitutional element (or solute) integrates in the host lattice and forms a stable solid solution, resulting in uniform properties in the material. However, if the these rules are not respected, the system becomes unstable, often leading to phase separation in the material, i.e. to the formation of secondary phases due to the non-uniform dissolution of the dopant[46,48].

Aliovalent doping leads to the formation of defects in the perovskite oxide's lattice, such as cation vacancies and oxygen vacancies. The former typically form under oxidative conditions or non-stoichiometry, to compensate for charge imbalances, while the latter arise because of aliovalent doping or reducing conditions, where charge imbalance is compensated with oxygen removal from the lattice[42,49]. The formation of such defects allows for the tailoring of the catalytic properties and electronic conductivity of perovskite oxides, improving their performance for applications in heterogeneous catalysis and fuel cells[42,50,51]. Overall, the possibility of tuning the surface properties of perovskite oxides by acting on defects engineering, together with their structural flexibility, makes them valuable candidates for energy applications such as CO_2 reduction and SOFCs[43,51,52].

2.1.1 Strontium titanate for heterogeneous catalysis

Strontium titanate ($SrTiO_3$) is a perovskite oxide material with a cubic unit cell and a lattice parameter of 3.905 Å. Its structure features a tightly bonded network of corner-shared TiO_6 octahedra, which highlights the structural symmetry of the compound[53]. At ambient temperature and pressure, $SrTiO_3$ exhibits a cubic perovskite structure[53]. In fact, while $CaTiO_3$ crystallizes with a orthorhombic structure derived from the cubic perovskite type, with distortions caused by tilting of the TiO_6 octahedra due to the small ionic radius of Ca^{2+} (ionic radius: 1.34 Å), in $SrTiO_3$ the substitution of the smaller Ca^{2+} ion with the larger Sr^{2+} ion (ionic radius: 1.44 Å) results in optimal filling of the cuboctahedral cavity at the A site, which has a coordination number of 12[54,55]. However, cooling it down to 105 K or below induces a phase transition from a cubic (space group: **Pm3m**) to a tetragonal crystal structure (space group: **P4mm**), accompanied by changes in its electrical properties.

The doping of $SrTiO_3$ with different transition metals allows for adjusting its band gap value (that for pure $SrTiO_3$ is 3.2 eV[56]) and for the obtainment of a material with enhanced electronic, ionic and mixed electronic-ionic conductivity[56–58]. Oxygen vacancies, introduced through doping or reducing conditions, enhance cationic

mobility and create active sites for possible catalytic reactions taking place at the surface of the material[53]. Moreover, strontium titanate is thermally stable, having a high melting point of 2080°C, making it suitable for high temperature applications. All of these properties allow for its use in photocatalysis[59], solid-oxide fuel cells[60] and heterogeneous catalysis[53,61,62]. The defect chemistry of strontium titanate will be discussed in detail in **Section 2.5**.

2.1.2 Lanthanum ferrite for Chemical Looping Reforming

Lanthanum ferrite ($LaFeO_3$) is a perovskite-oxide material that typically exhibits an orthorhombic crystal structure, presenting space group *Pnma* and lattice parameters approximately equal to a = 5.601 Å, b = 5.662 Å, c = 7.945 Å[63]. Fe atoms in $LaFeO_3$ reside at octahedral centers and form six covalent bonds with the neighboring oxygen atoms, forming a three-dimensional framework of corner-sharing FeO_6 octahedra, which are tilted to accommodate the atomic-radius mismatch between iron and lanthanum[64]. In fact, when La is paired with a 3d transition metal ion at the B-site (Fe^{3+}) structural distortions are formed, influencing the physicochemical properties of the material. $LaFeO_3$ is studied for its wide range of potential applications, including biosensors and photocatalysis, as well as for its magnetic, optical, and ferroelectric properties[65]. The $LaFeO_3$ lattice's ability to accommodate oxygen vacancies and its flexibility in forming solid solutions at the A-site and B-site allow for the obtainment of tailorable electronic and structural properties[66–68]. These characteristics, together with the thermally stable structure of $LaFeO_3$ as parent oxide, makes it suitable for applications as electrode materials in solid oxides fuel cells, and as heterogeneous catalysts for CO_2-splitting and as oxygen carrier for Chemical Looping Reforming (CLR)[69–73].

In particular, effective catalysts for CLR should possess high reactivity, good oxygen storage capacity, and resistance to coking and redox cycling degradation[74]. The introduction of elements with a lower oxidation state at the A-site of $LaFeO_3$ (i.e.,

Sr^{2+}, Nd^{2+}) has been shown to lead to enhanced CO selectivity, methane activation, and oxygen storage capacity. In particular, the introduction of Sr^{2+} cations (ionic radius: 1.44 Å) into the parent lanthanum ferrite host substituting La^{3+} (1.36 Å) determines the formation of a solid solution with composition $La_{1-x}Sr_xFeO_{3-\delta}$, which was shown to be a promising candidate for CLR[75–78]. This is because an electronic unbalance develops in the perovskite lattice, which can be compensated by the generation of oxygen vacancies and the oxidation of a fraction of Fe^{3+} ions to Fe^{4+}. The formation of oxygen vacancies determines the release of lattice oxygen under reducing conditions, while iron oxidation improves oxygen mobility and ensures efficient cycling between oxidized and reduced states during CLR[78,79]. Ca has also emerged as a promising dopant for substitution of lanthanum at the A-site in $LaFeO_{3-\delta}$, for use in volatile organic compounds (VOCs) oxidation and chemical looping reforming, since the similar ionic radii of Ca^{2+} and La^{3+} ensure structural compatibility, offering greater stability compared to Sr^{2+}, and enhancing the material's durability and performance[80]. Partial calcium substitution was shown to modify the orthorhombic structure of the $LaFeO_3$ perovskite towards a less distorted one, by also promoting the formation of Fe^{4+} species, which were attributed to an improvement of the catalytic activity of the material[81].

2.2 Titanium dioxide and its applications as photocatalyst

Titanium dioxide (TiO_2) is an inorganic compound existing in three primary allotropic forms: rutile (tetragonal, a = b = 4.854 Å, c = 2.953 Å), brookite (rhombohedral, a = 5.436 Å, b = 9.166 Å, c = 5.135 Å) and anatase (tetragonal, a = b = 3.782 Å, c = 9.502 Å)[82] (**Figure 3**), with rutile being the most thermodynamically stable. These forms differ in their crystal structures, physical properties and applications. In all three of them, each of the Ti^{4+} ions is surrounded by an irregular octahedron of oxide ions, with the number of edges shared by the octahedron increasing from two in rutile to three in brookite to four in anatase[82].
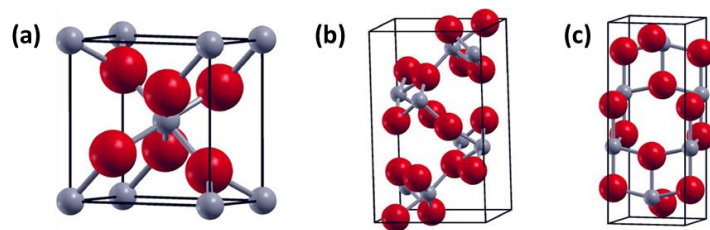
Figure 3. Allotropic forms of titanium dioxide: (a) rutile, (b) brookite and (c) anatase.

In 1972, Fujishima and Honda[83] published a groundbreaking study on hydrogen production using titanium dioxide photoelectrodes under UV light. This work established semiconductor photocatalysis as a highly promising method for both hydrogen generation and pollution control, allowing for a wide range of applications[84–87], such as in sustainable energy generation and in the removal of environmental pollutants[84]. Titania is widely used due to its good photocatalytic performance, robust chemical and biological stability, insolubility in water, resistance to acidic and basic environments, non-toxicity, affordability, and wide availability[84,88–90]. That is because TiO_2 is a semiconductor, with a band gap of 3.2 eV lying in the UV range and transparent in the visible region[82].

A widely studied use of titania is represented by photocatalytic water splitting, which allows for green hydrogen production by converting solar energy into chemical energy by splitting water (H_2O) into gaseous hydrogen (H_2) and oxygen (O_2)[91,92].

In the context of photocatalysis, anatase and rutile are the most commonly studied allotropes due to their stability and photocatalytic activity, while brookite is less common and metastable[93]. Anatase is stable at lower temperatures and features a pyramidal crystal structure, while rutile, characterized by a needle-like shape, becomes dominant at calcination temperatures ranging from 700 to 1000°C. For applications in photocatalysis, the anatase polymorph is generally preferred, as it has been observed to exhibit higher photocatalytic activity than rutile across various reaction media, making it suitable for different photocatalytic processes[94–99].

Precursor chemistry plays a crucial role in determining the nucleation and growth of TiO_2 polymorphs, as they depend on the reactants used. However, understanding nanoparticle formation is complicated by the wide range of experimental conditions

employed for synthesizing different TiO_2 phases, adding complexity to the study of its polymorphic behavior. The morphology and crystal structure of titanium dioxide are key determinants of its photocatalytic activity, with crystallite size and specific surface area being critical factors. TiO_2 1D nanostructures have garnered significant research interest due to their high aspect ratio, enhanced surface area, and efficient charge transport properties, showing better performances then 0D and 2D counterparts[99–102].

For explaining the mechanism by which semiconductors are used for photocatalysis, according to band energy theory, the discontinuous band structure of semiconductors consists of low-energy valence bands filled with electrons, high-energy conduction bands, and a band gap separating them[84]. When the energy of incident photons matches or exceeds the band gap, electron–hole pairs are photoexcited, initiating photocatalytic redox reactions. The photocatalytic process involves several key steps, including the generation, separation, recombination, and surface capture of photogenerated electron-hole pairs. A schematic of the photocatalytic pollutant degradation in water using a semiconductor is reported in **Figure 4**[84].

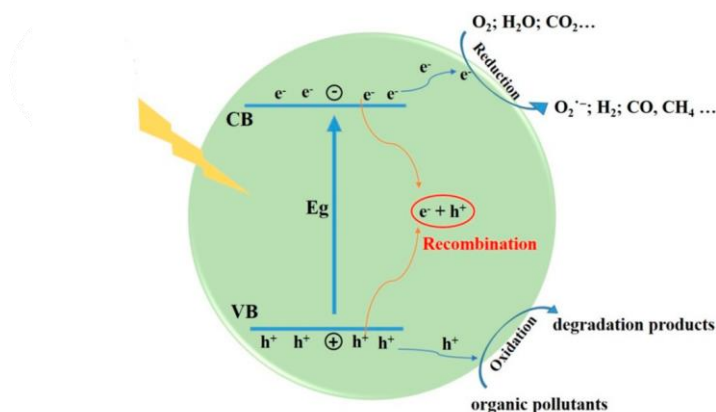**Figure 4.** Photocatalytic process in a semiconductor. Reported from Kang et. al[84].

Photochemical reactions occur on the catalyst's surface and include two half-reactions: oxidation by photogenerated holes and reduction by photogenerated electrons. However, a significant portion of charge carriers (e^-/h^+ pairs) recombines rapidly within the bulk material or at its surface, dissipating absorbed energy as light

(photon emission) or heat (lattice vibrations). This recombination reduces the availability of charge carriers for photocatalytic reactions, negatively impacting the overall efficiency of the process[84]. Electrons and holes that successfully migrate to the semiconductor surface without recombining participate in reduction and oxidation reactions, forming the basis for processes like the photodegradation of organic pollutants and photocatalytic water splitting to produce hydrogen. Photogenerated holes, as strong oxidizers, can directly mineralize organic pollutants or form hydroxyl radicals ($^{\bullet}OH$) with potent oxidizing properties. Meanwhile, photoexcited electrons can generate superoxide radicals ($O_2^{\bullet-}$) and $^{\bullet}OH$, which, along with e^-/h^+ pairs, drive various redox reactions. In water splitting, electrons reduce H^+ to produce hydrogen, while holes oxidize H_2O to form oxygen.

In the context of applications of titania for photocatalytic water splitting, a sufficient porosity in TiO_2 increases the specific surface area, which allows for increased light absorption and better interaction with water molecules, enhancing hydrogen production. Porous TiO_2 structures exhibit improved charge separation and reduced recombination of electron-hole pairs, which are critical for photocatalytic activity[103]. However, excessive porosity can also lead to faster recombination of electron-hole pairs, reducing photocatalytic efficiency. Thus, an optimal balance between porosity and crystallinity is essential for maximizing photocatalytic performance[93]. Among the disadvantages of using titanium dioxide for photocatalysis are to be mentioned its limited absorption of visible light, the rapid recombination of electron–hole pairs, and the slow charge carrier transfer to the surrounding medium, all of which significantly hinder its photocatalytic performance. To address these challenges, some strategies have been proposed, such as minimizing e^-/h^+ recombination by enhancing optical absorption through energy band tuning and control of the material's morphology[84].

2.3 Iron oxides

Iron can readily undergo oxidation and reduction reactions, transitioning between different oxidation states, and it is able to form a variety of oxides with different crystal structures and properties. The thermodynamic relationships and phase stability of iron oxides under varying conditions of temperature, pressure and oxygen partial pressure are described by the Fe–O phase diagram (**Figure 5**). Iron also forms mixed oxides with other transitional metals, like in the case of $NiFe_2O_4$. An overview of the single and mixed iron oxides mentioned in this dissertation is provided in the following sections.
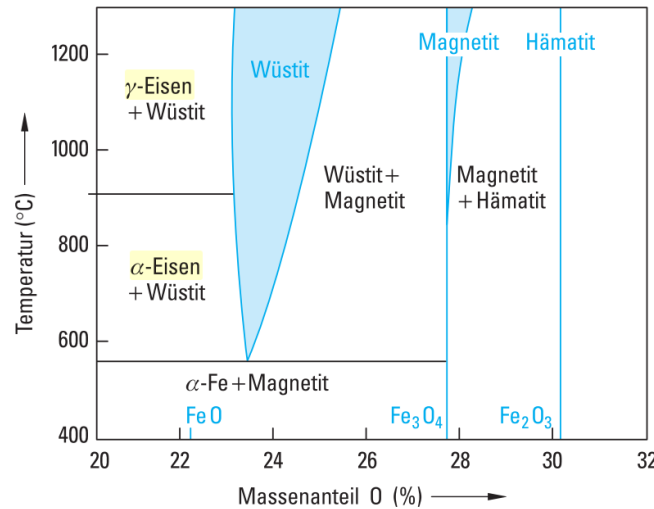
Figure 5. Fe-O phase diagram, plotted with the weight fraction of oxygen on the x-axis and the temperature on the y-axis[104].

2.3.1 Nickel ferrite

Nickel ferrite ($NiFe_2O_4$) is a spinel structure that crystallizes in the cubic space group $Fd\bar{3}m$ and has eight formula units per unit cell[105]. Spinels can be denoted by the general formula AB_2O_4, where A is a divalent and B is a trivalent transition metal cation[106]. In a prototypical AB_2O_4 structure, oxide ions form a (slightly distorted) cubic close-packed arrangement (stacking sequence ABC...), in which 1/8 of the tetrahedral voids are occupied by A ions and 1/2 of the octahedral voids are occupied

26

by B ions[105]. The spinel unit cell consists of 56 atoms: 32 oxygen (O^{2-}), 16 trivalent metal cations (B^{3+}) and 8 divalent metal cations (A^{2+}).

The spinel structure can be classified as either normal or inverse. In the normal spinel, divalent A cations exclusively occupy tetrahedral sites, while trivalent B cations are located at octahedral sites[107,108]. In the ideal inverse spinel, half of the B cations occupy tetrahedral sites, and A cations are found at octahedral sites, with no strong preference for specific interstitial positions[105]. Intermediate configurations also exist, characterized by the inversion degree (λ), which represents the fraction of B cations at tetrahedral sites. The extremes are $\lambda = 0$ for normal spinels and $\lambda = 0.5$ for inverse spinels. The inversion degree can also be temperature-dependent, and it depends on whether the synthesis route has been carried out at lower or higher temperatures[105]. In the case of $NiFe_2O_4$, bulk crystals exhibit an inverse spinel structure with degree of inversion equal to 85.5%, having a cubic lattice parameter of a = 8.337 nm[109] (**Figure 6**).
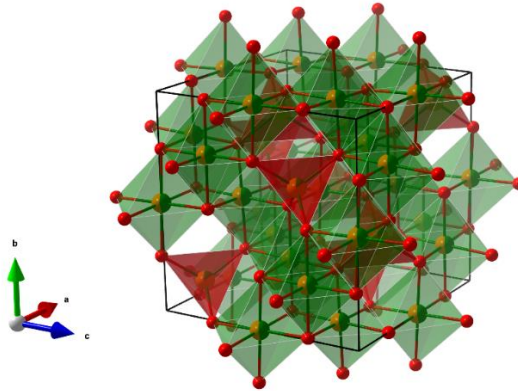

Figure 6. Crystal structure of $NiFe_2O_4$ partially inverse spinel. Image generated by Dr. Frank Hoffmann.

2.3.2 Wüstite

Wüstite is among the most studied non-stoichiometric compounds, and it is represented by the formula $Fe_{1-x}O$, with $0.04 < x < 0.12$. Unlike stoichiometric compounds, which exhibit fixed ratios of reactants and products based on positive

integers, non-stoichiometric ones have compositions that deviate from simple integer ratios, resulting in apparent non-rational formulas[110]. While the "ideal" stoichiometric compound FeO crystallizes in the cubic NaCl structure type (space group $Fm\bar{3}m$), it cannot exist as a stable phase at low pressures or at pressures in excess of 10 MPa. The non-stoichiometry is therefore accommodated by oxidation of a proportion of the metal ions and the creation of cation vacancies[111]. The stable, cation-deficient wüstite phase, represented as $Fe_{1+x}O$, forms at a pressure of 0.1 MPa and temperatures above 567 °C. Upon slow cooling to temperatures below 567 °C, this phase disproportionates into Fe metal and Fe_3O_4. At this temperature, the equilibrium curves of $Fe/Fe_{1+x}O$ and $Fe_{1+x}O/Fe_3O_4$ intersect. If, however, $Fe_{1+x}O$ is rapidly quenched from the equilibrium region, the non-stoichiometric form can be obtained as a metastable phase at room temperature[111]. The ideal structure of FeO can be described as two interpenetrating face-centered cubic lattices, on formed by Fe^{2+} and the other by O^{2-} ions (**Figure 7**). The cubic unit cell contains four formula units and, depending on the vacancy content, the lattice parameter ranges from 0.428± 0.431 nm[111].
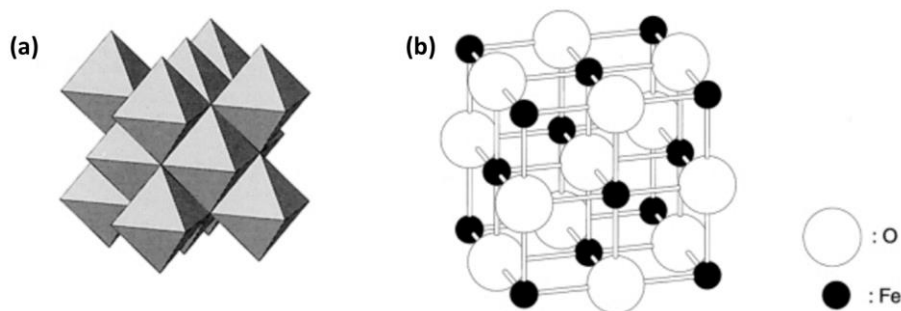
Figure 7. Structure of wüstite. (a) Arrangement of octahedra and (b) ball-and-stick model[111].

2.3.3 Magnetite

Magnetite (Fe_3O_4) was one of the first mineral structures studied using X-ray diffraction in 1915, marking a significant milestone in crystallography. It crystallizes as an inverse spinel structure, represented by the formula $(Fe^{3+})^{tet}[Fe^{2+}Fe^{3+}]^{oct}O_4$, where Fe^{3+} occupy tetrahedral sites and both Fe^{2+} and Fe^{3+} ions are located at

octahedral sites (Figure 8). Magnetite has a FCC unit cell composed of 32 O^{2-} ions, arranged in a cubic close-packed configuration along the [111] direction. The unit cell has an edge length of a = 0.839 nm and contains eight formula units. Unlike most other iron oxides, magnetite contains both divalent (Fe^{2+}) and trivalent (Fe^{3+}) iron, with a stoichiometric Fe^{2+}/Fe^{3+} ratio of 0.5. However, magnetite is often non-stoichiometric, exhibiting a cation-deficient Fe^{3+} sublattice. The divalent iron can be partially or fully replaced by other divalent ions, such as Mn^{2+} or Zn^{2+}. This substitution is facilitated by the flexibility of the oxygen framework, which can expand or contract to accommodate cations of varying sizes, leading to changes in the unit cell edge length. These structural and compositional features contribute to magnetite's unique physical and chemical properties[105,111].
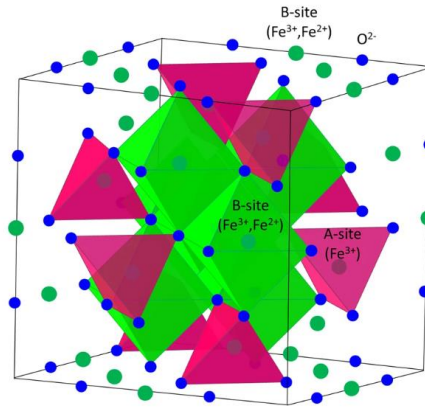
Figure 8. Inverse spinel crystal structure of magnetite[112].

2.3.4 Maghemite

Maghemite has a structure similar to magnetite but differs in that all or most of its iron exists in the trivalent state, with cation vacancies compensating for the oxidation of Fe^{2+}. It crystallizes as a cubic spinel structure with a lattice parameter of a = 0.834 nm, containing 32 O^{2-} ions, 21 1/3 Fe^{3+} ions, and 2 1/3 vacancies per unit cell. Eight cations occupy tetrahedral sites, while the remaining cations and vacancies are randomly distributed across octahedral sites, with vacancies confined to the octahedral sites. This arrangement contributes to maghemite's metastability and enables phase transitions to hematite (α-Fe_2O_3) at elevated temperatures, typically

above 700 °C. The extent of vacancy ordering is influenced by crystallite size, the nature of the precursor, and the amount of Fe^{2+} in the structure. It was also observed that as synthetic Fe_3O_4 crystals ($\approx$200 nm) were oxidized, a series of intermediate phases with decreasing Fe^{2+} levels formed, corresponding to a magnetite/maghemite solid solution. The cell edge length of this solid solution ranges continuously from 0.8338 to 0.8389 nm, reflecting the structural evolution of maghemite during oxidation[111,113].

2.4 Materials' preparation

2.4.1 Polymer complex route

A valuable route for the preparation of multicomponent phase-pure perovskite oxides at intermediate temperatures is the Pechini method. This involves incorporating chelating agents, such as citric acid, along with a polyol, typically ethylene glycol, into a solution containing metal precursors. Citric acid acts as a complexing agent for the metal cations, forming a metal-citrate monomer. Upon moderate heating at 130 °C, this monomer undergoes polymerization in the presence of the polyol through a polyesterification process. The reaction results in the homogeneous "trapping" of metal ions within a covalent network. Subsequent thermal treatment at high temperatures ($\leq$ 900 °C) leads to the decomposition of the organic components and the formation of a nanostructured single-phase multi-metal oxide[114,115]. The stability of the metal-citrate complex facilitates the uniform atomic-level distribution of metal ions within the polymer matrix, thereby preventing phase separation and ensuring phase purity[116]. A schematic of the steps involved in the Pechini process are reported in **Figure 9**[117].
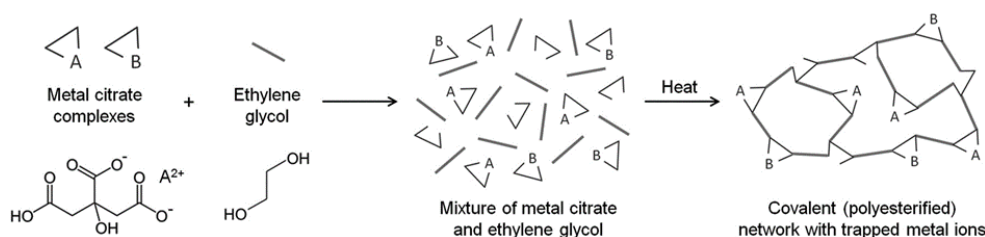
Figure 9. Schematic representation of the steps of the Pechini process[117].

The Pechini method has served as the foundation for numerous modifications aimed at optimizing the morphology and composition of the final product. These modifications often involve adjustments to cation precursors, complexing agents, solvents, and pH levels, and are commonly referred to as polymer complex routes. The core principle of these methods lies in the formation of a polymeric resin precursor composed of randomly branched polymer molecules, ensuring a homogeneous distribution of cations. Since the complexation of metal ions in organic solvents, such as citric acid, is strongly influenced by the solution's pH, precise control is essential for achieving uniform metal-chelate complexes and a consistent final metal oxide product. Bases like ammonia and ammonium hydroxide are typically used to regulate the pH of the metal citrate solution[117,118]. Although polymer complex synthesis typically excludes water, certain salts with low solubility in the metal-citrate solution, such as $(SrNO_3)_2$, require prior dissolution in water before incorporation. The addition of highly water-soluble metal precursors can lead to premature hydrolysis before complexation, resulting in a heterogeneous mixture and phase separation during calcination, accompanied by oxide formation. To counteract the rapid hydrolysis kinetics of metal precursors, such as nitrates, larger precursors like acetates are often used to enhance metal binding and preserve homogeneity[119].

2.4.2 Sol–gel process

The term 'sol' generally refers to a stable colloidal system where solid particles are suspended in a liquid medium[120]. These particles, though denser than the liquid, are small enough for dispersion forces to counteract gravity. Sols are classified as lyophobic or lyophilic, depending on the strength of interactions between the solvent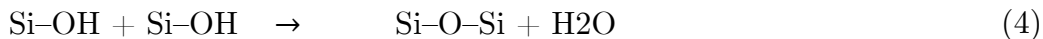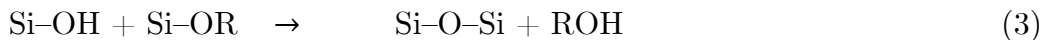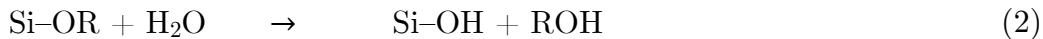 and particles. Lyophobic sols have weak solvent-particle interactions, while lyophilic sols exhibit much stronger ones. The stability of sols is driven by repulsive forces between particles, which prevent agglomeration and coagulation. However, when additives neutralize the particle charges, the system loses stability, leading to flocculation and eventually gel formation[82]. A 'gel' by contrast, is a porous, three-dimensional interconnected solid network that appears transparent due to the small size of its particles[121]. In simpler terms, a gel is a semi-solid, two-component system where a solid is dispersed in a liquid. Gelation is the process by which a sol or solution transforms into a gel, with the continuous solid network providing elasticity to the material. The solid particles within the gel can be amorphous, crystalline, or macromolecular. Gels are classified based on the nature of their solid network: if it consists of colloidal sol particles, the gel is termed colloidal, whereas networks formed from sub-colloidal chemical units are considered polymeric.

The sol-gel process is particularly well suited to create inorganic-organic hybrid materials, because the solids are formed at low temperatures, at which organic groups are not degraded[122]. This method involves transforming soluble molecular or oligomeric compounds into extended inorganic oxidic networks, resulting in amorphous or microcrystalline solids. Sol-gel processing proceeds in four steps: hydrolysis and condensation of the molecular precursors and formation of sols, gelation (i.e. sol-gel transition), aging and drying. Initially, colloidal particles (sol) are formed, which subsequently aggregate into an extended gel network[123]. Gel formation can occur in two ways: solid gels may be dissolved (peptized), with the resulting sols re-aggregated under different conditions (typically at a different pH), or sol particles can be generated through chemical reactions from molecular

precursors, such as hydrolyzable metal salts or metal and semi-metal alkoxides. Alkoxides are particularly significant as precursors for porous oxide materials, especially when preparing organically modified materials.

The chemical reactions involved during sol-gel processing of metal or semi-metal alkoxides can be formally described by **Equations 2, 3, 4** describing hydrolysis and condensation reactions[122]:

Si–OR + H_2O	$\rightarrow$	Si–OH + ROH	(2)
Si–OH + Si–OR	$\rightarrow$	Si–O–Si + ROH	(3)
Si–OH + Si–OH	$\rightarrow$	Si–O–Si + H2O	(4)

In the first part of Reaction 2, Si–OR groups are hydrolyzed, and reactive Si–OH groups are created. The Si–OH groups then undergo condensation reactions (by elimination of water or alcohol), which result in a stepwise build-up of the oxide network (Reaction 3 and 4). The formation of sol-gel materials is kinetically controlled, meaning that reaction conditions – such as solvent, pH, additives, concentration, and temperature – strongly influence the resulting network structure. Among these, pH is particularly critical, as processing $Si(OR)_4$ under acidic or basic conditions yields different types of silica networks[122]. Metal alkoxides exhibit much higher reactivity towards water compared to alkoxysilanes, often leading to spontaneous precipitation. While alkoxysilane reactions require acid or base catalysts to enhance reactivity, the reaction rates of metal alkoxides must be moderated to produce gels instead of precipitates. This is typically achieved by substituting some alkoxy groups with chelating or bridging ligands, forming compounds like $M(OR)_{n-x}L_x$ (L = bidentate anionic ligand). These ligands, such as acetates or β-diketonates, alter the reactivity, structure, and functionality of the precursors, and are largely retained during hydrolytic polycondensation.

Gels consist of a sponge-like, three-dimensional solid network with pores filled by a liquid, typically water or alcohol. The processing of the sol allows the creation of ceramics in different forms. Casting the sol into a mold results in a wet gel, which

can be dried and heat-treated to produce dense ceramics[82]. Wet gels formed via hydrolysis and condensation are termed aquagels, hydrogels, or alcogels. When the pore liquid is replaced by air without significant shrinkage or structural damage, aerogels are obtained. Conversely, conventional drying methods result in xerogels, which experience substantial shrinkage due to capillary forces acting on the pore walls during liquid evaporation. To prevent collapse of the porous network, specialized drying techniques, such as supercritical drying, are employed to produce aerogels[122]. Two approaches can be employed to incorporate organic groups into an inorganic network: embedding organic molecules into gels without chemical bonding and incorporating them through covalent bonding. Embedding organic molecules or polymers into the inorganic host is typically achieved by dissolving them in the precursor solution, where the gel matrix forms around and traps them. A wide range of organic or organometallic molecules can be utilized in this process, including dyes, catalytically active metal complexes, sensor compounds, biomolecules, or polymers[122]. Adjusting the sol's viscosity enables the drawing of ceramic fibers, while ultra-fine powders can be produced through precipitation, spray hydrolysis, or emulsion techniques. A summarizing schematic of these processes is reported in **Figure 10.**
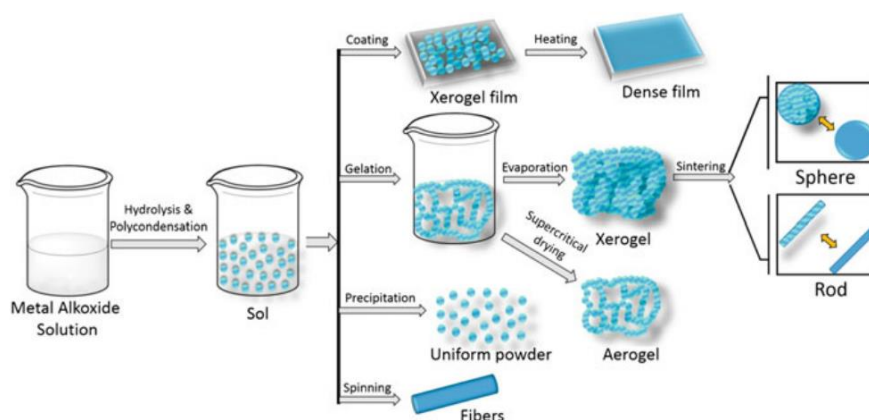

Figure 10. Schematic representation of the sol-gel process[82].

The sol-gel process for the synthesis of metal oxides offers several advantages, including enhanced chemical homogeneity in multi-component and doped systems, as well as the ability to produce high-surface-area powder materials. The method also

ensures considerable chemical purity in the final products by eliminating grinding and pressing steps. It requires only simple equipment and operates at relatively low preparation temperatures, making it accessible. However, the method also has drawbacks, such as the high cost of precursors, extended processing times, significant shrinkage during production, and the potential formation of hard agglomerates[82].

2.4.3 Synthesis of mesoporous materials via templating

A wide variety of porous inorganic frameworks is now well-known. These materials can be distinguished by the arrangement of the pores – either periodic or random – and the pore radii distribution, which may vary from narrow and uniform to broad and diverse. In the context of porous materials, not only pore size distribution and diameters are important for future applications, but also the connectivity and dimensionality of the pore system play a crucial role[124].

Hexagonally ordered mesoporous silicate structures were first identified in 1992 by Mobil Corporation (M41S materials) and independently by Kuroda, Inagaki, and their collaborators (FSM, folded sheet materials). These materials are mesoporous solids featuring a periodic and highly organized arrangement of well-defined pores, with adjustable pore sizes ranging from 2 to 50 nm. Silica-based variants typically feature an amorphous, inorganic framework and are characterized by their high specific surface area[124].

Supramolecular assemblies, which are structures formed through the self-organization of molecules via non-covalent interactions like hydrogen bonding, electrostatic forces, and van der Waals forces, can serve as templates for inorganic matrices. This process, known as supramolecular templating, leverages the ability of amphiphilic molecules, such as surfactants (e.g., soap in water), to self-assemble into micellar structures. In concentrated aqueous solutions, these micelles undergo further self-organization, forming lyotropic liquid crystalline mesophases. Molecular inorganic species can co-assemble with these structure-directing agents (templates) in a cooperative manner, eventually condensing to create the mesoscopically ordered inorganic framework of

the final material (**Figure 11**). The mesostructured nanocomposite is typically subjected to calcination or solvent extraction processes to yield a porous inorganic material. Their discovery gave a strong impulse in the field of templating and patterning inorganic structures to get periodic, regularly sized and shaped channels, layers and cavities[124].
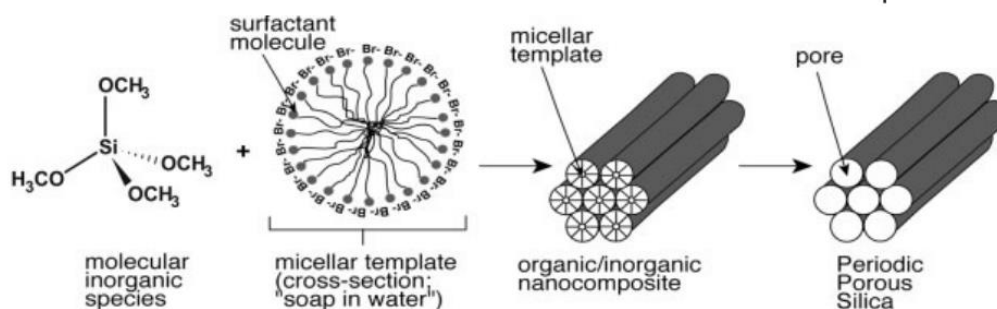
Figure 11. Synthetic cooperative self-organization pathway to M41S materials.

The pore size in porous materials synthesized with this method is primarily influenced by the chain length of the hydrophobic tail of the template molecule, typically ranging from 2 to 30 nm with a relatively monomodal size distribution.

Depending on the available liquid-crystalline phases – such as cubic, hexagonal, or lamellar arrangements – different porous structures with unique connectivity and dimensional properties can be formed in the resulting mesoporous material (**Figure 12**). The templating of a lamellar solvent-induced phase results in a non-porous inorganic matrix, as the lamellar structure collapses upon removal of the templating agent. In contrast, hexagonal phases produce one-dimensional channel systems with a high aspect ratio, where the channel length far exceeds the pore diameter. Cubic phases, on the other hand, create a three-dimensional pore network with cubic symmetry[124]. Examples of notable mesoporous silica matrices include MCM-41, which features hexagonal, one-dimensional pores and is synthesized using a cationic template under alkaline conditions, and SBA-15, which also exhibits a hexagonal, two-dimensional pore structure but is synthesized under acidic conditions with a neutral block copolymer template. For these materials, the inorganic framework is

often modified with organic groups to introduce specific surface chemistry or active sites within the pores or along their inner surfaces.
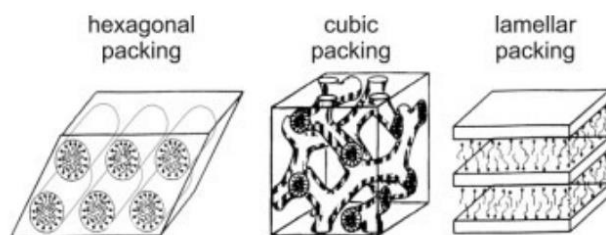
Figure 12. Hexagonal, cubic and lamellar packings resulting in 1-D and 3-D pore dimensionalities[124].

These modifications make the material suitable for applications in catalysis, sensing, separation technologies and other fields[124]. Block copolymer templating is widely employed for synthesizing mesoporous metal oxides, such as titanium dioxide. This technique utilizes amphiphilic block copolymers as structure-directing agents in nonaqueous solutions to organize metal oxide precursors into ordered mesostructures. By adjusting synthesis conditions, it enables precise control over pore size and framework properties. The resulting materials feature robust frameworks and thick channel walls capable of hosting nanocrystallites. This method has also been successfully applied to various other metal oxides, such as ZrO_2, Nb_2O_5, Ta_2O_5, and Al_2O_3[125].

2.5 Point defects

Defects play a vital role in determining the chemical and physical properties of solids, and a significant portion of modern materials science and technology is dedicated to leveraging or regulating their impact on solid materials. The simplest concept of a defect in a solid is a disruption in the crystal lattice, such as a missing atom or an impurity substituting a regular atom, referred to as point defects. Later, more complex defects, such as linear ones known as dislocations, were introduced to explain the mechanical behavior of metals. Additionally, planar defects like surfaces and grain boundaries, as well as volume defects such as rods, tubes, or precipitates, were

recognized as significant factors influencing the physical and chemical properties of solid materials[126]. Defects can therefore be categorized into a dimensional hierarchy, including point defects (zero-dimensional), linear defects (one-dimensional), planar defects (two-dimensional), and volume defects (three-dimensional). This section focuses on the discussion of point defects.

Two different types of simple point defects can occur in a pure crystal of an element M. One involves an atom missing from a normally occupied position, creating a vacancy, denoted as V_M. The second type occurs when an extra atom is incorporated into the structure, occupying a position in the crystal that is not a normally occupied site. This is referred to as an interstitial site, and the atom is called an interstitial, denoted as M_i (**Figure 13a**)[127].
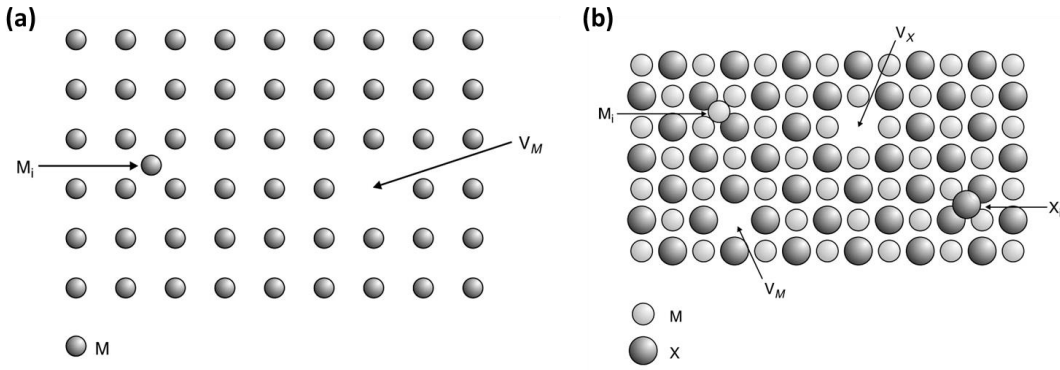
Figure 13. (a) Point defects in a pure monatomic crystal of an element M, a vacancy, V_M, and a self-interstitial, M_i. (b) Point defects in a crystal of a pure compound MX; V_M and V_X represent the vacancies of the species M and X, respectively, while M_i and X_i correspond to interstitial sites of species M and X, respectively. Reported from Tilley[126].

Point defects in a crystal, such as vacancies, interstitials, excess electrons, holes, and other configurations, are collectively referred to as native defects. Additionally, defects can form when the crystal is exposed to high-energy particles or radiation, and these are known as induced defects. When a pure crystal is heated at moderate temperatures for an extended period, the number of native defects changes gradually, but a population of point defects persists even in the purest crystal. These defects, which exist in thermodynamic equilibrium, are termed intrinsic defects, and their concentration depends on temperature[126]. Considering pure compounds, the same

intrinsic defects as described for a pure crystal can occur, but in these cases more than one set of atoms that can be affected. For example, in a crystal of formula MX, vacancies might occur on M positions, written V_M, or on X positions, given the symbol V_X, or both. Similarly, it is possible to imagine that interstitial M atoms, written M_i, or interstitial X atoms, written X_i, might occur (**Figure 13b**). The different groups of atom types within a crystal are often referred to as sublattices. For instance, one might describe vacancies as occurring on the M sublattice or the X sublattice. The intrinsic point defects that are formed in a crystal have an effective charge (q_e), which is defined as the charge that the defect has with respect to the charge that would be present at the same site in a perfect crystal. Thus, the value of the effective charge corresponds to the difference of the real charge of the defect species, z_d, subtracted by the real charge at the site occupied in a perfect crystal, z_s[126]:

$$q_e = z_d - z_s \qquad (5)$$

To distinguish effective charges from real charges, the superscript ′ is used for each unit of effective negative charge and the superscript • is used for each unit of effective positive charge. The real charges on a defect are still given the superscript symbols − and +[126]. Moreover, a neutral effective charge is expressed by employing the superscript x. This formalism for describing defect equilibria in ionic crystals is known as the Kröger-Vink notation[128,129]. The most common defects types found in $SrTiO_3$ are reported in **Table 1** using this notation.

Table 1. Kröger-Vink notation for typical defects found in $SrTiO_3$[128].

Type of defect	Kröger-Vink Notation
Fully ionized strontium vacancy	V_{Sr}''
Fully ionized oxygen vacancy	$V_O^{\cdot\cdot}$
Lanthanum substituted at strontium site	$La_{Sr}^{\cdot}$
Nickel substituted at titanium site	Ni_{Ti}''
Electrons	e'
Holes	$h^{\cdot}$
Neutral strontium at regular strontium site	Sr_{Sr}^x
Neutral titanium at regular titanium site	Ti_{Ti}^x
Neutral oxygen at regular oxygen site	O_O^x

In ionic compounds, point defects are charged and typically form in pairs to maintain electrical neutrality. Charge equilibrium can be achieved in two ways. A Schottky defect (**Figure 14a**) forms when vacancies of oppositely charged ions occur at lattice sites, compensating for each other and preserving charge balance, and these defects are frequently observed in perovskite oxides due to their structural characteristics. In contrast, Frenkel defects involve an ion moving to an interstitial position, leaving behind a vacancy of opposite charge (**Figure 14b**). The formation of such defects is energetically unfavorable in perovskite oxides, because of the tightly packed lattice structure[49,130]. No material is entirely pure, and foreign atoms are inevitably present. If these atoms are unwanted, they are referred to as impurities; however, if they are intentionally introduced to modify the material's properties, they are called dopant atoms. The deliberate addition of such impurities is known as aliovalent doping. Unlike intrinsic defects, which arise from the displacement of native lattice atoms, extrinsic defects are formed through the incorporation of dopants into the host perovskite lattice.
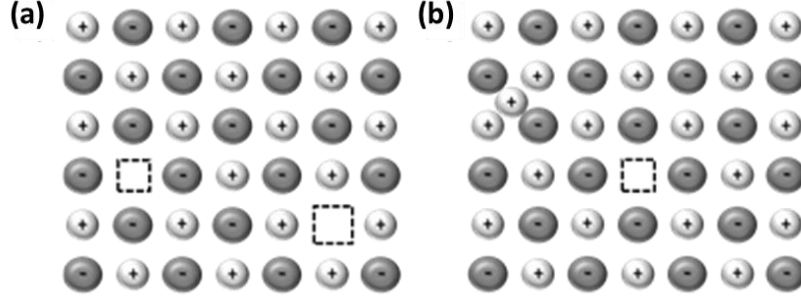
Figure 14. Schematic of Schottky (a) and Frenkel (b) defects[126].

When doping perovskite oxides such as $SrTiO_3$, the introduction of the dopant within the A or B sublattice of the host structure is largely dictated by its ionic radius. While many elements with an appropriate ionic radius can occupy various lattice positions within a material, only dopants with a different charge can generate point defects due to the requirement for charge compensation. In perovskites, this charge compensation can lead to the formation of defects such as holes, electrons, cationic vacancies, or oxygen vacancies, as will be discussed in the next subsection[131].

2.5.1 Donor-doping of SrTiO₃ with lanthanum

Doping $SrTiO_3$ with trivalent lanthanum ions (La^{3+}) determines the substitution of Sr^{2+} ions at the A-site of the perovskite structure. Due to its larger ionic radius, La^{3+} can only occupy this position to preserve the perovskite lattice. The site occupied by a cation dopant in the strontium titanate lattice is determined by its ionic radius and coordination number, as illustrated in **Figure 15**. Introducing a dopant with a higher valence than the native ion, such as La^{3+}, is referred to as donor doping[126]. The additional positive charge that La^{3+} introduces at the Sr-site has to be balanced for charge neutrality. This can occur either through the formation of negatively charged defects, such as cationic vacancies, or oxygen interstitials. However, due to the high atomic packing density of the perovskite structure, charge compensation typically occurs via the formation of cationic vacancies, as the creation of oxygen interstitials is not favored in perovskite oxides[132].
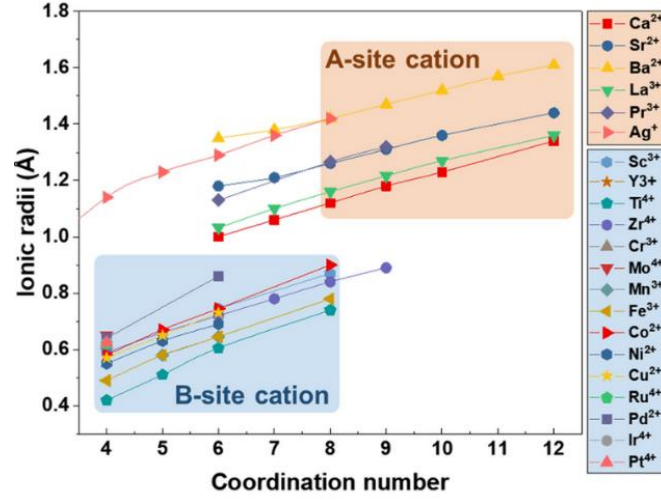
Figure 15. Metal cation radii as a function of their coordination number[36].

The formation of cation vacancies is influenced by the degree of lanthanum solubility, which depends on synthesis conditions such as atmosphere, oxygen partial pressure (pO_2), temperature, and duration. Based on the Hume-Rothery rules, 12-fold coordinated La^{3+} ions, with an ionic radius of 1.36 Å, demonstrate high solubility in $SrTiO_3$ due to their size similarity to strontium ions, which have an ionic radius of 1.44 Å in the same coordination environment[54].

The literature indicates that under oxidative synthesis conditions, lanthanum achieves complete solubility in $La_xSr_{1-x}TiO_3$, maintaining the cubic phase up to 40 at.% and transitioning to an orthorhombic distortion at 60 at.%[133]. Furthermore, it has been demonstrated that for doping levels up to 30 at.%, the charge compensation mechanism is exclusively governed by strontium vacancies (V_{Sr}''), while at doping levels beyond 40 at. % a minor fraction of titanium vacancies (V_{Ti}'''') begins to form. However, these titanium vacancies remain negligible compared to the predominance of strontium vacancies[133]. Therefore, ignoring the titanium vacancies, the charge compensation can be represented using the Kröger-Vink notation as (**Equation 6**):

$$La_2O_3 \,(3SrTiO_2) \rightarrow 2La_{Sr}^\bullet + V_{Sr}'' + 3Ti_{Ti}^X + 9O_O^X \qquad (6)$$
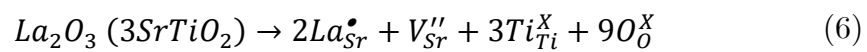
The formation of cationic vacancies plays a critical role in the exsolution process, as the exsolvable metal cations segregate and migrate through the lattice via oxygen vacancies. These oxygen vacancies also act as initial nucleation sites for the growth of metal nanoparticles[134].

2.5.2 Acceptor-doping of SrTiO₃ with nickel

Acceptor dopants in a compound are impurity ions of lower valence than that of the parent ions at the same lattice site[126]. Introducing dopants at the B-site of perovskite oxides significantly impacts both their crystal lattice and electronic structure. Structurally, doping can stabilize specific phases, such as cubic or orthorhombic configurations, by minimizing lattice distortions[42]. Additionally, B-site doping modifies the electronic structure, enabling the tuning of charge transport properties and catalytic activity[135]. Doping with a single metal or co-doping with multiple elements has been demonstrated to enhance oxygen ion migration and facilitate the formation of oxygen vacancies, both of which are essential for increasing ionic conductivity[136–138]. The formation of these vacancies also plays a crucial role in nanoparticle exsolution, as the release of oxygen is the key step initiating the process[139].

Considering the acceptor B-site doping of SrTiO₃ with Ni, the substitution of Ni^{2+} ions (0.69 Å) for Ti^{4+} ions (0.605 Å) in the lattice occurs due to their comparable ionic radii[54]. This substitution at the B-site results in charge imbalance, which is compensated by the formation of oxygen vacancies in the oxide lattice, as described by **Equation 7**:

$$NiO\ (SrTiO_2) \rightarrow Ni''_{Ti} + V_O^{\bullet\bullet} + Sr_{Sr}^X + 2O_O^X \qquad (7)$$
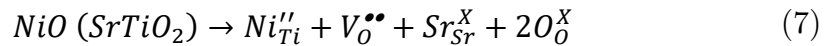
The solubility limits of Ni in stoichiometric SrTiO₃ are reported to range between 2% and 5%, depending on the synthesis method[140]. This low doping level is consistent with solubility rules, given the significant size mismatch and charge difference between the ions. However, as will be discussed later, A-site deficiency in perovskite

oxides facilitates increased B-site doping by generating additional oxygen vacancies and enhancing structural flexibility. This enables the lattice to accommodate higher concentrations of dopant metals, resulting in the formation of solid solutions at the B-site. For instance, in a 20% A-site deficient, La-doped $La_{0.4}Sr_{0.4}Ti_{1-x}Ni_xO_3$ host lattice, the Ni content can be increased to 20–25 at.%[141,142].

As mentioned earlier, the structural flexibility of perovskite oxides enables the incorporation of two or more aliovalent metal cations at B-site positions, either by introducing a second dopant (up to 5 at.%) or by forming a solid solution. Incorporating multiple metal cations leverages synergistic effects that are not obtainable with monometallic doping, making co-doping a widely used strategy for tailoring the functional properties of perovskite oxides for applications in heterogeneous catalysis[22,70,143,144].

2.5.3 Acceptor-doping of SrTiO₃ with iron

The perovskite solid solution family $SrTi_{1-x}Fe_xO_{3-\delta}$ represents a versatile system, ranging from slightly iron-doped $SrTiO_3$, which is a model for acceptor-doped large band gap electroceramics, to iron-rich compositions that exhibit excellent electronic and ionic conductivity. These mixed conductors are pivotal for applications in fuel cells, electrochemical sensors, permeation membranes, and catalytic processes. In this system, Fe replaces Ti^{4+} in both Fe^{3+} and Fe^{4+} oxidation states, with the relative proportions of Fe^{3+} and Fe^{4+} influenced by the total iron concentration, oxygen partial pressure, and temperature[145,146]. When doping $SrTiO_3$ with Fe, its incorporation as Fe^{3+} as B-site cation results in the formation of oxygen vacancies for charge compensation (**Equation 8**).

$$Fe_2O_3\ (2SrTiO_3) \rightarrow 2Fe'_{Ti} + V_O^{\bullet\bullet} + Sr_{Sr}^X + 5O_O^X \qquad (8)$$

The $SrTi_{1-x}Fe_xO_{3-\delta}$ family of materials forms a continuous solid solution between strontium titanate ($SrTiO_3$) and strontium ferrite ($SrFeO_3$) over the entire

composition range $0 < x < 1$[147]. The significant inherent deficiency in the oxygen sublattice of these systems, driven by the mixed-valence states of Ti^{4+} and Fe^{3+}/Fe^{4+} B-site cations, leads to defect equilibria dominated by oxygen vacancies and interstitials formed via the anion Frenkel reaction. This results in predominant ionic conductivity under intermediate oxygen partial pressures. Additionally, increasing Fe content reduces the band-gap energy, effect that can be attributed to the systematic broadening of the Fe-derived 3d band located above the O-derived 2p valence band[147]. The crystal structure of the $SrTi_{1-x}Fe_xO_{3-\delta}$ system changes as Fe content increases, driven by differences in the B-site cation ratio and oxygen stoichiometry. At low Fe content ($x \approx 0$), the substitution of Fe^{4+} with Fe^{3+} as a dopant introduces minor lattice distortions due to the slightly larger ionic radius of Fe^{3+} (0.645 Å) compared to Ti^{4+} (0.605 Å). This results in a slight decrease in the lattice parameter[63,148]. With increasing Fe content, Jahn-Teller distortions around Fe^{4+} ions intensify, resulting in notable local structural changes. These effects are most evident at intermediate compositions ($x \approx 0.3$), where the interaction between Ti and Fe ions disrupts the lattice order[146]. At high Fe content ($x \approx 1$), the structure transitions to a brownmillerite-type phase, characterized by ordered oxygen vacancies and layered arrangements of FeO_6 octahedra and FeO_4 tetrahedra, reflecting the dominance of Fe ions in the lattice[149].

2.5.4 Donor doping of TiO₂ with niobium

Doping titanium dioxide with aliovalent transition metals is a commonly used technique for tailoring its optical properties and enhance its photocatalytic activity for applications in water splitting and pollutant degradation[150–152].

Doping TiO_2 with Nb^{5+} determines the substitution of Ti^{4+} ions with Nb^{5+} ions in the lattice. This is classified as donor doping (or n-type doping), which introduces negatively charged donor states in the material. The substitution leads to the formation of titanium vacancies $V_{Ti}^{4\prime}$, which form for preserving charge neutrality.

The defect equation (**Equation 9**) can be written as:

$$2Nb_2O_5\ (5TiO_2) \rightarrow 4Nb_{Ti}^{\bullet} + V_{Ti}^{4\prime} + 10O_O^X \qquad (9)$$
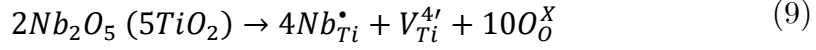
The ionic radius of Nb^{5+} (0.64 Å) is slightly larger than Ti^{4+} (0.605 Å), allowing Nb^{5+} to substitute Ti^{4+} in the lattice by preserving the original tetragonal crystal structure[153]. The n-type doping with Nb^{5+} is widely used to tailor the electronic and optical properties of TiO_2, improving photocatalytic activity for water splitting, pollutant degradation, and hydrogen generation by enhancing charge separation and light absorption[154–157]. Additionally, Nb^{5+} doping stabilizes the anatase phase and enhances carrier density, leading to improved electrical conductivity and optical transmittance. However, excessive niobium doping may result in the formation of secondary phases, such as Nb_2O_5, depending on the synthesis conditions.

2.5.5 Acceptor doping of TiO$_2$ with iron

Doping TiO_2 with Fe^{3+} replaces Ti^{4+} ions with Fe^{3+} ions in the lattice, resulting in p-type conductivity. The charge imbalance is compensated by the formation of oxygen vacancies. For the defect chemistry of Fe-doped titania, see the **Subsection 2.5.3**.

2.6 Exsolution of metal dopants from metal oxides

2.6.1 Conventional vs. exsolved catalysts

Metal-supported catalysts are extensively used in heterogeneous catalysis due to their versatility and straightforward preparation. To ensure the stabilization and uniform dispersion of the metal nanoparticles that form the active phase, heterogeneous composites incorporating a support material are used to immobilize the high-surface-area catalytic particles. The supports for these catalysts typically consist of oxides, zeolites, or carbon-based substrates and play a vital role in stabilizing metal particles, improving dispersion, and promoting metal-support interactions[27,158]. Most

supported particles are synthesized using deposition techniques, such as chemical vapor deposition (CVD) or chemical infiltration methods[27]. The latter consists in depositing a catalyst precursor into an oxide precursor via infiltration, followed by thermal treatments and a reduction step to generate metal particles supported on the outer surface of a host metal oxide (**Figure 16a**)[26]. These methods, although widely applicable, offer limited control over particle interaction with the support during deposition and over time, resulting in deactivation by agglomeration or coking[159,160]. Additionally, conventionally prepared supported catalysts often encounter issues like particle agglomeration, sintering, and deactivation under harsh operating conditions, stemming from weak metal-support interactions and the vulnerability of metal particles to thermal and chemical degradation[27,158,161].
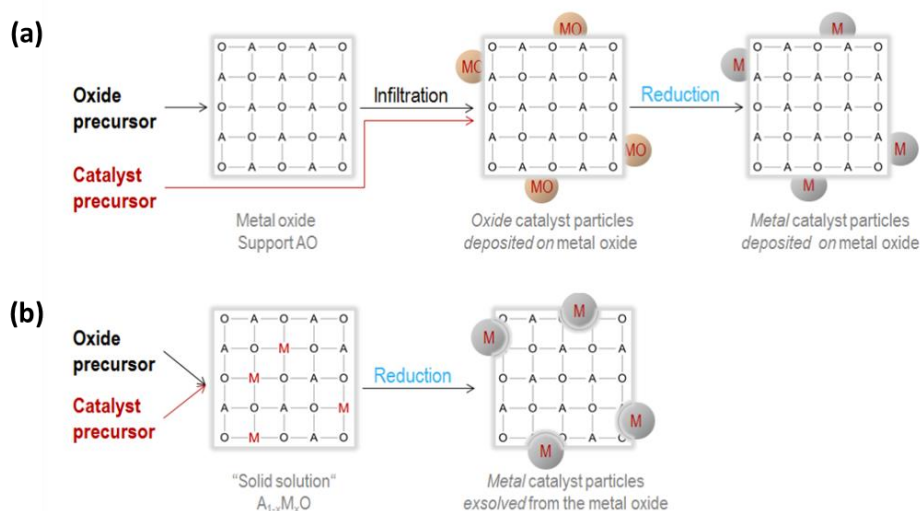
Figure 16. (a) Steps of a chemical infiltration method for the development of conventional metal-support catalysts. An oxide precursor MO is infiltrated in a metal oxide support AO, before being subjected to high-temperature thermal treatment and subsequent reduction to form M^0 nanoparticles. (b) Direct exsolution process, where the cation M^{n+} incorporated in the host $A_{1-x}M_xO$ is exsolved as a metallic phase M0 upon reduction treatment. Adapted from Neagu et. al.[26].

Exsolved catalysts offer a novel solution to these limitations. During the exsolution process, metal catalysts are segregated and grown in-situ from a host oxide lattice onto the oxide surface under a reducing atmosphere[26,27]. This method results in nanoparticles that are "socketed" into the support, creating a strong metal-support interface that prevents agglomeration and improves their thermal stability[162,163].

Exsolved catalysts demonstrate exceptional resistance to sintering and coking, ensuring high durability under extreme conditions. Additionally, the exsolution process enables precise control over nanoparticle size and distribution, enhancing catalytic activity[26,27,164]. Among the various applications of these materials, they have shown superior performance in processes such as methane reforming, ammonia synthesis, and CO_2 utilization, where thermal stability at high temperatures is critical[163]. Moreover, the redox nature of the exsolution process enables catalyst regeneration through the reversible reincorporation of exsolved particles into the perovskite host oxide lattice under a reducing atmosphere[35,165]. The regeneration of exsolved perovskite materials and their potential applications in catalysis will be thoroughly examined later in **Section 2.8**.

The exsolution of metal cations can be applied to various host oxide lattices, including spinel and fluorite structures; however, the majority of studies focus on perovskite-based systems[166]. The perovskite lattice is particularly interesting from the materials' science point of view because of its compositional flexibility, which allows for an easier tuning of its functional properties in catalysis, and its ability to accommodate a wide range of point defects[27]. Additionally, perovskites exhibit enhanced charge carrier mobility and greater phase stability compared to other oxide lattices, both which are critical factors in facilitating nucleation and growth during the exsolution process[166].

2.6.2 Reduction mechanism in perovskites

The particle exsolution from host oxides is a chemically induced phase separation, whose mechanism involves the release of lattice oxygen triggering the reduction of metal cations, their diffusion within the lattice and subsequent nucleation, socketing and growth[36] (**Figure 17a**). This process is triggered by a reduction in oxygen partial pressure within the material and elevated temperatures, which are thermodynamically necessary to achieve a Gibbs free energy of reduction $\Delta G_{red} < 0$, thereby reducing targeted cations and associated oxygen ions. To achieve low pO_2,

various studies have adjusted gas conditions using H_2, CO, CH_4, or ultra-high vacuum, with forming gas (5% H_2 in N_2) being the most commonly employed method[36,167]. During the exsolution process, as the perovskite material is exposed to a reducing atmosphere, lattice oxygen in the host oxide reacts with hydrogen, resulting in water production. This reaction leads to the formation of oxygen vacancies ($V_O^{\bullet\bullet}$) and free electrons (e^-). These electrons facilitate the reduction of the exsolvable cation (M_M^x) to its metallic state (M^0), accompanied by the creation of cation vacancies ($V_M^{n'}$). Formalizing these steps with Kroger-Vink notation (**Equation 10**):

$$M_M^x + \frac{n}{2}O_O^x \rightleftharpoons M^0 + V_M^{n'} + \frac{n}{2}V_O^{\bullet\bullet} + \frac{n}{4}O_2 \tag{10}$$
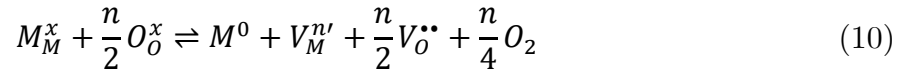
The main parameter determining which cations are going to reduce when subjected to reducing atmosphere is their reduction potential at the specified temperature[36]. In **Figure 17b**, an overview of the ΔG_{red} of oxide reduction at different temperatures in reported.
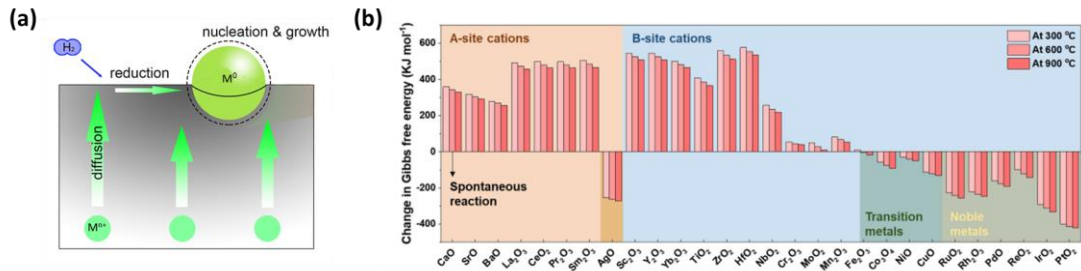
Figure 17. (a) Schematic illustration of the exsolution process under reducing atmosphere. Adapted from Gao et. al.[168] (b) Change in Gibbs free energy of oxide reduction reaction under H_2 atmosphere at 300, 600 and 900 °C. Adapted from Kim et. al.[36].

The position of cations at either the A-site or the B-site is determined by their coordination numbers and ionic radii[36]. A-site cations typically have larger ionic radii and higher coordination numbers compared to B-site cations. For instance, alkaline earth metals and lanthanides (e.g., Ca, Sr, La), which have larger ionic sizes and lower reducibility ($\Delta G_{red} > 0$ in H_2 at 900 °C), are commonly used as A-site host

ions, where they have 12-fold oxygen coordination. As it can also be seen from **Figure 17b**, except for Ag, all ions occupying the A-sublattice of the perovskite structure have $\Delta G_{red} > 0$ and therefore are non-reducible at temperatures up to 900 °C. Highly reducible noble and transition metals, such as Ru, Pd, Ni, and Co, are typical exsolution metals occupying the B-site. Other B-site ions, like Ti, Mo, and Mn, which exhibit $\Delta G_{red} > 0$, are also employed as B-site dopants to ensure redox stability. While Ni is commonly used at the B-site, its placement at the A-site can depend on the synthesis method and lattice structure. Fe, on the other hand, remains stable as a B-site host under low-temperature reduction conditions and can also exsolve at high temperatures[36].

2.6.3 Non-stoichiometry and role of point defects

Since cation reduction is initiated by oxygen release, and oxygen mobility is strongly influenced by the concentration of oxygen vacancies, the compositional flexibility of the perovskite structure can be leveraged to enhance the exsolution process by incorporating structural defects[131]. In fact, one primary disadvantage of exsolving stoichiometric ABO_3 perovskite oxide systems with A/B = 1 lies in their limited ability to generate oxygen vacancies, which are crucial for facilitating the exsolution process. When exsolving stoichiometric perovskites, B-site cations' exsolution is accompanied by undesired exsolution a A-site side phase (**Equation 11**):

$$ABO_{3-\delta} \rightarrow (1-\alpha)ABO_{3-\delta'} + \alpha AO + \alpha B \qquad (11)$$
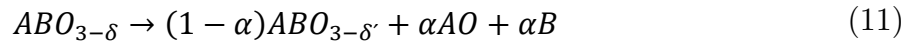
Therefore, A-site deficient perovskites (A/B < 1) have been proposed to overcome these issues. In fact, the exsolution of B-site cations from an A-site deficient perovskite results in a larger amount and size of the exsolved particles, without forming any A-site cation-rich side phases (**Equation 12**). A-site deficiency effectively creates an excess of B-site cations, causing the thermodynamically

unstable perovskite lattice to drive B-site exsolution as a mechanism to restore structural stability.

$$A_{1-\alpha}BO_{3-\delta} \rightarrow (1-\alpha)ABO_{3-\delta''} + \alpha B \tag{12}$$
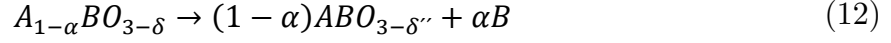
Moreover, even cations that are more difficult to exsolve can be exsolved, with the process primarily occurring on the surface of the perovskite material[169]. For example, in A-site deficient $La_{0.4}Sr_{0.4}TiO_3$, extremely stable Ti cations can be exsolved as TiO_2 on the surface of the perovskite[36]. Based on this finding, researches have been conducted in the past few years on the topic of nanoparticles' exsolution from A-site deficient perovskites. Neagu et. al.[23] carried out a systematic study on the role of A-site deficiency in B-site exsolution. The study demonstrated that the degree of A-site deficiency α could be used to control the ratio between the size and density of exsolved metal nanoparticles. Specifically, when $\alpha = 0.1$, the surfaces exhibited a high density of nanoparticles with intermediate dimensions, whereas increasing the deficiency to $\alpha = 0.2$ resulted in larger particles but with lower particle density. The authors therefore concluded that at $\alpha = 0.1$ the nucleation of a larger number of nanoparticles is favored over growth, highlighting the potential of A-site deficiency as a tool for optimizing their size and distribution for catalytic applications. Furthermore, an A-site deficient host lattice is essential for suppressing the formation of A-cation segregation layers on the surface, as these layers would otherwise inhibit oxygen release from the lattice, which is the trigger for cation reduction. This suppression is attributed to a reduction in surface elastic energy, which stabilizes the lattice and facilitates the exsolution mechanism[131]. In another study from Tsiotsias et. al.[22], A-site deficiency in the perovskite structure was tuned to modulate the concentration of oxygen vacancies, which directly influenced the exsolution process and the composition of exsolved FeNi bimetallic nanoparticles. By increasing the A-site deficiency in $La_{0.4}Sr_{0.6-\alpha}Ti_{0.6}Fe_{0.35}Ni_{0.05}O_{3\pm\delta}$ (with $\alpha = 0, 0.1, 0.2$), the concentration of oxygen vacancies associated with penta-coordinated Fe^{3+} sites increased. These vacancies facilitated the reduction of Fe^{3+} to metallic Fe, leading to

the formation of bimetallic FeNi nanoparticles with increasing Fe content. This modulation of oxygen vacancies enabled precise control over nanoparticle composition and size, facilitating the development of advanced catalysts with tunable catalytic properties for applications such as Oxidative Dehydrogenation of Ethane (ODH) and Dry Ethane Reforming (DER).

2.7 Bimetallic exsolution

Bimetallic and multimetallic exsolution, i.e. the exsolution of two or more B-site metal cations from the parent perovskite oxide, has emerged as a promising approach for the design of bimetallic systems for catalysis over the past decade. This method is remarkable not only for generating highly stable nanoparticles but also for allowing precise control over key particle attributes, including size, composition, structure, and morphology[31]. The advantages of employing bimetallic exsolution in catalysis arises from their adjustable composition and structure, where atomic interactions can modulate the catalyst's properties, resulting in unique geometric, electronic, and synergistic effects[170]. Among the bimetallic systems studied for catalytic applications, Fe-containing compositions are the majority, followed by Ni-based systems, mainly finding applications in electrochemistry and heterogeneous catalysis for processes such as methane conversion, CO oxidation, water gas shift and ethane dehydrogenation[22,31,171,172].

2.7.1 Structure of bimetallic nanocrystals

The shared energy band of bimetallic crystals allows for the tuning of the electronic structure and geometric configuration by altering the alloy composition. In fact, adjusting the distance between the d-band position of the metal and the Fermi energy level modifies the adsorption capacity of nanoparticles for reactants and products, thereby influencing the catalyst's performance. The physicochemical properties of bimetallic nanocrystals are closely linked to their spatial arrangement, atomic

ordering, and the proportion of different atoms. These properties are highly adjustable and can be precisely tailored by optimizing the composition and structure to meet specific catalytic requirements[173]. According to the atomic ordering and configuration of the two metals involved, bimetallic nanostructures can be classified into three main types: alloyed structures, which in turn are divided into intermetallic and solid solutions, core-shell structures and heterostructures (**Figure 18**).
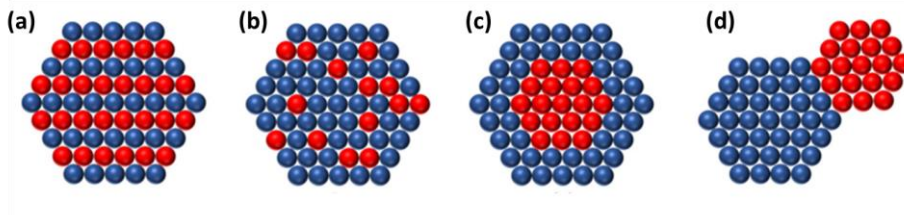
Figure 18. Bimetallic nanostructures: (a) intermetallic alloy, (b) solid solution alloy, (c) core-shell structure and (d) heterostructure[173].

Alloyed materials are known to exhibit distinctive physicochemical properties that go beyond the mere combination of the inherent characteristics of the constituent metals. Bimetallic nanocrystals in alloyed structures form homogeneous mixtures with a specific geometric arrangement of atoms, where metal bonds are established between the individual metal atoms. Based on the atomic arrangement, alloyed structures can be categorized into two types: intermetallic compounds and solid solutions[173]. Intermetallic alloys (**Figure 18a**) are characterized by strong bonding between their components, resulting in compounds with long-range atomic order and a fixed atomic ratio. In contrast, solid solution alloys (**Figure 18b**) involve the mutual dissolution of components, leading to a random mixing of metal atoms without long-range order. In XRD patterns, the distinct diffraction peaks of the individual metals disappear, and new alloy-specific reflection emerge, differing from those of the pure metal constituents. This classification is important because intermetallic compounds and solid solutions, despite having identical elemental compositions and stoichiometry, often display significantly different properties. These differences in atomic arrangement influence their performance, making the distinction critical for applications in catalysis, magnetism, and materials science[173].

Instead, the core-shell structure is an ordered assembly structure, which is composed of an inner core completely coated with a shell made another metal by chemical bonds or other forces. When the precursors of the two metal ions have different reducing abilities, the precursor with the higher reduction potential could be preferentially reduced to the metal atom and form the nucleation center, and then the metal ions with the lower potential are reduced to metal atoms and deposited on the nucleation center, finally forming the core-shell structure. The catalytic activities of the core-shell structured nanocrystals mainly depend on the composition of the shell metal[173].

2.7.2 Fundamentals of alloy exsolution

The simultaneous exsolution of two or more reducible metal species from a host oxide typically results in the formation of alloy particles, as supported by modeling studies. Two main mechanisms for exsolution are identified: "bulk alloy formation" and "surface alloy formation," as shown in **Figure 19** for the case NiCo alloys[174]. The process is driven by oxygen vacancies created during reduction, which tend to migrate from the bulk to the surface, facilitating the segregation of exsolvable metals alongside them (co-segregation) due to the lower energy required for this process[31].

In this model for bimetallic exsolution mechanism proposed by Kwon et. al.[174], bulk alloy ($Co-O_v-Ni$) formation (**Figure 19a**) starts with the segregation of the two metal cations and aggregation of $Co-O_v-Co$ and $Ni-O_v-Ni$ in the bulk of the parent oxide, by locating each B metal into the nearest neighbor site with the sharing of an oxygen vacancy. Then, $Co-O_v-Ni$ segregates toward the surface. On the other hand, surface alloy ($Co-O_v-Ni$) formation (**Figure 19b**) starts with the independent segregation of $Co-O_v-Co$ and $Ni-O_v-Ni$ towards the surface, followed by the aggregation of $Co-O_v-Co$ and $Ni-O_v-Ni$ to form a nearest neighbored $Co-O_v-Ni$ on the surface of the parent oxide matrix.
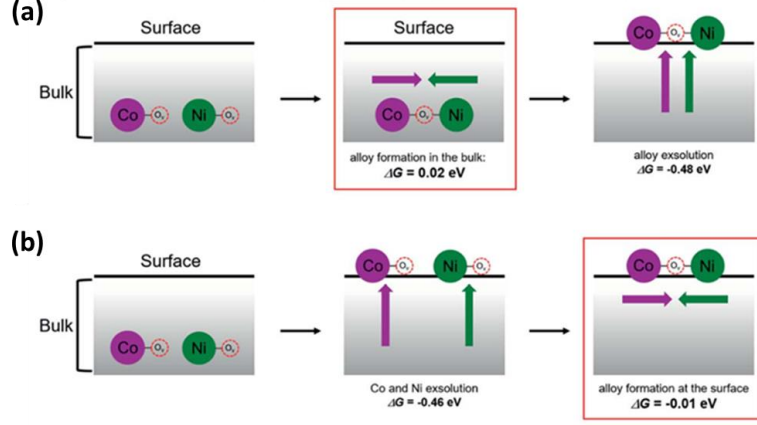
Figure 19. Schematic illustration and energetics of (a) bulk alloy formation and (b) surface alloy formation during bimetallic exsolution of NiCo particles[175].

Although the initial and final states are identical for both pathways, the energy requirements differ significantly. The Gibbs free energies of aggregation (ΔG_{aggr}) for Co–O_v–Ni at the surface (surface alloy formation) and in the bulk (bulk alloy formation) are -0.01 eV and +0.02 eV, respectively, indicating that surface alloy formation is energetically more favorable. Additionally, the Gibbs energies for co-segregation (ΔG_{seg}) of Co, Ni, and NiCo with an oxygen vacancy are exothermic (-0.53, -0.39, and -0.48 eV, respectively), making co-segregation thermodynamically favorable in all cases. These findings suggest that metal segregation is energetically easier than alloy formation, and that the exsolution is more likely to follow the surface alloy formation mechanism due to the lower alloy formation energy at the surface[174]. This has also been demonstrated experimentally using *in-situ* techniques: X-ray diffraction revealed that, during reduction and exsolution, separate Ni and Co reflections emerged at lower temperatures, while a NiCo reflection formed at higher temperatures, at the expense of the individual Ni and Co ones. Similarly, *in-situ* scanning transmission electron microscopy demonstrated comparable exsolution behavior for CoFe alloys, where Co-based nanoparticles appeared first, followed by CoFe alloy formation as the reduction temperature increased[31,174,176]. Some metals, like Fe, are unlikely to exsolve on their own from the B-site of a perovskite lattice because of their high segregation energy. However, they can exsolve when paired with another metal, such as Ni or Co, who have a lower segregation energy. For example,

Lv et. al.[177] reported how in the FeCo-doped $Sr_2Fe_{1.5}Mo_{0.5}O_{6-\delta}$ system cobalt shows a less negative segregation energy with oxygen vacancies then Fe (-0.64 versus 0.91 eV, respectively). Therefore, when under reducing conditions the critical concentration of oxygen vacancies for Co exsolution is reached, the formation of cation defects and additional oxygen vacancies forming due to cobalt diffusion facilitates Fe exsolution, as shown from the decrease of its segregation energy. Moreover, in systems with mixed cations, the Gibbs energy of reduction was shown to depend on the metal-oxygen bond strength of both metals. Adding more easily reducible metals lowers ΔG_{red} energy, making exsolution easier[176,177]. Additionally, studies have shown that doping with Co raises the total energy of the perovskite system, making it easier for Co−Fe bonds to form compared to Fe−Fe bonds due to their lower formation energy, additionally explaining the beneficial effect of Co in promoting Fe exsolution[178]. It is worth noting that, based on current research in the literature, an experimentally verified mechanism for alloy exsolution has not yet been established, leaving several questions unanswered regarding how the interaction between the two metals influences the process.

2.7.3 Exsolution of FeNi alloys

In perovskite-based systems, the A-site stoichiometry determines whether exsolution tends to be irreversible or reversible. In reversible exsolution, the matrix is stoichiometric, and the process results in a less stable mixture of A-site oxide and B-site exsolved components. These phases can recombine, allowing the exsolved nanoparticles to re-dissolve back in the host oxide depending on the gas environment, as will be better discussed later in **Section 2.8**. This regeneration capability enhances the durability of the material, and this behavior is observed in both single-metal and bimetallic systems[174]. In contrast, exsolution from A-site deficient perovskites results in the formation of a more stable A-site stoichiometric perovskite alongside the exsolved particles. Additionally, nanoparticles exsolved from A-site deficient perovskites are partially embedded in the surface, reducing their ability to re-dissolve

during re-oxidation. This socketing effect enhances the alignment between the support and the exsolved particles, leading to highly active, coke-resistant materials[23,26,31,179]. This is also the case for exsolution of FeNi alloys, which are widely employed as cathodes for CO_2 and steam electrolysis due to their high catalytic activity, stability under operating conditions, and resistance to carbon deposition and nanoparticle sintering, attributed to the strong anchorage of exsolved particles on the support. For instance, the interface between exsolved FeNi nanoparticles and the $Sr_2Fe_{1.35}Mo_{0.45}Ni_{0.2}O_{6-\delta}$ substrate, enriched with oxygen vacancies, was shown by Lv et. al.[180] to enhance CO_2 adsorption and activation, significantly improving the performance of the CO_2 reduction reaction compared to cathodes made from pristine perovskite. Moreover, exsolved FeNi alloy systems have also been utilized as heterogeneous catalysts for energy-related applications such as partial oxidation of methane, CO oxidation and ethane dehydrogenation reactions[22,171,172,181]. A relevant contribution on the use of FeNi for ethane conversion was conducted by Tsiotsias et. al.[22], who explored the exsolution of FeNi bimetallic heterostructures from perovskite oxides with increasing A-site deficiency to develop catalysts with tunable composition and morphology for CO_2-assisted Oxidative Dehydrogenation (ODH) and Dry Ethane Reforming (DER). It was found that A-site deficiency determines the concentration of oxygen vacancies associated with iron, controlling its reduction. The extent of exsolved metallic Fe and Ni increased with A-site deficiency, influencing nanoparticle size and catalytic properties. In fact, exsolution led to the formation of bimodal Fe/Ni_3Fe heterostructures, with pure Fe^0 domains adjacent to intermetallic nanoparticles, as confirmed by TEM and Mössbauer spectroscopy. Catalytic testing revealed that the exsolved catalysts exhibited superior stability compared to a commercial Ni-based catalyst supported on Al_2O_3. Interestingly, an improvement in the selectivity towards ODH was observed when restructuring the metallic nanoparticles into mixed Fe-Ni oxides during catalysis. In another study on methane partial oxidation, by Jiang et. al.[182] employed FeNi nanoparticles exsolved from $Sr_{0.9}Fe_{0.81}Ta_{0.09}Ni_{0.1}O_{3-\delta}$ in a catalytic membrane reactor for methane partial oxidation, achieving nearly complete CH_4 conversion and close to 100% selectivity

for CO and H_2. To avoid the re-dissolution of exsolved nanoparticles into the perovskite lattice, an oxygen-permeable membrane was employed to regulate the oxygen partial pressure near the nanoparticles, effectively preventing their dissolution and maintaining catalytic performance. In addition to conventional bimetallic exsolution, Joo et. al.[183] prepared FeNi exsolved catalysts through a so-called "topotactic exsolution" method. These consists in introducing Fe as a guest cation onto the surface of a Ni-containing perovskite through infiltration or atomic layer deposition. The exsolution process in this case is driven by ion exchange between Fe and Ni, which is facilitated by the differing segregation energies of the two metals. This exchange promotes the migration of additional Ni species to the surface, resulting in the formation of a high density of FeNi alloy nanoparticles. These demonstrated enhanced activity for methane dry reforming compared to monometallic Ni catalysts produced via conventional exsolution, while retaining excellent durability[31].

2.7.4 FeNi alloys

FeNi alloys exist in different crystal structures and composition intervals, with their physical properties being highly dependent on their phase and atomic arrangement. The most common structures are the Face-Centered Cubic (FCC, γ-FeNi) and Body-Centered Cubic (BCC, α-FeNi) phases. The FCC structure is dominant in Ni-rich alloys, particularly those with compositions near 50% Ni, and is stable at high temperatures. This phase is characterized by its cubic symmetry and is associated with excellent ductility and magnetic properties. In contrast, the BCC structure is more prevalent in Fe-rich compositions and at low temperatures. The BCC phase offers higher strength and stiffness compared to the FCC phase but exhibits reduced ductility[184,185]
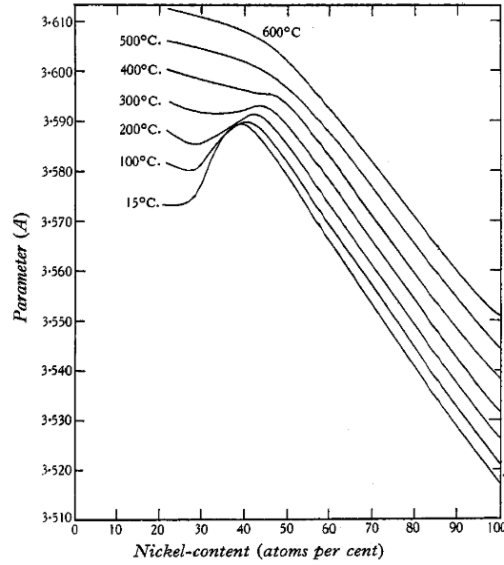
Figure 20. Values of the lattice parameters as a function of the atomic Ni content in γ-FeNi alloys, measured at different temperatures[186].

FeNi alloys exhibit a dependence between their lattice parameters and their composition. The lattice structure of FeNi alloys transitions between BCC and FCC phases depending on the nickel content. According to Owen et. al.[186] the γ-FeNi phase, having FCC structure, is prevalent in alloys containing more than approximately 28 at.% Ni. In this range, the lattice parameter increases almost linearly with nickel content, reaching a maximum value of 3.589 Å at 39 at.% nickel content. Beyond this composition, the lattice contracts as Fe content increases (**Figure 20**). On the other hand, the BCC structure, or α-phase, is observed in alloys with nickel content below approximately 24 at.%. The lattice parameters of the α-phase is similar to the one of pure BCC α-Fe and decreases steadily with increasing nickel content, with the phase disappearing at higher temperatures (above 350°C) and transitioning to the γ-phase[186].

2.8 Regeneration of exsolved catalysts

The regeneration of exsolved perovskite catalysts refers to the ability of metal nanoparticles, exsolved from the perovskite lattice under reducing conditions, to reincorporate into the lattice upon oxidation. This reversibility is driven by the

structural flexibility of perovskites and their ability to accommodate oxygen vacancies and metal ions. This process allows the catalyst to recover its original structure, making it more durable and reusable in redox environments[187–189]. Metal oxides are in fact prone to deactivation during their operation due to exposure to reaction conditions, contaminants, and thermal stress. In order to restore their catalytic activity, possible routes include oxidative thermal treatments for burning deposited carbon, which is the most widely used option, redox cycling and chemical regeneration[190–192]. As mentioned in **Subsection 2.6.1** in metal oxides synthesized through metal-support impregnation methods, the aging conditions that arise during their use typically determine the coalescence of the active phase, leading to particle growth and corresponding loss of dispersion of the active phase and of specific surface area, which is essential for good catalytic conversion[31,36,193–195] (**Figure 21**). Instead, in the case of exsolved catalysts the active phase is already present as metal cations in the material and is recalled by subjecting them to reducing atmosphere. The exsolution process makes it possible to avoid coalescence and deactivation phenomena typical of conventional metal-supported catalysts, also thanks to the well-socketed metal nanoparticles on the surface[36,159].
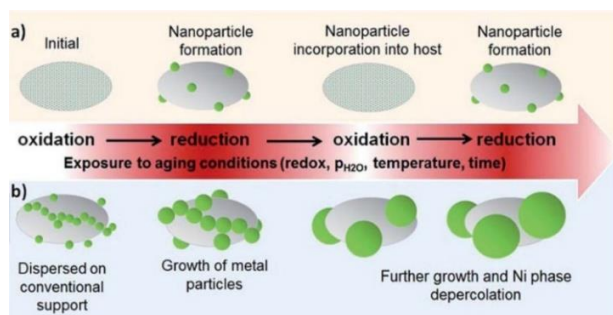
Figure 21. Differences between redox cycling of an exsolved metal catalyst (a) and a conventional metal-support impregnated catalyst (b). Reported from Burnat et. al.[35].

For exsolved catalysts, regeneration also involves the complete or partial restoration of the perovskite phase originally present in the material before its use as catalyst. In a typical regeneration treatment through redox cycling, from the as-synthesized material in its pristine state (**Figure 22a**), in which the B-site metal cations M^{n+}

are present as B-site cations in the lattice of the parent oxide matrix, metal ions are exsolved through a reduction step or employed for catalysis in reducing atmosphere, causing the exsolution of the metal active phase M^0 (**Figure 22b**). A subsequent step of re-oxidation of the material under air allows for the reincorporation of the B-site metals as M^{n+} back into the perovskite parent matrix (**Figure 22c**), allowing for a subsequent new re-exsolution process for re-activating the catalyst and thus employing it again for catalysis (**Figure 22d**).

Figure 22. Schematic representing the redox cycling of exsolved perovskite oxides materials.

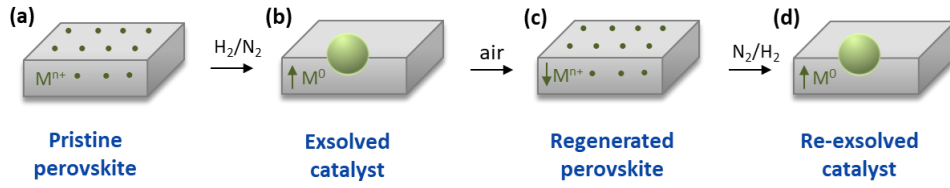Despite the potential of regeneration in exsolved materials, only a few studies have been carried out in recent years for studying nanoparticles' re-incorporation in exsolved materials, as part of the attempt of functionalizing metal oxides for subsequent use as self-regenerating smart materials for energy related applications. Being the increase in the A-site deficiency in B-site doped perovskite oxides a commonly employed technique to promote nanoparticle exsolution[23,196], Burnat et. al.[35] investigated this aspect by conducting a study on the regenerability of a perovskite oxide with variable A-site deficiency and doped with nickel at the B-site. First, higher levels of A-site deficiencies led to an increase in the reducibility of the species at the B-site position of the perovskite lattice, with up to a maximum of 5 at.% of Ni reincorporated in the perovskite phase. The study of the redox cyclability of the material was then performed by monitoring the Ni^0 nanoparticles reflections by X-ray diffraction. On a total of 5 regeneration cycles, the disappearance of nickel reflections upon oxidation was shown, together with their reappearance during reduction, without presence of nickel oxide side-phases.

Steiger at al.[197] also investigated the reversibility of the exsolution process of Ni^0 particles in a lanthanum ferrite perovskite with variable nickel doping on the B-site,
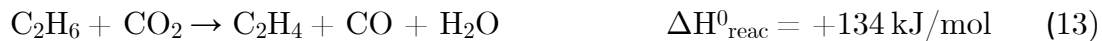
for their subsequent use in the Sabatier reaction, i.e. the catalytic hydrogenation of CO_2. After reduction at 600°C, an increase in the amount of reduced Ni proportional to the amount provided by the stoichiometry of the material has been pointed out, and a regeneration of the nanoparticles with subsequent reincorporation of the same with re-oxidation at 650°C was observe through XRD, XAS and SEM measurements. Nickel segregation linked to the exsolution process led to an overall good catalytic activity and stability of the material when subjected to redox cycling, without observing growth of the dispersed active phase.

Considering instead the regeneration of bimetallic systems, Komarala et al.[198] investigated the regenerative properties of Fe- and Mn-substituted $LaNiO_3$ perovskites. For doing so, they synthesized perovskite nickelates as catalysts for Dry Methane Reforming (DMR) with 20% doping at the B-site, and conducted redox cycling experiments at high temperature to investigate the exsolution process and the related catalytic properties in the materials through TEM and *in-situ* XRD. Two different materials have been synthesized, and the exsolution of NiFe bimetallic nanoparticles (for $LaNi_{0.8}Fe_{0.2}O_3$) and Ni nanoparticles (in the case of $LaNi_{0.8}Mn_{0.2}O_3$) was investigated. Both catalysts demonstrated reversible exsolution of Ni nanoparticles during reduction and regeneration of the perovskite structure upon re-oxidation. The oxidation step required longer times (8 h at 800°C) compared to the reduction step (2 h), due to slower solid-state diffusion for the same temperature. Results after one redox cycle underlined the recovery of the initial structure and the reincorporation of the surface reduced species within the crystalline matrix. Fe-substituted catalysts showed superior coke resistance due to stronger metal-support interactions. In another study, Lv et. al.[199] investigated the reversible exsolution and dissolution of CoFe alloy nanoparticles in Co-doped $Sr_2Fe_{1.5}Mo_{0.05}O_{6-\delta}$ perovskite during redox cycling, focusing on their regenerative properties and application in CO_2 electrolysis. *In-situ* XRD and STEM measurements showed how, under reducing conditions, metallic Co exsolved from the perovskite promoted by Fe, transforming the structure from double perovskite to layered perovskite at 800 °C. The nanoparticles anchored strongly to the substrate, preventing agglomeration and

ensuring thermal stability. After that, oxidizing conditions reversed this process, with the materials showing a phase change from FeCo metallic nanoparticles to FeCo oxides at 600°C and subsequent re-dissolution of nanoparticles from the surface to the bulk of the perovskite, passing from layered perovskite back to the double perovskite structure. The cyclability and regenerability of the materials as cathodes for CO_2 electrolysis showed very stable performances over 230 h and 12 redox cycles.

2.9 CO$_2$-assisted oxidative dehydrogenation of ethane

Carbon Capture and Utilization (CCU) processes have emerged as a promising approach to mitigate climate change by repurposing carbon dioxide emissions into valuable industrial resources. These technologies not only reduce emissions but also replace conventional raw materials. CCU applications are broadly categorized into four areas: using CO_2 as a solvent, converting it into chemicals, producing fuels, and employing it in Enhanced Oil Recovery (EOR) and Enhanced Coal Bed Methane (ECBM) techniques[200]. The use of CO_2 as a reactant to convert it into valuable chemicals includes processes like CO_2-assisted Oxidative Dehydrogenation (ODH) of light alkanes, such as ethane. This promising approach produces light alkenes like ethylene, a critical feedstock for the chemical industry. In addition to meeting the increasing demand for ethylene, this process functions as a CCU technology, with CO_2 acting as a mild oxidant to enhance selectivity and suppress carbon deposition[170]. The process involves the following reactions:

$$C_2H_6 + CO_2 \rightarrow C_2H_4 + CO + H_2O \qquad \Delta H^0_{reac} = +134\,\text{kJ/mol} \qquad (13)$$

$$C_2H_6 + 2CO_2 \rightarrow 4CO + 3H_2 \qquad \Delta H^0_{reac} = +429\,\text{kJ/mol} \qquad (14)$$

$$C_2H_6 \rightarrow 2C + 3H_2 \qquad \Delta H^0_{reac} = +85\,\text{kJ/mol} \qquad (15)$$

These are all non-spontaneous at room temperature, as can be seen from the positive values of the standard enthalpy of reaction ΔH^0_{reac}, but become feasible at elevated temperatures, typically above 600 °C. While higher temperatures favour ethane

conversion, they also increase the risk of catalyst deactivation due to sintering and carbon deposition. The role of the catalyst is critical in selectively breaking the C–H bonds in ethane while minimizing undesired C–C bond cleavage, which leads to side reactions such as dry reforming (**Reaction 14**). Dry Ethane Reforming (DER) is particularly favored at high temperatures, typically above 800 °C, where the thermodynamics become more favorable for the highly endothermic reaction. DER is also promoted under conditions where CO_2 is present in excess, as this shifts the equilibrium toward syngas production. Catalysts with strong CO_2 activation properties, such as Ni-based systems, are especially effective in facilitating DER. However, DER competes with ODH and thermal cracking of ethane (**Reaction 15**), and its selectivity increases at higher temperatures and lower CO_2-to-ethane ratios, which favor C–C bond cleavage over C–H bond activation[201]. Catalyst materials for ODH are designed to facilitate the selective activation of ethane while maintaining stability under harsh reaction conditions. Traditional systems, such as Cr-based, Ga-based, and noble metal catalysts, rely on their redox properties to enable oxygen atom transfers essential for dehydrogenation. However, these catalysts are highly toxic and often face challenges such as sintering and carbon deposition, which limit their long-term performance. Transition metal oxides, particularly those with high oxygen mobility, have shown to be promising in enhancing selectivity and stability[201]. In the field of catalysis for ODH, the adjustable composition and structure of bimetallic catalysts often result in superior performance compared to monometallic ones, offering enhanced catalytic activity, selectivity, and stability[201]. Recent studies have highlighted the exceptional performance of bimetallic catalysts in the dehydrogenation of light alkanes under CO_2 atmospheres[202,203]. The FeNi bimetallic active system is especially suitable for ODH, as it forms Ni-Fe_yO_x interfacial sites that selectively cleave C–H bonds while maintaining the C–C bond in ethane, resulting in high ethylene selectivity[29,204]. Yan et al.[29] prepared FeNi-based catalysts supported on various oxides (SiO_2, ZrO_2, and CeO_2) for ODH, identifying Fe_3Ni/CeO_2 as the most effective. The Ni-ZrO_2 and FeNi-CeO_2 interfaces acted as active sites, enhancing catalytic performance. Notably, the reducible nature of CeO_2

facilitated the formation of active $FeNi/CeO_2$ interfacial sites, which promoted CO_2 activation and ethylene generation. In contrast, Fe_3Ni/ZrO_2 and Fe_3Ni/CeO_2 favored CO_2 conversion to CO via the dry ethane reforming pathway. Moreover, Li et al.[204] combined the impregnation method with plasma treatment to prepare a more efficient bimetallic $SrCr/SiO_2$ catalyst. Plasma treatment improved metal dispersion and increased oxygen vacancies, achieving an ethane conversion of 78% and CO_2 conversion of 59.3%, demonstrating the potential of surface modifications to enhance catalytic efficiency in bimetallic systems. Finally, the use of the exsolution technique also is an important tool for the design of catalysts for these processes. In fact, bimetallic exsolved FeNi alloy nanoparticles have already been shown to act as effective catalysts for ODH. The work of Tsiotsias et al.[22] provides significant insights in this sense. Their study focuses on bimetallic exsolved heterostructures derived from $La_{0.4}Sr_{0.4+\alpha}Ti_{0.6}Fe_{0.35}Ni_{0.05}O_{3\pm\delta}$ perovskites, which exhibit tunable catalytic properties based on the composition and size of the exsolved nanoparticles. The Fe/Ni ratio in the exsolved nanoparticles was shown to significantly affect the catalytic performances. Systems with a higher Fe fraction favored DER, as Fe promotes C–C bond cleavage, leading to syngas production (**Figure 23**). On the other hand, systems with a lower Fe fraction exhibited increased selectivity toward ODH, as Ni facilitates C–H bond activation, favoring ethylene production. This compositional control allows for the tailoring of the catalyst to specific reaction pathways, making the FeNi alloy an easy-to-tune viable alternative as heterogeneous catalyst for ethane dehydrogenation.
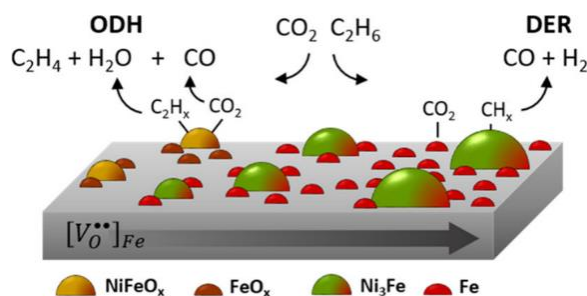

Figure 23. Schematic representation of the catalytic mechanisms for ODH and DER over the exsolved FeNi catalysts[21].

Chapter 3

Characterization Methods

3.1 X-ray diffraction

Following Wilhelm Röntgen's discovery of X-rays in 1895, Max von Laue demonstrated their diffraction within crystals in 1912. Building on this, William Bragg and William Lawrence Bragg developed a geometric framework in 1913 to describe the interaction between X-rays and crystal lattices, enabling the analysis of diffraction patterns[205]. These contributions laid the foundation for modern X-ray crystallography. Nowadays, X-ray diffraction (XRD) has become a fundamental technique for characterizing long-range ordered solids, which constitute approximately 95% of all solid materials. This is due to the fact that each crystalline material produces a distinct and unique diffraction pattern, enabling precise structural analysis. A crystal is defined as a three-dimensional lattice characterized by a periodic and repetitive arrangement of atoms at fixed lattice points[206]. The interatomic distances, typically in the range of a few Ångstroms, align with the wavelength of X-rays (0.5–2.5 Å), making crystals ideal for diffraction studies[207]. When a crystalline sample is exposed to X-rays, the electromagnetic radiation interacts with the electron shells of the atoms, leading to elastic scattering of the incident rays. This scattering occurs across all atoms and lattice planes, which collectively act as a diffraction grating. Constructive interference emerges when the diffraction conditions are met, as defined by Bragg's law (**Equation 16**):

$$n \, \lambda = 2d_{hkl} \, sin(\theta) \tag{16}$$

In Bragg's law, n represents the diffraction order corresponding to various crystal planes, λ is the wavelength of the incident X-ray, θ is the angle of incidence, and d_{hkl} denotes the interplanar spacing between the (hkl) crystal planes. Bragg conditions are satisfied when X-rays scattered at a specific angle (θ) by two parallel lattice planes have a path length difference (d) that corresponds to an integer multiple of the wavelength, as shown in **Figure 24**. This results in constructive interference, producing a diffraction peak. Conversely, when the Bragg equation is not fulfilled, destructive interference occurs, causing the scattered beam to be extinguished. By varying the irradiation angle across a wide range, a distinctive diffraction pattern of the crystal sample can be obtained.
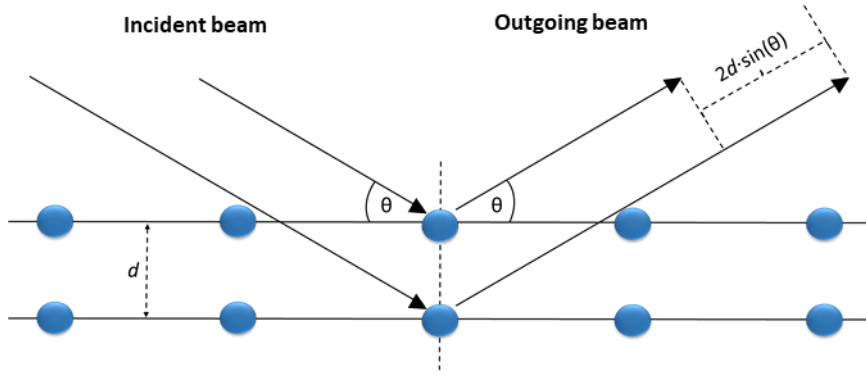

Figure 24. Schematic illustration of X-ray diffraction on the lattice planes of a crystalline material. Adapted from Rudolph[131].

Analyzing the XRD diffraction pattern based upon the positions of the reflections offers valuable insights into the lattice symmetry (space group) and unit cell geometry of the material. In order to calculate the lattice parameter of a crystalline phase from an X-ray powder diffractogram, the diffraction peaks corresponding to specific Miller indices (hkl) are identified. Subsequently, Bragg's law is used for calculating the interplanar distance d for each diffraction peak (**Equation 17**):

$$d_{hkl} = \frac{\lambda}{2\sin(\theta)}$$

(17)

In the case of a cubic system, the interplanar spacing d_{hkl} is related to the lattice parameter a and Miller indices h, k, l according to the **Equation 18**[206]:

$$\frac{1}{d_{hkl}^2} = \frac{h^2 + k^2 + l^2}{a^2} \tag{18}$$

from which it is possible to calculate the lattice parameter a of the cubic unit cell (**Equation 19**):

$$a = d\sqrt{h^2 + k^2 + l^2} \tag{19}$$

For non-cubic systems, the calculation of lattice parameters from the XRD diffractogram is more complex, since the interplanar spacing d depends on multiple lattice parameters (e.g. a, b, c) and angles (α, β, γ), which are specific of the crystal system. Unlike cubic systems, where d is directly related to a single lattice parameter, non-cubic systems require solving equations that incorporate the symmetry and geometry of the unit cell[208]. The average crystallite size in a sample can be also determined using the Scherrer equation[209]:

$$D_{hkl} = \frac{K \cdot \lambda}{\beta_{hkl} \cdot sin(\theta)} \tag{20}$$

In **Equation 20**, D_{hkl} represents the crystallite size, K is the shape factor, typically estimated as 0.9, λ is the wavelength of the X-ray radiation incident on the crystal, β_{hkl} is the diffraction broadening determined from the full-width at half maximum (FWHM) of the XRD signal, with Miller indices *hkl* expressed in radians, and θ is the Bragg angle corresponding to the diffraction peak position. The Miller indices define the various planes of atomic arrangement within the lattice.

3.2 X-ray absorption spectroscopy

X-ray absorption spectroscopy (XAS) is a versatile analytical technique used to investigate oxidation states, electronic structures, and local coordination environment of atoms within a material[210]. Due to the unique absorption characteristics of specific wavelengths for each element, this technique enables the investigation of the local

atomic structure and electronic state of a target element within a sample by precisely adjusting the energy of the incoming X-rays. The significant penetration depth of high-energy X-ray radiation, ranging from 2 to 35 keV, ensures the inherent bulk sensitivity of XAS, allowing for the acquisition of fundamental insights that are unattainable through other methods. This makes it applicable to a wide range of materials, including liquids and solids, regardless of their crystalline or amorphous nature, and can be employed to study structures from the bulk scale down to the nanoscale[131,210]. While the specifics of data acquisition vary depending on the experimental setup, this characterization technique can achieve time resolutions on the order of milliseconds or microseconds. This capability allows for the study of reaction dynamics and kinetics in time-resolved experiments[211–213].

The fundamental principle governing the absorption of electromagnetic waves as they interact with matter is described by the Beer-Lambert law (**Equation 21**). When X-rays pass through a material, their intensity is attenuated, and this attenuation can be characterized by the absorption coefficient:

$$I_T = I_0 \, e^{-\mu(E)t} \tag{21}$$

where I_0 represents the incident X-ray intensity, I_T denotes the transmitted X-ray intensity, t is the sample thickness, and $\mu(E)$ is the absorption coefficient, which depends on the photon energy. XAS measures the energy-dependent fine structure of the X-ray absorption coefficient[210]. The linear absorption coefficient μ depends on the energy of the incoming photons. For most X-ray energies, μ exhibits a continuous energy-dependent behavior, with its value determined by the sample density ρ, atomic number Z, atomic mass A, and X-ray energy E[214]. The empirical relation can be expressed as follows:

$$\mu(E) \sim \frac{\rho Z^4}{AE^3} \tag{22}$$

Equation 22 expresses the dependence of the linear absorption coefficient μ on both atomic number Z and photon energy E. This dependence is illustrated by plotting

μ/ρ against photon energy, as shown in **Figure 25a.** The graph highlights the capability of X-ray absorption spectroscopy to distinguish between different elements. In addition to variations in μ/ρ spanning approximately five orders of magnitude, the plot reveals distinct jumps at specific energies. These features, known as absorption edges, occur when the photon energy is sufficient to excite a core electron from an atom within the sample.
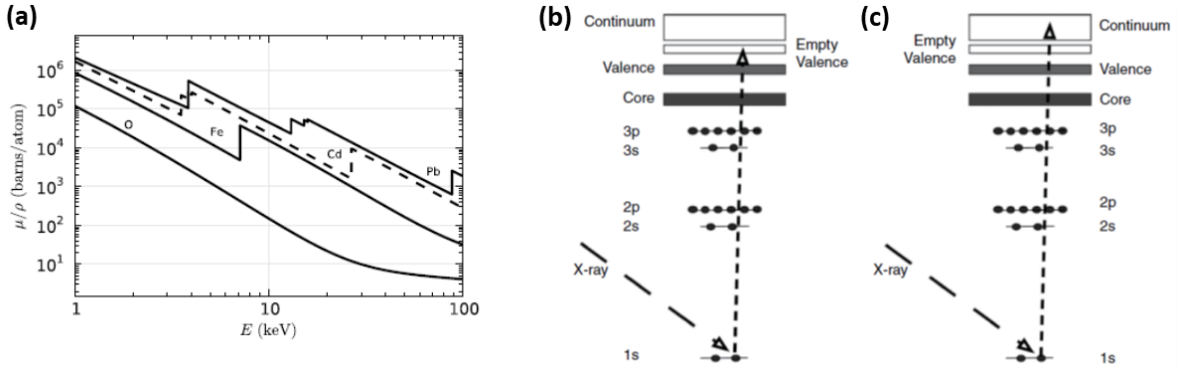

Figure 25. (a) Variation of the absorption cross-section for multiple elements as a function of photon energy in the range of 1 to 100 keV[214]. Transitions responsible for XANES (b) and EXAFS (c) features in the XAS spectrum[215].

Since each atom has core-level electrons with unique binding energies, adjusting the wavelength of the incident photon allows selective targeting of specific elements. The absorption edge and its underlying mechanism can be explained by the atom's excitation process: when an incoming photon interacts with an atom, it excites a core electron (referred to as a photoelectron) from the K-edge, specifically from the 1s orbital, promoting it to an unoccupied state above the Fermi level. Two types of unoccupied states can then be considered: transitions to an empty valence orbital (**Figure 25b**) or, at higher energies, into the continuum (**Figure 25c**). The former corresponds to features near the absorption edge threshold, including pre-edge peaks. This region, extending up to 30–40 eV above the edge, is known as X-ray Absorption Near-Edge Structure (XANES) region in the XAS spectrum. XANES spectroscopy is sensitive to the oxidation state and electronic structure of the absorbing atom. The latter transition occurs for photon energies between 40 and 1000 eV above the

71

absorption edge and is characterized by the oscillatory behavior of the absorption coefficient as a function of energy. This region, referred to as Extended X-ray Absorption Fine Structure (EXAFS), provides information on bond distances, coordination numbers, and the types of neighboring atoms[210].
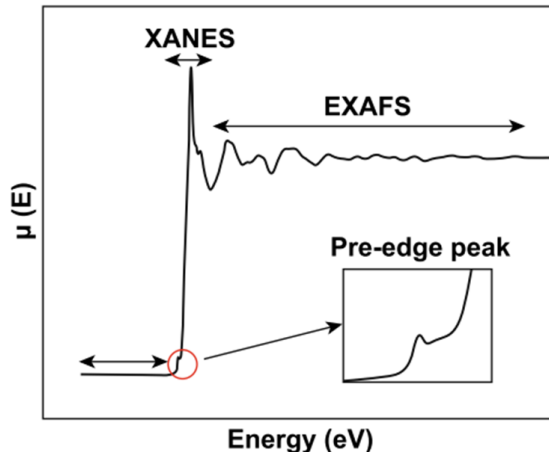

Figure 26. Schematic of XAS including the pre-edge, XANES, and EXAFS regions[210].

In **Figure 26**, a schematic of an XAS spectrum including the pre-edge, XANES and EXFAS regions is depicted. The flat region in the first part of the spectrum arises from the weak interaction between X-rays and electrons when the incident X-ray energy is insufficient to overcome the binding energy of the electron in the element's orbital (e.g., the s orbital), preventing its excitation to the highest unoccupied state. However, some unfavored transitions, such as 1s to 3d in transition metals, can manifest as pre-edge peaks in the spectrum. Once the X-ray energies are high enough to excite core electrons to the unoccupied state, X-ray is strongly absorbed leading to a large jump that constitutes the XANES region, while the core electrons excited to continuum state form the outgoing and scattering wave interference with neighboring atoms representative of the EXAFS region[210].

The electronic transitions of the photoelectron in the XANES region adhere to dipolar selection rules ($\Delta l \pm 1$), resulting in both dipole-allowed and dipole-forbidden transitions[216]. For K-edge absorption edges, where the ground state is in the 1s orbital ($l = 0$), allowed transitions occur to p-orbitals ($l = 1$), while transitions to d-orbitals

(l = 2) are considered forbidden. Consequently, the main absorption peak (i.e. the so-called white line) for a 3d transition metal like nickel corresponds to transitions from 1s to 4p orbitals[217,218]. The near-edge region in a XAS spectrum reflects the unoccupied density of states, incorporating contributions from bonding and geometry, which account for its complex shape. The position of the white line edge is influenced by the oxidation state and can be identified by the maximum of the first derivative. Higher oxidation states shift the edge energy to higher values, while lower valence states result in a shift to lower energies[219]. Although s to d transitions are forbidden under the selection rules for electric dipole transitions, weaker quadrupole transitions ($\Delta l \pm 2$) can still occur, appearing as pre-edge peaks below the white line due to orbital mixing, such as p-d hybridization[220]. The lower intensity of these peaks is attributed to the reduced transition probability.

3.3 Nitrogen physisorption

The surface characterization of porous materials is most commonly performed using gas physisorption techniques. Porosity is defined as the ratio of pore volume (void space) to the total volume of the material. According to the International Union of Pure and Applied Chemistry (IUPAC), porous materials are classified into three categories based on pore size: micropores ($<$ 2 nm), mesopores (2–50 nm), and macropores ($>$ 50 nm)[221]. The characteristic properties of a porous material, including surface area, pore volume, and pore size distribution, can be accurately determined through physisorption measurements, typically conducted using nitrogen adsorption at 77 K[222].

Physisorption, or physical adsorption, occurs when a gas (referred to as the adsorptive) comes into contact with the surface of a solid (the adsorbent). The material in the adsorbed state is termed the adsorbate, distinguishing it from the adsorptive, which is the gas or vapor undergoing adsorption. The forces driving physisorption are van der Waals interactions, which encompass both long-range London dispersion forces and short-range intermolecular repulsion[223].

A physisorption isotherm can be obtained by monitoring the incremental uptake and release (desorption) of the adsorptive under equilibrium conditions as a function of relative pressure (P/P_0), where p represents the absolute pressure and p_0 denotes the saturated vapor pressure of the adsorptive. The shape of the hysteresis is influenced by the size and geometry of the pores being analyzed, resulting in distinct sorption curves. Consequently, the IUPAC classifies physisorption isotherms into six general types, as shown in **Figure 27a**[221].
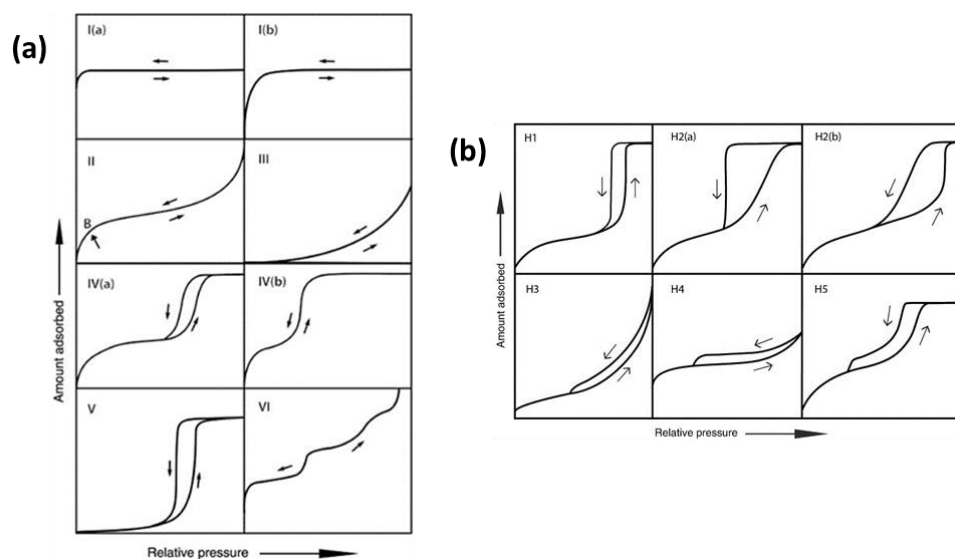

Figure 27. Classification of physisorption isotherms (a) and of hysteresis loops (b) according to IUPAC[221].

Microporous materials, such as metal-organic frameworks and zeolites, exhibit significant adsorption at very low pressures (< 0.1 p/p_0), followed by a nearly flat plateau, corresponding to type I isotherms. Type I(a) is associated with narrow micropores (< 1 nm), while type I(b) relates to wider pores (≈ 2.5 nm) with broader size distributions. Type II isotherms describe non-porous or macroporous adsorbents, where initial adsorption forms a monolayer, followed by multilayer adsorption after the 'B' point. In contrast, type III isotherms lack a 'B' point, indicating no monolayer formation, and their concave shape arises from weak adsorbent-adsorbate interactions and clustering of adsorbed molecules near favorable sites on non-porous or macroporous surfaces. Type IV isotherms are characteristic of mesoporous

materials, initially resembling type II with mono- and multilayer adsorption, followed by capillary condensation (gas condensing into a liquid-like phase within pores at pressures below the bulk liquid's saturation pressure). At higher relative pressures, a saturation plateau at higher pressures indicates complete pore filling. Type IV(a) features a hysteresis loop for mesopores > 4 nm, while type IV(b) is reversible for smaller pores (< 4 nm). Type V isotherms show weak adsorbent-adsorbate interactions at low pressures, with pore filling at higher pressures for microporous-mesoporous materials. Type VI isotherms, fully reversible, represent layer-by-layer adsorption on uniform non-porous surfaces.

The IUPAC classification also includes four main types of hysteresis loops, each reflecting specific features of pore structure and adsorption mechanisms (**Figure 27b**). Type H1 hysteresis loops correspond to uniform mesopores with a narrow pore size distribution, indicating well-defined pore geometry. In contrast, type H2 loops are associated with less uniform pore structures, often resulting from complex or interconnected pore networks. Type H3 hysteresis loops are characteristic of non-rigid aggregates or particles with plate-like shapes, suggesting structural flexibility during adsorption. Type H4 hysteresis loops combine features of type I and II isotherms, showing significant adsorption at low relative pressures, which is typically attributed to micropores. These loops are linked to narrow, slit-shaped pores. Lastly, the rarely observed type H5 hysteresis loops are associated with mesopores that are open but partially blocked, indicating unique pore arrangements that hinder complete adsorption or desorption[221]. The Brunauer-Emmett-Teller (BET) method is among the most commonly utilized techniques for determining the surface area of mesoporous, macroporous, or non-porous materials through physisorption measurements[224]. The BET method expands upon the Langmuir adsorption theory by introducing the concept of monolayer formation, where gas molecules are adsorbed onto a homogeneous, perfectly planar surface with uniform adsorption sites. Additionally, the BET model incorporates the formation of multilayers, treating each layer as an independent monolayer without interactions between them. This multilayer approach provides a more accurate representation of gas adsorption

behavior on porous surfaces, thereby extending the applicability of the BET model to a wider range of materials and experimental conditions. By applying these assumptions and transforming the physisorption isotherm into a BET plot, the method yields **Equation 23**:

$$\frac{p/p_0}{n\,(1-p/p^0)} = \frac{C-1}{n_m C} \cdot p/p_0 + \frac{1}{n_m C} \qquad (23)$$

where n describes the amount of adsorbed gas molecules, p/p_0 is the relative pressure, n_m is the specific monolayer capacity and C corresponds to the BET constant, which gives an indication of the order of magnitude of the attractive adsorbent-adsorbate interactions[223]. It is defined by the formula $C = e^{\frac{E_1 - E_l}{RT}}$, where E_1 is the heat of adsorption for the first layer, E_l is the heat of liquefaction of the adsorbate, R is the gas constant, and T the temperature. A higher C value reflects stronger adsorbent-adsorbate interactions, while a lower value means weaker ones. This parameter is affected by factors such as temperature, surface chemistry and adsorbent heterogeneity. For instance, polarizing metal-oxygen bonds in oxide surfaces enhance van der Waals forces, leading to increased C values, while elevated temperatures decrease adsorption energies, thereby reducing the C constant[225,226]. Plotting $\frac{p/p_0}{n\,(1-p/p^0)}$ against p/p_0 should yield a linear graph in the relative pressure range between 0.05 and 0.3. Microporous materials experience pore filling at low pressures, requiring additional criteria to ensure accurate and consistent evaluation of adsorption behavior. The calculation of the specific monolayer capacity n_m according to **Equation 24** can be subsequently used to determine the BET surface area (S_{BET}):

$$S_{BET} = n_m \cdot a_m \cdot N_A \qquad (24)$$

in which a_m is the cross-sectional area of the gas molecule and N_A the Avogadro constant. For nitrogen sorption experiments at 77 K, a_m corresponds to 0.162 nm[2221]. For mesoporous materials, the characteristic plateau observed at high relative pressures (> 0.95) can be utilized to estimate the total pore volume V_p[227]. Moreover,

the pore size distribution in mesoporous materials is typically assessed using methods based on Density Functional Theory (DFT). Initially developed to analyze simple slit pores in activated carbon, nonlocal density functional theory (NLDFT) has demonstrated broad applicability for mesostructured materials. It provides reliable estimations when sufficient information regarding pore geometry, surface structure, and adsorbate properties is available[222].

3.4 Water vapor physisorption

Water vapor physisorption involves the physical adsorption of water molecules onto the surface of a material through weak intermolecular forces, such as van der Waals interactions and hydrogen bonding[228]. Unlike chemisorption, which involves chemical bond formation, physisorption is a reversible process influenced by external conditions like temperature and relative humidity. The process is governed by the material's surface properties, including hydrophilicity or hydrophobicity, pore size, and surface chemistry. Hydrophilic surfaces enhance adsorption due to strong hydrogen bonding, while hydrophobic surfaces exhibit weaker interactions. The adsorption behavior is typically represented by water vapor sorption isotherms, which describe the relationship between the amount of water adsorbed and the relative humidity at constant temperature. These isotherms are also classified by IUPAC, reflecting different adsorption mechanisms and material properties[221].

The instruments employed for carrying out water physisorption measurements operate based on two primary measurement principles, which divide them between volumetric and gravimetric methods. Volumetric devices quantify adsorption by measuring pressure changes within a closed system. These instruments are well-suited for high-throughput studies due to their speed and ability to analyze complete isotherms efficiently[228]. Volumetric water vapor physisorption is less sensitive to surface changes when compared to the gravimetric technique, since it measures changes in gas pressure, which can be affected by factors such as system leaks, temperature changes, and gas behavior. These factors make it harder to detect

small amounts of water vapor adsorption. On the other hand, gravimetric methods measure the weight change of the sample directly, making them more accurate and sensitive for detecting small adsorption amounts[229].

Volumetric water physisorption measurements, though less sensitive than gravimetric techniques, provide benefits such as faster measurement times and the ability to accommodate larger sample sizes. These methods are commonly used to investigate adsorption behavior under different relative humidity conditions. A volumetric adsorption instrument includes a part of the system of precisely known volume known as the manifold. The manifold is linked to other sections of the system via pneumatic valves. By utilizing highly sensitive pressure sensors, the precise quantity of gas contained within these interconnected volumes can be determined at any moment. **Figure 28** shows the basic process and instrumentation diagram (P&ID) of a general volumetric water physisorption system.
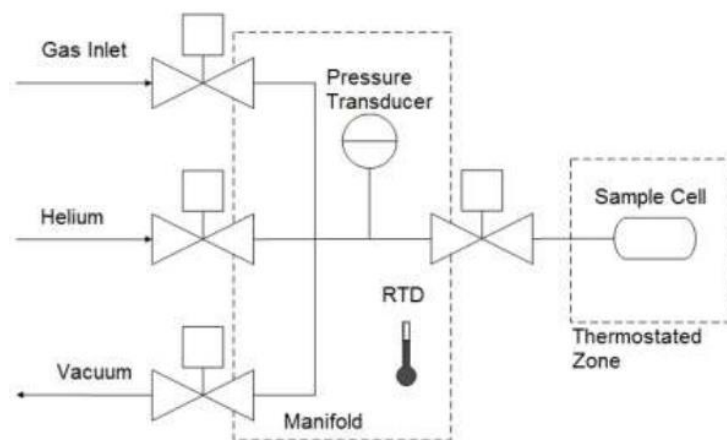

Figure 28. P&ID diagram of a general volumetric water physisorption systems. Reported from Quantachrome Instruments[230].

In the volumetric water physisorption measurements carried out in this dissertation, to quantify the amount of gas adsorbed by a sample, the system was first completely evacuated. Subsequently, the gas inlet valve is opened, allowing gas to fill the manifold until a predetermined pressure is achieved. Since the pressure, temperature, and volume of the system are known variables, the total amount of gas within the system can be calculated. Following this, the valve connecting the manifold to the

sample cell is opened, enabling the adsorbate to flow into the sample cell. The system is then allowed to reach equilibrium pressure. Given that the cell volume is determined through a helium expansion calibration step, the final system pressure can be theoretically predicted. However, the actual remaining pressure will deviate from the calculated value due to a portion of the gas being adsorbed onto the sample. The difference between the actual system pressure and the calculated pressure indicates the amount of gas adsorbed onto the powder material[230].

On the other hand, gravimetric devices such as Dynamic Vapor Sorption (DVS) instruments measure mass changes in a sample as water vapor is adsorbed or desorbed, and are widely used for their high sensitivity and precision. These devices utilize microbalances to detect minute mass changes, making them ideal for studying water vapor physisorption isotherms, adsorption kinetics of water uptake and release, thermodynamics and equilibrium properties.
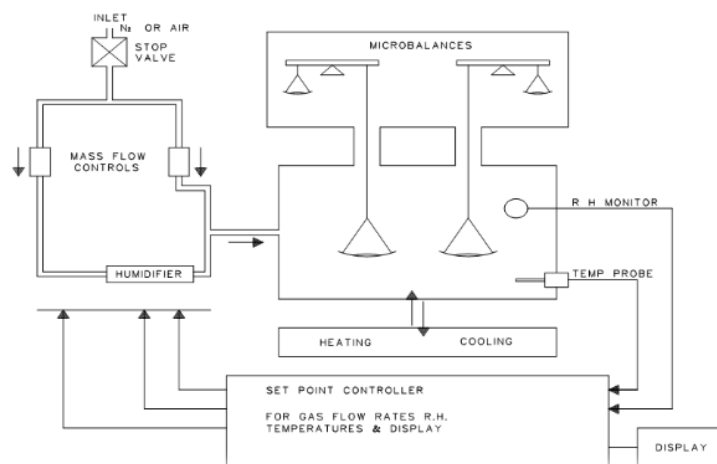

Figure 29. Schematic diagram of the gravimetric DVS system utilized in this dissertation.

In the gravimetric measurements carried out for this dissertation, dry gas, in this case nitrogen, is supplied from a gas bottle to two proportional flow controllers (**Figure 29**). The system uses two controllers: one to manage the gas flow through the humidifier and the other to regulate the dry gas flow. The gases are directed through pipes to the weighing chamber. Inside the chamber, a calibrated humidity probe monitors and adjusts the relative humidity. The apparatus includes two

microbalances in a temperature-controlled chamber, separate from the weighing chamber. Thin metal rods from the balance arms extend into the weighing chamber to hold sample carriers (pans), and a microprocessor manages gas flows and temperatures, enabling the construction of physisorption isotherms.

Gravimetric methods are particularly advantageous for analyzing small sample sizes and provide highly detailed data, although they typically require longer measurement durations compared to volumetric techniques[231].

3.5 Electron microscopy

The human eye's ability to visually distinguish details is limited to a range of 0.1 to 0.2 mm. Instruments capable of resolving finer details, below 0.1 mm, are categorized as microscopes. Microscopy has been a cornerstone in the investigation of structures beyond the resolution of the human eye, enabling the study of materials at micrometer, nanometer, and atomic scales[232]. Standard visible light microscopes function within the visible spectrum (400–700 nm) and are constrained by the wavelength of light used to illuminate the specimen. In optical systems, the resolution (δ) – the smallest detectable distance between two points – is governed by the Rayleigh criterion:

$$\delta = \frac{0.61\,\lambda}{\mu\,sin\beta} \qquad\qquad (25)$$

Here, λ represents the wavelength of radiation, μ is the refractive index, and β denotes the semi-angle of the lens's collection aperture. **Equation 25** indicates that using shorter wavelengths enhances resolution, allowing for the observation of smaller features. For example, a visible light microscope operating at a wavelength of 550 nm achieves a resolution of approximately 300 nm. While optical microscopy, pioneered by van Leeuwenhoek, provided foundational insights into biological and material systems, its resolution is fundamentally constrained by diffraction and

optical aberrations[232,233]. Similarly, electron microscopes utilize high-energy electrons to study specimens, achieving sub-Ångström resolutions. This is based on the de Broglie wavelength principle, introduced in 1924, which relates an electron's wavelength (λ) to its kinetic energy (E). The maximum resolution for an electron microscope is approximated by **Equation 26**:

$$\lambda \approx \frac{1.22}{\sqrt{E}} \tag{26}$$

Neglecting relativistic effects, higher-energy electrons exhibit shorter wavelengths, enabling the resolution of smaller structures. For instance, electrons with a kinetic energy (E) of 100 keV correspond to a theoretical wavelength (λ) of approximately 4 pm, far smaller than an atom's diameter. However, practical resolution is limited by lens imperfections such as spherical aberrations. Modern transmission electron microscopes typically operate with high voltage sources between 60 and 400 kV, achieving image resolutions below 1 Å[233–235].

3.5.1 Transmission electron microscopy

Transmission Electron Microscopy (TEM) employs high-energy electron beams to achieve atomic-scale imaging, representing a powerful technique that allows visualization of materials at the atomic scale by transmitting a high-energy electron beam through an ultrathin specimen. This method provides crucial insights into the structure, morphology, and crystallography of materials, making it indispensable in fields such as materials science, nanotechnology, and biology[235]. In transmission electron microscopy, electrons are accelerated to high energies, typically ranging from 100 to 300 keV, and directed into a narrow beam using electromagnetic lenses. As the beam passes through the specimen, it interacts with the sample, producing transmitted or scattered signals (**Figure 30**). These signals are then used to create images or diffraction patterns, which are either displayed on a fluorescent screen or digitally recorded for further analysis[232]. When electrons are directed at a solid

specimen, they can follow several interaction paths. If the sample is thinner than 100 nm, the electron beam may either pass through unchanged or scatter in the forward direction. The scattering can be classified as coherent elastic scattering, occurring at angles between 1°–10°, incoherent elastic scattering, at angles exceeding 10°, and inelastic scattering arises at very small angles ($< 1°$) due to interactions between the primary electrons and the sample's electrons.

When transmitted electrons are captured on a photosensitive plate or a CCD (charge-coupled device) camera, an image of the sample's local structure is generated. The most widely used imaging technique in transmission electron microscopy (TEM) is bright-field (BF) imaging, which is formed by the direct electron beam. Contrast in BF images arises from variations in sample thickness and/or differences in atomic numbers, as these factors influence the intensity of electrons reaching the detector. Thicker samples and those with higher atomic numbers appear darker due to reduced transmission of the incident electron beam. In contrast, dark-field (DF) or annular dark-field (ADF) imaging utilizes scattered electrons by blocking the primary beam with physical apertures, allowing selective collection of scattered electrons.

Further analysis of scattered electrons is performed using scanning transmission electron microscopy (STEM), which achieves spatial resolutions below 1 Å, enabling imaging at atomic resolution. In STEM, a highly focused electron beam (<0.2 nm) scans the sample in a raster-like pattern, providing detailed insights into inelastic scattering. Scattered signals are collected by a high-angle annular dark-field (HAADF) detector positioned at large angles, forming an annular pattern around the beam's center. HAADF imaging is highly sensitive to atomic numbers, offering enhanced signal detection compared to direct beam methods. This results in brighter regions in the analyzed area, as scattered electrons are directly detected. Furthermore, in-situ TEM techniques allow real-time observation of dynamic processes, such as phase transitions or chemical reactions, under controlled environmental conditions[232].
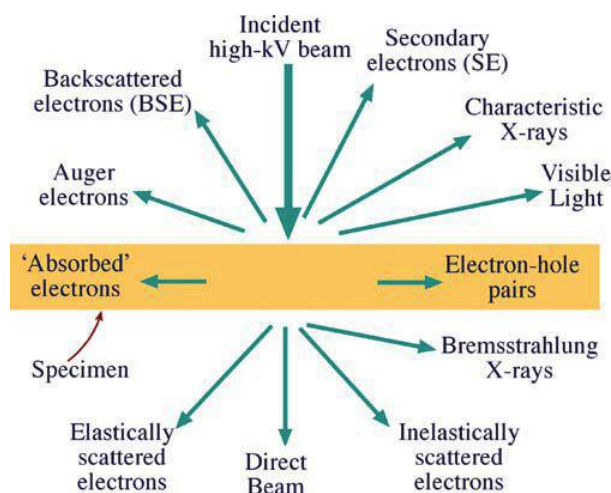
Figure 30. Potential signals produced from the interaction between a high-energy electron beam and a specimen. Reported from Williams et. al.[235].

3.5.2 Energy dispersive X-ray spectroscopy

Spectroscopic techniques are often integrated with electron microscopy to examine various signals generated by electron interaction with the specimen. Energy-dispersive X-ray spectroscopy (EDXS) is frequently used for this purpose, providing insights into the sample's local elemental composition. When a focused electron beam strikes a specimen, atoms in the sample can become excited, causing an electron to be ejected from their inner electron shells. Subsequently, an electron from a higher-energy outer shell transitions to fill the vacancy in the inner shell, releasing the excess energy as X-rays, whose energies are characteristic of the specific element. These characteristic X-rays, captured by an energy-dispersive detector, enable both qualitative and quantitative analysis, providing information on the elemental types and concentrations within the sample. Additionally, the data can be utilized to visually represent the material's chemical composition through techniques such as elemental mapping and line scans. Energy-dispersive X-ray spectroscopy is especially proficient in detecting elements with atomic numbers Z ranging from 4 to 92, achieving an analytical accuracy of approximately 2%[236].

3.5.3 Selected area electron diffraction

Selected Area Electron Diffraction (SAED) is a characterization technique employed in transmission electron microscopy that offers insights into the crystallographic structure of crystalline materials[237]. It is widely applied in crystallography to determine lattice parameters and crystal symmetry, but it is also used for phase identification in multiphase systems and for analyzing structural defects such as dislocations and grain boundaries. SAED operates on the principle of electron diffraction, where a focused electron beam interacts with the periodic atomic arrangement of a crystalline material, producing a diffraction pattern that reflects the material's structural properties. When an electron beam interacts with the sample, the scattered electrons form a diffraction pattern. A selected-area aperture in the TEM is used to isolate a specific region of the sample, ensuring that the diffraction pattern originates solely from that area. This capability allows to focus on individual grains, phases, or defects within a heterogeneous material. The diffraction process is governed by Bragg's law (**Equation 16**), which relates the angles of diffraction to the spacing between atomic planes in the crystal, and the interaction of the beam with crystal lattice leads to constructive interference that occurs at specific angles, producing a pattern of light spots on the detector. The microscope alternates between imaging and diffraction modes, with the electron lenses configured to focus the beam either on the sample or on the diffraction plane, depending on the desired output. Accurate intensity measurements and effective background subtraction are critical for reconstructing atomic structures and determining material phases[237].

3.6 Ultraviolet-visible spectroscopy

Ultraviolet-visible UV-Vis spectroscopy is an analytical technique used to measure the absorption or transmission of ultraviolet (UV) or visible light by a sample relative to a reference or blank sample. The absorption characteristics are determined by the

sample's composition, offering valuable information about its constituents and concentrations.

The energy of light is inversely proportional to its wavelength, with shorter wavelengths carrying higher energy and longer wavelengths carrying lower energy. The energy required to excite electrons to higher energy states depends on their bonding environments, leading different substances to absorb light at specific wavelengths. Visible light spans wavelengths from approximately 380 nm (violet) to 780 nm (red), while UV light encompasses shorter wavelengths, extending down to 100 nm. UV-Vis spectroscopy leverages these wavelength-specific absorption patterns to analyze and identify substances by determining the wavelengths of maximum absorbance[238].

The energy of a photon E_P is mathematically expressed as inversely proportional to its wavelength λ (**Equation 27**):

$$E_P = hv = \frac{hc}{\lambda} \tag{27}$$

where c is the velocity of light (2.998×10^8 m s^{-1}) and h is the Planck's constant (6.636×10^{-4} J·s). The visible spectrum, detectable by the human eye, spans a narrow wavelength range of about 400–800 nm, while ultraviolet radiation consists of higher-energy photons with wavelengths ranging from 10 to 400 nm (**Figure 31**). The absorption of UV-Vis photons can promote electronic transitions in atoms and molecules from lower to higher energy states. Since the energy levels of the atomic and molecular orbitals are quantized, only a precise amount of photonic energy will be absorbed to induce an electronic transition[239]. This way UV-Vis spectroscopy offers valuable information about the chemical composition, functional groups, and conjugation within a sample.
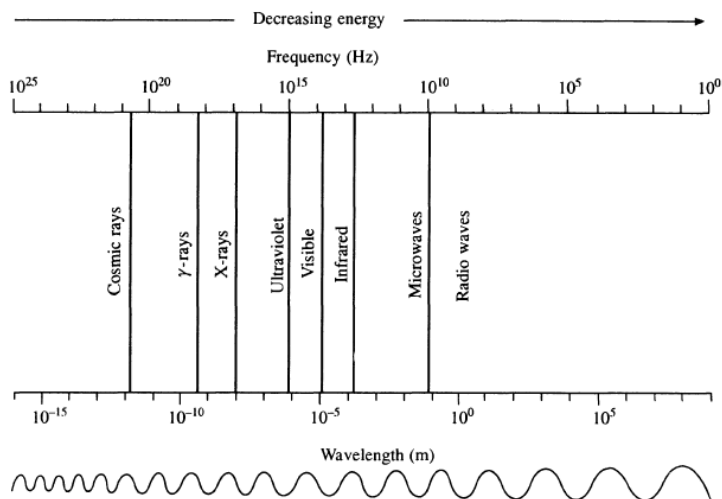
Figure 31. The complete electromagnetic spectrum. Reported from Yadav[239].

UV-Vis spectroscopy measures the fraction of absorbed photons absorbed by a sample across varying wavelengths, typically expressed as transmittance, T:

$$T = \frac{I}{I_0} \tag{28}$$

where I_0 and I denote the intensities of incident and transmitted radiation, respectively. The transmittance is inversely related to the concentration of the substance in the solution and the optical path length. This relationship is described by the Beer-Lambert law using absorbance A[240]:

$$A = -\log T = \varepsilon\, c\, I \tag{29}$$

Here, ε represents the molar extinction coefficient (absorptivity), a material-specific constant measured in $M^{-1}cm^{-1}$; c denotes the concentration of the solution in moles per liter (M); and I corresponds to the optical path length in centimeters (cm). Additionally, quantitative analysis of UV-Vis active molecules can be performed using the Beer-Lambert law. When UV-Vis radiation interacts with powdered solids, a substantial fraction of the light is scattered in various directions due to surface irregularities, a phenomenon known as diffuse reflectance[241]. Under such conditions, accurate measurement of absorbance becomes challenging. To address this limitation, the UV-Vis spectrometer can be utilized in diffuse reflectance mode, in which the

scattered reflected beams are detected simultaneously, and the sample's reflectance is compared to that of a non-absorbing reference. Following data collection, the optical properties of the powdered sample are typically analyzed using the Kubelka-Munk model[242–244]. This model assumes an infinitely thick sample with particle size smaller or equal to the wavelength of the incident radiation. The Kubelka-Munk function $F(R)$ is then given as:

$$F(R) = \frac{(1-R)^2}{2R} \tag{30}$$

where, R is the measured reflectance.

After converting reflectance values to F(R), the relationship between band gap and absorption strength, as described for a direct allowed electronic transition by Tauc et al.[245], can be utilized to determine the material's band gap:

$$\alpha h\nu = A_1 \, (h\nu - E_{BG})^{0.5} \tag{31}$$

Where $h\nu$ represents the photon energy, α denotes the material's absorption coefficient, E_{BG} corresponds to the band gap energy, and A_1 is a proportionality constant. Since the absorption coefficient α is proportional to the $F(R)$, **Equation 31** can be rewritten as:

$$|F(R) \, h\nu|^2 = A_2 \, (h\nu - E_{BG}) \tag{32}$$

In which A_2 is a proportionality constant. The linear region of the curve is extrapolated using the Tauc plot, which illustrates the variation of $|F(R) \, h\nu|^2$ as a function of photon energy ($h\nu = \frac{1239.7}{\lambda}$ eV). The band gap energy E_{BG} is determined from the solution of the linear fit, where the extrapolated curve intersects the y-axis at zero. This value serves as a critical characterization parameter for semiconductor photocatalysts, as it defines the minimum photon energy required to initiate the photocatalytic reaction.

3.7 Infrared spectroscopy

Infrared spectroscopy (IR) is an analytical technique that uses the absorption of infrared radiation by molecules to determine their structure. Infrared radiation is divided into three regions: near-infrared (12800–4000 cm^{-1}), mid-infrared (4000–200 cm^{-1}), and far-infrared (50–1000 cm^{-1})[246].

Infrared photons lack sufficient energy to initiate electronic transitions but can cause changes in the quantized vibrational and rotational energy levels of molecules. These vibrational and rotational modes correspond to distinct molecular motions, such as bending, stretching, scissoring, rocking, and twisting. Since these motions are characteristic of the functional groups present in the sample, IR spectroscopy serves as a powerful technique for acquiring fingerprint information to identify the chemical composition of materials (**Figure 32**). A molecule is defined as IR-active if its vibrational modes cause a change in the dipole moment during the interaction with infrared radiation[247]. For a molecule containing n atoms, the total number of vibrational modes is determined as 3n−6, reflecting the molecule's overall 3n degrees of freedom. Of these, three degrees of freedom correspond to translational motion, while another three are associated with rotational motion. In the case of linear molecules, the number of vibrational modes is reduced to 3n−5, as only two degrees of freedom are needed to describe rotational motion[248].
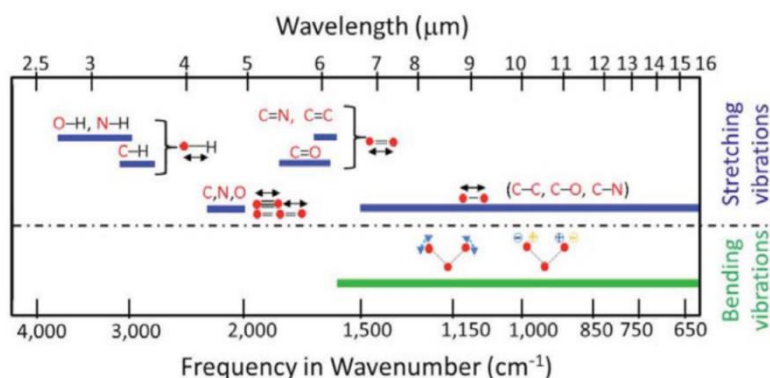

Figure 32. Characteristic IR modes of different functional groups. Reported from Loutherback et. al.[249].

A basic FT-IR spectrometer operates using transmission principles: its core component, the interferometer, includes an IR source, a beam splitter, stationary and moving mirrors, and a detector. IR radiation is split, reflected by the mirrors, recombined, and passed through the sample to the detector, creating an interferogram via constructive and destructive interference. The interferogram, a Fourier transform of the sample's IR spectrum, is processed by a computer to generate the final IR spectrum. Attenuated Total Reflectance (ATR) spectrometry is an alternative to transmission spectroscopy, where the IR beam passes through a high-refractive-index crystal, such as diamond, ZnSe, or Ge, at an angle exceeding the critical angle, causing total internal reflection at the crystal surface in contact with the sample (**Figure 33**). This reflection generates an evanescent wave that penetrates the sample to a depth of 0.5–5 µm. Absorption of IR radiation by the sample attenuates the evanescent wave, and the modified IR beam exits the crystal to be recorded by the detector. ATR combined with FT-IR, known as ATR-FTIR, enhances reproducibility between samples and reduces spectral variation among users, making it a robust tool for consistent analysis[250].
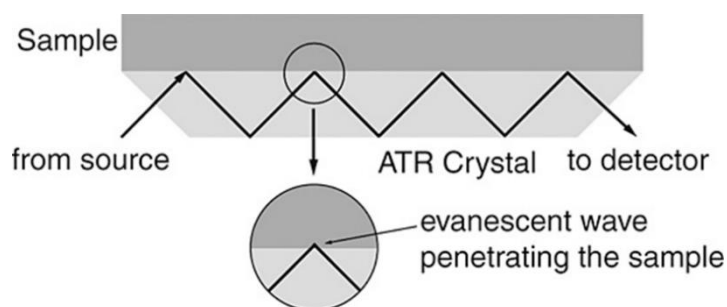

Figure 33. Schematic representation of an ATR crystal with four reflections. Reported from Blum et. al.[250].

3.8 Mössbauer spectroscopy

Mössbauer spectroscopy is an analytical technique that provides detailed information about the local chemical environment and magnetic properties of a system[251].

The method is based on the "Mössbauer effect", which refers to the recoilless emission and absorption of gamma rays during nuclear transitions. This phenomenon occurs when a nucleus in an excited state emits a gamma photon, which is absorbed by another nucleus of the same isotope in its ground state, resulting in resonance absorption. The absorber nucleus transitions to the excited state and subsequently returns to the ground state by re-emitting a photon. The recoilless emission is achieved in solid-state samples, where atoms are tightly bound within a crystal lattice, preventing recoil.

In Mössbauer spectroscopy, ^{57}Co is typically used as a gamma-ray source due to its advantageous decay properties, such as a long lifetime and emission of gamma rays at energies well-suited for the technique. The Doppler effect is applied to shift the energy of the emitted gamma rays, facilitating resonance absorption by the sample. This process generates Mössbauer spectra, which display relative energy transmission as a function of Doppler velocity. These spectra reveal hyperfine interactions, which provide critical insights into the structural and electronic properties of materials. The interactions include isomer shift, electric quadrupole splitting, and magnetic Zeeman splitting, each serving as a unique fingerprint for material characterization. The isomer shift, caused by Coulomb interactions between protons and surrounding electrons, offers information on oxidation states, spin states, and bonding properties. Electric quadrupole splitting arises in nuclei with electric quadrupole moments interacting with non-uniform electric fields, uncovering symmetry distortions within the sample. Magnetic Zeeman splitting, resulting from interactions between nuclear magnetic dipoles and external magnetic fields, divides nuclear states into substates, producing complex spectral patterns. Together, these hyperfine parameters enable detailed analysis of the material's properties[251].

A conventional Mössbauer spectrometer consists of a velocity driver that moves a gamma-ray source, a collimator to focus the radiation, and a detector to measure photon absorption (**Figure 34**). This setup enables the technique to be applied to a wide range of materials, including crystalline, amorphous, and nanostructured systems. The ^{57}Fe isotope is the most extensively studied using Mössbauer spectroscopy due to its high natural abundance and favorable Mössbauer properties, such as a high recoil-free fraction, which ensures efficient recoilless emission and absorption of gamma rays – critical for achieving high-resolution spectra. Additionally, ^{57}Fe Mössbauer spectroscopy provides detailed insights into oxidation states, spin states, and bonding environments, making it an essential tool for investigating iron-containing compounds in materials science.
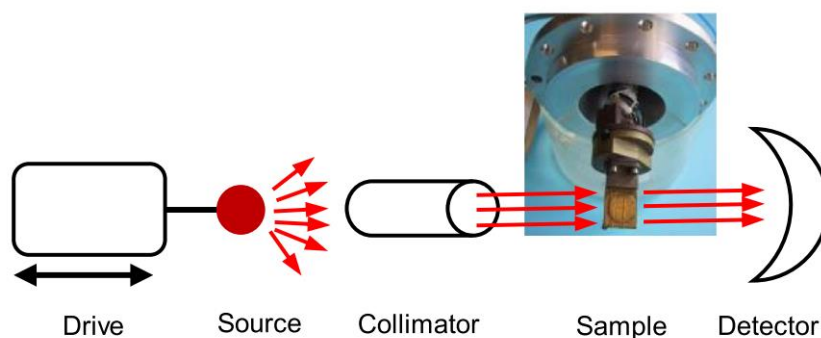

Figure 34. Schematic of a Mossbauer spectrometer. Reported from Bianchi et. al.[251]

This technique is widely used in diverse fields such as materials science, physics, chemistry, biology, and cultural heritage. It is particularly effective for identifying iron oxides and their magnetic properties, differentiating oxidation states, and characterizing amorphous phases undetectable by other techniques such as X-ray diffraction. The accuracy of Mössbauer analyses is influenced by errors in spectrum fitting, calibration and thermal corrections. While the technique is sensitive to relative amounts of resonant isotopes, determining absolute concentrations is challenging due to factors like the recoilless fraction[251].

Chapter 4

Objectives of the Thesis

The aim of this thesis is to explore innovative techniques for tailoring metal oxide surfaces for enhancing their application in sustainable catalytic processes. This was achieved by focusing on the multimetallic exsolution process from perovskite oxides and the surface modification of mesoporous titanium dioxide.

The objective of **Chapter 5** is the understanding of the mechanism of exsolution of FeNi bimetallic particles from a perovskite oxide of composition $La_{0.4}Sr_{0.4}Ti_{0.60}Fe_{0.35}Ni_{0.05}O_3$. The study aims to investigate the influence of temperature on the reduction kinetics of Fe and Ni species, and how the reduction of the two reduction processes are interrelated. Additionally, it seeks to evaluate how variations in the reduction kinetics influence the composition of the nucleated and grown bimetallic FeNi nanoparticles, establishing a correlation between the steps of reduction and particle growth of the exsolution process.

In **Chapter 6** the focus is instead put on the surface design of bimetallic catalysts with switchable catalytic selectivity for use in CO_2-assisted oxidative dehydrogenation of ethane. This was done by tuning the composition and morphology of the bimetallic nanoparticles from the $La_{0.4}Sr_{0.4}Ti_{0.60}Fe_{0.35}Ni_{0.05}O_3$ system by varying the exsolution temperature, and by exploiting the possibility of re-incorporating exsolved metal nanoparticles back into the perovskite host matrix through redox cycling of the material, making use of the redox chemistry of iron. This study is conducted in order to lay the foundation for the development of Fe-based redox catalysts via the exsolution process for their use in Carbon Capture and Utilization (CCU) techniques.

The objective of **Chapter 7** is also focused on CCU processes and the redox cycling behavior of Fe-based perovskite catalysts, and involves the surface design of a material with composition $La_{0.6}Ca_{0.4}Fe_{0.95}M_{0.05}O_{3-\delta}$ (M = Ni, Co, NiCo) for its use as oxygen carrier in Chemical Looping Reforming (CLR) of methane coupled with CO_2-splitting. The intent is to enable the exsolution of trimetallic FeCoNi alloy nanoparticles under reducing conditions, and the subsequent switching to NiCo bimetallic nanoparticles under oxidizing atmospheres by re-incorporating Fe cations back into the parent oxide matrix, so as to obtain a regenerable smart catalyst having good thermal and redox stability.

Finally, **Chapter 8** focuses on the systematic analysis of the surface interactions between water and mesoporous titania using water vapor physisorption measurements, with a view toward the potential application of these materials in photocatalytic water splitting. These measurements were carried out following surface modifications of the titania through electro- and photo-thermal treatments, as well as doping with aliovalent transition metals.

Chapter 5

Study of the Exsolution Mechanism of Bimetallic FeNi Nanoparticles from La$_{0.4}$Sr$_{0.4}$Ti$_{0.6}$Fe$_{0.35}$Ni$_{0.05}$O$_3$ through *In-situ* XANES and Synchrotron XRD

5.1 Introduction

Considerable efforts have been made in the past few years for a better understanding of the mechanism of exsolution of metal nanoparticles from perovskite oxides, with a view to its use as a valuable tool for the development of sustainable heterogeneous metal catalysts[27,36,131,163,175,252,253]. This phenomenon occurs because of the structural flexibility of these materials, which are able to accommodate various metal ions in their lattice without compromising its original crystal structure. Metal exsolution practically consists is the treatment of perovskite oxides at high temperatures under reducing conditions, determining the release of oxygen from the material. The formation of oxygen vacancies destabilizes the lattice, inducing the reduction of B-site metal cations and lowering the energy barrier for their migration through the host oxide, leading to their subsequent nucleation as metal nanoparticles onto the material's surface and in the bulk of the perovskite matrix (one speaks in this case of endogenous exsolution)[27,196,254–256]. In the case of the so-called bimetallic exsolution, two B-site metals are exsolved from the perovskite matrix. This results in a synergistic interaction between them, that leads to enhanced activity and selectivity when utilized as heterogeneous catalysts, retaining resistance against sintering and agglomeration due to their good socketing in the host oxide[31,257]. The selection of the appropriate combinations of B-site metal cations and the optimization

of exsolution conditions enables the design of bimetallic nanoparticles with tailored functionalities for a wide range of catalytic applications, such as in energy conversion, environmental catalysis, solid oxide fuel cells and CO_2 conversion techniques[36,70,258–264]. These potential advantages also come with some challenges, including the difficulty in controlling nanoparticle composition and distribution and the complexity of their real-time characterization[265–267]. The mechanism of exsolution is influenced by various factors, including temperature, dopant composition, A-site deficiency, type of reducing atmosphere, and treatment duration[22,168,252,268,269]. This process becomes even more intricate when two metals are involved, as differences in reduction and segregation potentials, redox behaviors, and reduction kinetics lead to uneven nucleation, varying growth rates, and compositional variations in the resulting nanoparticles[31,269]. Exsolved bimetallic FeNi alloys on metal oxide substrates have been reported for use in various applications, including cathodes for CO_2 electrolysis, SOFC anodes, methane reforming, and CO oxidation[22,143,270,271]. The formation of oxygen vacancies plays a crucial role in the exsolution of bimetallic FeNi nanoparticles. Tsiotsias et. al.[22] demonstrated that the introduction of an increasing A-site deficiency α into the $La_{0.4}Sr_{0.6-\alpha}Ti_{0.6}Fe_{0.35}Ni_{0.05}O_{3-\delta}$ perovskite system allows for the control of the concentration of oxygen vacancies, and therefore of the nanoparticles composition in terms of Fe/Ni ratio. The reduction potential of the Ni^{2+}/Ni^0 pair is -0.25 V, whereas that of the Fe^{2+}/Fe^0 pair is -0.44 V. This indicates that nickel is more readily reduced to its metallic state than iron, as its less negative potential signifies a greater tendency for reduction under standard conditions[272]. Their segregation during exsolution is influenced not only by the redox chemistry of the two metals but also by factors such as cation sizes, lattice strain induced by their exsolution within the parent perovskite host, differences in surface diffusivity of the cations, and the Gibbs free energy of nanoparticle formation. These factors all play a crucial role in tailoring the properties of perovskite materials for applications in energy conversion technologies[175]. Although bimetallic FeNi systems are widely used across various applications, the mechanism underlying bimetallic exsolution remains poorly understood in the literature. Addressing this complex interplay of factors

requires advanced characterization techniques to examine the oxidation state and coordination environment of metal ions as they reduce and diffuse within the perovskite oxide lattice, as well as insights into the nucleation and growth of metal nanoparticles. The study of the bimetallic exsolution process is also particularly demanding because it involves tracking two metals simultaneously, requiring the use of advanced techniques involving the use of synchrotron radiation. This is further complicated by the need to distinguish between mixed and segregated phases at the nanoscale and to determine the composition of the bimetallic nanoparticles[134]. The correlation in the reduction dynamics between the two metals during bimetallic exsolution could only be tackled with an *in-situ* study, meaning an analysis of what is happening with a real-time observation of the phenomenon. However, only few of such *in-situ* studies addressing exsolution from the mechanistic point of view are available in the literature[273–275]. Because of this, the focus of **Chapter 5** is the *in-situ* analysis of the correlation that exists between the reduction processes of Fe and Ni, and how their interrelation affects the nucleation and growth of bimetallic metal nanoparticles from the host oxides. This was done for a better understanding the dependence of the reduction kinetics of the two metals from the exsolution temperature, and for assessing how it affects lattice parameter and composition of the FeNi alloy nanoparticles. *In-situ* X-ray Absorption Near-Edge Structure (XANES) spectroscopy and synchrotron X-ray Diffraction (XRD) have been used for monitoring the processes of reduction and particle growth over time, respectively, during the exsolution of FeNi alloy nanoparticles from a nanostructured perovskite oxide system of formula $La_{0.4}Sr_{0.4}Ti_{0.60}Fe_{0.35}Ni_{0.05}O_3$, referred to as LSTFN2. The exsolution process was studied under isothermal conditions at increasing temperatures of 600 °C, 700 °C, 800 °C and 850 °C. These measurements were performed with the means of a specifically designed and implemented experimental apparatus, described in **Section 10.4.1** of the **Experimental Methods** chapter. While *in-situ* XANES allowed for the identification of subtle changes in the local environment of each metal, *in-situ* synchrotron XRD was employed for monitoring the decomposition and growth of crystalline phases, as well as the evolution over

time of their lattice parameters. Following an initial detailed characterization of the as-synthesized LSTFN2 starting material, the combination of these two methods enabled a comprehensive investigation of the reduction kinetics of the B-site metal species, and its correlation with the compositional changes of the resulting bimetallic FeNi nanoparticles as a function of temperature, as reported in the following section.

5.2 Results and discussion

5.2.1 Ex-situ characterization of the parent perovskite structure

The as-synthesized LSTFN2 starting perovskite material has been synthesized according to the procedure reported in **Section 10.2.1** of the **Experimental Methods** chapter. As a first step in describing this system, an *ex-situ* characterization of the material was carried out.

The results of X-ray diffraction in **Figure 35a** show a main perovskite phase with the $Pm\bar{3}m$ cubic space group, typical of a $SrTiO_3$ structure (PDF Nr. 01-079-0175)[22]. Additionally, a secondary spinel phase identified as $NiFe_2O_4$ (PDF Nr. 00-034-0641) was observed, possibly forming due to partial phase reconstruction linked to significant A-site deficiency during high-temperature treatment. The crystallite size and lattice parameter of the main perovskite phase, calculated from the X-ray diffraction pattern of the as-synthesized material using the Scherrer equation, are of 45 nm and 3.910 Å, respectively (**Table 2**).

LSTFN2 is characterized by a fair specific surface area (SSA) of 16 m^2/g determined by nitrogen physisorption (**Figure A1a** in the Appendix). The formation of this quite porous morphology was verified by Transmission Electron Microscopy (TEM, **Figure 35b**), which evidences the presence of a nanostructured material with intraparticle porosity. The atomically resolved HR-TEM image of LSTFN2 is also reported in **Figure 35c,** showing the presence of a cubic perovskite with a d-spacing of 2.877 Å in the (110) plane.
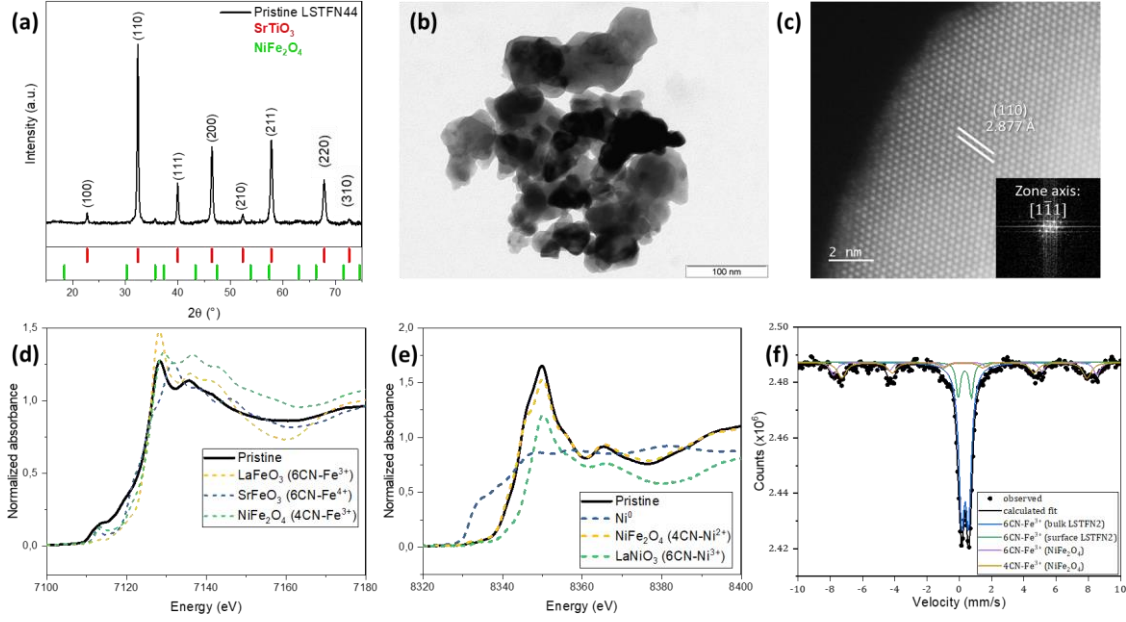
Figure 35. (a) Powder diffractograms of the as-synthesized LSTFN2 material. (b) TEM picture of the as-synthesized LSTFN2 material. (c) HRTEM images of the as-synthesized LSTFN2, with detail on the lattice spacing calculation. (d) XANES spectrum of the Fe K-edge for the as-synthesized LSTFN2 material, plotted together $SrFeO_3$, $LaFeO_3$, $NiFe_2O_4$ as reference standards. (e) XANES spectrum of the Ni K-edge for the as-synthesized LSTFN2 material, plotted together with Ni^0, $LaNiO_3$ and $NiFe_2O_4$ as reference standards. (f) Collected and fitted Mössbauer spectra of the as-synthesized LSTFN2 material, with related attributions.

It is also noticeable how every metal element is homogeneously occupying the bright cation site without any segregation, implying the successful synthesis of the scaffold without any significant amount of second-phase formation. In addition to these results, Energy Dispersive X-ray Spectroscopy (EDXS) from the HR-TEM measurements was performed to investigate the elemental distribution within the as-synthesized LSTFN2 starting material. All the cations, including Fe^{n+} and Ni^{n+}, are homogeneously distributed within the oxide structure (**Figure A1b** in the Appendix), thus showing that, although present, the spinel side phase is marginal compared to the perovskite phase. In order to get more precise information on the oxidation state and local structure of the metals, and particularly of the Ni and Fe species at the B-site, XANES spectroscopy has been performed *ex-situ* on the as-synthesized material. The XANES spectra of Fe and Ni in LSTFN2, along with the reference spectra of $SrFeO_3$, $LaFeO_3$ (for the Fe K-edge), $LaNiO_3$ and $NiFe_2O_4$ (for the Ni K-edge) are reported in **Figure 35d** and **Figure 35e**. The Ni K-edge

spectrum closely resembles that of $NiFe_2O_4$, suggesting that Ni species are predominantly present in the spinel phase, as supported by XRD results, although this interpretation remains uncertain. Moreover, the results of XANES spectroscopy allow for a qualitative estimation of the oxidation states of the parent matrix Fe^{n+} and Ni^{n+} in the as-synthesized material. For Fe, this evaluation is based on a comparison of the absorption edge and white line of LSTFN2 with those of the $NiFe_2O_4$ and $LaFeO_3$ standards (**Figure 35d**). The fact that the spectrum of the material shows a lower white line with respect to the two considered standards suggests a difference in the coordination geometry of Fe[276]. Overall, the Fe K-edge spectrum indicates that iron species in LSTFN2 exhibit features resembling a mixture of $LaFeO_3$ and $NiFe_2O_4$, as evidenced by the distinct white line at 7130 eV and additional shoulders at approximately 7135 eV and 7142 eV. Furthermore, the measured Fe K-edge absorption edge at 7125.3 eV for LSTFN2 lies between the values for the $NiFe_2O_4$ spinel (7122.5 eV) and pure $LaFeO_3$ (7126.4 eV). The oxidation state of pure $LaFeO_3$ is $+3$[277], although studies in the literature report the presence of mixed oxidation states, including Fe^{2+}, often associated with the presence of oxygen vacancies[278]. In the partially inverse spinel structure of $NiFe_2O_4$, Ni^{2+} ions occupy octahedral sites, while Fe^{3+} ions are distributed between tetrahedral and octahedral sites[279]. Considering the inverse spinel configuration and the nanostructured nature of the material, which may lead to non-equilibrium conditions with incomplete spinel inversion[280], an average fractional oxidation state for Fe in LSTFN2 between $+2$ and $+3$ can be assumed. As for the oxidation state of Ni, the as-synthesized LSTFN2 material exhibits an absorption edge at 8344.7 eV (**Table 2**), higher than that of Ni in the $NiFe_2O_4$ spinel (8343.2 eV), where Ni has oxidation state $+2$ in octahedral coordination[281]. For reasons analogous to those mentioned earlier for Fe in the host oxide, the average oxidation state of Ni in the as-synthesized LSTFN2 sample can also be estimated being between $+2$ and $+3$. In **Figure 35f**, the Mössbauer spectrum of the as-synthesized LSTFN2 is reported, showing a strong paramagnetic absorption centered at approximately 0.36 mm/s, along with a broad

sextet attributed to magnetically coupled species. Spectrum fitting identified two doublets, associated with bulk (Δ = 0.44 mm/s) and defective (Δ = 0.82 mm/s) ferric sites in the LSTFN2 perovskite lattice. The hyperfine parameters (**Table A1**) of two additional sextets correspond to octahedral and tetrahedral sites in a partially inverse spinel structure, such as $NiFe_2O_4$[282]. The broad linewidths for these sites finally imply some level of disorder around the ferric sites due to varied local environments. The results of the aforementioned characterization techniques of the as-synthesized LSTFN2 are reported in **Table 2**. This material was used as the starting one of the following *in-situ* XANES and synchrotron XRD experiments.

Table 2. Values of the crystallite size calculated from Scherrer equation (Φ_{XRD}), lattice parameter (a), relative amounts in % of the Fe species calculated via Mossbauer spectroscopy, and Ni and Fe K-edges positions determined from XANES spectra. $6CN_{matrix}$ refers to hexa-coordinated iron of the host perovskite oxide, $6CN/4CN_{spin}$ to the hexa- and tetra-coordinated iron of the $NiFe_2O_4$ spinel.

Sample	Φ_{XRD} (nm)	a (Å)	Fe^{3+} (%)			Fe^{2+} (%)	Fe^{0} (%)	Ni K-edge position (eV)	Fe K-edge position (eV)
			$6CN_{matrix}$	$6CN_{spinel}$	$4CN_{spin}$				
LSTFN2	45	3.910	70	10	20	-	-	8344.7	7125.3

5.2.2 In-situ XANES results

The description of the experimental apparatus for performing the *in-situ* XANES spectroscopy measurements is reported in **Subsection 10.4.1** of the **Experimental Methods** chapter. The reduction of Fe and Ni during exsolution in LSTFN2 under isothermal conditions at different temperatures was first monitored by analyzing the 3D waterfall plots over time (**Figure 36**).
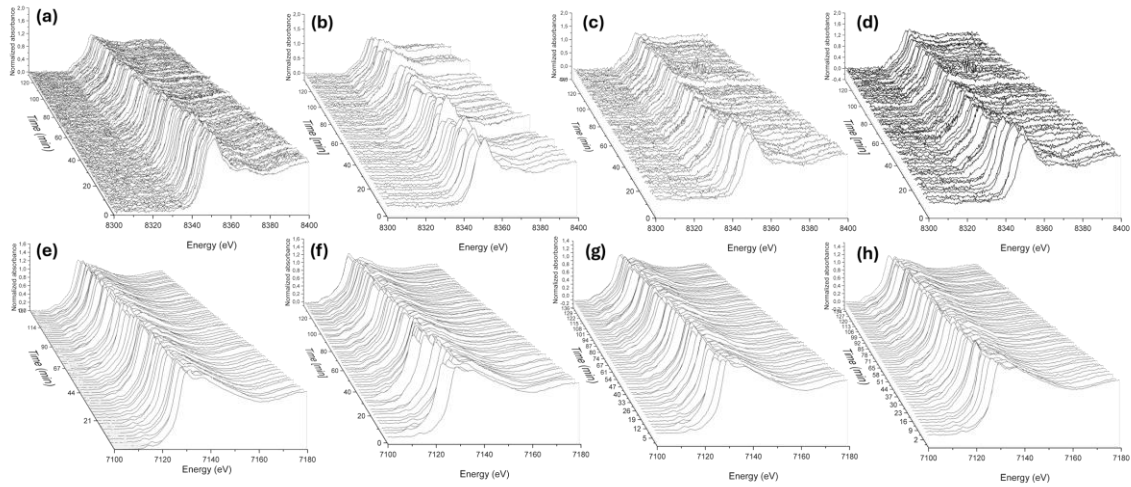

Figure 36. *In-situ* XANES waterfall plots recorded over time at 600, 700, 800 and 850 °C for the Ni K-edge (a, b, c, d) and for the Fe K-edge (e, f, g, h).

A certain thermal noise in the absorbance values of the spectra of the two metals is observed for both Fe and Ni, partially affecting the quality of the plots. This can be attributed to the thermal and static disorder brought about at high temperatures by the Debye-Waller effect, which describes the effect of temperature on the thermal vibrations and on the statistical disorder of the atoms in the lattice[216,283]. The signal noise introduces a systematic error across all *in-situ* measurements and is evident in the high-temperature XANES spectra of both Fe and Ni. However, the Ni spectra show greater disorder across all temperature ranges from 600 to 850 °C, whereas for Fe, this disorder appears only from 700 °C onward and is less pronounced compared to Ni. This difference can be attributed to the lower atomic fraction of Ni (5 at.%) compared to Fe (35 at.%) at the B-site of LSTFN2. The reduced Ni content likely

leads to a weaker signal-to-noise ratio, making Ni more prone to noise during fluorescence data collection[284]. Additionally, the lower absorption cross section of Ni, which reduces the likelihood of absorption events during X-ray interaction with the sample, contributing to weaker spectral signals[284,285].

A first overview of the cascade plots in **Figure 36** for both the Fe and Ni K-edges reveals that increasing exsolution temperatures, measured through *in-situ* XANES, result in a progressive decrease in the white line intensity. This decrease indicates a change in the coordination geometry of the two metals and is accompanied by a shift of the absorption edge toward lower energy values, which is associated with a reduction in the oxidation states of Fe and Ni[216]. Moreover, the trend of the waterfall plots reveals that, by the end of the *in-situ* exsolution experiment, the Ni species undergo a greater extent of reduction compared to Fe, as evidenced by a more pronounced leftward shift of the absorption edge and a corresponding decrease in white line intensity. This is generally due to the lower reduction potential and lower segregation energy of Ni when compared to Fe, which makes the process of Ni reduction thermodynamically more favorable at equal temperature and experimental conditions[22,177,253]. For a quantitative description of the reduction process, linear combination fitting (henceforth abbreviated as LCF) has been performed. This was done by using different reference spectra, as reported in **Section 10.3.2** the **Characterization Methods** section. The standards used in the fitting have been chosen as representative of the oxidation states and coordination environments expected in the sample during the reduction process[286]. For each temperature, XANES spectra have been collected and fitted via LCF for the quantification over time of the amounts of the cations of each species in terms of atomic (at.%) and weight fractions (wt.%). By way of example, the LCF fitting results of the XANES spectra of Ni and Fe in the material reduced at 600 °C are shown in **Figure 37**. These spectra were acquired at the end of the exsolution experiment, i.e. after 120 min from the beginning of the reduction, and are presented along with R-factor and χ^2 values for both Fe and Ni. These parameters, which evaluate the quality of the

fitting based on statistical consistency and the magnitude of residuals, indicate a good fit for the XANES spectra, especially considering the high temperatures at which the measurements were performed, which determine lower signal-to-noise ratios[287–290]. The same plots shown in **Figure 37**, for all other exsolution temperatures analyzed, along with R-factor and χ^2 values for both Fe and Ni recorded after 120 min of reduction, are reported in **Figure A2** in the Appendix.
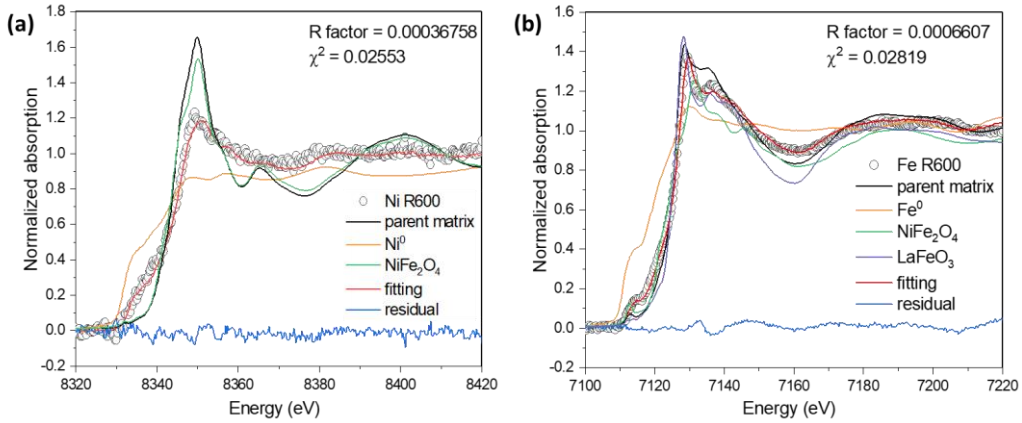

Figure 37. Ni K-edge (a) and Fe K-edge (b) spectra of R600 recorded after 120 min exsolution, plotted together with the one of the correspondent parent matrixes spectra and the reference spectra for LCF, i.e. Ni^0 and $NiFe_2O_4$ for the Ni K-edge, and Fe^0, $NiFe_2O_4$, and $LaFeO_3$ for the Fe K-edge. The LCF fitting (red line), the residual plots (blue line, calculated with A^{exp}-A^{fit}, with A the normalized absorbance) and the final values of R-factor and χ^2 are also reported.

The results of the LCF fitting of the Ni K-edge spectra for the exsolution experiments at 600 °C (R600), 700 °C (R700), 800 °C (R800) and 850 °C (R850) are presented in **Figure 38**. The experimental trends have been plotted together with a continuous fitted line for better visualization.

The reduction behavior of Ni species follows a consistent reduction trend across all exsolution temperatures, characterized by a stepwise transition from the Ni^{n+} state (the oxidation state of Ni in the parent perovskite matrix) to Ni^{2+}, and eventually to metallic Ni^0. With 'stepwise' it is intended a process in which the monotonic decrease of parent Ni^{n+} is followed by the gradual reduction to Ni^{2+}. Once Ni^{2+} reaches its maximum concentration at a specific temperature, part of it is further reduced to Ni^0. Additionally, the reduction of Ni^{n+} and the subsequent

formation of Ni^{2+} and Ni^0 occurs more gradually at lower temperatures (600 °C and 700 °C) and proceed much faster at higher temperatures (800 °C and 850 °C).
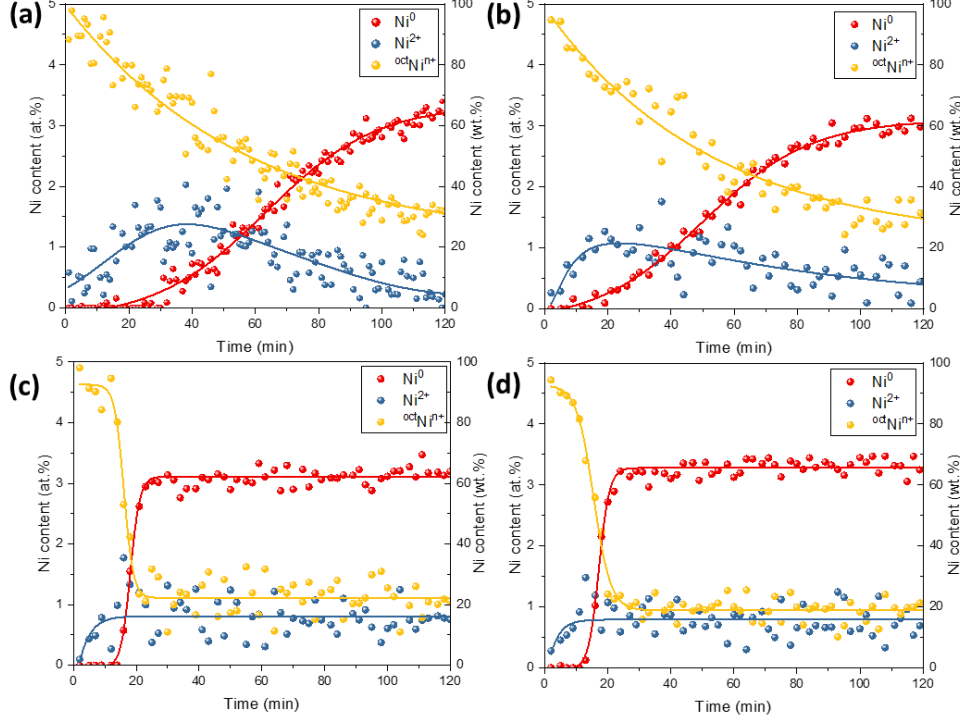

Figure 38. *In-situ* XANES plots of the LCF results for the Ni K-edge showing the variation of the various species present over time during reduction for R600 (a), R700 (b), R800 (c) and R850 (d). Solid lines have been added to the plots for better visualization.

Going more into detail about the individuals Ni species, considering the parent matrix nickel, a gradual decrease in Ni^{n+} content is observed for R600 (**Figure 38a**) and R700 (**Figure 38b**), reaching 1.6 at.% and 1.5 at.% after 120 min, respectively. In contrast, for R800 and R850, the Ni^{n+} amount remains relatively constant during the first 10 min of the reduction process, after which an abrupt decrease after 20 min to 1 at.% in R800 (**Figure 38c**) and R850 (**Figure 38d**) is observed. This trend shows that a larger amount of parent matrix Ni^{n+} is reduced within the material at higher temperatures (800–850 °C) compared to lower temperatures (600–700 °C). This phenomenon is related to the improved oxygen release kinetics and increased thermodynamic favorability of the reduction process at higher temperatures. From the kinetic point of view, the activation energy required for oxygen release from the

lattice is more readily overcome, enabling a larger extent of reduction of Ni^{n+} cations from the perovskite lattice. Moreover, the increased vibrational energy of atoms at higher temperatures (i.e., 800 °C and 850 °C) determines a faster oxygen release. This accelerates the reach of the critical concentration of oxygen vacancies required to overcome the activation energy for Ni reduction, which is the rate-determining step of the process[131,291,292]. As oxygen vacancies form, they facilitate the diffusion of Ni cations and the subsequent rapid reduction of Ni ions to lower oxidation states. Additionally, higher temperatures result in a thermodynamically favorable reduction of Ni. This is due to a more negative the larger entropic contribution ($T\Delta S$) to the Gibbs free energy ($\Delta G = \Delta H - T\Delta S$), which promotes the reduction of parent oxide Ni^{n+}[131]. In all cases, the complete reduction of Ni^{n+} is not observed, as some nickel remains in the parent matrix oxidation state even after 120 minutes. This indicates that only a fraction of Ni^{n+} is reduced to Ni^{2+} and subsequently to Ni^{0}. In fact, even at relatively high temperatures, oxygen release from the perovskite lattice is limited by the maximum concentration of oxygen vacancies set by the materials' stoichiometry, which lead some substitutional species to remain in the pristine matrix. Moreover, the strong interaction between dopant cations and the host lattice contributes to resisting full reduction, as excessive oxygen vacancy formation would destabilize the perovskite structure[131,196,266]. Considering instead the reduction kinetics at lower temperatures (600 °C and 700°C), the slower depletion rate of parent matrix Ni for R600 and R700 can be attributed to less effective oxygen vacancy formation, which is essential for the reduction of Ni^{n+} to lower oxidation states (Ni^{2+} and Ni^{0}). This contrasts with the greater oxygen release observed at higher temperatures. Additionally, the reduced mobility of Ni^{n+} cations within the perovskite lattice at lower temperatures limits the rate of Ni diffusion, while for R800 and R850 the increased oxygen release and enhanced Ni diffusion through segregation with oxygen vacancies significantly accelerates the onset of Ni^{n+} reduction[256,257,293]. From a thermodynamic perspective, the smaller entropic contribution to oxygen vacancy formation at lower temperatures results in a less negative Gibbs free energy,

thereby diminishing the driving force for both oxygen vacancy formation and subsequent Ni reduction[139,294].

Moving on to the reduction trend of Ni^{2+}, the disparity in the amount of Ni^{n+} recorded after 120 minutes translates into corresponding differences in the kinetics of formation of Ni^{2+} species. **Figure 38** indicates that Ni^{2+} acts as an intermediate state during reduction, following the stepwise mechanism where Ni^{n+} is first reduced to Ni^{2+} and subsequently to Ni^0 as the reduction progresses. The amount of Ni^{2+} over time varies depending on the reduction temperature. For R600, Ni^{2+} concentration reaches a maximum after 40 min, and then gradually decreases to approximately 0.2 at.% after 120 min. In R700, the maximum concentration of Ni^{2+} is reached earlier, at 25 min, and decreases more slowly, reaching 0.4 at.% after 120 min (**Figure 38a,b**). At higher temperatures (R800 and R850), a different behavior is observed. Here, the rapid reduction of Ni^{n+} is accompanied by a sharp increase in Ni^{2+}, which reaches a maximum after 20 minutes and stabilizes at 0.8 at.% for both temperatures (**Figure 38c,d**). This leads to conclude that for R600 and R700 less Ni^{n+} is reduced to Ni^{2+}, whereas at R800 and R850 more Ni^{n+} is consumed, resulting in higher Ni^{2+} recorded levels at equilibrium. This difference could be attributed to the limited release of lattice oxygen (β-oxygen) at lower temperatures, which restricts the formation of Ni^{2+} intermediates[131]. However, despite the differences in the relative amounts of Ni^{n+} and Ni^{2+}, the amount of metallic Ni^0 recorded at the end of the process is the same regardless of the reduction temperature, stabilizing at 3.2 at.%. For R600 and R700, a plateau in the final amount of Ni^0 was not reached after 120 minutes, unlike in the cases of R800 and R850. This fact can be attributed to the slower reduction rates at lower temperatures, as the process likely has not reached its final equilibrium due to kinetic limitations, including slower oxygen release and therefore reduced diffusion of Ni ions within the perovskite matrix[131]. Therefore, extending the exsolution time beyond 120 min would likely result in the same final amount of Ni^0. This same final amount of Ni^0 species at equilibrium across different temperatures can be attributed to the intrinsic properties of the A-site-deficient perovskite structure of LSTFN2. Specifically, the final atomic fraction of the exsolved

metals is governed by the initial stoichiometry (i.e. the composition) of the parent perovskite oxide[22,271]. The increased concentration of oxygen vacancies resulting from 20% A-site deficiency plays a crucial role in facilitating the reduction process, enabling the effective reduction of Ni species[22]. In addition to that, some differences are also found in the induction time of reduction to Ni^0, defined as the time interval between the beginning of the reduction process (e.g., beginning of the exposure to a reducing atmosphere) and the onset of observable Ni reduction from LCF, as shown in **Figure 38a-d**. Its values are influenced by factors such as the rate of oxygen release from the host oxide lattice[139], as proposed by Rudolph at. al., who pointed out how the induction time for Ni nanoparticle exsolution from nanoporous perovskites was linked to the oxygen release kinetics[256]. For LSTFN2, the induction time for Ni^0 does not exhibit a clear trend. At 600 °C, the onset of nickel reduction occurs relatively late, i.e. after 30 min. In contrast, shorter induction times are observed at higher temperatures. At 700 °C, the reduction of Ni^0 begins after 10 min, while at 800 °C and 850 °C it starts after approximately 15 min in both cases, followed by a rapid decrease in Ni^{n+} until the final value of 3.2 at.% is reached. The smaller induction time for metal exsolution at lower temperatures is also in this case primarily due to lower rates of oxygen vacancy formation and cation diffusion. The diffusion of metal cations (e.g., Ni^{n+} and Ni^{2+}) within the perovskite lattice is slower at lower temperatures. Therefore, lower temperatures lead to lower diffusion coefficients and therefore to lower the mobility of oxygen and cations within the lattice, delaying the reduction of the Ni^{n+} species[36,293,295].
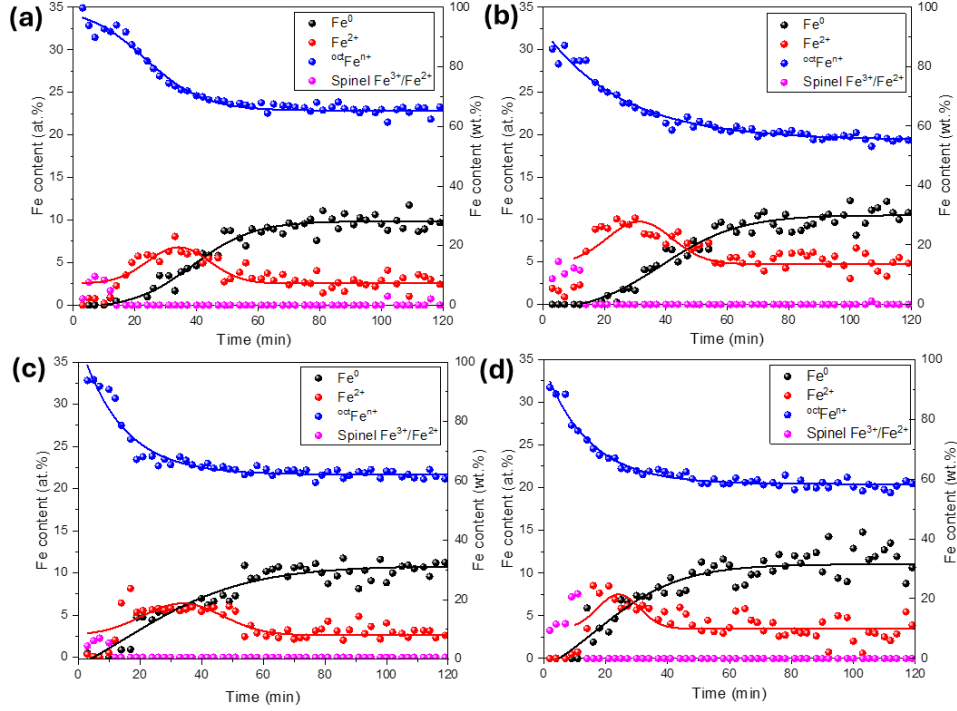
Figure 39. *In-situ* XANES plots of the LCF results at the Fe K-edge showing the variation of the various species present over time during reduction for R600 (a), R700 (b), R800 (c) and R850 (d). Solid lines have been added to the plots for better visualization.

Moving to the reduction trend of Fe observed from LCF, the species used for the fitting were chosen to be Fe^{n+}, representative of the parent perovskite matrix and the $NiFe_2O_4$ spinel phase; Fe^{2+} species, which are representative of wüstite (FeO_{1+x}) and again for the $NiFe_2O_4$ spinel, being the latter a partially inverse oxide with mixed oxidation state of Fe^{2+}/Fe^{3+}, together with Fe foil for Fe^0. The results of the LCF conducted for the exsolution treatments at 600 °C (**Figure 39a**), 700 °C (**Figure 39b**), 800 °C (**Figure 39c**) and 850 °C (**Figure 39d**) reveal a 'step-wise' reduction trend similar to that observed for Ni reduction. At all temperatures, a monotonic decrease in the parent matrix Fe^{n+} is observed within the first few minutes of the experiment, coinciding with the reduction of iron species that can be reasonably attributed to the spinel $NiFe_2O_4$ phase (comprising a mixture of Fe^{2+} and Fe^{3+}). Once these species are depleted, a gradual increase in Fe^{2+} can be observed, which, after reaching a maximum at around 30 min, starts to gradually further reduce in favor of metallic Fe^0, whose formation begins to be significantly observable between

40 and 50 min after the onset of reduction, for all of the exsolution temperatures investigated (i.e. for R600, R700, R800 and R850). This shows how Fe transitions from larger to lower oxidation states to eventually go to form Fe^0 species due to lattice oxygen removal, independently from the temperature of reduction and therefore on the kinetics of oxygen release. Furthermore, the trends of the LCF results (**Figure 39a-d**) for Fe reduction are similar to each other and consistent across the different temperatures examined, unlike the case of the Ni K-edge (**Figure 39a-d**), where a clear difference in the reduction kinetics is observed when transitioning from lower temperatures (600 °C and 700 °C) to higher temperatures (800 °C and 850 °C). This can be explained by the fact that Ni is more easily reduced than Fe due to its lower reduction potential and segregation energy, and the reach of a critical concentration of oxygen vacancies triggering Ni reduction is the rate-determining step of the bimetallic reduction process in LSTFN2. The reach of this critical concentration of oxygen vacancies also dictates the kinetics of Fe^{n+} reduction, which is triggered by Ni reduction and sis independent by temperature[22,131,253].

Focusing on the individual Fe species, the parent oxide Fe^{n+} undergoes a gradual monotonic reduction from the start of the process, stabilizing approximately after 60 min. However, the equilibrium amount of Fe^{n+} varies with temperature, similar to the trend observed for the LCF of the Ni K-edge. For R600 less Fe^{n+} is reduced, reaching a final value of 22.8 at.%. For R700, greater matrix Fe consumption occurs, reducing to 19.3 at.%. For higher temperatures (R800 and R850), Fe^{n+} stabilizes at 21.6 at.% after 120 minutes. Except for R700, higher temperatures lead to greater Fe^{n+} consumption, since they enhance the thermodynamic driving force for oxygen release, facilitating its reduction of Fe^{n+} to lower oxidation states[22,252].

In addition to that, the reduction of Fe^{n+} undergoes an acceleration once the Fe^{3+} attributed to $NiFe_2O_4$ spinel (pink points) is consumed. The presence of this phase is confirmed from the beginning of the process, as seen in **Subsection 5.2.1**, and reaches values included between 10 wt.% (recorded for R600) and 20 wt.% (in the case of R850). It is however reduced within about 10 min from the beginning of the experiments, regardless of the exsolution temperatures, as the reduction of the

$NiFe_2O_4$ can occur already at temperatures as low as 600 °C under these experimental conditions[296]. The disappearance of the contribution always coincides, at each of the temperatures examined, with the beginning of the reduction of Fe^{n+} to Fe^{2+}. The reduction of Fe^{n+} to Fe^{2+} follows a consistent trend across all materials, with an induction time for its formation of 10 min observed at each temperature. This uniformity is primarily governed by the initial stoichiometry of LSTFN2, which are intrinsic of the material and are not significantly affected by temperature during the initial stage of reduction at the Fe K-edge. The amount of Fe^{2+} reaches a maximum of 5–10 at.% for all temperatures after 20 min, gradually decreasing and stabilizing at a plateau of 2.6 at.% after 60 min, except for R800, where Fe^{2+} forms earlier (after 40 min) and stabilizes at a higher final value of approximately 4.8 at.%.

In general, at equilibrium, a consistent residual amount of Fe^{2+} is recorded for all of the investigated reduction temperatures. This could be related to structural constraints to further iron reduction within the perovskite matrix, through which Fe^{2+} may be stabilized by lattice distortions that prevent its complete reduction to metallic iron[36]. Moreover, Fe^{2+} may also serve to preserve the structural integrity of the perovskite, as complete reduction to Fe^0 could destabilize the lattice[27]. The presence of these Fe^{2+} species is of fundamental importance in further explaining the morphology of the exsolved FeNi nanoparticles, as it will be discussed later in **Chapter 6**. Similarly to the case of nickel reduction, the final amounts of Fe^{n+} and Fe^{2+} do not influence the final amount of Fe^0 species, which remains constant across all temperatures. The reduction to Fe^0 begins once Fe^{2+} reaches its maximum atomic fraction, approximately 40–50 min into the process, and continues until a plateau is reached, where the Fe^0 content stabilizes at around 10 at.%. The stepwise reduction from Fe^{2+} to Fe^0, occurring independently of temperature, highlights the requirement for a critical threshold concentration of oxygen vacancies in the perovskite lattice before Fe^{2+} can be fully reduced to Fe^0, which is independent of the reduction temperature. The fact that the kinetics of Fe reduction are largely unaffected by the exsolution temperature, as shown in **Figure 39**, and that the reduction of Ni^{n+} triggers the reduction of the less-reducible Fe^{n+} cation, suggests that the

concentration of oxygen vacancies associated with Ni in LSTFN2 controls the reduction process. Moreover, the same induction time for Fe^0 formation recorded across all temperatures aligns with the final amount of Fe^0 being the same at each temperature[139]. To summarize the considerations made so far regarding the different reduction kinetics between Fe and Ni and the extent of exsolution for each temperature, the reduction trends of M^{n+} and M^0 (M = Ni, Fe) over time and parametric with respect to the exsolution temperature are shown in **Figure 40**. Focusing first on the trend of Ni^0 (**Figure 40a**), the different Ni reduction kinetics depending on the exsolution temperature is even more evident. For R800 and R850 the faster rate of formation of Ni^0 is underlined, with the reason for this different kinetics being the faster oxygen release from the host matrix[131,295]. Moreover, the final amount of reduced Ni^0 is the same once thermodynamic equilibrium is reached, since its value is determined by the stoichiometry chosen at the material design stage, in which the presence of A-site deficiency, as in the case of LSTFN2, plays an important role[22]. Similarly, in the case of the trend of the parent matrix Ni^{n+} over time (**Figure 40b**), the enhanced oxygen release rate and greater thermodynamic favorability of reduction that occur at larger temperatures for R800 and R850 allow for a larger extent of reduction of Ni^{n+} from the perovskite lattice, net of different reduction kinetics as exsolution temperature increases. Turning to the trend of Fe^0 (**Figure 40c**), regardless of the temperature of exsolution the same kinetics of Fe reduction is observed, since the reduction of Ni is the critical driving force for the Fe reduction during bimetallic exsolution, due to its lower reduction potential[22]. Finally, in spite of this, the depletion of the parent matrix Fe^{n+} is greater for R800 and R850 than for R600 and R700 (**Figure 40d**), as elevated temperatures increase the thermodynamic driving force for oxygen release, thereby facilitating the reduction of Fe^{n+}. Finally, the analysis of the trends Ni^{2+} and Fe^{2+} with different temperature was not possible due to their complexity (**Figure A3** in the Appendix), despite its potential relevance in describing the reduction process. However, as mentioned earlier, the presence of these residual species in the material at equilibrium reflects

on the composition of the exsolved bimetallic nanoparticles, as it will pointed out in
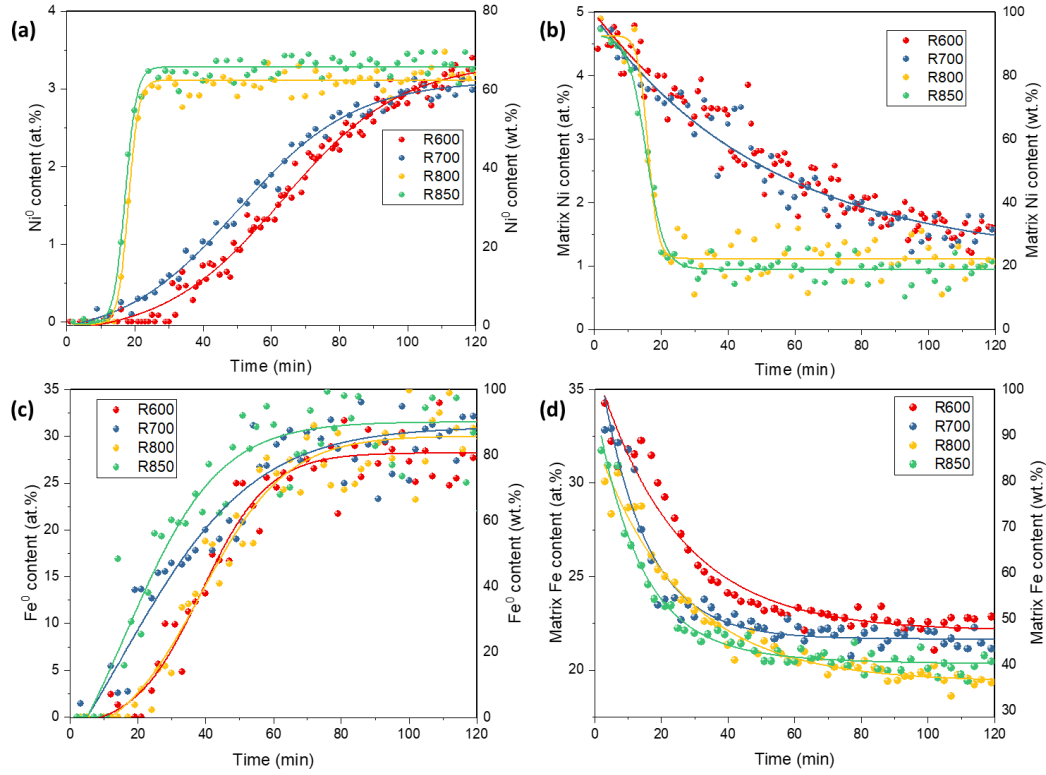
Chapter 6.

Figure 40. Overview of the reduction over time of Ni^0 (a), matrix Ni^{n+} (b), Fe^0 (c) and matrix Fe^{n+} (d). Solid lines have been added to the plots for better visualization.
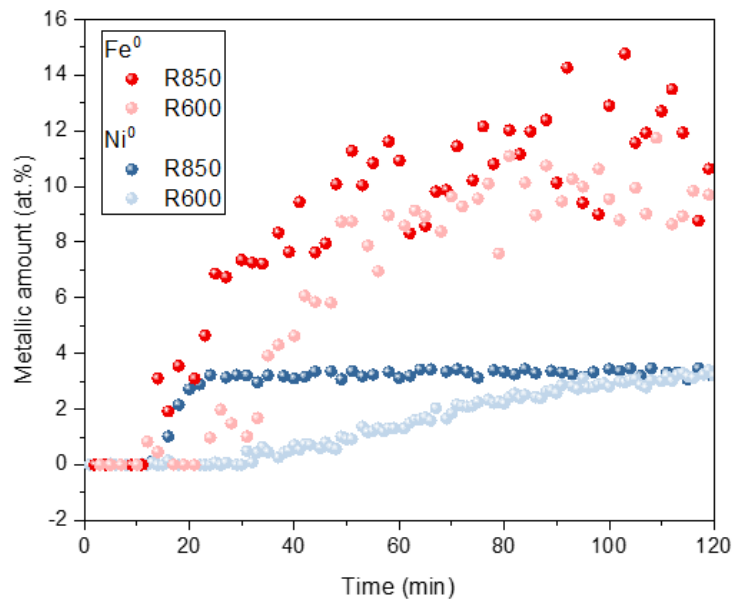

Figure 41. Trend of the metallic amounts for Ni^0 and Fe^0 reduction over time for R600 and R850.

After analyzing the reduction behavior of each metal cation individually, the focus shifted to the formation of metallic species. **Figure 41** compares the reduction trends of Fe^0 and Ni^0 over time to explore their correlation. This comparison focuses on the material exsolved at the lowest temperature (R600) and the highest temperature (R850), representing the distinct reduction kinetics observed at these conditions.

The difference in the formation kinetics of Ni^0, slower at 600 °C and faster at 850 °C, is evident in **Figure 41**. In the case of Ni reduction in R600, the process begins approximately 30 minutes after the start of the *in-situ* experiment (including the induction time). The reduction proceeds slowly, driven by the gradual formation of oxygen vacancies and the migration of Ni cations, following a stepwise transition from Ni^{n+} to Ni^{2+} and eventually to metallic Ni[35,36]. For Fe reduction in R600, the transition from Fe^{n+} to Fe^0, involving the intermediate formation of Fe^{2+}, begins approximately 30 min after the onset of Ni^0 formation. Similarly, in R850, the same phenomenon is observed: the reduction to Ni^0 occurs earlier, at around 17 min from the start of the process, due to faster oxygen release and enhanced diffusion of metal cations within the perovskite matrix. This coincides with the simultaneous formation of Fe^0 species, which subsequently increase over time. As already discussed, this is because the reduction of Ni triggers the one of Fe, having the first one a lower reduction potential compared to Fe, making it more easily reducible which lower the energy barrier for the reduction of Fe[22,297]. Moreover, the reduction from M^{2+} to M^0 in LSTFN2 happens for both Fe and Ni at the same time, once the temperature of exsolution is set, with the reduction to Ni^0 setting the kinetics of the process and triggering the parallel reduction of the Fe^0 species, induced by cation diffusion at high temperature once the critical oxygen vacancy concentration is reached. This is also evident from the fact that both Fe^0 and Ni^0 show the same onset of metal reduction, i.e. the same induction time, which is equal to 10 min for both temperatures. The induction time represents the period required to achieve a critical level of oxygen deficiency, which initiates the reduction of metal cations. Identical induction times suggest that both species are governed by the same oxygen release dynamics rather than their individual diffusion rates. In other words, depending on

the exsolution temperature (which directly affects the Ni reduction kinetics), the system reaches a critical threshold of oxygen vacancies that triggers the reduction of both metal cations, starting with Ni^{n+} and followed by Fe^{n+}. Once the reduction process starts, it proceeds with the gradual reduction of both metals to lower oxidation states, until reaching the reduction to the metallic species with the same onset, i.e. with the same induction time, as can be seen in **Figure 41**. Finally, these results clearly show that, irrespective of the exsolution temperature and the associated reduction kinetics, the equilibrium concentrations of Ni^0 and Fe^0 remain unchanged, as previously discussed. To summarize the results of the *in-situ* reduction process and to better visualize the combined reduction behavior of both Fe^0 and Ni^0 over time, a parameter that takes into account the atomic quantities of both metals is introduced, i.e. the atomic fraction X_{Fe} (**Equation 33**):

$$X_{Fe} = \frac{at.\%_{Fe}}{at.\%_{Fe} + at.\%_{Ni}} \tag{33}$$
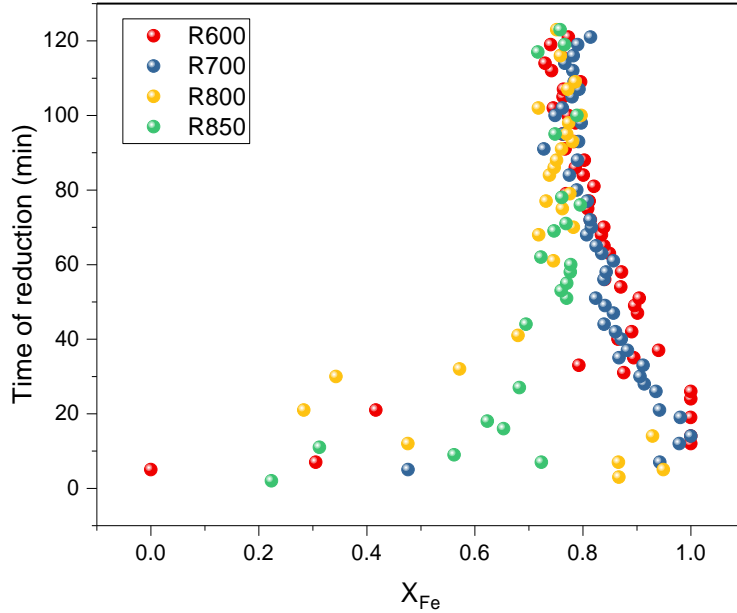
Figure 42. Trend of the value of the atomic fraction of metallic Fe (X_{Fe}) over the reduction time for isothermal exsolution treatments at 600 °C, 700°C, 800°C and 850 °C.

The variation of X_{Fe} over time at the different exsolution temperatures is reported in **Figure 42**: the trend shows clear difference in the atomic fraction in the first 30

min of the process between low and high temperature. For R600, $X_{Fe} \approx 1$ during the first 30 min of the experiment, indicating that more Fe^0 than Ni^0 is available for metal nanoparticle nucleation. In contrast, for R850, $X_{Fe} < 0.8$ in the first 40 min, stabilizing after 60 min, with significant Ni^0 present alongside Fe^0 early in the process, influencing the formation of FeNi bimetallic nanoparticles. By the end of the process (120 min), X_{Fe} converges to ≈ 0.77 for all materials, corresponding to $Fe^0 = 2.33Ni^0$, regardless of the exsolution temperature. This suggests that the first 60 min are critical in determining the relative amounts of Fe^0 and Ni^0 available for nanoparticle formation. For R600 and R700, a sluggish reduction kinetics results in less Ni^0 within the first 30 minutes, while for R800 and R850 X_{Fe} values between 0.5 and 0.8 indicate a greater presence of Ni^0. This shows how the difference in the reduction kinetics of Ni at different temperatures leads to varying relative amounts of Fe^0 and Ni^0 during the reduction process. To determine how this affects the composition of bimetallic nanoparticles, *in-situ* synchrotron XRD measurements have been carried out, allowing for a correlation of both reduction and particle growth processes.

5.2.3 Composition of the exsolved FeNi nanoparticles

Basing on the XANES results, which offer insights into the dynamics of metal cation reduction within the perovskite matrix, the analysis progressed to the next stage of the exsolution process, i.e. the nucleation and growth of bimetallic nanoparticles. The oxygen vacancy formation and electron transfer taking place under reducing conditions, determining the reduction of the cations from Ni^{n+} and Fe^{n+} to their metallic state, is a prerequisite for the subsequent nucleation of metal nanoparticles in the exsolution process, together with the migration of these species to the surface, where the growth can occur[36,266,294]. Moreover, after the induction time is overcome and the reduction process proceeds, the growth and the reduction steps can occur in parallel, as the growth of bimetallic nanoparticles is influenced by the availability of reduced metal species, which depends on the ongoing reduction process[36,139]. In studies available in the literature addressing perovskite systems different than

LSTFN2, the kinetics of reduction has also been shown to influence the morphology of the exsolved nanoparticles, with relatively lower reduction temperatures resulting in the formation of smaller nanoparticles with higher population densities, and higher temperatures lead to fewer but larger nanoparticles[253,256,266,298]. For example, Guo et. al.[266] demonstrated that nanoparticles exsolved at 350 to 400 °C were smaller ($\approx$2.3 nm) and more uniformly distributed when compared to those formed 450 °C ($\approx$3.7 nm), where particle growth was driven by enhanced ion diffusion and coalescence[266]. Similarly, Rudolph et. al.[256] observed that, when exsolving Ni particles from strontium titanate-based perovskite hosts, at low temperatures (500 °C) sluggish ion kinetics favored the formation of many nuclei with limited growth, whereas higher temperatures (700-900 °C) promoted the growth of existing nuclei into larger particles. In addition to that, the temperature during multimetallic exsolution significantly influences the composition of the nanoparticles formed: again, Guo et. al.[266] demonstrated that at lower temperatures (350–450 °C), bimetallic Ni-Ru nanoparticles nucleated with a higher Ru content, while higher temperatures led to larger particles with a more balanced Ni-Ru composition. Similarly, Tsiotsias et. al.[22] already observed that the Fe/Ni ratio in bimetallic nanoparticles could be tuned by adjusting the reduction temperature, with lower temperatures favoring Fe-rich phases and higher temperatures promoting the formation of intermetallic $FeNi_3$ alloy nanoparticles.

In light of this, to correlate reduction and particle growth, the average composition of FeNi bimetallic nanoparticles at the end of the process (after 120 minutes under a 5% H_2/N_2 atmosphere) was evaluated for each of the exsolution temperatures investigated. This was achieved through *ex-situ* XRD by recording the 2ϑ value of the (111) reflection attributed to the γ-FeNi alloy and calculating its average lattice parameter using Bragg's law. Diffractograms of exsolved materials at increasing temperatures, focusing on the 2ϑ range of the FeNi alloy (42.5–45°), are shown in **Figure 43a**. A rightward shift of the reflection is observed with increasing exsolution temperature, indicating a decreasing lattice parameter, as shown in **Figure 43b**. The lattice parameter decreases from 3.588 Å for R600 to 3.578 Å for R850, corresponding

to a cubic lattice contraction of 0.01 Å. This contraction is attributed to compositional changes and atomic rearrangements in the alloy, as higher temperatures promote denser atomic packing of Fe and Ni[297].

To quantify the composition of the exsolved FeNi alloy nanoparticles, the measured lattice parameters were compared with literature data available for FeNi alloys. Specifically, a systematic study from Owen et. al.[186] was used as reference, as it provides insights into the lattice parameter variations of FeNi alloys across different compositions and temperatures, exploring the behavior of both the FeNi y-phase (Face-Centered Cubic, FCC) and α-phase (Body-Centered Cubic, BCC) alloys.
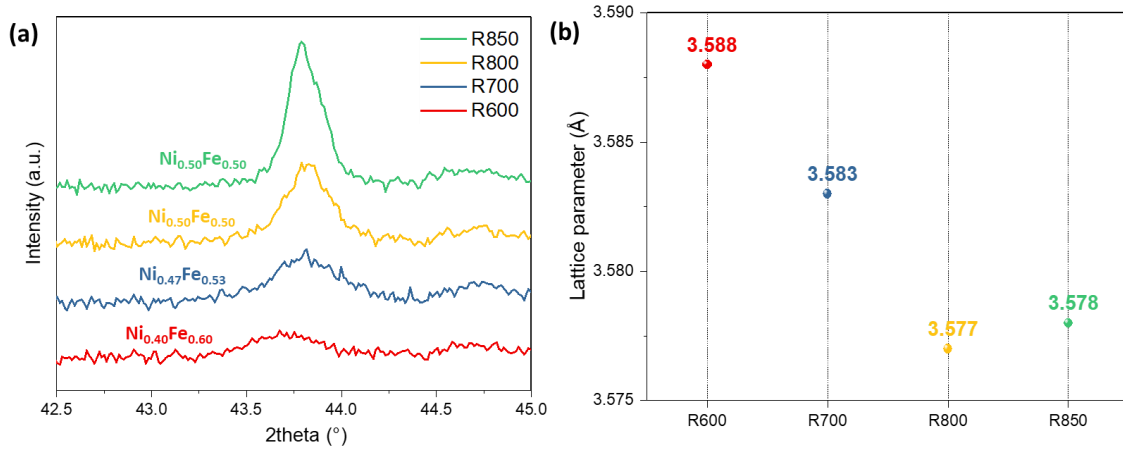
Figure 43. (a) *Ex-situ* XRD of the FeNi alloy reflection of R600, R700, R800 and R850, after 120 min exsolution, measured with a conventional laboratory powder diffractometer. (b) Values of the lattice parameters of the FeNi alloy nanoparticles calculated via Bragg's law based on the *ex-situ* XRD diffractograms measured after 120 min exsolution.

By comparison with the data of **Figure A4** in the Appendix, the lattice parameter values shown in **Figure 43b** correspond to those of a γ-FeNi alloy[63], with compositions ranging from $Fe_{0.6}Ni_{0.4}$ for R600 to $Fe_{0.5}Ni_{0.5}$ for R850. A complete overview is reported in **Table 3**, together with the values of the crystallite sizes of the FeNi alloys calculated via Scherrer equation from the X-ray diffractograms. These findings lead to conclude that an increase in the exsolution temperature results in a decrease of the lattice parameter, correspondent to the nucleation and growth of bimetallic γ-FeNi nanoparticles with reduced Fe incorporation and increased Ni amount. Correlating these results with the *in-situ* XANES experiments reveals that,

while the equilibrium amounts of reduced Fe^0 and Ni^0 are identical across all temperatures, differences in Ni reduction kinetics between R600/R700 and R800/R850 result in variations in the final average composition of the grown nanoparticles. Comparing the temperature-dependent compositions in **Table 3** with the results in **Figure 41**, a relationship between reduction kinetics and nanoparticle composition emerges. For R600, the slower reduction of Ni^0 after 30 minutes allows Fe^0, to be present in larger amounts in the grown nanoparticles, leading to Fe-rich particles with a larger amount of iron ($Ni_{0.4}Fe_{0.6}$). In contrast, at R850, the faster reduction of Ni^0 results in a higher incorporation of metallic Ni into the nanoparticles, yielding a composition of $Ni_{0.5}Fe_{0.5}$ by the end of the process.

Table 3. Values of the lattice parameters and correspondent alloy composition calculated from Owen et. al.[299] for the LSTFN2 materials exsolved at increasing temperatures, together with values of the average crystallite sizes.

LSTFN2 material	Lattice parameter (Å)	Alloy composition (-)	Crystallite size (nm)
R600	3.588	$Ni_{0.40}Fe_{0.60}$	36
R700	3.583	$Ni_{0.47}Fe_{0.53}$	38
R800	3.577	$Ni_{0.50}Fe_{0.50}$	48
R850	3.578	$Ni_{0.50}Fe_{0.50}$	64

5.2.4 In-situ synchrotron XRD results

While the results on the composition of nucleated nanoparticles at the end of exsolution provide valuable insights, the relationship between reduction and nucleation remains unclear. To further investigate the structural evolution of LSTFN2 and the growth of bimetallic nanoparticles during the exsolution process at different temperatures, *in-situ* XRD experiments were conducted in a manner analogous to the *in-situ* XANES experiments. These involved the continuous collection of XRD diffractograms of LSTFN2 under the same experimental conditions, including the reducing atmosphere and exsolution temperatures, as described in **Subsection 10.4.1** of the **Experimental Methods** chapter.

The waterfall plots of the time-resolved *in-situ* X-ray diffractograms are shown in **Figure 44** for $30° < 2\vartheta < 50°$. Prior to analysis, a necessary correction was applied to account for the shift toward higher 2ϑ values across the entire diffractogram, caused by lattice expansion effects that become more pronounced at elevated temperatures during the *in-situ* exsolution process[300]. This was done by comparing the 2ϑ value of the (110) reflection of the parent perovskite matrix measured at room temperature with those measured at higher temperatures (i.e. 600–850 °C), and subsequently shifting the diffractograms to the left. The analysis was first focused on the time-dependent intensity and position of some key reflections: the (110) reflection of the parent perovskite matrix at 32.4° (PDF No. 01-079-0175), the (111) reflection of γ-FeNi alloys, centered between 44° and 46° depending on their composition, and the (311) reflection of the $NiFe_2O_4$ spinel phase at approximately 35.7° (PDF No. 00-003-0875).
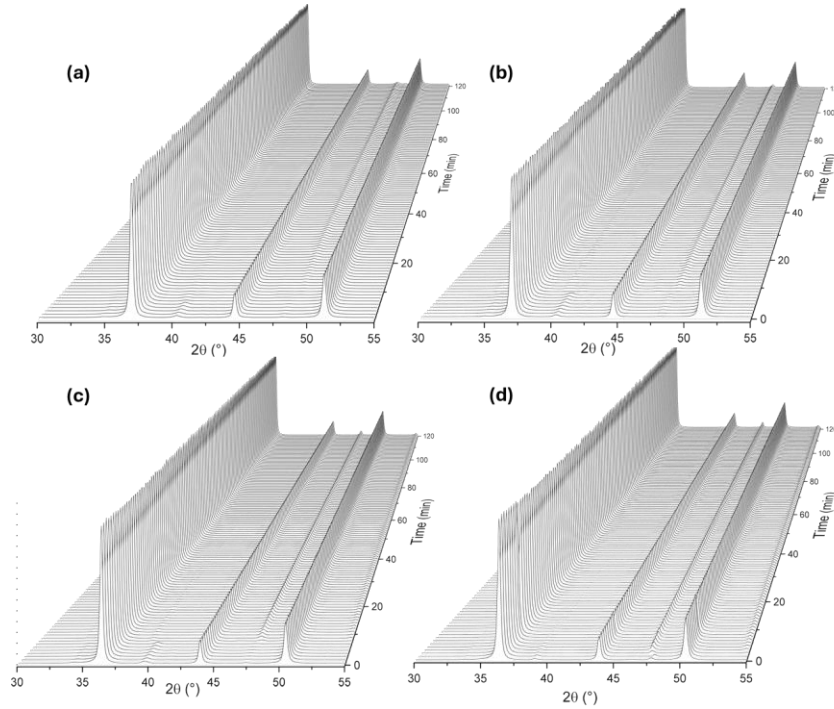
Figure 44. Cascade plots of the *in-situ* XRD diffractograms measured over time during isothermal exsolution treatment at 600 °C (a), 700 °C (b), 800 °C (c) and 850 °C (d).

A first overview of the waterfall plots shows that the (110) main perovskite reflection does not exhibit any significant changes in its 2ϑ value or intensity during each high-temperature treatment, indicating the structural stability of the perovskite matrix host lattice under reduction conditions, while retaining its cubic symmetry[131].

The reflection corresponding to the $NiFe_2O_4$ spinel phase shows a rapid decrease in intensity and a shift to lower 2ϑ values at the onset of the exsolution experiment, leading to its decomposition within the first few minutes. This rapid degradation of $NiFe_2O_4$ at the high temperatures of the exsolution process is attributed to its thermodynamic instability and the tendency of Fe and Ni ions to migrate and redistribute under thermal stress, driven by oxygen release and increased diffusion rates in the material under a reducing atmosphere[301,302]. More specifically, the instability of its crystal structure is linked to the preferential breaking of octahedral metal-oxygen bonds in the spinel structure, which facilitates the release of Ni and Fe ions that subsequently form simpler oxides at high temperatures[303]. In contrast, the $SrTiO_3$ parent perovskite matrix is significantly more stable at high temperatures than the $NiFe_2O_4$ spinel, owing to its robust crystal structure and thermodynamic properties, which resist cation migration and phase changes. Thermodynamic studies indicate that $SrTiO_3$ maintains a stable heat capacity and thermal expansion up to 1800 K, with no significant phase transitions or bond breaking[304,305]. The characteristic times of start and end of the decomposition of the spinel phase are reported in **Table 4.**

Table 4. Start and end times of spinel phase decomposition for each exsolution temperature considered in the *in-situ* exsolution experiments.

	R600 (min)	R700 (min)	R800 (min)	R850 (min)
Start of spinel phase decomposition	7	7	6	-
End of spinel phase decomposition	9	8	8	8

Observing these results, the decomposition of the $NiFe_2O_4$ phase begins at approximately the same time across all temperatures except at R850, where the spinel

phase lacks well-defined XRD reflections, making its decomposition time difficult to determine. These distorted diffraction patterns may be due to insufficient interaction of X-rays with the minor phase, as the spinel is much less abundant than the parent perovskite oxide in LSTFN2. Nevertheless, the decomposition of the spinel phase is complete at all exsolution temperatures within about 10 min from the start of the experiments. This behavior may be attributed to the kinetics of oxygen release, as previously discussed for the case of the perovskite phase. Spinel phase decomposition appears to follow a similar oxygen release mechanism, which is temperature-independent. As a result, decomposition begins once a critical concentration of oxygen vacancies is reached, leading to comparable characteristic times for phase decomposition[131,139]. After the $NiFe_2O_4$ phase, the focus was then moved on to the evolution of the BCC γ-FeNi reflection over time at each exsolution temperature. This analysis complemented the *ex-situ* XRD measurements performed earlier, which determined the average composition of the grown nanoparticles, and aimed to provide deeper insights into the mechanism of γ-FeNi nanoparticle nucleation and growth, as well as its correlation with the *in-situ* XANES results. In particular, the focus was put on monitoring and recording the changes in the position of the reflection throughout the entire duration of the exsolution experiments to estimate the lattice parameter of the γ-FeNi alloy. Using the radiation wavelength, which was converted from the synchrotron value (0.689 Å) to the reference Cu Kα value (1.54 Å), the lattice parameter of the (111) γ-FeNi reflection was calculated for each temperature. The trend over time for R600, R700, R800 and R850 is shown in **Figure 45a**, starting from the time at which the first clear reflection of γ-FeNi nanoparticles was detectable.

The most notable result is the variation of the lattice parameter over time, which exhibits distinct trends across the exsolution temperatures examined. For R600 and R700, a gradual change in the lattice parameter of the FeNi alloy is observed, with a significant difference between the values at the start and end of the experiments. In contrast, for R800 and R850, a rapid increase in the lattice parameter occurs within the first few minutes, reaching a maximum value that remains constant.
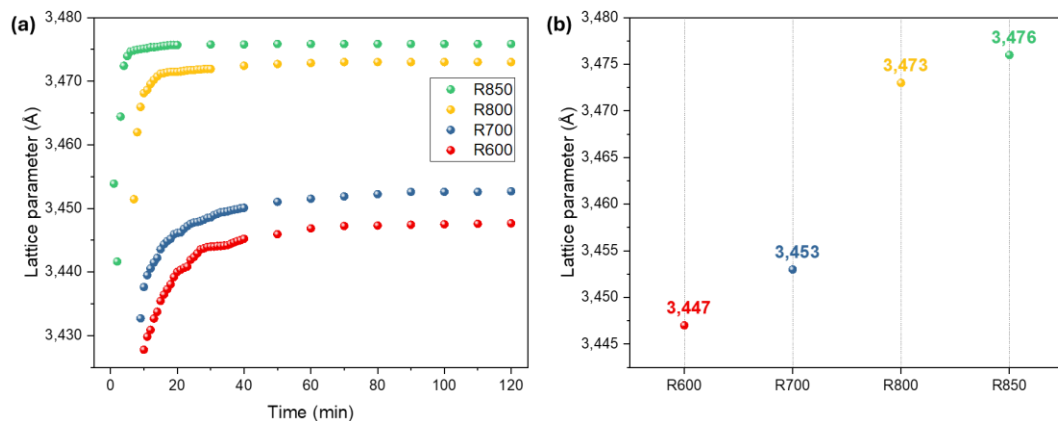
Figure 45. (a) Trends of the evolution over time of the lattice parameter of the FeNi alloy for the R600, R700, R800 and R850 materials. (b) Values of the lattice parameters calculated via Bragg's law based on the *in-situ* XANES powder diffractograms at the end of the exsolution experiment (120 min).

This behavior at 800–850°C is attributed to accelerated nucleation driven by enhanced atomic diffusion and faster oxygen vacancy formation in the perovskite lattice, promoting nanoparticle nucleation and growth. Conversely, at 600–700°C, slower atomic mobility and reduced oxygen vacancy formation rates result in more gradual structural changes during the nucleation process[256]. It is also evident from **Figure 45a** how the nucleation kinetics of the γ-FeNi alloy at the various temperatures under consideration resembles in trend that of the reduction of nickel to Ni (**Figure 40**). Since reduction is a prerequisite for nanoparticle nucleation and growth, this indicates that Ni reduction kinetics serve as the rate-determining step for the nucleation of the FeNi alloy. Additionally, the exsolution temperature, which impacts the rate of diffusion and oxygen vacancy formation within the A-site-deficient perovskite, influences the composition of the nanoparticles, as will be discussed in greater detail later in **Chapter 6**. The morphology of the nucleated nanoparticles may also be influenced by the exsolution temperature. For example, the findings of Rudolph et. al.[256] show that, in A-site-deficient nanostructured perovskites, increased ion mobility and oxygen release at higher temperatures promote the growth of existing nanoparticles, whereas lower temperatures result in a higher density of smaller nanoparticles. In the case of the results of **Figure 45a**,

the formation of many FeNi nanoparticles having lattice parameter gradually increasing over time is observed, as in the case of R600 and R700, while having a constant value over time for R800 and R850. Moreover, the lattice parameters after 120 min are larger as the exsolution temperature increases, ranging from 3.447 Å at 600 °C to 3.476 Å at 850 °C, as it can be seen from **Figure 45b**. The few data available from the literature show how an increase in the lattice parameter of γ-FeNi alloys is associated with changes in their composition, and in particular in the relative amounts of nickel and iron[299]. For example, Han et. al.[297] demonstrated that the addition of Fe to Ni clusters causes lattice expansion due to the larger atomic radius of Fe compared to Ni, as confirmed by XRD and EXAFS analyses. Moreover, Owen et. al.[299] confirmed that changes in the lattice parameter of γ-FeNi alloys are directly linked to their composition across a range of temperatures. Their results also demonstrated that incorporating Fe into Ni causes the nickel lattice to expand almost linearly with composition until reaching a maximum lattice parameter, beyond which further addition of iron leads to lattice contraction. However, when interpreting the results in **Figure 45b**, the lattice parameter values calculated from the diffractograms fall outside the range reported in the literature for γ-FeNi alloys, which typically span from 3.524 Å for pure Ni to a maximum of 3.589 Å for an alloy containing 39 at.% Ni[299]. This discrepancy is most likely related to the thermal expansion correction applied to the measured diffractograms to account for high-temperature measurements. The parent oxide matrix and the metallic phase might exhibit distinct thermal expansion behaviors under identical experimental conditions. For this reason, the thermal compensation based on the main (110) perovskite reflection may have underestimated the actual lattice expansion of the alloy, resulting in lattice parameter values outside the typical range for γ-FeNi alloys. In addition, the discrepancy in the lattice parameter values may be influenced by the thermal and magnetic properties of the alloy. The magnetic and structural properties of FeNi alloys are closely interconnected and exhibit significant temperature dependence within the range of 600–850 °C. As temperature increases, thermal agitation reduces the ferromagnetic order in FeNi alloys, eventually leading to a transition to a

paramagnetic state above the Curie temperature. This transition is composition-dependent and typically occurs below 850 °C for γ-FeNi alloys[306]. Thermal expansion generally causes the lattice to expand with increasing temperature, determining a loss of ferromagnetic order can induce changes in the lattice parameters[307]. Finally, for a comprehensive overview of the exsolution mechanism, considering reduction and particle growth, the correlation between the results of *in-situ* XANES and *in-situ* synchrotron XRD is presented in **Figure 46**. Since the two results are derived from different experiments, in the case of the trend related to the change in lattice parameter overtime (**Figure 46b**) the timescales have been adjusted so that the results of the two experiments are related to one another.
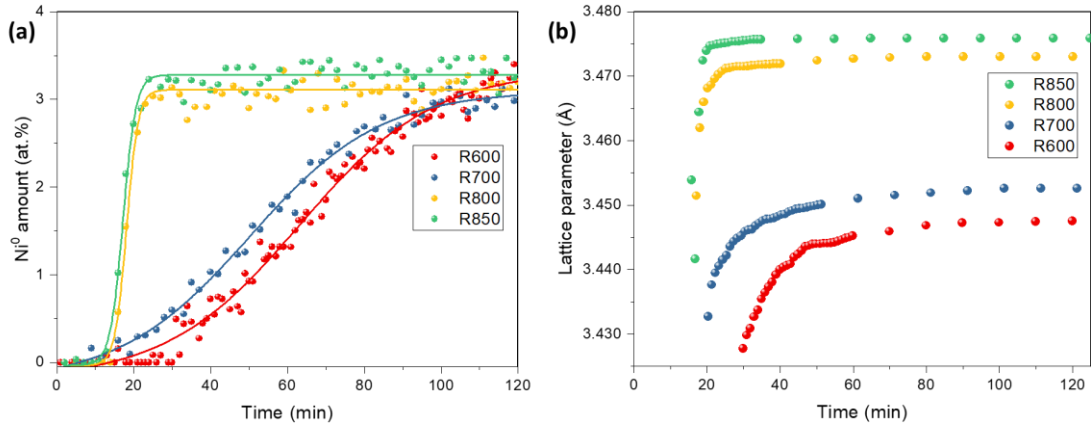
Figure 46. Reduction trend over time to Ni[0] for R600, R700, R800, and R850. (b) Growth trend over time of the lattice parameter of the γ-FeNi alloy for R600, R700, R800, and R850.

Starting with R600, the experimental points (in red) in **Figure 46a** show that, after an induction time of 30 min, the gradual formation of Ni[0] species begins. The onset of reduction coincides with the initial nucleation of γ-FeNi alloy particles (red experimental points in **Figure 46b**), which progresses as Ni[0] species diffuse and nucleate within the LSTFN2 material. A similar trend is observed for R700, with a slightly faster reduction rate attributed to faster rate of oxygen release, with the alloy growing progressively as the reduction of nickel proceeds. The key outcome is that the lattice parameter, linked to the alloy composition, evolves gradually due to the sluggish reaction kinetics. Notably, if the experiments were stopped at 60 min instead of 120 min, a different final alloy composition would be observed. This is because the

reduction kinetics of Ni directly influences the kinetics of growth of the γ-FeNi alloy, thereby affecting its lattice parameter. On the other hand, when correlating the reduction and growth trends for the R800 and R850 materials, the very fast reduction kinetics, driven by faster oxygen release at elevated temperatures, results in the formation of bimetallic particles within a few minutes. These particles exhibit a nearly constant lattice parameter over time, stabilizing at their equilibrium value. However, as previously discussed, no conclusions about the composition or morphology can be drawn from the *in-situ* synchrotron XRD results, as these values cannot be directly compared with literature data and therefore remain uninterpreted. Insights into the composition of the nanoparticles can only be derived from the *ex-situ* XRD results (**Figure 43**), which indicate greater incorporation of Ni into the γ-alloy at higher temperatures.

After examining the formation of the γ-FeNi alloy, the last phase analyzed from the *in-situ* XRD experiments is the one characterized by a growing reflection centered around 2θ = 49.3°. This reflection first appears, with low intensity, approximately 60 min after the onset of nucleation for R600 (**Figure 47a**) and 40 min for R700, alongside the γ-FeNi phase (**Figure 47b**). Moreover, it is only observed at these two temperatures and does not form at the higher temperatures of exsolution considered (800 °C and 850 °C).
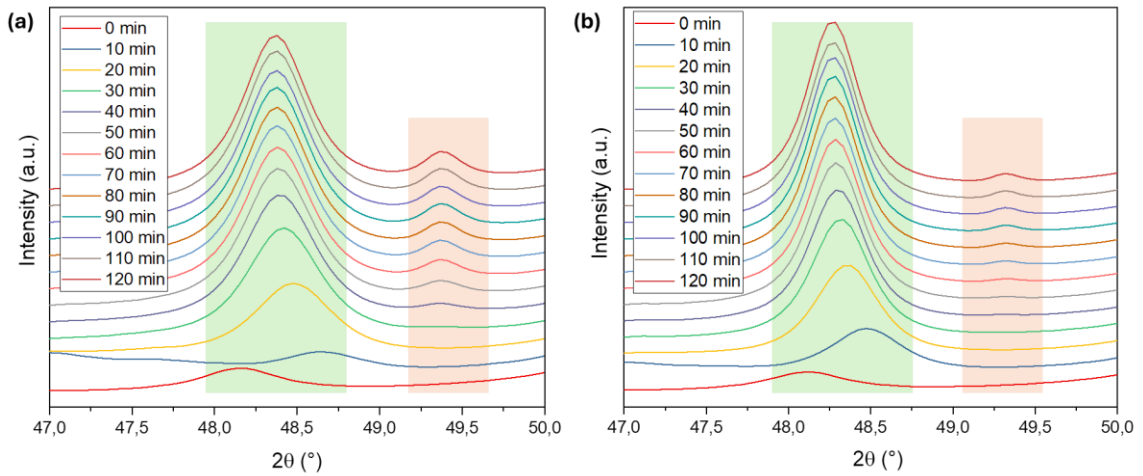
Figure 47. XRD diffractograms over time for R600 (a) and R700 (b), focusing on the region 47° < 2ϑ < 50°, showing the evolution of γ-FeNi alloy nanoparticles (green) and α-FeNi nanoparticles (red).

Considering X-ray diffraction data available in the literature, this reflection can be attributed either to that of α-Fe (ferrite, PDF Nr. 00-006-0696), which has a lattice parameter that is reported to be 2.860 Å and body-centered cubic (BCC) crystal structure[186], or to that of a α-FeNi alloy, whose lattice parameter depends on the alloy's composition but has similar values to those of α-Fe, ranging from 2.860 Å (0 at.% Ni) to 2.863 Å (23.5 at.% Ni)[186]. In **Table 5**, together with the onset time at which the BCC reflection is detectable from the diffractograms, the 2θ value of the reflections and the corresponding value of the lattice parameter for the α-phase calculated with Bragg's law are reported. Considering that the 2θ value of this reflection does not change over time, it is not possible to determine whether it is attributable to that of a pure α-Fe phase or that of an α-FeNi alloy with a constant Fe/Ni ratio. In addition, the corresponding lattice parameter value of 3.19 Å does not match that of an α-FeNi alloy or that of α-Fe[0]. However, as with the γ-FeNi alloy, a misleading contribution from thermal correction could affect the calculated values, making them differ from those reported in the literature. However, as with the γ-FeNi alloy, a misleading contribution from thermal correction could affect the calculated values, making them differ from those reported in the literature.

Table 5. Characteristic times marking the onset of spinel phase decomposition and the first detected nucleation of γ-FeNi and α-FeNi alloys at different exsolution temperatures for LSTFN2.

Exsolved material	Appearance α-Fe reflection (min)	Reflection position (2θ, °)	Lattice parameter (111) α-FeNi reflection
R600	40	49.36	3.195
R700	60	49.32	3.198
R800	-	-	-
R850	-	-	-

For this reason, the available measurements do not allow determination of whether these reflections correspond to the nucleation and growth of α-Fe or α-FeNi nanoparticles. To distinguish between these possibilities, complementary techniques such as EDXS and SAED would be helpful for further interpretation. However, final considerations can be made regarding the kinetics of nucleation of the α-phase, particularly its earlier nucleation in R700 compared to R600, which can be attributed

to the thermally activated nature of diffusion, reduction, and nucleation processes. In fact, high temperatures could enhance the diffusion of metal cations from the perovskite bulk to the surface and favor their reduction to the metallic state, reducing the energy barrier for nucleation, and allowing it to occur more rapidly[27,36]. Additionally, the BCC Fe phase is likely absent at 800 °C and 850 °C due to enhanced particle growth being favored over nucleation at these temperatures. The increased mobility of metal cations promotes the growth of existing γ-FeNi nanoparticles rather than the nucleation of new ones, including secondary metallic phases such as α-Fe[256].

5.3 Summary

In **Chapter 5**, *in-situ* XANES and synchrotron XRD were employed to investigate the mechanism of bimetallic exsolution in $La_{0.4}Sr_{0.4}Ti_{0.60}Fe_{0.35}Ni_{0.05}O_3$ (LSTFN2) at increasing exsolution temperatures. This material, synthesized with 5 at.% Ni and 35 at.% Fe forming a solid solution at the B-site, initially contains a minor amount of $NiFe_2O_4$ spinel phase alongside the nanostructured perovskite host matrix, as confirmed by X-ray diffraction, XANES, and Mössbauer spectroscopy.

The study focused on monitoring the reduction and particle growth processes of FeNi alloy nanoparticles *in-situ* and correlating these steps to elucidate the mechanism of bimetallic exsolution. *In-situ* XANES spectroscopy showed how the kinetics of Ni reduction is the rate-determining step in the bimetallic exsolution process, driving Fe reduction, which is independent of temperature. The extent of reduction for both metals, i.e. the maximum amounts of Fe^0 and Ni^0 achievable, is controlled by the rate of oxygen vacancy formation in the perovskite lattice and by the initial stoichiometry of the material. The reduction of Ni^{n+} to Ni^0 showed two temperature-dependent behaviors. At higher exsolution temperatures (800–850 °C), Ni reduction occurs more rapidly, and this was attributed to two factors, one kinetic and one thermodynamic. Kinetically, increased atomic vibrational energy at higher temperatures enhanced oxygen vacancy formation and accelerates oxygen release, enabling the critical concentration of vacancies needed to overcome the activation

energy for Ni reduction. This facilitates the reduction of Ni^{n+} to Ni^{2+} and ultimately to Ni^0, achieving the maximum metallic nickel content dictated by the material's stoichiometry. From the thermodynamic point of view, higher temperatures increase the entropic contribution ($T\Delta S$) to Gibbs free energy ($\Delta G = \Delta H - T\Delta S$), making ΔG more negative and favoring Ni reduction. The oxygen release from the lattice further boosts the system entropy, enhancing the thermodynamic favorability of the process. Conversely, at lower exsolution temperatures (600–700 °C), slower oxygen vacancy formation limits electron availability for Ni reduction, which is considerably slower, and the reduced entropic contribution results in a less negative ΔG, diminishing the driving force for oxygen vacancy formation and subsequent Ni reduction. XANES spectroscopy was also employed to monitor the reduction kinetics of Fe in LSTFN2. At the end of the exsolution experiments, similar amounts of Fe^{2+} species were observed at the end of the process for all of the investigated temperatures. This could be explained by the fact that a complete reduction of Fe^{n+} to Fe^0 is not thermodynamically favored, as it would excessively destabilize the perovskite lattice. Moreover, the reduction kinetics of Fe was shown to be independent from the reduction temperature, being driven by the one of nickel, which has a low reduction potential and is more easily reducible, under the same experimental conditions.

In-situ XRD provided complementary insights into the structural and compositional evolution during exsolution. The perovskite phase remained intact throughout the process, with no significant structural changes observed. The reduction kinetics of Ni influenced the composition of the γ-FeNi alloy, with higher temperatures leading to Ni-richer alloys (with composition $Fe_{0.5}Ni_{0.5}$ at 850 °C) and lower temperatures having a larger Fe incorporation ($Fe_{0.6}Ni_{0.4}$ at 600 °C). This behavior was attributed to the gradual availability of Ni^0 for particle growth at lower temperatures, driven by slower oxygen release from the lattice. Lattice parameter calculations further highlighted the impact of temperature on nanoparticles' growth dynamics. At lower temperatures, the lattice parameter evolved gradually over time, offering greater tunability in alloy composition. In contrast, higher temperatures (800–850 °C) led to

the rapid formation of alloys with constant parameter over time. Finally, the monitoring of the reflections of the $NiFe_2O_4$ spinel phase over time showed its decomposition at similar rates across all temperatures, though its behavior at 850 °C could not be conclusively analyzed due to difficulties in identifying reflections. Moreover, the formation of an α-Fe or α-FeNi phase was observed, although its precise composition remains unclear.

Overall, these findings provide a detailed understanding of the reduction and particle growth mechanisms in bimetallic exsolution, emphasizing the interplay between temperature and oxygen vacancy formation in dictating the kinetics and final composition of FeNi alloy nanoparticles. The ability to adjust the exsolution temperature to fine-tune the average composition of exsolved FeNi alloy nanoparticles from LSTFN2 highlights the potential use of these material as heterogeneous catalysts in sustainable energy conversion applications, as shown in the following chapter.

Chapter 6

Design of Exsolved FeNi Nanoparticles from La$_{0.4}$Sr$_{0.4}$Ti$_{0.60}$Fe$_{0.35}$Ni$_{0.05}$O$_{3-\delta}$ with Switchable Catalytic Selectivity

6.1 Introduction

The results of **Chapter 5** allowed for a better understanding of the underlying mechanistic processes happening in LSTFN2 during exsolution, such as dopant diffusion and reduction as well as nanoparticle nucleation and growth. This represented a first step for developing exsolved perovskite materials for applications in catalysis, and especially for CCU processes. In fact, as already mentioned, the design of exsolved perovskite oxide-based multimetallic catalysts attracted significant attention in the past few years for such applications, due to their ability to enhance catalytic performance and selectivity by fine-tuning their structure and composition[22,143,171,172,183,194,257,262,266,308–312]. A previous study by Tsiotsias et. al.[22] on a perovskite oxide system similar to LSTFN2 demonstrated that the surface state of exsolved Fe-based bimetallic nanoparticles – whether metallic or oxidized – plays a crucial role in determining its selectivity in CO$_2$-assisted ethane oxidation, promoting either syngas production or ethylene formation, respectively[22]. Furthermore, the results of the in-depth synchrotron investigations reported earlier confirm LSTFN2 as a promising candidate for use as a heterogeneous catalyst. These in fact not only showed that Ni reduction kinetics, which can be easily changed by varying the exsolution temperature, influences the composition of the bimetallic nanoparticles, but also pointed out the presence of a substantial amount of Fe^{2+} at the end of the

process, which can be associated with the presence of iron oxides in the material, along with Fe^0 and Fe^{n+}. This opens up the possibility of fine-tuning the material design of LSTFN2 via bimetallic exsolution, both in terms of composition and morphology, going on to create a catalyst that, starting from the same parent host oxide, can be adapted in its composition to be used for two CCU reactions, the CO_2-assisted Oxidative Ethane Dehydrogenation (ODH) and the Dry Ethane Reforming (DER). In the work of Tsiotsias et. al.[22], this was done by tuning the Fe/Ni ratio of the bimetallic nanoparticles, going to modify the stoichiometry of the material by increasing the A-site deficiency and thus the concentration of surface oxygen vacancies. Instead, in the results of **Chapter 6**, the composition of the exsolved alloy nanoparticles, was tuned by acting on the exsolution temperature, and so on the kinetics of reduction and growth of these metal cations. While on the one hand the LSTFN2 materials with different composition thus obtained were later found to be differently selective for ODH and DER, leveraging on their different surface composition and nanoparticle's morphology, the additional objective of this chapter is the implementation of a switching catalyst in terms of composition and catalytic selectivity, by exploiting the unique property of perovskite oxides to re-incorporate the active phase back into perovskite oxides as metal cations, when subjecting them to high-temperature oxidation treatments. These regeneration treatments determined a structural transformation of the perovskites surface, and a switching of the catalytic selectivity for DER and ODH, showing a long-term stability comparable to that of the freshly exsolved systems. The findings of this chapter propose a novel design strategy for heterogeneous catalysis, focusing on the utilization of widely available and cheaper elements as active phases instead of noble metals, supporting progress in the creation of functional materials for sustainable technologies.

6.2 Results and discussion

6.2.1 Parent perovskite oxide

The as-synthesized $La_{0.4}Sr_{0.4}Ti_{0.65}Fe_{0.35}Ni_{0.05}O_3$ (LSTFN2) material is the same one that was characterized and studied in **Chapter 5**. The characterization of the material has been addressed in **Subsection 5.2.1**.

6.2.2 Exsolved materials

The effect of the exsolution temperature on the as-synthesized LSTN2 parent oxide was studied by subjecting the material to reduction treatments analogous to the ones carried out for the *in-situ* synchrotron experiments performed in the previous chapter, in order to promote the exsolution of the FeNi nanoparticles. The experimental conditions are reported in detail in **Subsection 10.4.2** of the **Experimental Methods** chapter and are different from the ones of **Chapter 5**. In fact, in the *ex-situ* treatments carried out in this chapter, the heating ramp for reaching the final reduction temperature was set to a slower rate and the system was heated up under inert argon atmospheres. Moreover, in this case, the reduction time is longer (3 h) compared to the reduction treatments performed using the synchrotron setup (2 h). This difference does not affect the comparability of the results, since it was shown in the previous chapter that the system achieves equilibrium within two hours, with the final concentrations of the reduced metal species remaining consistent over time (**Figure 38**). The exsolution treatments were carried out at increasing temperatures, i.e. at T = 400 °C, 650 °C and 850 °C, with the intent of controlling the final composition of the exsolved material (the materials will be referred from now on as R400, R650 and R850, respectively). This was done based on the results of the previous chapter, which showed that, under the same reducing atmosphere and reduction time, different temperatures lead to varying nickel reduction kinetics. These differences result in bimetallic nanoparticles with varying compositions, designed to be used as catalytically active phases. XRD analyses were performed to

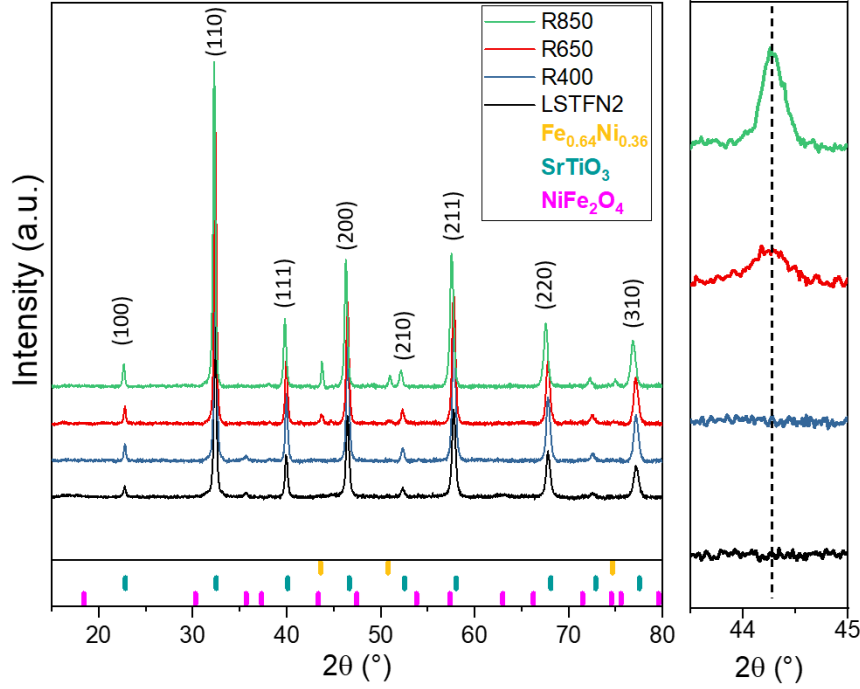investigate the structural properties of the reduced systems, as reported in **Figure 48**.

Figure 48. (a) XRD patterns of the as-synthesized LSTFN2, R400, R650 and R850 materials, including a magnified view of the 2θ range corresponding to bimetallic alloys reflections. The 2θ values for the reflections of $Fe_{0.64}Ni_{0.36}$, $SrTiO_3$ and $NiFe_2O_4$ are also reported as references (PDF Nrs. 00-047-1405, 01-079-0175 and 00-034-0641, respectively).

Considering the X-ray diffraction pattern of the material reduced at 400 °C, no metallic phases are visible from the diffractogram. However, the darker color of the powder after reduction (**Figure 49a**) and, more significantly, the hydrogen consumption observed in the mass spectrogram acquired during the exsolution process (**Figure 49b**), prove that the reduction process took place even at such a low temperature. It is also evident how the host perovskite matrix retained the cubic $Pm\bar{3}m$ structure even after a high-temperature reduction at 850 °C. Moreover, the $NiFe_2O_4$ spinel phase initially present in the as-synthesized LSTFN2 material disappears after the reduction treatment at 650 °C: this is in accordance with the results of **Chapter 5**, in which it was observed that the spinel phase already decomposes at 600 °C.
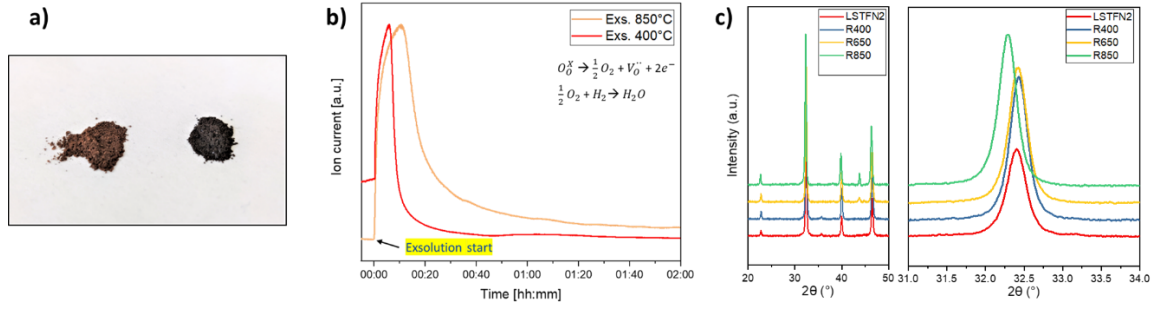
Figure 49. (a) Photograph of the as-synthesized LSTFN2 (left) and R400 (right) materials. b) Mass spectrometry signals showing water production for R400 and R850; t = 0 corresponds to the injection of the reducing agent into the system, marking the start of the exsolution process. (c) Zoomed view of the (110) reflection for the as-synthesized and reduced LSTFN2 materials.

The reflection at $2\vartheta = 44.8°$ was attributed to an α-phase, either Fe or Fe-Ni (lattice parameter a = 2.86 Å[63]), whereas the more prominent reflection centered at $2\vartheta = 44.3°$ (see magnification in **Figure 48**) is ascribed to the bimetallic Fe_3Ni γ-phase (PDF-Ref. Nr. 00-047-1405) having an average crystallite size of 30 nm, calculated with Scherrer equation. An increasing of the exsolution temperature to T = 850 °C determines an increase in intensity of the Bragg peak of the γ-phase, with a crystal growth up to 42 nm. These values of the crystallite sizes of the FeNi alloy nanoparticles calculated with Scherrer equation differ from the ones calculated in **Chapter 5**, while remaining in the same order of magnitude (**Table 3**). This is mainly because of the different batch of as-synthesized starting material used and the different exsolution setup, together with the fact those provided Scherrer calculations are average values mediated over the whole powder sample. The α-phase contribution in the R850 case is absent, as observed with the *in-situ* XRD experiments of **Chapter 5**, suggesting that at high temperature the alloy phase evolves to the $Fm\bar{3}m$ allotrope, i.e. a γ-FeNi, which is the most thermodynamically stable phase[313]. It can also be noticed that the position of the (110) reflection of the perovskite parental structure shifts to the left with respect to the pristine material after exsolution, thus indicating a lattice expansion, with the lattice parameter passing from 3.910 Å to 3.923 Å (**Figure 49c**), probably due the metal cation reduction and diffusion within the perovskite lattice occurring during the exsolution

process. Although this phenomenon cannot be properly elucidated due to the very complex defect chemistry of the perovskite material, it is indicative of the fact that the reduction process also involves the substitutional metal ions in the perovskite, and not only the spinel side phase. That is, the nickel that participates in the reduction and subsequent nucleation can belong to either the perovskite matrix host phase or the spinel phase.

Further information regarding the reduction process of Fe and Ni in the exsolved materials after the exsolution process at different temperatures was provided by XANES spectroscopy (**Figure 50**). In particular, this technique has been used for an analysis on the extent of reduction due to the exsolution treatments at increasing temperatures. Differently from the previous chapter, where LCF was conducted, the analysis of these XANES measurements was carried out by only qualitatively comparing the shape of the profiles of the collected spectra. In fact, in the case of *in-situ* experiments, the high measurement temperatures, which ranged from 600 °C to 850 °C, caused the presence of substantial systematic background noise, and the standard spectra of the Fe and Ni compounds used for fitting were sufficient to fit a XANES profile with acceptable residual. In contrast, measurements conducted *ex-situ* at room temperature on these materials show more accurate results and spectra of higher quality, for which due to the complex stoichiometry and defect chemistry of the material a fitting with the available standards does not allow for acceptable goodness of the fit. Concerning the Fe K-edge, from the spectra of R400 (**Figure 50a**), a slight increase in the pre-edge feature and an overall decrease in white line intensity are observed, suggesting that the reduction process begins already at such relatively low temperatures. More pronounced changes are observed for R650 and R850, with a clear shift of the absorption edge to lower energies, indicative of the presence of Fe^{2+} and Fe^0. In addition to that, the white line shape and other spectral features increasingly resemble the ones of the spectrum of Fe^0.
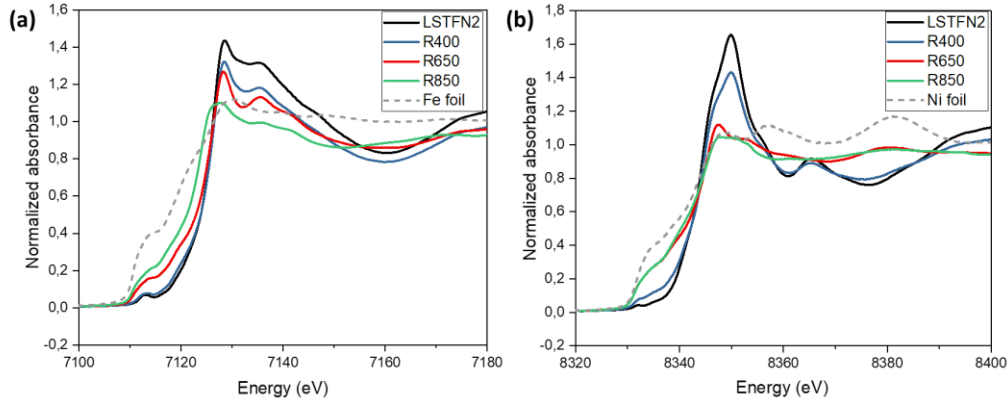
Figure 50. (a) XANES absorption spectra for the Fe K-edge of the as-synthesized, R400, R650 and R850 perovskite materials, along with the reference spectrum of Fe^0. (b) XANES spectra for the Ni K-edge of the as-synthesized, R400, R650 and R850 materials, along with the reference spectrum of Ni^0.

Notably, as the reduction temperature reaches 650 °C, the white line peak, at E = 7128.6 eV, becomes sharper. A comparison with reference spectra (**Figure 51**) suggests that this effect is likely due to the consumption of the $NiFe_2O_4$ side phase, which has been present already in the as-synthesized LSTFN2 material, consistently with the XRD data.
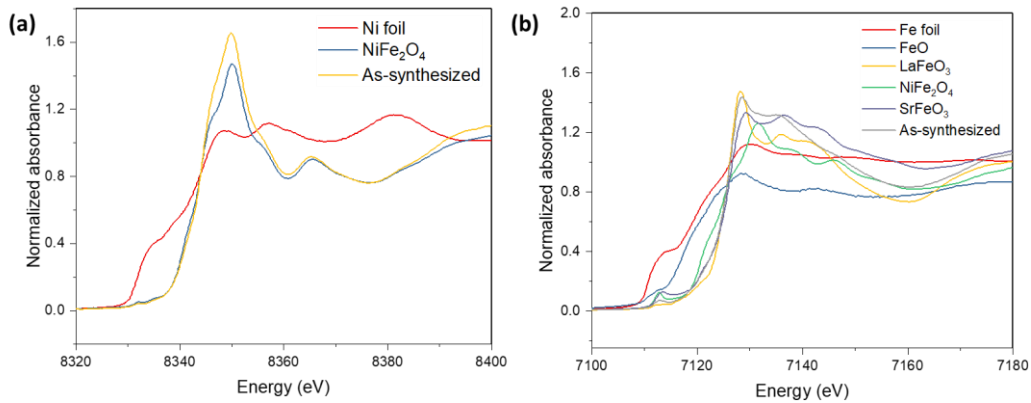
Figure 51. XANES spectra of the standards for qualitative evaluation of the Ni K-edge (a) and the Fe K-edge (b) spectra of the exsolved LSTFN2 materials.

At temperatures above 650 °C, the perovskite component $LaFeO_3$ undergoes substantial conversion into the $Fe_{1-x}O$ (wüstite) and Fe^0 phases, as can be seen from the similarities between the spectra and the ones of the wüstite and Fe foil standards.

As for the Ni K-edge spectrum of R400, a reduction in white line intensity accompanied by an increase in the pre-edge feature suggests the presence of Ni^0 within the material. Moreover, the spectra for samples reduced at 650 °C and 850 °C are almost identical, closely resembling the one of pure metallic nickel, and allowing to conclude two key points: first, nearly all Ni in the original material has been reduced to its metallic state, and second, a substantial portion of the Ni ions originated from $NiFe_2O_4$. Comparing the reduction profiles of Ni and Fe, it becomes evident that the reduction of Ni is complete by 650 °C, whereas Fe reduction continues up to 850 °C. At lower temperatures (400 °C), the concentration of metallic Ni is higher than that of metallic Fe, whereas at higher temperatures (850 °C), reduced metallic Fe dominates over metallic Ni. The difference in the relative amounts of Fe^0 and Ni^0 basing on the exsolution temperature was the most relevant outcome of **Chapter 5**, where this has been attributed to the different reduction kinetics of Ni between lower (600 °C) and higher (850 °C) temperatures. These results confirm how, regardless of the different measurement conditions, varying the exsolution temperature allows for adjusting the ratio of Fe^0 and Ni^0 within the exsolved material (**Figure 42**), in the perspective of tuning their surface composition for using them as heterogeneous catalysts for ODH and DER.
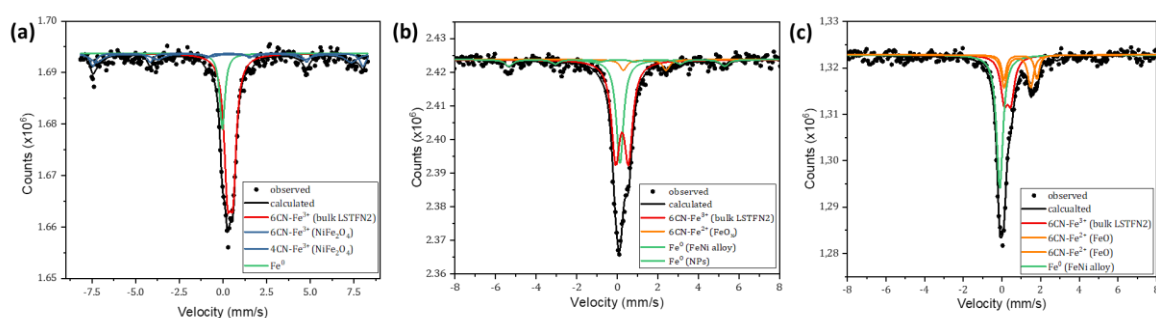
Figure 52. Mössbauer spectra of the R400 (a), R650 (b) and R850 (c) materials, respectively.

In addition to XRD and XANES, Mössbauer spectroscopy were conducted, in collaboration with Luca Nodari from the University of Padua. This was done in order to gain deeper insight into the oxidation state and coordination environment of iron

species during the exsolution process (**Figure 52**). The spectrum of the R400 material (**Figure 52a**) is characterized by a broad, intense, and asymmetric absorption centered around 0.28 mm/s, along with a magnetically coupled component of smaller intensity. The fitting reveals four components: a singlet, a doublet, and two sextets: the doublet corresponds to distorted ferric sites within the LSTFN2 lattice, while the singlet represents approximately 15% metallic iron (or an iron-nickel alloy) in a superparamagnetic state, indicating and confirming that significant iron reduction to the metallic state occurs even at 400 °C. The two sextets align with octahedral (6CN) and tetrahedral (4CN) iron sites in a partially inverted spinel structure. These findings are consistent with those pointed out by XRD and XANES, linking the ferric sites to the $NiFe_2O_4$ spinel phase, which remains largely unchanged from the pristine state after reduction at 400 °C. When the reduction temperature is increased to 650 °C, the metallic iron phase grows to 35% of the total iron content. Additionally, a new contribution from Fe^{2+} species in octahedral coordination appears, accounting for 5% of the total, indicating the formation of iron oxides during the reduction process. At the final reduction stage at 850 °C, the metallic iron or iron alloy content rises to 43%, and Fe^{2+} species increase to 29%. The ferrous sites are attributed to two distinct species, likely corresponding to Fe^{2+} in wüstite ($Fe_{1-x}O$) and magnetite (Fe_3O_4) configurations, and the coexistence of these oxides is consistent with the iron-oxygen phase diagram. A more extensive overview of the findings in terms of hyperfine parameters and assignments, both for these materials and for all others analyzed in this chapter, is reported in **Table A2**. TEM investigations of the exsolved materials, conducted by DongHwan Oh at KAIST, show that exsolved FeNi alloy nanoparticles were observed over the parent scaffold with nanoparticles of 20 nm diameter after exsolution treatment at 400 °C (**Figure 53a**), confirming the Mössbauer analyses, the mass spectrometry results and the color change relate to the reduction happening in the material. This discrepancy between the size of the FeNi nanoparticles detected with XRD and the one detected with TEM is related to the fact that the former is a volumetric technique averaged on the whole material, whereas by microscopy only a small portion is considered. Furthermore, TEM enables the visualization of nanoparticles through the segregation of Fe and Ni within the analyzed portion of the material. However, it cannot

139

differentiate the phases to which these metal species belong, leading to an overestimation of particle size.
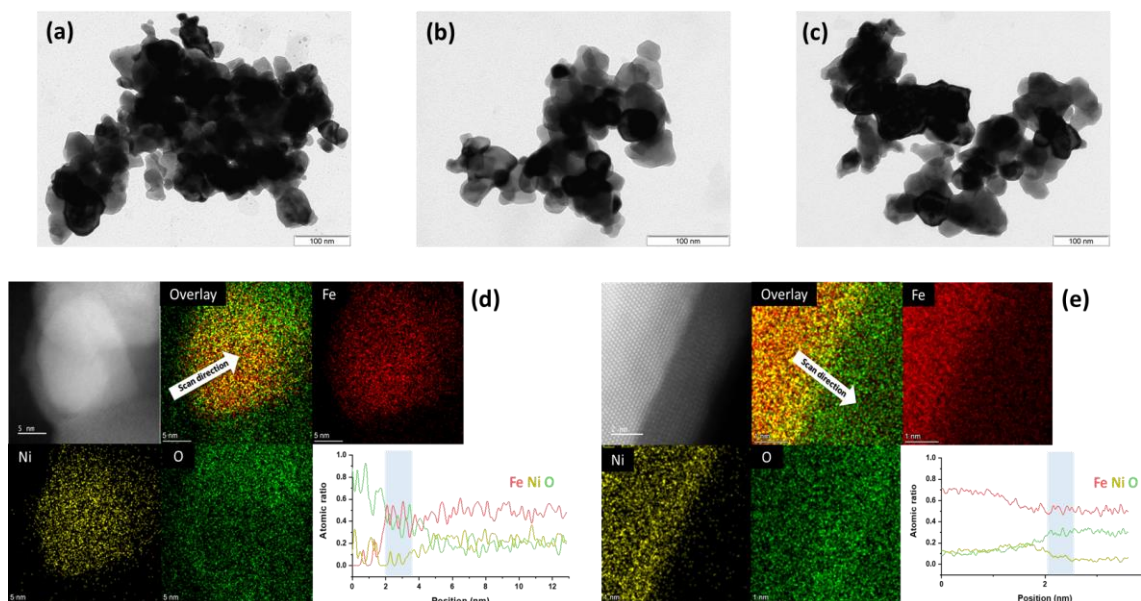

Figure 53. TEM pictures of the (a) R400, (b) R650, and (c) R850 materials. (d) HR-TEM, EDX mapping and FeNi nanoparticle line-scan of the R400 material. (e) HR-TEM, EDX mapping and FeNi nanoparticle line-scan of the R850 material.

However, it should be noted that Fe is not readily reduced at low temperatures: the Fe exsolution was most likely achieved due to the hydrogen spillover effect and nucleation role mediated by the reduction of Ni, which having a smaller reduction potential happens earlier and induces the co-reduction of Fe[314]. As the temperature of the reduction treatment was increased up to 850 °C, the exsolved FeNi alloy particles resulted to be larger, reaching around 150 nm in diameter with higher crystallinity (**Figure 53c**). In addition to that, a distinct separation between a skin shell phase on the topmost area and a core region of different composition is observed. To investigate the microscopic structure of exsolved FeNi species, high-resolution TEM analysis coupled with EDX mapping was also performed. In R400 (**Figure 53d**), exsolved nanoparticles exhibit low crystallinity and are coated with a thin (≈1 nm) amorphous shell, which was identified as iron oxide (Fe_yO_x) through EDXS-line scan analysis. The metallic core revealed to be constituted by an Fe_3Ni alloy, and the core-shell structure likely forms upon air exposure after exsolution, creating an

amorphous oxide passivation layer. For R850 (**Figure 53e**), the nanoparticles also show a core-shell structure, but instead with a crystalline outer layer, separated from the Fe_3Ni core by a thin Ni layer, as observed with EDXS line scans. This difference in the iron oxide shell's structure between R400 and R850 suggests its formation depends on the exsolution temperature, corroborating Mössbauer spectroscopy findings of defective iron oxide formation above 650 °C. These results agree with those determined by *in-situ* synchrotron measurements, in which it was noted that after 2 h of reduction Fe^{2+} species attributable to iron oxides are present (**Figure 39**), consistently with the nucleation of nanoparticles having a Fe_yO_x shell and a FeNi alloy core. To further explore the formation of this core-shell structure, *in-situ* TEM experiments (**Figure 54**) were conducted under vacuum to eliminate air exposure effects.
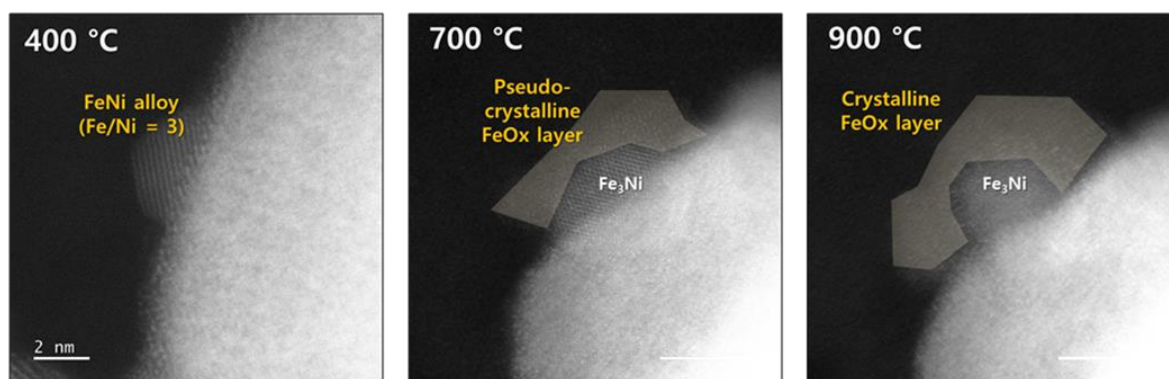
Figure 54. *In-situ* TEM pictures showing the evolution of the exsolved FeNi alloy nanoparticles over the LSTFN support at increasing temperature of 400, 700 to 900°C.

At 400 °C, the appearance of FeNi nanoparticles was observed without the formation of an oxide layer: as the temperature increased, a pseudo-crystalline overlayer developed on the FeNi alloy, fully covering it at 900 °C. EDX spectroscopy showed that this shell comprises iron and oxygen, likely originating from the support material under high vacuum, rather than gaseous oxygen. The formation of the crystalline iron oxide shell at high temperatures could be attributed to the Strong Metal-Support Interaction (SMSI) of iron oxide. At lower temperatures (i.e., at 400 °C), exsolution occurs in the subsurface region (≈10 nm) involving low-coordinated iron species

bound to alpha oxygen[315,316]. With increasing temperature, SMSI transitions to bulk iron oxide species with high coordination bound to beta oxygen. Another potential and more likely mechanism responsible for this crystalline core-shell morphology could be Reverse Oxygen Spillover (ROS), where oxygen species migrate from an oxygen-deficient substrate to form an oxide layer on supported metal nanoparticles[317–321]. Since the LSTFN2 material is 20% A-site deficient and becomes highly oxygen-deficient during exsolution, ROS could occur at T > 650 °C, leading to the immediate reaction of oxygen with the Fe_3Ni nanoparticle surface, and being Fe more electropositive than Ni, to the formation of a crystalline Fe_yO_x shell with a metallic Ni interface. A schematization of the outcome of the *ex-situ* and *in-situ* HR-TEM measurements is reported in **Scheme 1**.
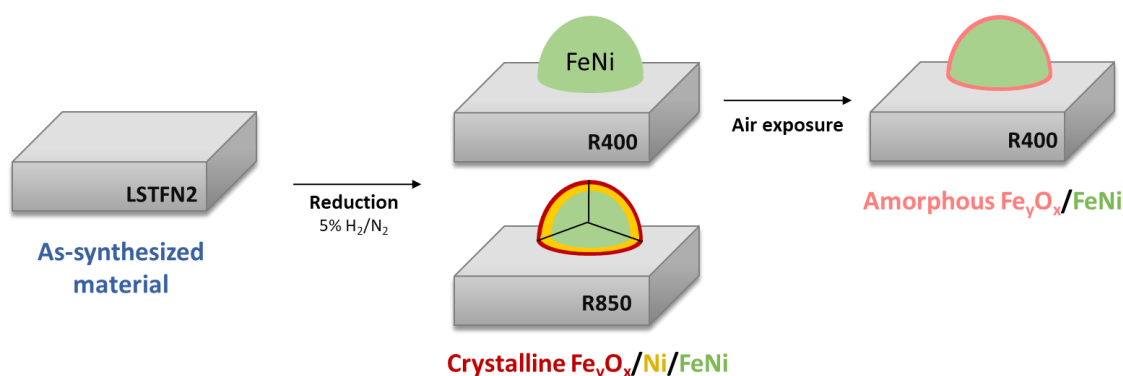
Scheme 1. Mechanism of nanoparticle formation on the LSTFN support, highlighting the formation of the crystalline core-shell structure at high exsolution temperatures and the amorphous Fe_yO_x overlayer formation at low exsolution temperatures.

6.2.3 Switching exsolution behavior

So far, it has been demonstrated that exsolved nanoparticles with distinct structures and compositions can be achieved by performing reduction treatments at low and high reduction temperatures. This section will show how it is feasible to transition between these two nanoparticle configurations within the same material by incorporating an oxidative step under air at 850 °C, partially restoring the original perovskite structure while re-dissolving the metal nanoparticles. After that, the corresponding re-oxidized materials will then be re-exsolved at the corresponding

opposite temperature. That is, R400 will be re-oxidized (R400-O) and switched by exsolving the regenerated material at 850 °C (R400-O-R850). Likewise, R850 will also be regenerated by oxidation at high temperature (R850-O) and then switched at the lower temperature examined so far, i.e. at 400 °C (R850-O-R400). A simple schematization of all the different exsolution steps of this study is provided in **Scheme 2**.
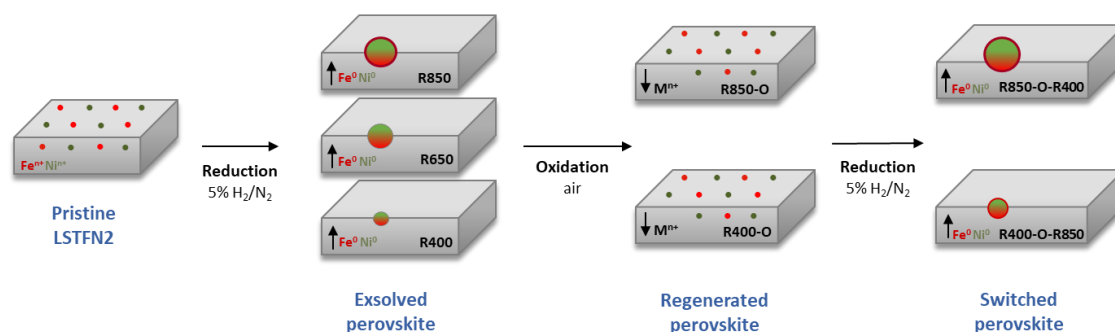
Scheme 2. Overview of the exsolution and regeneration treatments conducted in this chapter: the first reduction treatment at increasing temperatures (R400, R650 and R850); the subsequent regeneration by oxidation at 850 °C of R400 and R850 (R400-O and R850-O); and finally, the switching to the corresponding opposite temperatures (R400-O-R850 and R850-O-R400).

Starting from the re-oxidized systems derived from the oxidation at 850 °C for 5 h of R400 and R850 (R400-O and R850-O, respectively), a detailed analysis was conducted by using XRD, XANES, and Mössbauer spectroscopy, for evaluating how effectively the perovskite structure was restored after the treatment and how the metal nanoparticles were re-dissolved back into the parent host perovskite. The Mössbauer spectroscopy measurements were performed by Luca Nodari of the University of Padua. Overall, it was found that, for R850-O, where the temperatures of oxidation and reduction are the same, the achievement of the complete reincorporation of the exsolved ions into the perovskite matrix is quite challenging, as evidenced by the more pronounced XRD reflections of the spinel side phase and the residual signal of bimetallic nanoparticles (**Figure 55a** and **Figure A6**).
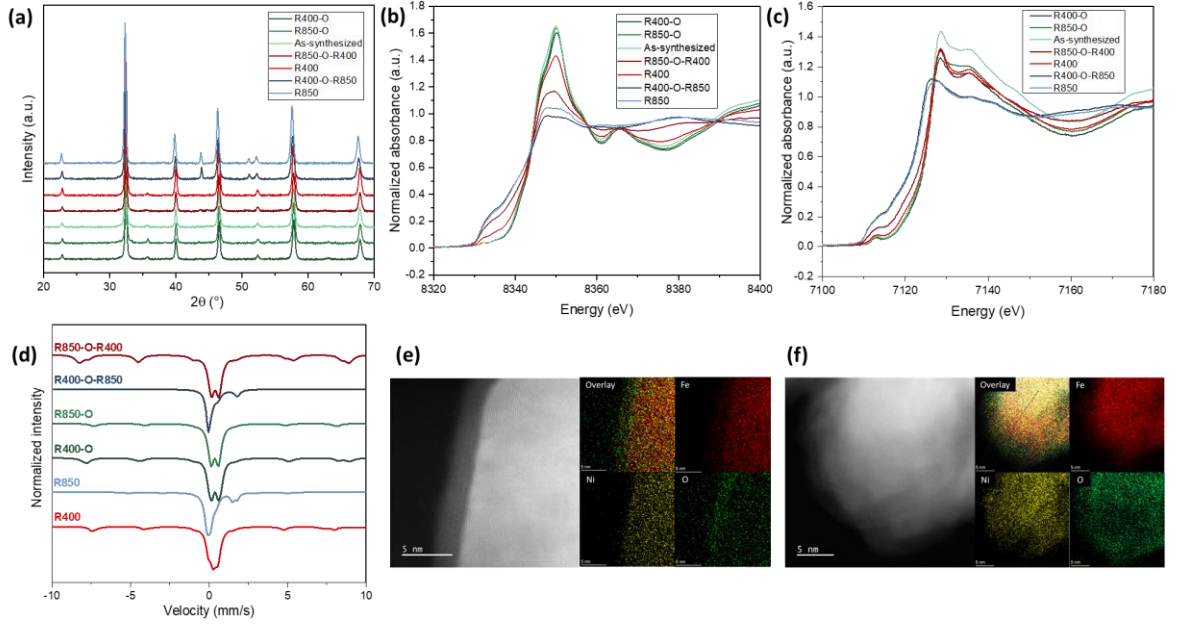
Figure 55. (a) XRD patterns, (b) Ni K-edge XANES spectra, (c) Fe K-edge XANES spectra and (d) Mössbauer spectra of the R400-O, R850-O, as-synthesized, R850-O-R400, R400, R400-O-R850 and R850 exsolved materials. HR-TEM pictures and EDX mapping of the (e) R400-O-R850 and (f) R850-O-R400 exsolved LSTFN materials.

Considering the results of XANES spectroscopy on the regenerated materials, i.e. R400-O and R850-O, the complete overlap of the Ni spectra (**Figure 55b**) suggests that, after the re-oxidation treatments, Ni can restore its chemical environment to match that of the as-synthesized LSTFN2 system. In contrast, a different behavior is observed for the Fe K-edge. The XANES curves for the re-oxidized samples in this case exhibit a similar shape to those of the pristine system (**Figure 55c**), but with their intensity notably weaker. This can be attributed to the presence of residual metallic iron, as suggested by the XRD pattern of R850-O, and to the formation of disordered iron oxide species during re-oxidation. This hypothesis is further supported by Mössbauer analysis (**Figure 55d**, **Table A2**). Both R400-O and R850-O samples, in addition to the doublet signals corresponding to the perovskite phase, display a sextet associated with ferric sites in a highly defective environment, which is attributed to cation-deficient spinel maghemite (γ-Fe_2O_3). This also explains the increased intensity of the spinel reflection in the XRD pattern of R850-O. Thus, re-oxidation of the reduced materials results in only partial reincorporation of the exsolved ions into the oxide matrix[70] (as will be discussed in more detail in **Chapter 7**). This effect is particularly pronounced for iron species, which, due to their

significantly lower mobility compared to nickel and to its different redox chemistry compared to nickel, tend to form a wider range of additional defective iron oxide phases[179,322]. Finally, the last step of the experimental protocol involved the analysis of the efficiency of the switching exsolution process, meaning reducing the re-oxidized materials back to their corresponding opposite exsolution temperatures (see **Scheme 2**). Considering the XRD results, the pattern for R400-O-R850 is identical to that of R850, showing a strong signal attributed to metallic exsolved Fe_3Ni particles (**Figure 55a**). However, a comparison of R850-O-R400 with R400 after the switching process reveals that the metallic nanoparticles' reflections remains clearly visible, suggesting incomplete dissolution of the metallic phase in R850-O. XANES spectroscopy (**Figure 55b,c**) further supports these findings: the results show a marked increase in the white line and pre-edge features of the Ni K-edge spectra for both switched R400-O-R850 and R850-O-R400 materials compared to the R400 and R850 systems, indicating a stronger reduction of Ni species after the switching process. In contrast, the Fe K-edge spectra show no significant changes before and after switching. The higher metallic content observed in R850-O-R400 (evidenced by increased pre-edge intensity) results from the incomplete dissolution of the metallic phase in R850-O, as confirmed by XRD. These observations are further corroborated by Mössbauer spectroscopy (**Figure 55d**, **Table A2**): for the R850-O-R400 material, re-exsolution at 400°C facilitates the formation of magnetically ordered phases, as can be seen from the Mössbauer spectra. A narrow absorption at ≈0.4 mm/s corresponds to ferric sites in the LSTFN2 configuration, while a broad magnetic pattern with two sextets suggests the formation of magnetically ordered phases akin to those in R400-O, linked to a partially inverse spinel structure. Conversely, the spectrum of the R400-O-R850 material matches that of R850 (blue spectra in **Figure 55d**), indicating the presence of an iron metallic phase (40%) and a highly defective iron oxide (25%). Finally, the strong similarity between materials exsolved and switched at high temperatures was further validated by TEM-EDX analysis (**Figure 53d,e** and **Figure 55e,f**). As with R850, TEM micrographs of R400-O-R850 show large alloy nanoparticles surrounded by a thick crystalline Fe_yO_x shell. Similarly, R850-O-R400 exhibits a nanoparticle structure and elemental distribution comparable to R400, with an Fe_3Ni core encased

by a thin amorphous oxide shell. However, the particle size in R850-O-R400 is significantly larger, likely due to metallic residues from R850-O serving as nucleation sites for further particle growth. Overall, these results show how the process of switching the material composition and morphology is partially achievable and depends largely on the metal cations involved in the process.

6.2.4 Catalytic testing for ODH and DER

The final part of this chapter was carried out in collaboration with Anastasios Tsiotsias of the University of Western Macedonia, and it involves the study of the developed materials for applications as heterogeneous catalysts for DER and ODH. To do so, the catalytic activity and selectivity of the exsolved perovskites at 400°C and 850°C (R400, R850) were analyzed for the reaction between C_2H_6 and CO_2. In **Figure 56** the conversions of the reactants along with the selectivity values for C_2H_4 and CO are reported, while **Table 6** summarizes the reaction metrics at the conclusion of the experiment.
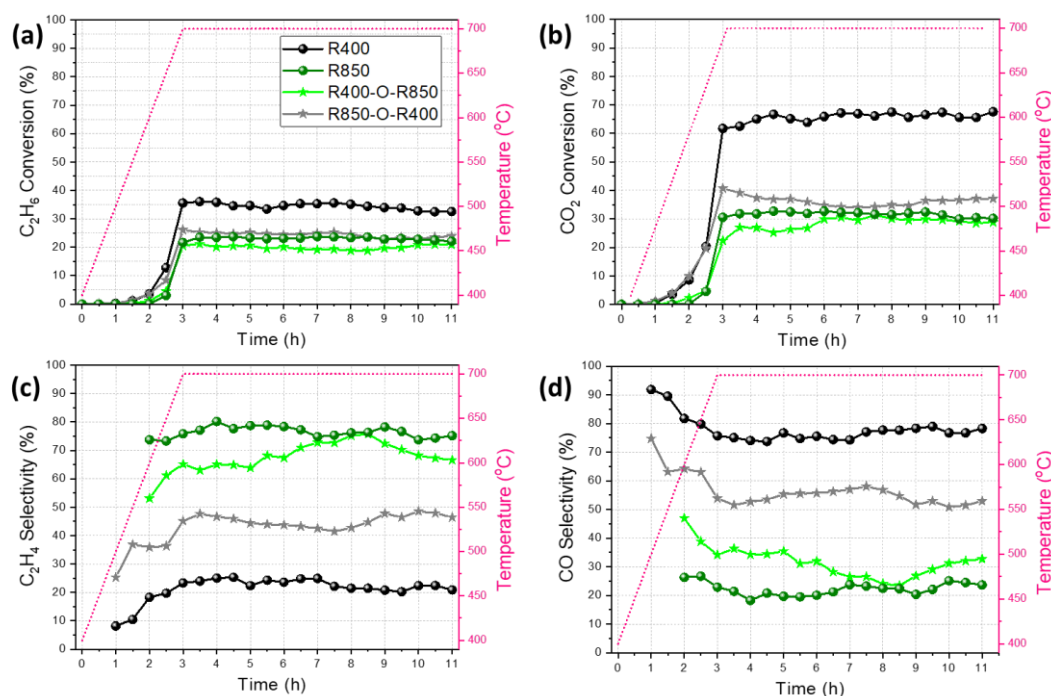
Figure 56. Trend over time of the (a) C_2H_6 conversion, (b) CO_2 conversion, (c) C_2H_4 selectivity (dehydrogenation) and (d) CO selectivity (reforming) during the catalytic testing.

Table 6. Summary of the catalytic activity results following 11 h of reaction, i.e. 3 h of temperature ramping (400–700 °C) + 8 hours time-on-stream (700 °C).

Material	Conversion (%)		Yield (%)				Selectivity (%)			H_2/CO
	C_2H_6	CO_2	C_2H_4	CO	H_2	CH_4	C_2H_4	CO	CH_4	
R400	32.6	67.6	6.8	29.2	17.3	0.3	20.8	78.3	0.9	0.58
R850	22.1	30.2	16.6	12.1	6.0	0.3	75.2	23.6	1.2	0.49
R400-O-R850	23.9	37.1	11.1	13.9	7.7	0.2	46.3	52.9	0.8	0.55
R850-O-R400	20.9	28.8	13.9	11.0	5.7	0.2	66.7	32.6	0.7	0.52

It is worth mentioning that a minor amount of methane is also formed as a result of ethane cracking[323–325], but the yield and selectivity of methane are quite low (below 1.5%) and are therefore omitted from the presented graphs; however, the CH_4 yield and selectivity values are included anyway in **Table 6**. During the temperature ramp from 400°C to 700°C (over the first 3 h), the reactant conversions and product yields show a steady increase, stabilizing upon reaching the final temperature of 700°C. The minimal variation in reactant conversions and product selectivity values beyond this point (i.e. between the 3rd and 11th hour) further highlights the good catalytic stability of the exsolved perovskite material[22,70,256,326]. The differences in reactant conversion between the LSTFN2 materials exsolved at 400°C and 850°C (R400 and R850) are reported in **Figure 56a,b**. Overall, R400 achieves significantly higher conversions for both ethane and carbon dioxide than R850, with the disparity being particularly pronounced for CO_2 conversion. More notably, substantial differences are observed in the selectivity toward C_2H_4 and CO (**Figure 56c**), as well as in the reaction pathways for Ethane Oxidative Dehydrogenation (ODH) and Dry Ethane Reforming (DER). For R400, the reforming pathway is predominant, with CO selectivity stabilizing at approximately 78% at 700°C (**Table 2**). On the other hand, for R850, the dehydrogenation pathway takes precedence, as C_2H_4 selectivity stabilizes at around 75% at 700°C (**Scheme 3**).
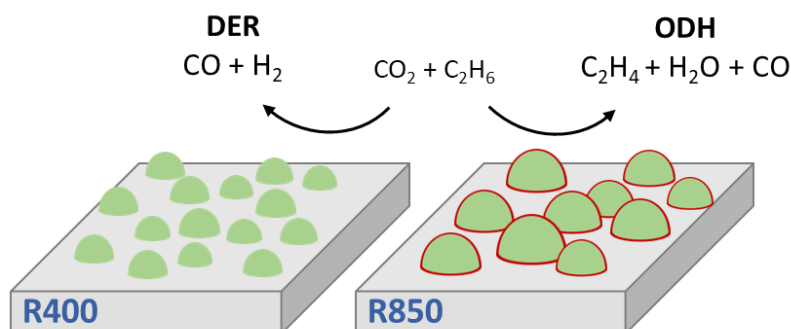
Scheme 3. Schematic of the catalytic reactions taking place on R400 and R850.

These findings demonstrate that varying the exsolution treatments applied to the same perovskite oxide material (LSTFN2) can effectively tailor the reaction selectivity toward either the dehydrogenation or reforming pathway. The significant difference in product selectivity during the reaction between C_2H_6 and CO_2 can be attributed to the distinct physicochemical properties of the two materials, such as the oxidation state of the Fe and Ni active metals, the nanomorphology of the material, and the nature of the exposed catalytically active surface sites. For R400, the exsolved metal nanoparticles are composed of Fe_3Ni, and the thin amorphous Fe_yO_x shell observed via HRTEM (**Figure 53**), likely formed due to air exposure, is expected to be easily removed under the reducing conditions of the reaction[327]. As a result, the surface-exposed Fe_3Ni metallic sites, anchored on the redox-active and defect-rich LSTFN2 perovskite support, are expected to enhance the material's activity toward the ethane reforming pathway[22,324,328,329]. On the other hand, for R850, the perovskite material shows larger Fe_3Ni metallic nanoparticles encapsulated by a crystalline Fe_yO_x overlayer. This metal oxide/metal (M′OX/M) inverse interface has been previously shown to favor the ethane dehydrogenation pathway over the reforming pathway[29,204,330–332]. Guo et al.[332] and Yan et al.[29,204] prepared various Fe-Ni bimetallic catalysts on different supports and concluded that a high concentration of Fe_yO_x (either as overlayers or at interfacial sites) inhibits C-C bond scission while selectively promoting C-H bond cleavage. This effect is attributed to the "weakly" electrophilic oxygen species supplied by Fe_yO_x[332]. In particular, "weakly" electrophilic

oxygen species can arise in some metal oxides (incl. Fe_yO_x), serving as Lewis acid sites, and favoring ethane dehydrogenation to ethylene[332–335]. Furthermore, the presence of an Fe_yO_x overlayer on top of a metallic core has been identified as more active compared to bulk Fe_yO_x or just Fe_yO_x adjacent to the support[204,331]. In the case of the study reported in this Chapter, the crystalline Fe_yO_x overlayer on the metallic Fe_3Ni particles, which was formed due to reverse oxygen spillover during exsolution, is most likely more resistant to reduction under catalytic reaction conditions. It is also expected to provide the "weakly" electrophilic oxygen species necessary for selective C-H activation, while simultaneously blocking access of the gaseous reactants to the reduced metallic sites (metal core), which are selective for C-C bond scission[204,331,332]. The switched materials, i.e. R850-O-R400 and R400-O-R850, were also catalytically tested (**Figure 56, Table 6**). Their catalytic performance differs significantly from that of the original R400 and R850 materials. This result is somehow expected, due to the different characteristics of the host matrix and re-exsolved nanoparticles, such as their incomplete dissolution during re-oxidation, which results in the formation of different surface-active sites following the switching process. Notably, the R400-O-R850 material exhibits catalytic performances relatively similar to R850, with only slightly lower reactant conversion and C_2H_4 selectivity. This is attributed to the presence of the Fe_yO_x overlayer and the inverse M'OX/M interface, which are also present in R400-O-R850 (**Figure 55e**)[204,331,332]. In contrast, R850-O-R400 exhibits significantly lower reactant conversions compared to R400 and reduced selectivity for ethane reforming. This is attributed to substantial surface reconstruction during the preceding re-oxidation at 850 °C (R850-O), involving residual spinel oxide and bimetallic FeNi side phases, as confirmed by XRD, XANES, and Mössbauer spectroscopies. During the subsequent re-reduction step for R850-O-R400, these residual phases most likely promote additional particle growth, resulting in much larger Fe_3Ni metal nanoparticles compared to R400. This limits the availability of active reforming sites (responsible for C-C bond scission). Consequently, while the switching treatment of the LSTFN2 material is effective for the transition from the DER to ODH, it proves to be

challenging for the switch from ODH to DER due to incomplete regeneration of the perovskite matrix during re-oxidation in the latter case. Thus, the switchability of catalytic performance and selectivity strongly depends on the re-oxidation treatment's ability to restore the original oxide structure. As a comparison, a commercial monometallic Ni/Al_2O_3 catalyst with a low Ni loading (1 wt.%) was tested (**Figure A8** in the Appendix). As expected for Ni-based catalysts[323,324], this material demonstrated higher activity toward the dry ethane reforming pathway. Despite undergoing a pretreatment step at 850 °C under a flow of pure H_2, the commercial reference catalyst exhibited a continuous and gradual increase in C_2H_6 and CO_2 conversions, even well after reaching the final reaction temperature of 700 °C. This suggests ongoing, slow activation of the material under the reactant stream, highlighting the relatively unstable nature of the commercial catalyst compared to the more stable perovskite-based catalysts. Post-catalysis characterization of the spent materials revealed no evidence of coke deposition on the perovskite catalysts. In contrast, significant coke formation was observed on the spent Ni/Al_2O_3 catalyst, as indicated by the pronounced D and G bands in its Raman spectra (**Figure 57**), which are characteristic of turbostratic carbon[336–340].
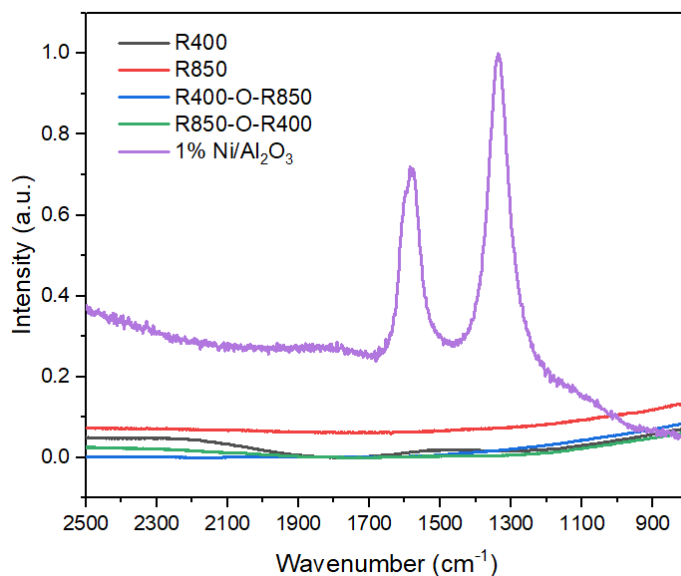
Figure 57. Raman spectra of the spent catalysts.

TEM images of the spent perovskite catalysts further confirm the absence of carbon deposition on these materials (**Figure A9, Figure A10, Figure A11, Figure A12** in the Appendix). In contrast, the Ni/Al_2O_3 catalyst displays the formation of typical carbon baffles, while XRD analysis conducted on the spent catalysts, although with the presence of a high amount of quartz sand in the catalyst leading to intense quartz (SiO_2) diffraction peaks, showed how the perovskite reflections remain clearly visible in the exsolved and switched materials, along with the crystalline Fe_3Ni alloy phase at $2\vartheta = 43.7°$ (**Figure A13** and **Figure A14** in the Appendix).

6.3 Summary

In **Chapter 6**, the exsolution behavior of FeNi nanoparticles from the LSTFN2 host matrix was examined across different temperatures. Moreover, the regeneration of these previously exsolved materials by re-oxidation has also been investigated, along with the possibility of switching the materials for the purposes of use as heterogeneous catalysts in ODH and DER processes by subjecting them to redox cycling. This was done by using various analytical techniques, including XRD, XANES, Mössbauer spectroscopy and HRTEM, whose results demonstrated how, by tailoring the structure and composition of bimetallic nanoparticles, catalytic performance, particularly selectivity, can be significantly enhanced. Concerning the effect of the increasing temperature of reduction of the as-synthesized LSTFN2 material, the results of X-ray diffraction and Mössbauer spectroscopy showed how the reduction process already takes place at relatively low temperatures, i.e. at 400 °C, and that the host perovskite matrix retained the cubic structure even after a high-temperature reduction at 850 °C. Moreover, the analysis of the diffractograms showed how reduction involved the substitutional metal ions in the perovskite, and not only the initially present $NiFe_2O_4$ spinel side phase. However, the XANES spectra of samples reduced at 650 °C and 850 °C are nearly identical, closely matching that of pure metallic nickel, which led to conclude that almost all the Ni present in the

original material has been fully reduced to its metallic state, and second, a significant fraction of the Ni ions originated from the spinel phase, initially present in the LSTFN2 host matrix. The findings also suggest that at lower temperatures (400 °C), the concentration of metallic Ni is larger than that of metallic Fe, whereas at higher temperatures (850 °C), metallic Fe becomes the dominant reduced species over metallic Ni. Regarding the morphology of the exsolved nanoparticles, HR-TEM results indicate the presence of a core-shell structure in the nucleated nanoparticles, consisting of a Fe_3Ni core, a Ni skin, and an external Fe_yO_x shell. Depending on the exsolution temperature, the external Fe_yO_x shell was found to be amorphous at 400 °C, due to air exposure, and crystalline at 850 °C, as a result of the strong metal-support interaction (SMSI) between iron oxide and the parent perovskite matrix. Regarding the materials regenerated by oxidation at 850 °C, the re-incorporation of exsolved ions was found to be influenced by their chemical and structural characteristics. On one hand, nickel fully restores its chemical environment to match that of the as-synthesized LSTFN2 system, while residual metallic iron and disruptions in the geometric symmetry of Fe cations are observed through XRD and XANES, likely due to the formation of disordered iron oxide species during re-oxidation. For the switched materials, the XRD pattern of R400-O-R850 closely matches that of R850, displaying a prominent reflection corresponding to metallic exsolved Fe_3Ni particles. In contrast, a comparison between R850-O-R400 and R400 after the switching process indicates that the metallic phase in R850-O is only partially re-dissolved during the preceding re-oxidation step. HR-TEM further confirmed that the core-shell structure present in the exsolved material is retained in the switched ones, with crystalline Fe_yO_x observed in the FeNi nanoparticles of R400-O-R850 and amorphous Fe_yO_x in the case of R850-O-R400. Finally, the catalytic testing on the exsolved and switched perovskite materials demonstrates that modifying the exsolution treatments applied to the same perovskite oxide material (LSTFN2) allows precise control over reaction selectivity, directing it toward either the dehydrogenation or reforming pathways. The switchability of catalytic performance and selectivity was found to strongly depend on the re-oxidation

treatment's ability to restore the original oxide structure. TEM and RAMAN spectroscopy measurements on the spent perovskite catalysts further confirmed the absence of carbon deposition, while the minimal changes in reactant conversions and product selectivity observed between the 3rd and 11th hour highlight the excellent catalytic stability of the exsolved perovskite material, particularly when compared to a commercially available Ni/Al_2O_3 catalyst.

Chapter 7

Redox Cycling of NiCo Nanoparticles from the La$_{0.6}$Ca$_{0.4}$FeO$_{3-\delta}$ Oxygen Carrier for Chemical Looping Reforming coupled with CO$_2$ Splitting

7.1 Introduction

In this chapter, to conclude the discussion on the use of the redox cycling of Fe-based perovskite oxides for heterogeneous catalysis, the results of an additional study on the design, characterization and catalytic testing of a perovskite with composition La$_{0.6}$Ca$_{0.4}$FeO$_{3-\delta}$ (named LCFO), for usage as oxygen carrier for a CCU technique is presented. As already discussed regarding the use of an Fe-Ni doped perovskite oxide systems for ODH and DER, CCU technologies involve a number of reactive strategies to re-utilize carbon dioxide and therefore lowering CO$_2$ emissions. One promising example is the so-called Chemical Looping Reforming (CLR), a process that not only captures CO$_2$, but also produces valuable outputs such as energy, pure oxygen, syngas, and ethylene with high efficiency. CLR is a process that converts methane (CH$_4$) into syngas, a mixture of carbon monoxide (CO) and hydrogen (H$_2$), through cyclic oxidation and reduction reactions involving a metal oxide as an oxygen carrier[341,342]. This has the advantage of avoiding typical direct oxidation routes, such as the partial oxidation of methane, which has the disadvantage of producing harmful by-products (e.g., NO$_x$) and requiting additional purification steps for the final product[343]. Syngas is a resource used as a reactant or as precursor in a number of different industrial chemical engineering applications, including Fischer-Tropsch synthesis of hydrocarbons, methanol production and ammonia synthesis[344,345], as well

as for its use as fuel in SOFCs[346–349]. Chemical looping reforming employs metal oxide carriers as oxygen sources, avoiding direct contact between methane and oxygen while preserving the benefits of oxy-combustion. In the two-step CLR process, methane first reacts isothermally with the lattice oxygen of the metal oxide (**Equation 34**), reducing it and producing syngas ($CO + 2H_2$):

$$CH_4 + MeO_x \rightarrow CO + 2H_2 + MeO_{x-\delta} \tag{34}$$
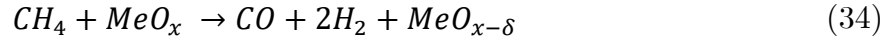
The oxygen vacancies in the reduced metal oxide carrier ($MeO_{x-\delta}$) are then replaced by an oxidizing agent, in our case CO_2 (**Equation 35**):

$$MeO_{x-\delta} + CO_2 \rightarrow MeO_x + CO \tag{35}$$
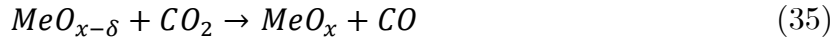
When CO_2 is used as the oxidant in the second step, additional CO is generated, and CO_2 is consumed, offering a dual benefit of syngas production and CO_2 utilization[350–352]. The use of perovskite oxides as oxygen carriers for this combined CLR and CO_2-splitting technology is justified by their good oxygen storage capacity, resistance to deactivation by coking, and, most importantly, their structural flexibility, which facilitates ion movement during redox cycling[353], as extensively discussed in **Chapter 5** and **Chapter 6**. In particular, Ca-doped lanthanum ferrites ($LaFeO_{3-\delta}$) have been employed because of its promotion of methane activation and CO selectivity, with recent studies showing promising performances of $La_{0.6}Ca_{0.4}FeO_{3-\delta}$ as an oxygen carrier for chemical looping syngas generation[354]. Moreover, the applicability of the exsolution concept for this combined application is straightforward, given the possibility of inducing the movement of metal ions, in this case Ni and Co, from lattice metals at the B-site to bimetallic nanoparticles on the surface of the perovskite materials, by directly recalling them through redox cycling. The use of exsolved nanoparticles over a perovskite oxide hosts have been shown to give a good syngas production with superior stability during the CLR process[253,355].

In view of these considerations, the $La_{0.6}Ca_{0.4}Fe_{0.95}M_{0.05}O_{3-\delta}$ (with M = Ni, Co, NiCo) perovskite oxide material was adopted for this study as oxygen carrier for CLR coupled with CO_2 splitting, by making use of the multimetallic exsolution process. The design of the system and the sol-gel synthesis of the perovskite material, as well as part of the characterization and the complete assessment of the redox properties and catalytic testing of the materials, were conducted by DongHwan Oh of the Korea Advanced Institute of Science and Technology (KAIST). The metal oxides were designed by introducing Ni and Co in the LCFO system both as single dopants (with $x_{Ni}/x_{Co} = 5$ at.%) and together as co-dopants (with $x_{Ni} = x_{Co} = 2.5$ at.%). A first assessment of the reactive properties of the LCFO materials when using them as oxygen carriers first included the evaluation of the activation temperature for CH_4 conversion and of the outlet gas composition through Methane Temperature Programmed Reduction (MTPR), together with methane pulse tests for monitoring the critical point of carbon coking, the CO selective regime and the degree of catalysts degradation. These screening measurements revealed that co-doping the parent host oxide with equimolar concentrations of Ni and Co (2.5 at.% each), as in the case of the LCFO-based material with composition $La_{0.6}Ca_{0.4}Fe_{0.95}$ $Co_{0.025}Ni_{0.025}O_{3-\delta}$, determines the most significant CH_4 conversion and an oxygen storage capacity of the perovskite oxygen carrier. Moreover, the catalytic testing of these materials for CLR and CO_2 splitting showed good syngas production, as well as a high thermal stability and resistance to carbon deposition.

These results can be attributed to structural transformations occurring during redox cycling. Under a reducing CH_4 atmosphere, a FeCoNi alloy is proposed to exsolve and nucleate as trimetallic nanoparticles on the material's surface. During oxidative conditions induced by CO_2, these nanoparticles transition into a NiCo alloy, driven by a reversible partial reintegration of Fe atoms into the host perovskite lattice[70] (**Figure 58**). To validate the hypothesis of rocking-chair behavior of Fe cations, the second part of this study focused on analyzing the Ni-Co doped material at each stage of the process – namely the as-synthesized, reduced, and re-oxidized LCFO materials. This analysis employed a multi-technique approach, incorporating bulk

methods such as X-ray diffraction, XANES spectroscopy and Mössbauer spectroscopy, which was performed in collaboration with Luca Nodari of the University of Padua. These results provide valuable insights into the partial re-incorporation of multimetallic exsolved nanoparticles, enabling both qualitative and quantitative characterization of the structural transformations occurring in the material during redox cycling, in the context of their application in CLR and CO_2 splitting.
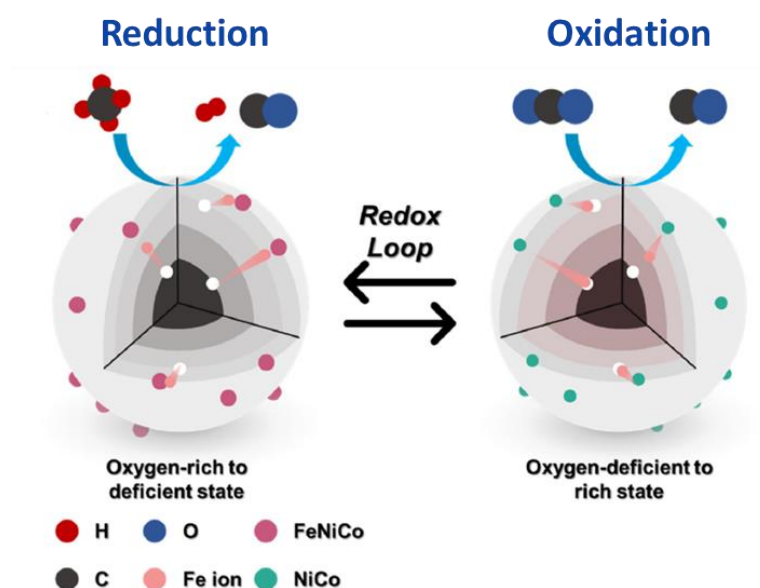

Figure 58. Simplified schematic of the redox cycling of the FeNiCo and NiCo nanoparticles during CLR coupled with CO_2 splitting. Reported from Oh & Colombo et. al.[70].

7.2 Results and discussion

7.2.1 Interactions between the oxygen carriers and the reactant gases

The as-synthesized LCFO perovskite oxygen carrier ($La_{0.6}Ca_{0.4}FeO_{3-\delta}$), as well as the materials with both Ni and Co introduced as single dopants (having $La_{0.6}Ca_{0.4}Fe_{0.95}Ni_{0.05}O_{3-\delta}$ and $La_{0.6}Ca_{0.4}Fe_{0.95}Co_{0.05}O_{3-\delta}$) and the co-coped Ni-Co perovskite ($La_{0.6}Ca_{0.4}Fe_{0.95}Ni_{0.025}Co_{0.025}O_{3-\delta}$) were synthesized by DongHwan Oh of KAIST, following the protocol described in **Subsection 10.2.2** of the **Experimental Methods** chapter.

In the first part of this study, experiments were performed by the collaboration partners at KAIST to evaluate the reactivity of the as-synthesized and doped LCFO systems, focusing on their redox and thermal stability as oxygen carriers. These experiments included temperature-programmed methane reduction (MTPR), methane transient pulse tests, and multi-cycle tests for Chemical Looping Reforming and CO_2 splitting.

First, MTPR was performed to examine the activation temperature of CH_4 over the catalyst materials and to analyze the composition of the resulting gases. This was achieved by subjecting the materials to a temperature ramp from 25 °C to 850 °C under a reducing atmosphere of 5% CH_4 in Ar. **Figure 59a** presents the results for the Ni-Co-doped sample ($La_{0.6}Ca_{0.4}Fe_{0.95}Ni_{0.025}Co_{0.025}O_{3-\delta}$, in the rest of this chapter also referred to as LCFO-NiCo),but similar trends are observed in all other samples. The minimal CO_2 production and the predominant conversion of CH_4 into CO (**Figure 59b-c**) for all samples indicate that LCFO carriers are well-suited for the partial oxidation of methane, favoring the production of syngas over complete combustion. Notably, the doped carriers started producing substantial amounts of syngas at around 700 °C, while the undoped carrier generated only minimal quantities at temperatures exceeding 800 °C, highlighting the critical role of doping in anticipating CH_4 activation. Among the samples tested, the Ni-doped carrier exhibited the lowest CH_4 activation temperature, followed by the Ni-Co-doped, Co-

doped, and undoped carriers, respectively (**Figure 59d**). These findings are consistent with previous results available in the literature, which demonstrate that Ni exhibits superior catalytic activity for CH_4 activation compared to Co, while Fe shows the lowest reactivity for the process[356].
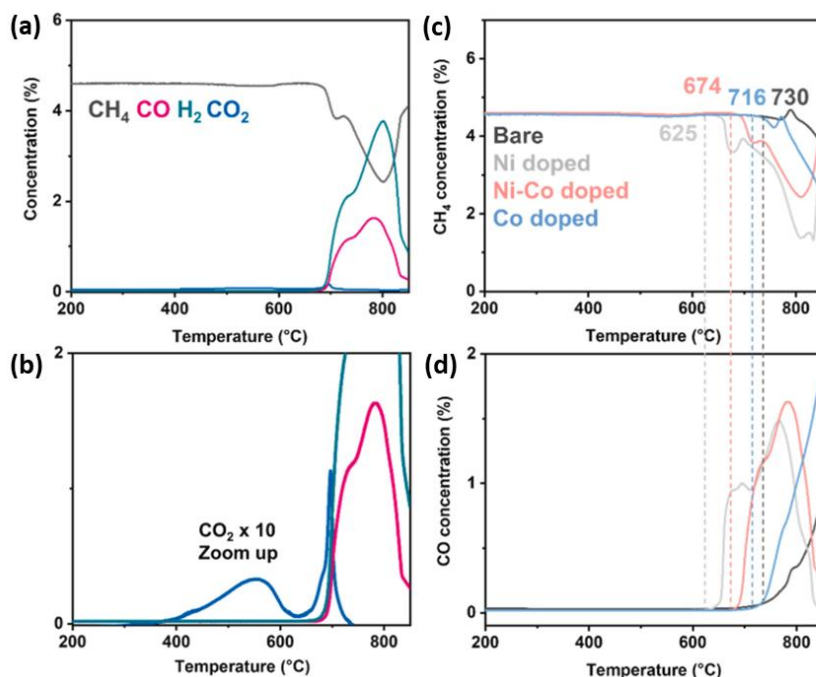

Figure 59. Overview on the results of methane temperature programmed reduction results for the LCFO-NiCo material under 5% CH_4/Ar atmosphere. (a) Overall product profile from Ni-Co doped sample versus temperature during the test, together with (b) zoom into the CO_2 production signals between 400 °C and 850 °C. (c) CH_4 concentration traces over the various type of samples. The indicated temperature values reveal the corresponding CH_4 activation temperature. (d) Outlet CO concentration profile for each sample.

To further investigate the CH_4 oxidation process, transient CH_4 gas injections were conducted under short contact times to reduce interference from secondary reactions[357]. For doing so, a gas mixture containing 5% CH_4/Ar and pure Ar gas was alternately injected in pulses under isothermal conditions at 850 °C, for a total of 30 times. Monitoring the gas signals during these experiments offered valuable insights into critical phenomena such as carbon coking, the CO-selective regime, and catalyst degradation[358]. The results for the Ni-Co-doped oxygen carrier (LCFO-NiCo) during the pulse reaction are shown in **Figure 60a,** with again similar trends observed for other carriers.
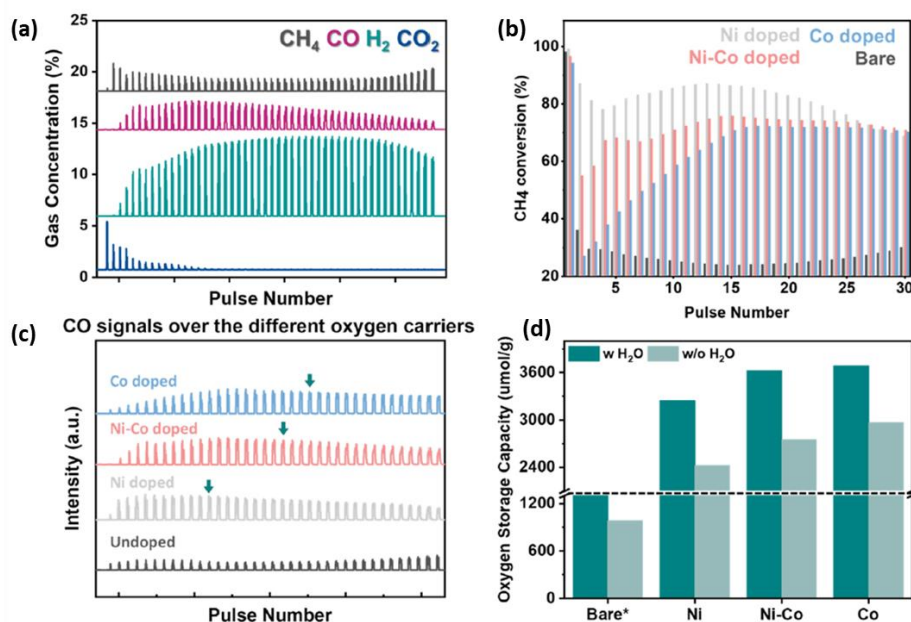
Figure 60. Methane transient pulse tests on the LCFO oxygen carriers. (a) Outlet gas species during the pulse reaction for the Ni-Co-doped carrier. (b) CH_4 conversion rates of the prepared samples over 30 pulse injections. (c) CO gas signals for various oxygen carriers, with the green arrow indicating the specific moment where the CO signal begins to decline. (d) Oxygen storage capacity (OSC) of doped oxygen carriers prior to the onset of carbon coking.

Initially, CO_2 is the main product, but its signal gradually decreases over time. This behavior suggests that surface oxygen (or weakly bound oxygen) primarily drives the complete oxidation of CH_4 in the early stages[359]. As surface oxygen is depleted, the CO_2 signal diminishes, and the CO signal increases due to the partial oxidation of CH_4 with lattice oxygen. The reactivity of the material towards CH_4 was also analyzed in detail (**Figure 60b**), revealing that doping significantly enhances CH_4 conversion. The Ni-doped carrier exhibited the highest CH_4 conversion rate, even beyond the complete oxidation stage. In contrast, the Co-doped carrier showed lower CH_4 conversion during the initial pulses, requiring additional injections to reach a similar conversion level as the Ni-doped sample. The Ni-Co-doped carrier instead demonstrated intermediate performance, consistent with the MTPR results. The CO signals during the pulse tests are presented in **Figure 60c**, where the onset of signal deterioration (marked by the green arrow) denotes carbon coking. By analyzing the amounts of oxygen-containing products, the oxygen storage capacity (OSC) was determined (**Figure 60d**). In fact, the oxygen involved in the reaction is assumed to

161

come from the lattice oxygen of the carrier material, and by tracking the amounts of CO_2 and CO produced during the pulses, the oxygen contribution can be determined. Although the Ni-doped carrier exhibited the highest CH_4 reactivity, its low OSC rendered it less suitable as a dopant, likely due to insufficient available oxygen to sustain its high activity. Additionally, the trend of the H_2/CO ratio reveals that the Ni-doped carrier experienced a rapid increase in the ratio by the seventh pulse, likely due to CH_4 thermal cracking, indicating severe coke formation. In contrast, the Ni-Co-doped and Co-doped carriers showed more stable behavior, with the LCFO-NiCo achieving the best balance between high CH_4 conversion and improved oxygen storage capacity.

7.2.2 Multiple cycle tests for CLR and CO₂ splitting

The screening process presented in **Subsection 7.2.1** allowed to point out how LCFO-NiCo, i.e. the oxygen carrier material with equimolar doping of Ni and Co (2.5 at% each), emerges as an excellent candidate for the reforming step, combining good redox performances in CO_2 atmosphere and high CH_4 conversion rates, with enhanced coking resistance and OSC. To evaluate its multi-cycle behavior for chemical looping syngas production, the partial oxidation of CH_4 coupled with a CO_2 splitting redox cycle was conducted at 850 °C (**Figure 61**). On average, the Ni-Co-doped carrier achieved a 70% gas conversion (**Figure 61a**) with 90% CO selectivity, while the as-synthesized LCFO carrier exhibited only 10% gas conversion. The product yield of the Ni-Co-doped carrier in the 50th cycle was higher than the yield from the 1st cycle of the as-synthesized bare carrier, indicating improved durability and reactivity (**Figure 61b**). Despite the low doping concentration, surface modifications in the NiCo-doped carrier appear to enhance reaction kinetics with CH_4 and CO_2, leading to improved performance compared to the undoped carrier. Instead, the Ni-doped carrier showed similar CH_4 conversion to the co-doped sample, but repeated redox cycling resulted in an H_2/CO ratio exceeding 2, suggesting increased H_2 formation from coking reactions. The Co-doped catalyst instead exhibited lower

fuel conversion ($\approx 50\%$) and an H_2/CO ratio of ≈ 1.6, indicating how co-doping with Ni and Co effectively modifies the properties of the LCFO oxygen carriers, leading to improved reactivity and redox stability.
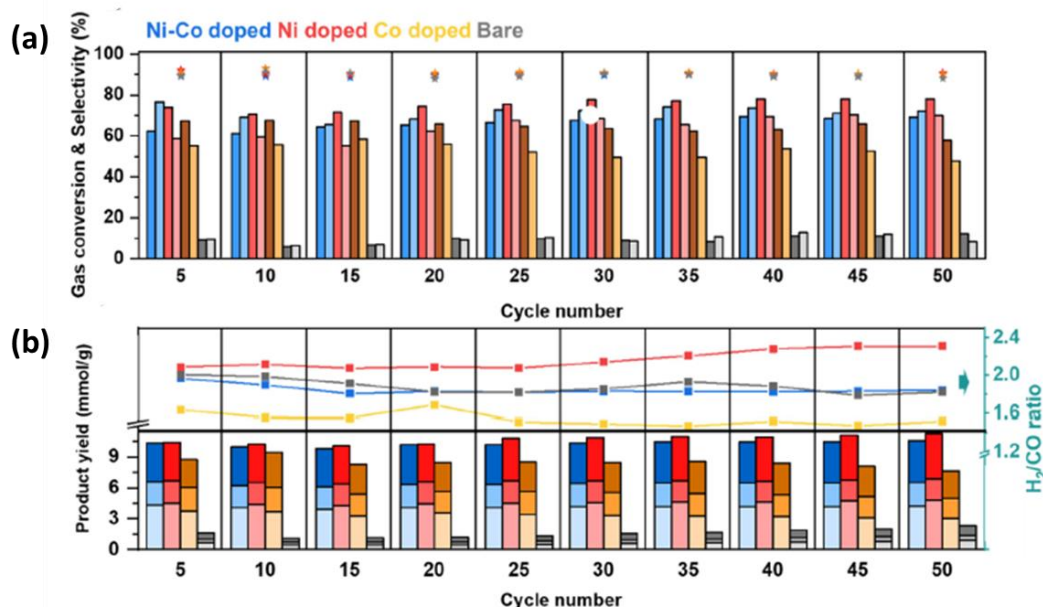

Figure 61. Multiple redox cycle test results for doped and pristine oxygen carriers (blue: NiCo-doped, red: Ni-doped, yellow: Co-doped, gray: as-synthesized LCFO). (a) Gas conversion and CO selectivity: deep-colored bars represent CH_4 conversion, light-colored bars indicate CO_2 conversion, and star symbols denote CO selectivity. (b) Product quantities during cycle tests: stacked columns show the amounts of H_2 from CH_4 reforming, CO from CH_4 reforming, and CO from CO_2 splitting (bottom to top). The line graph above the columns illustrates H_2/CO ratio trends across cycle numbers.

7.2.3 Structural evolution under redox conditions

The first two subsections of this chapter evaluated the catalytic performance of the material for CLR and CO_2 splitting. In contrast, the second part focuses on the in-depth characterization of LCFO, emphasizing the structural and compositional changes in the NiCo doped material during redox cycling under alternating reducing (CH_4) and oxidizing (CO_2) atmospheres. This analysis was conducted using a combination of surface characterization techniques, including scanning electron microscopy (SEM) and high-angle annular dark-field energy-dispersive X-ray spectroscopy (HAADF-EDX), alongside bulk characterization methods such as X-ray diffraction (XRD), X-ray absorption near-edge structure (XANES) spectroscopy,

and Mössbauer spectroscopy. This integrated approach provided a comprehensive understanding of both surface and bulk phenomena in the oxygen carriers during redox cycling. First, SEM and HAADF-EDX measurements were performed by DongHwan Oh and collaboration partners at KAIST. These analyses offered preliminary insights into the surface characteristics of the LCFO material. SEM images obtained after exposure to CH_4 reveal the formation of numerous nanoparticles on the surface of the NiCo-doped sample. These nanoparticles are notably absent in the as-synthesized LCFO oxygen carrier, indicating surface modifications induced by the reducing CH_4 atmosphere (**Figure 62a, Figure A15**). After CO_2 injection, i.e. under oxidizing conditions, metal nanoparticles were still observed on the NiCo-doped sample (**Figure 62b**), with a reduction in nanoparticle size attributed to compositional changes in the CO_2 atmosphere. The results of the HAADF-EDX analysis (**Figure 62c**) highlight the presence of trimetallic FeNiCo particles in specific areas of the sample's surface after CH_4 reduction and NiCo particles after CO_2 oxidation. The exact composition of this alloy, due to the complexity of the system, cannot be definitively determined but may consist of various combinations of transition elements, such as bimetallic NiFe, FeCo, or monometallic Fe. Therefore, as schematized earlier in **Figure 58**, it was suggested that redox cycling leads to the exsolution of FeNiCo alloy nanoparticles (or variants such as NiFe, CoFe, or Fe) during CH_4 injection, i.e. under reducing conditions, which are subsequently replaced by NiCo alloy nanoparticles during CO_2 splitting, as Fe is selectively re-oxidized and reincorporated into the perovskite matrix. Although these results are promising and provide valuable insights into the surface characteristics of the materials when subjected to redox cycling, a key drawback of surface-sensitive techniques like TEM is that they are able to analyze only localized regions of the material, which may not accurately reflect the overall structure or composition of the entire sample.
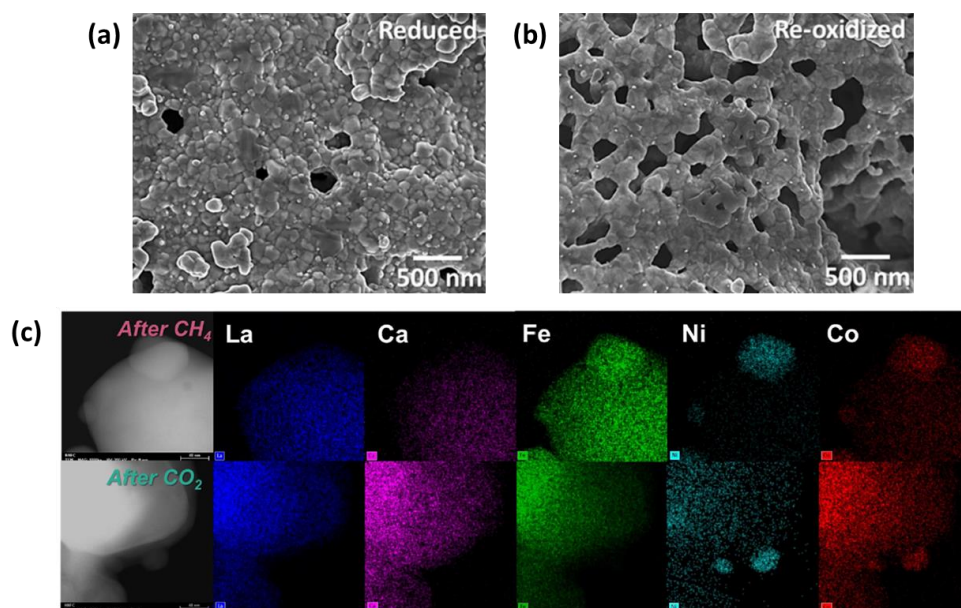
Figure 62. (a) TEM picture showing the surface morphology of the NiCo-doped carrier following CH$_4$ annealing. (b) TEM picture showing the surface structure of the carrier after CO$_2$ treatment immediately following CH$_4$ reduction. (c) HADDF-EDX analysis of the NiCo-doped oxygen carrier after thermal exposure to CH$_4$ and subsequent regeneration with CO$_2$.

To overcome this limitation and verify the rocking-chair-like behavior of Fe cations during redox cycling, a multi-technique approach was employed, combining three bulk characterization methods: XANES spectroscopy, Mössbauer spectroscopy, and X-ray diffraction. This methodology enabled a more comprehensive understanding of the material by making use of the complementary strengths of these techniques. Each characterization method was systematically applied at different stages of the redox cycling of Fe, i.e. for as-synthesized, reduced, and oxidized states. XANES probed the electronic and local atomic environment, Mössbauer spectroscopy offered detailed information on the oxidation states and magnetic properties of Fe-containing phases, and XRD provided insights into the crystalline structure. By integrating these results, a representative analysis of the material was achieved, ensuring that both surface and bulk properties were considered and allowing for a qualitative and quantitative description of the chemical and structural changes occurring during redox cycling. XANES spectroscopy was employed to obtain detailed insights into the chemical states of the transition metals. However, due to the nearly complete occupation of Fe at the B-site and the close proximity of the absorption K-edges of

Fe, Ni, and Co (7112 eV, 7709 eV, and 8333 eV, respectively), it was not possible to analyze the Co and Ni dopants in fluorescence mode because of signal overlap and of the very small atomic fractions of such dopants when compared to iron (0.025 at.% for Co and Ni vs. 0.95 at.% for Fe). Therefore, XANES spectroscopy was conducted exclusively at the Fe K-edge for the as-synthesized, reduced, and re-oxidized perovskite oxide samples, as reported in **Figure 63a**. Linear combination fitting was conducted to identify the Fe speciation in both the reduced and re-oxidized samples, utilizing reference spectra from the as-synthesized material, metallic Fe, FeO, and Fe_2O_3 (**Figure 63b** and **Figure A16**).
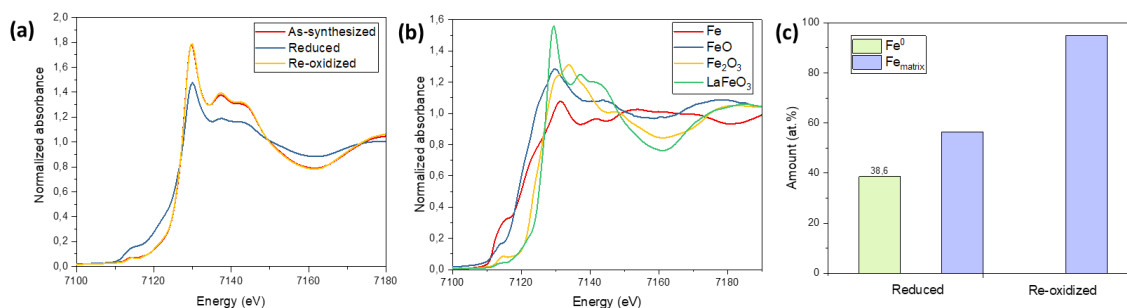
Figure 63. (a) XANES spectra of the Fe K-edge for the pristine, reduced and re-oxidized materials. (b) Reference spectra of the employed standards and (c) results of the linear combination fitting.

For the reduced sample, a notable decrease in the white line intensity and an increase in the signal at 7115 eV were observed, resembling features of the Fe^0 spectrum. LCF analysis revealed that approximately 40% of the Fe had been reduced to Fe^0 (**Figure 63c**). Interestingly, once the perovskite material has been exposed to the mild oxidative CO_2 atmosphere, the whole metallic Fe content turned back to the ferric state. The shape of the white line suggested that Fe^{3+} was reincorporated into a perovskite-like chemical environment (**Figure 63a**). Unfortunately, the overlapping signals from Co and Ni limited the extraction of more detailed information from EXAFS analysis, which would have been indicative of the coordination environment of such ions. Therefore, from the XANES results it can be concluded that the Fe^0 species are re-incorporated back into the perovskite matrix, i.e. they have oxidation state +3, but their coordination environment cannot be specified. To address this

limitation, Mössbauer spectroscopy was performed by Luca Nodari from the University of Padua on the three systems and compared with the XANES and the powder diffraction results (**Figure 64**).
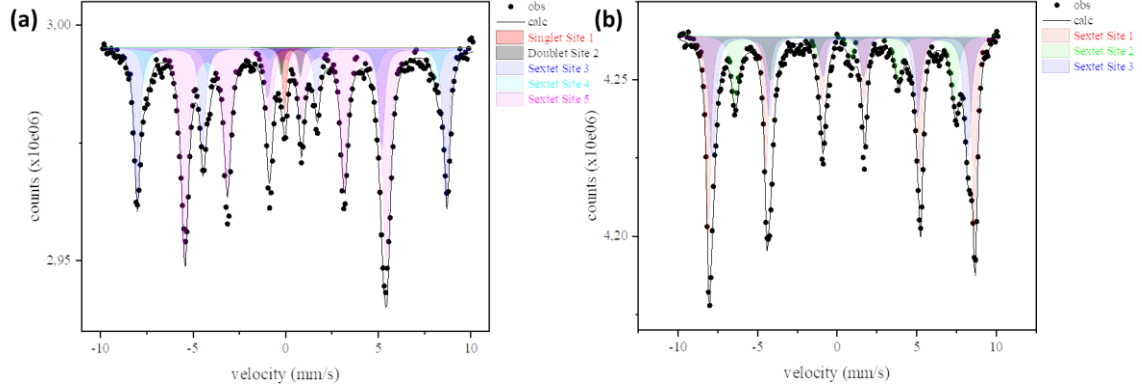

Figure 64. ^{57}Fe Mössbauer spectra along with the different components of the (a) reduced and (b) re-oxidized materials.

For the as-synthesized pristine material (**Figure A17** in the Appendix), the spectrum showed an overlapping broad sextet and an asymmetric doublet. The sextet suggested a relaxation spectrum, indicating that the sample was near its magnetic order-disorder transition. However, this relaxation component complicated the fitting process, preventing accurate determination of local Fe interactions. After reduction (**Figure 64a**), the spectrum was fitted using a combination of magnetically coupled components and paramagnetic/superparamagnetic species. The best fit included five components: three sextets corresponding to magnetically ordered Fe nuclei and two additional components (a doublet and a singlet) linked to non-magnetically coupled species. The hyperfine parameters are listed in **Table A3**. The most intense sextet (55%) likely corresponds to electron-rich Fe, such as metallic α-Fe and/or Fe alloys, in agreement with XANES data. The other two sextets represent Fe^{3+} in octahedral environments, with the one having the highest B-value likely associated with $LaFeO_3$ and the other with Fe^{3+} oxides. The doublet and singlet, which together account for 4% of the total area, probably correspond to small amounts of perovskite and metallic Fe/alloy in a superparamagnetic state. After re-oxidation (**Figure 64b**), the Mössbauer spectrum showed significant changes in Fe nuclei interactions. The

spectrum was fitted with three sextets: two corresponding to octahedral Fe^{3+} and one to tetrahedral Fe^{3+}. As before, the sextet with the highest B-value was linked to $LaFeO_3$, while the other two were assigned to a spinel phase, likely magnetite or maghemite. Notably, all metallic Fe in the reduced sample was fully oxidized to Fe^{3+}, consistent with both XANES and XRD data.

Finally, to shed lights into the structural changes during reduction and re-oxidation processes, XRD was performed after each treatment. The phase analysis was carried out at first for the "as-synthesized" LCFO material and for the NiCo co-doped perovskite both after the CLR process ("Reduced") and the subsequent CO_2 splitting redox cycle ("Re-oxidized"), whose results are shown in **Figure 65**.
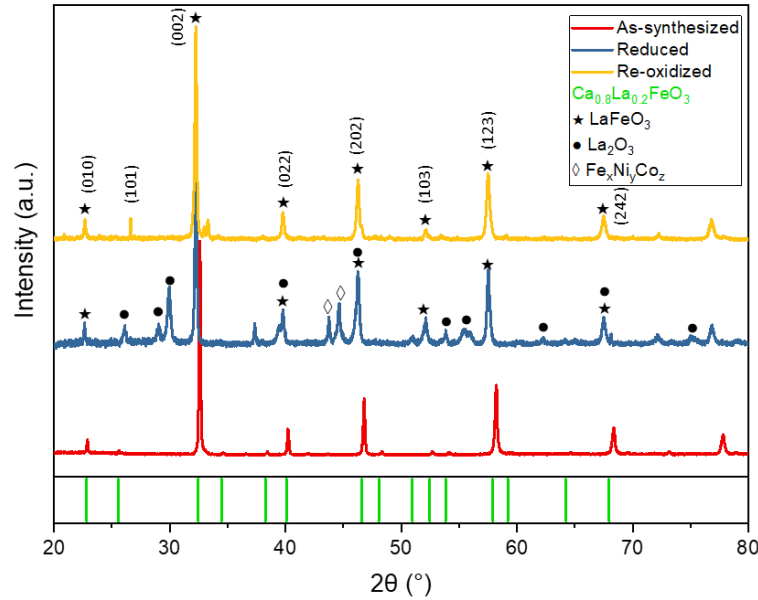
Figure 65. XRD patterns of the as-synthesized, reduced and re-oxidized $La_{0.6}Ca_{0.4}Fe_{0.95}Co_{0.025}Ni_{0.025}O_{3-\delta}$ materials.

Upon reduction of the phase-pure $La_{0.6}Ca_{0.4}Fe_{0.95}Co_{0.025}Ni_{0.025}O_{3-\delta}$, Fe-alloy exsolution occurs alongside the formation of a La_2O_3 and Ca-enriched $La_{1-x}Ca_xFeO_{3-\delta}$ phase (with $x > 0.4$), resulting from structural rearrangements of the parent material. Notably, following CO_2-driven oxidation, the metallic components' reflections vanish, with iron reintegrating into the perovskite structure $LaFeO_3$ and forming a spinel phase, consistent with the results of Mössbauer spectroscopy.

7.3 Summary

A perovskite system based on the $La_{0.6}Ca_{0.4}FeO_{3-\delta}$ (LCFO) host oxide with general formula $La_{0.6}Ca_{0.4}Fe_{0.95}$ $M_{0.05}O_{3-\delta}$ (with M = Ni, Co, NiCo) was designed as metal oxide oxygen carrier catalyst for use in Chemical Looping Reforming coupled with CO_2 splitting. In the case of the bimetallic-doped material, named LCFO-NiCo and with formula $La_{0.6}Ca_{0.4}Fe_{0.95}Co_{0.025}Ni_{0.025}O_{3-\delta}$, the exsolution of a trimetallic FeCoNi alloy nanoparticles was observed via HR-TEM under reducing CH_4 conditions, switching under oxidizing CO_2 atmosphere to NiCo bimetallic nanoparticles, with a re-incorporation of the Fe cations into the original oxidation state and coordination environment. A bulk multi-technique characterization approach, analogous to the one used for characterizing the redox cycling of LSTFN2 in **Chapter 6**, was used for a more in-depth investigation of exsolution and re-oxidation processes, with a view to more efficient design of heterogeneous regenerating catalysts for CLR. Powder diffraction revealed that Fe-alloy exsolution occurred concurrently with the formation of a La_2O_3 phase and a Ca-enriched $La_{1-x}Ca_xFeO_3$ phase, while following CO_2-induced re-oxidation the metallic component reflections disappeared as iron was mainly reintegrated into $LaFeO_3$. This is in agreement with of both XANES and Mossbauer spectroscopy, whose results confirms the presence of a metallic Fe^0 alloy. Moreover, after exposure to an oxidative atmosphere, only partial re-incorporation of metallic Fe into the ferric Fe^{3+} state within the perovskite environment was observed. This was evidenced by the presence of magnetite and/or maghemite phases detected through Mössbauer spectroscopy, which complemented the XANES analysis and was further confirmed by XRD results. This highlights the validity of the adopted methodology, which combines three mutually complementary bulk techniques to provide a comprehensive overview of the structural and chemical changes of the metal species involved in the redox cycling process. Furthermore, these findings confirm the adaptability of perovskite oxides and of the processes of exsolution and regeneration, extending beyond Fe-based strontium titanate perovskites to include lanthanum ferrite systems. This demonstrates their potential

as a viable alternative to traditional catalysts for CLR and CO_2 splitting, offering advantages in terms of improved redox and thermal flexibility, catalytic performance, and durability.

Chapter 8

Analysis of the Surface Interactions between Water and Mesoporous TiO$_2$

8.1 Introduction

The last chapter of this dissertation concerns the study of the surface chemistry of titanium dioxide (TiO$_2$) and its surface modification for applications in sustainable catalysis. In particular, the subject deals with the effect of different surface modifications performed on titania in order to investigate its surface interactions with water. This gains importance in all those applications where titania is employed as heterogeneous catalyst, including photocatalytic water splitting to produce hydrogen gas. Hydrogen is a clean energy carrier that releases a significant amount of energy (ΔH° = –284 kJ mol^{-1}) upon combustion, producing only water as a byproduct[91]. It also serves as important raw material for producing industrially significant chemicals, including methanol and ammonia. Nowadays, most of the hydrogen produced worldwide is derived from fossil fuels like coal (black hydrogen) and natural gas (gray hydrogen), processes that inevitably result in CO$_2$ emissions[91,360]. Therefore, photocatalytic water splitting is a promising method for sustainable hydrogen production, converting solar energy into chemical energy by splitting water (H$_2$O) into gaseous hydrogen (H$_2$) and oxygen (O$_2$) in a 2:1 ratio (**Equation 36**), by using a heterogeneous photocatalyst:

$$2H_2O_{(l)} \rightarrow 2H_{2\,(g)} + O_{2\,(g)} \qquad (36)$$
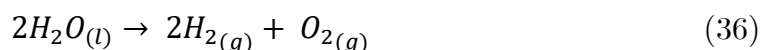
The research on the topic of photocatalytic water splitting is aimed to achieve efficient solar-to-hydrogen energy conversion on a large scale, producing carbon-neutral (also known as "green") hydrogen[91,92], which represents a valuable contribution to the development of energy processes for decarbonization and sustainable energy transition from fossil fuels to renewable sources. Typically, photocatalytic water splitting employs semiconductor materials as photocatalysts to absorb sunlight, generating electron-hole pairs that drive redox reactions[91]. To achieve efficient photocatalytic water splitting, the catalyst material should possess key properties such as good conductivity, redox potential and band gap, strong light absorption and ease of synthesis and production[361]. Among the different metal oxides that have been reported in the literature as potential candidates[362,363], TiO_2 has emerged as a promising one due to its relative abundance, non-toxicity, chemical inertness, low cost and abundance[90]. However, this also brings with it a number of disadvantages, such as its high energy bandgap (3.0–3.2 eV), which results in the absorption of light only in the UV-spectrum, and the suffering from high electron-hole recombination rates, which hinder its efficiency[364]. While TiO_2 exists in three different crystal polymorphs (anatase, rutile and brookite[363]), for applications in photocatalysis anatase is generally preferred over the other two, because of its higher photocatalytic activity. Luttrel et. al.[95] attributed this effect to a more efficient charge separation and to a longer lifetime of excitons in this polymorph, which are bound states of an electron and a hole in a semiconductor, formed by Coulomb attraction and capable of transporting energy without charge[96]. In particular, using epitaxial TiO_2 films of anatase and rutile polymorphs, photocatalytic activity was analyzed as a function of the thickness of the film. In anatase, activity increases up to ≈5 nm thickness, whereas rutile reaches peak activity at ≈2.5 nm, indicating that charge carriers generated deeper in the bulk contribute more to surface reactions. Moreover, anatase has been observed to exhibit higher photocatalytic activity than rutile across various reaction media, particularly in the presence of oxygen as an oxidizing agent, making it suitable for many diverse photocatalytic processes[94]. This applies also for water splitting, with different studies investigating the possible use

172

of anatase TiO_2 as photocatalyst for hydrogen production. Damkale et. al.[365] synthesized porous anatase nanocuboids with specific surface areas in the range of 85.7-122.9 $m^2 g^{-1}$ via hydrothermal method, and assessed their photocatalytic performance for H_2 production through water splitting under UV-Vis light, comparing it with commercial titania. These nanocuboids showed significantly higher photocatalytic activity (3866.44 μmol h^{-1} g^{-1}) compared to commercial anatase (831.30 μmol h^{-1} g^{-1}), which was attributed to their high crystallinity, specific surface area, and more efficient charge separation. Another important aspect in the design of semiconductors for water splitting is represented by the suppression of charge recombination, which represents a significant source of energy loss that reduces the quantum yield of the entire photocatalytic process[366,367]. A possible strategy in this sense consists in doping the material with other elements, both metals and non-metals, as this can modify the electronic structure of TiO_2, extending its light absorption into the visible spectrum and improving charge carrier dynamics by enhancing the formation of oxygen vacancies and the lifetime of electrons and holes[368,369]. Different dopants introduced into the titanium dioxide's lattice determine different effects on the material's properties, as they can induce modifications in its electronic structure, surface chemistry, band gap, and crystallinity. In fact, doping induces impurity states that alter the electronic structure of TiO_2, enhancing visible-light absorption and influencing water adsorption and dissociation mechanisms. The effectiveness of doping depends on factors like dopant concentration, electronic configuration, and distribution within the TiO_2 lattice[370]. A number of studies are available in literature regarding acceptor and donor doping of titanium dioxide for photocatalysis. Umezawa et. al.[371] showed that in nitrogen-doped TiO_2 the hybridization of nitrogen p-states with titanium d-states creates defect-impurity bands near the valence band edge, reducing the band gap to ≈2.4 eV, and thus facilitating visible-light-driven photocatalysis. Moreover, nitrogen-doped TiO_2 formed stable complexes that eliminated hole-trapping centers, also enhancing charge migration and photocatalytic activity under visible light. Other studies address the effect of doping titanium dioxide on properties such as acidity and hydrophilicity.

Among them, Tang et. al.[372] showed how vapor-phase fluorination of TiO_2 single crystals enhanced its surface acidity due to formation of surface hydroxyl radicals, making the material more hydrophilic. Moreover, surface fluorination enhanced its photocatalytic activity without altering its bulk crystal structure or its optical absorption, in agreement with another study on the enhanced photocatalytic efficiency of fluorine-doped TiO_2 carried out by Dozzi et. al.[373]. On the other hand, doping with metals such as Fe, Cr and Pt have also been shown to stabilize the anatase phase and reduce the band gap energy, enabling visible-light absorption[370]. Donor dopants such as Nb, Ta and W stabilize the anatase phase and introduce Ti^{3+} centers, making TiO_2 an n-type semiconductor[370,374,375], while acceptor dopants such as Fe, Co and Cr introduce holes and enhance p-type conduction[271,376,377]. Yue et. al.[157] synthesized mesoporous Nb-doped TiO_2 thin films and showed that doping with Nb^{5+} improved conductivity and charge storage mechanisms by altering the band structure and carrier concentration, suppressing charge recombination and enhancing photocatalytic activity. Moreover, the creation of oxygen vacancies through Fe-doping of TiO_2 nanoparticles was also shown to improve charge separation and suppress charge recombination, as shown by Khalid et. al.[378], translating in enhanced catalytic efficiency. The presence of oxygen vacancies is also critical for enhancing the photocatalytic performance of anatase TiO_2 in water splitting, as they improve visible-light absorption by narrowing the bandgap and creating mid-gap states, which enhance charge carrier generation and separation[368,379]. Additionally, oxygen vacancies promote the formation of Ti^{3+} sites, which facilitate the migration of photogenerated electron-hole pairs[380,381]. For these reasons, the concentration and distribution of these vacancies are key factors influencing anatase efficiency in hydrogen production[50]. The photocatalytic activity of TiO_2 is also influenced by factors such as porosity and crystallinity of the material[382]. The porosity of a heterogeneous catalyst plays a significant role in enhancing its photocatalytic performance, and that is also valid for TiO_2. A porous structure increases the specific surface area of the photocatalyst, providing more active sites for the adsorption and reaction of water molecules[383], as well as improving charge carrier dynamics[384–386].

Furthermore, porous TiO$_2$ facilitates better separation of photogenerated electron-hole pairs, reducing recombination rates and increasing the efficiency of the photocatalytic process[383]. Porous structures also showed to be relevant in enhancing charge transport and providing abundant active sites for improved catalytic water splitting performances both in the cases of hydrogenated TiO$_2$/SrTiO$_3$ porous microspheres[387] as well as single crystalline-like TiO$_2$ monoliths[388]. Among the few studies on the analysis and characterization of pure and doped water-titania interactions available in the literature, most of them either involve theoretical or mixed theoretical/experimental studies[389–393], or work on ideal systems such as thin films[394–397]. An example of the first category is a study by Huang et. al.[390], who employed molecular dynamics simulations to examine how water interacts with five distinct titanium dioxide surfaces, including rutile (011), rutile (110) and anatase (001). The simulations revealed that water dissociated on most surfaces, forming Ti–OH and O-H reactive groups, and showing how reactive surfaces facilitated hydrogen bonding and influenced the orientation of water molecules near the surface. Vittadini et. al.[393] also used density functional theory (DFT) to investigate water adsorption on TiO$_2$-B surfaces, a metastable polymorph of titanium dioxide with a monoclinic crystal structure. They observed dissociative adsorption on the (100) surface, while mixed molecular/dissociative adsorption occurred on (010) and (110). Moreover, high-temperature desorption altered surface terminations, explaining why surface hydroxyls were not fully regenerated after heating and cooling cycles. Moving to TiO$_2$ films, Kuźmicz-Mirosław et. al.[396] investigated the effects of various surface treatments – oxygen plasma, UV light, and hydrogen peroxide (H$_2$O$_2$) – on the morphological properties and on the wettability of titanium dioxide thin films. Oxygen plasma and UV treatments were found to significantly enhance the hydrophilicity of the films, reducing water contact angles to approximately 10°, thereby creating superhydrophilic surfaces. Plasma treatment was also particularly effective in generating stable hydroxyl groups and smoothing the surface, while UV activation primarily removed organic contaminants, contributing to sustained hydrophilicity. In contrast, H$_2$O$_2$ treatment resulted in less pronounced hydrophilic

behavior, with contact angles around 58°, and its effects were unstable over time due to the formation of peroxy-complexes with minimal chemical changes. Plasma and UV-treated surfaces demonstrated long-term and stable water wettability, making them promising for applications requiring durable hydrophilic properties, and underscoring the importance of selecting appropriate activation methods to optimize surface properties for specific functional applications. In another study, doped titanium dioxide thin films were synthesized by Mardare et. al.[397] using RF sputtering and pulsed-laser deposition (PLD) on substrates like indium tin oxide-coated glass (ITO) and strontium titanate (STO). Iron doping lead to an increase in the anatase phase, particularly on ITO substrates, and PLD films on STO showed the presence of pure anatase with larger grain sizes. Higher surface roughness in PLD films improved hydrophilicity, measured by reduced water contact angles under UV-light. Fe-doped ITO films also exhibited superior hydrophilic properties and faster UV activation, making them suitable for photocatalysis and self-cleaning applications. Despite these findings on titania-water interactions, there is limited research in the literature focusing on the systematic study of the interactions between water and mesoporous anatase TiO_2 powders. This is notable given that mesoporous materials are extensively used in heterogeneous photocatalysis due to their high surface area and adjustable pore sizes, which play a crucial role in water adsorption, dissociation, and subsequent catalytic processes. Therefore, addressing this gap is crucial for improving the design of mesoporous TiO_2 materials tailored for enhanced water-oxide interactions and catalytic performance.

For these reasons, in **Chapter 8**, the systematic analysis of the surface interactions between water and mesoporous anatase TiO_2 powders has been conducted. An optimized synthesis route for the production of pure TiO_2 with different porosities and thus with different amounts of hydroxyl groups on the surface and their comprehensive characterization was carried out, together with the analysis of titania-surface interactions by water vapor physisorption. Such measurements have also been conducted after the modification of the surface acidity by defect formation through extrinsic doping of porous anatase with Nb^{5+} and Fe^{3+}. Moreover, additional

techniques for inducing the formation of oxygen vacancies on the surface included electrothermal and photo-thermal treatments, for pure and doped materials. The interaction between modified titanium dioxide surfaces and water was also in this case analyzed by measuring water vapor physisorption coupled with FT-IR spectroscopy, in order to monitor the evolution of surface hydroxyl groups, responsible for changes in surface hydrophilicity.

The results of this chapter have been collected within the framework of the research group "Control of the special properties of water in nanopores", a project that was part of the State Research Funding Hamburg 2020 and that has been funded by the Hamburg Authority for Science, Research and Equal Opportunities. The consortium of different research groups that collaborated to the project included the research groups of Prof. Dr. Simone Mascotto (Universität Hamburg), Prof. Dr. Michael Fröba (Universität Hamburg), Prof. Dr. Michael Steiger (Universität Hamburg), Prof. Dr. Nils Huse (University of Hamburg), Prof. Dr. Patrick Huber (Technische Universität Hamburg Harburg) and Dr. Felix Lehmküler (Deutsches Elektronen Synchrotron).

8.2 Results and discussion

8.2.1 Pure TiO$_2$

8.2.1.1 Mesoporous anatase TiO$_2$

All materials were synthesized according to the synthesis procedure reported in **Subsection 10.2.3** of the **Experimental Methods** chapter. This procedure was first used for the synthesis of the reference mesoporous TiO$_2$ powder, which having been calcined at 400 °C will henceforth be referred to as 'TiO$_2$-400'.
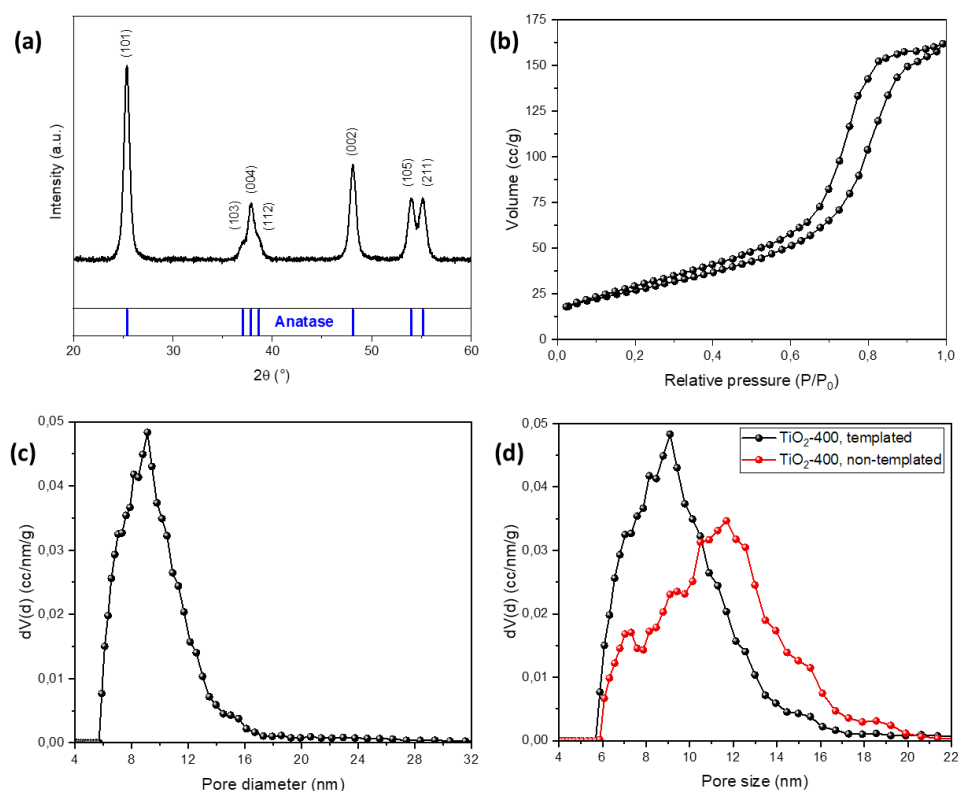
Figure 66. (a) XRD diffractograms of the pure as-synthesized TiO$_2$-400 anatase powder. (b) N$_2$-physisorption isotherms and (c) DFT pore size distribution of TiO$_2$-400. (d) DFT pore size distributions of TiO$_2$-400, comparing the synthesis with and without the organic template.

The XRD powder diffractograms of TiO$_2$-400 show the presence of pure, crystalline anatase titanium dioxide (**Figure 66a**), with an average crystallite size calculated with Scherrer equation from the FWHM of the (101) reflection of 15 nm. The type IV N$_2$-physisorption isotherm of TiO$_2$-400 (**Figure 66b**) confirms that mesoporous

titania was obtained, with a BET specific surface area (SSA) of 100 m^2/g. The relatively narrow DFT pore size distribution (PSD) of the material, reported in **Figure 66c**, corresponds to values of the average pore diameter and total pore volume of 9 nm and 0.24 cc/nm/g, respectively. A confirmation of the templated structure of TiO_2 can be inferred from the PSD of the material synthesized with same synthesis procedure but without the presence of the template, which is considerably less regular and less homogeneous than the PSD of the templated material (**Figure 66d**), attesting the presence of an ordered mesoporous network[223]. Finally, additional RAMAN and UV-Vis spectroscopy measurements also confirmed the phase purity of the synthesized materials (**Figure A18** in the Appendix).

8.2.1.2 Effect of the concentration of surface –OH groups
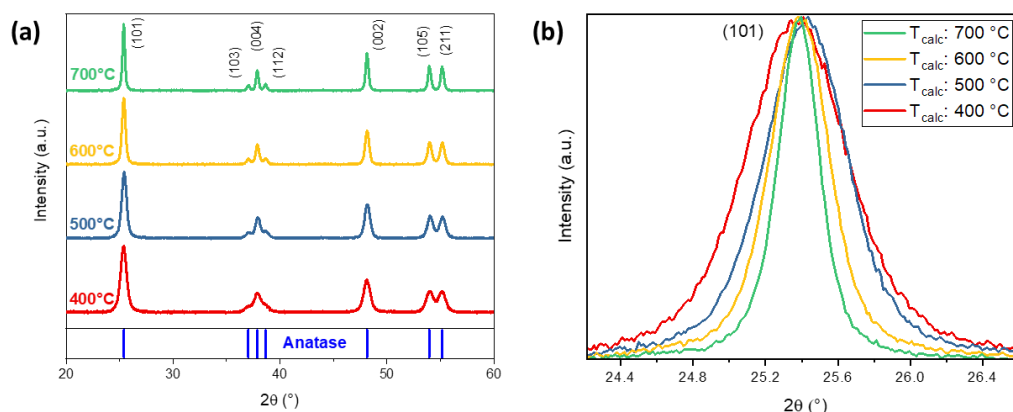
Figure 67. (a) XRD diffractograms of the pure as-synthesized anatase powders, with (b) magnification on the (101) reflection, highlighting the increase in crystallite size with increasing calcination temperature.

In order to tailor the concentration of hydroxyl groups (–OH) on the surface of the synthesized TiO_2, and so its Brønsted acidity, the materials have been calcined at increasing temperatures of 400 °C (TiO_2-400), 500 °C (TiO_2-500), 600 °C (TiO_2-600) and 700 °C (TiO_2-700). The XRD powder diffractograms of the pure TiO_2 calcined at different temperatures show the presence of pure, crystalline anatase titanium dioxide powders (Figure 67**a**). A focus on the (101) reflection reveals a broadening of the reflection, indicating a gradual growth of the crystallite size, as calculated from

the Scherrer equation (Figure 67**b**). The crystallite size increases from 15 nm at T_{calc} = 400°C and 18 nm at 500°C, to 27 nm at 600°C, reaching 40 nm at 700°C.
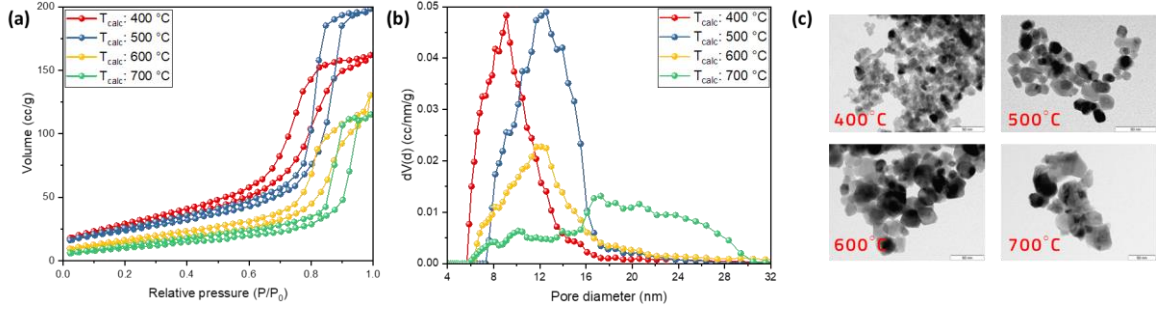
Figure 68. (a) N_2-physisorption isotherms and (b) DFT pore size distribution of the pure TiO_2 samples calcined at different temperatures. (c) TEM micrographs of TiO_2 calcined at increasing temperatures.

The nitrogen-physisorption results reported in **Figure 68a** underline the obtainment of mesoporous titania, as can be seen from the type IV isotherms of the materials. The values of the BET specific surface areas space from 100 m^2/g, obtained at a calcination temperature of 400°C, down to 39 m^2/g at 700°C. According to these results, it is clear that the morphology of the materials can be significantly altered by simply varying the calcination temperature. Specifically, different calcination temperatures result in different specific surface areas, due to variations in diffusion rates and mass transport phenomena within the material. At lower calcination temperatures, such as 400 °C and 500 °C, diffusion is limited, which minimizes atomic migration and helps preserve the mesoporous structure. As a result, higher SSA values are observed, since the pores remain intact and crystallite sintering is avoided. Conversely, increasing the calcination temperature to 600 °C and 700 °C enhances atomic diffusion due to the higher thermal energy. This promotes particle coalescence and grain growth, leading to the collapse of the mesoporous framework and a consequent reduction in SSA[398,399]. No phase transition from anatase to rutile was observed with increasing calcination temperature, resulting in anatase titania with varying porosities. As the calcination temperature increases, different pore size distributions are obtained: tighter PSDs with smaller average pore sizes are seen at 400 °C and 500 °C, while wider PSDs are observed at 600 °C and 700 °C (**Figure**

68b). This behavior can be attributed to the fact that more porous structures tend to exhibit tighter and more uniform pore size distributions, resulting from the retention of a controlled and regular pore network. In fact, at calcination temperatures of 400 °C and 500 °C, limited atomic diffusion helps preserve this templated framework, leading to smaller average pore diameters and consistent distributions, as the uniform pore structure remains intact. In contrast, at 600 °C and 700 °C, enhanced atomic diffusion promotes sintering and grain growth. This results in broader and more irregular pore size distributions, as structural rearrangements driven by increased mass transport occur unevenly throughout the material. Consequently, the original templated architecture is disrupted, leading to the formation of non-uniform pores[400–402]. The mesoporous structure of the materials is also confirmed by TEM measurements (**Figure 68c**). An overview of the values of BET specific surface areas, pore size distributions and total pore volume of the materials is reported in **Table 7**.

Table 7. Values of the BET specific surface area, average pore size and DFT total pore volume for pure TiO_2 samples calcined at increasing temperatures.

Calcination temperature (°C)	SSA (m²/g)	Average pore size (nm)	Total pore volume (cc/nm/g)
400	100	9	0.24
500	87	12	0.30
600	52	13	0.18
700	39	17	0.17

Such a variety of different specific surface areas and PSDs allows for the tuning of the concentration of surface hydroxyl (–OH) groups of titanium dioxide, and so of its Brønsted acidity, through adjustments of the calcination temperature. At lower calcination temperatures, such as 400 °C, the removal of water molecules and hydroxyl groups from the surface is minimal. Combined with the higher specific surface area, this provides more active sites for hydroxyl group formation. In contrast, at higher temperatures, such as 700 °C, the specific surface area decreases due to sintering and particle growth, leading to fewer available surface hydroxyl sites.

Moreover, increased thermal desorption and condensation reactions at elevated temperatures promote the elimination of hydroxyl groups, either by releasing them as water or by forming Ti–O–Ti bonds, resulting in a notable reduction in surface hydroxyl density[403–405]. Overall, the presence of surface –OH groups is known to be of fundamental importance in describing the surface interactions of titania with water for applications in photocatalysis[19,396,406].
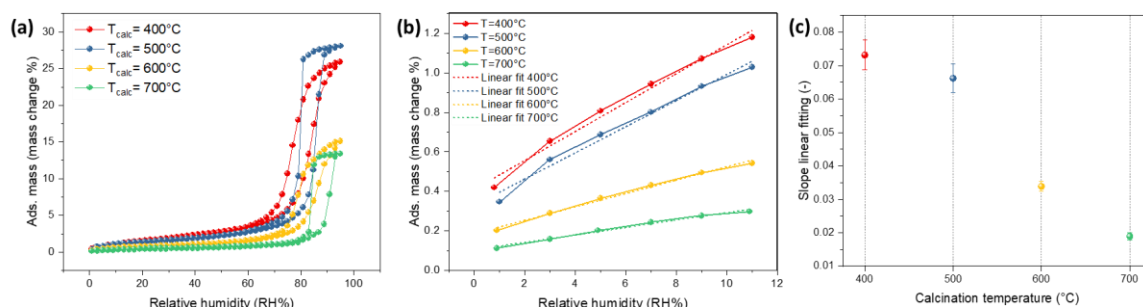

Figure 69. (a) Gravimetric H_2O-physisorption isotherms of the pure TiO_2 samples calcined at different temperatures. (b) Plot of the slope of the linearized curves, focusing on the 0–12% relative humidity region, for the pure TiO_2 samples at increasing calcination temperatures. (c) Slopes of the linearized adsorption curves at low pressure for TiO_2 at different calcination temperature.

The interactions between water and the material's surface were evaluated via water vapor physisorption (**Figure 69a**), with the results attesting the obtainment of physisorption isotherms that can be classified between type IV and type V. This is due to the scarce hydrophilicity of titania, when compared for example with silica[223], and reflects a mesoporous material with heterogeneity in pore geometry and surface sites that interact weakly with adsorbates[407]. The shape of the physisorption curves indicates a more consistent water uptake with larger porosities, with capillary condensation occurring at lower relative humidity (RH) for the most porous samples. As the specific surface area decreases, the onset of capillary condensation shifts to higher RH values. This behavior is linked to the fact that a lower SSA, resulting from the formation of larger crystallites at higher calcination temperatures, promotes the condensation of Ti–O–Ti units in titanium dioxide. Consequently, this leads to a reduction in surface –OH groups and a less hydrophilic TiO_2 surface. However, no

studies are available in the literature for direct comparison with these findings, as the research on water vapor physisorption in metal oxides with comparable systems has primarily focused on porous silica[228,408]. Oh et. al.[408] investigated water physisorption on ordered mesoporous silicas with varying pore sizes (2–10 nm) and shapes, observing type V water isotherms with a hysteresis loop. Similar to the findings of this research, the capillary condensation uptake in their study depended on pore size. These results are comparable to those of Naono et. al. on MCM-41[409]. Another insight into water interaction is provided by the study of the onset of water adsorption, which occurs at low relative humidity, in the range of 0 to 12% RH. The initial part of the adsorption branch, in terms of relative humidity, corresponds to the formation of the first monolayer of adsorbate molecules on the surface. During this stage, adsorption is primarily driven by strong interactions, such as hydrogen bonding, between the water vapor and the adsorbent surface[410]. At low RH, adsorption primarily occurs on high-energy sites, such as hydroxyl groups, reflecting the material's hydrophilicity. As can be seen from **Figure 69b** and **Figure 69c**, the trend of the linearized adsorption curve at low RH aligns with that of capillary condensation, showing larger water uptake for TiO_2-400 and TiO_2-500. This indicates a higher number of surface –OH groups available in these materials. The exact values of the slope of the adsorption branch at low RH obtained through linear fitting is reported in **Table 8**.

Table 8. Slopes resulting from the linear fitting of the $P/P_0 < 0.3$ region of the water adsorption branches, for all of the pure TiO_2 materials calcined at increasing temperature.

Calcination temperature (°C)	Slope linear fitting (-)
400	0.0732± 0.0044
500	0.0662± 0.0043
600	0.0338± 0.0014
700	0.0189± 0.0010

From the linear fit of the curves in this region and from the trend of the slope at varying calcination temperatures it is possible to comment on the heat of water

adsorption of the process. The heat of adsorption, assuming BET adsorption model, is a complex quantity, depending mostly from the adsorption of the monolayer of water on the TiO_2 surface and therefore being representative of the surface chemistry of the material. In order to calculate it, several water physisorption measurements at different temperatures should be conducted, taking also into account the isosteric heat of adsorption and applying the Clausius-Clapeyron equation[411,412], which is not the main interest of this analysis. However, to obtain a qualitative estimate of it, a linear fit of the adsorption isotherms at low partial pressures was performed for the different materials. The results show a gradual decrease of the slope of the linearized adsorption branch (**Figure 69c**), meaning a weaker gas-solid interaction with decreasing porosity of the materials. The steeper slope in this region indicates that the material adsorbs water more readily at lower RH levels, suggesting a higher heat of adsorption and an initial uptake of water molecules, as well as a greater density of surface hydroxyl groups. This was further confirmed by ATR-IR spectroscopy conducted on pure TiO_2 synthesized at different temperatures, with focus on the 3900 to 3000 cm^{-1} wavenumber range (**Figure 70**).
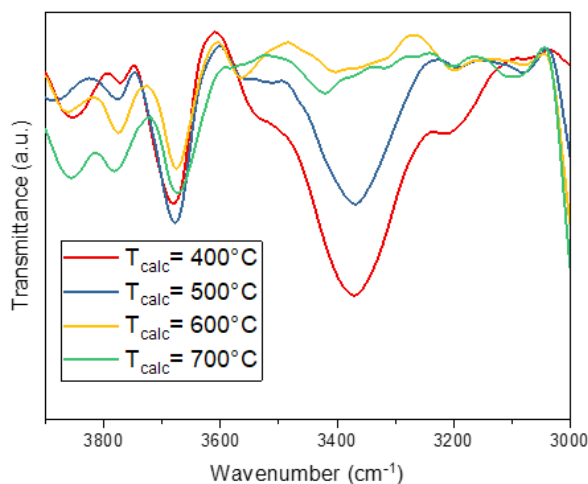
Figure 70. FT-IR spectra of pure TiO_2, with focus on the 3900-3000 cm^{-1} region.

A gradual decrease in the intensity of the signal is observed with increasing calcination temperature of the titania powder, indicating a reduction in the amount of surface –OH groups. This decrease in signal intensity coincides with enhanced

hydrogen bonding among –OH groups, which can cause a shift to lower wavenumbers, as well as an increase in the intensity of the –OH stretching vibration[413], and therefore in the concentration of surface –OH groups[414,415]. More specifically, Mino *et. al.*[416] conducted a combined theoretical and experimental analysis to examine the location, chemical environment, and vibrational characteristics of –OH groups attached to the surface of titania nanoparticles. By comparing the FT-IR spectra of three different anatase-based TiO_2 samples, the broad IR signals in the 3600–3000 cm^{-1} range can correspond to both hydrogen-bonded –OH groups and water, while the signals in the 3700–3600 cm^{-1} range were primarily attributed to isolated hydroxyl groups bound to individual titanium atoms and not involved in hydrogen bonding, whose signal has constant intensity independently from the material[416]. In the case of this study, the hydrogen bonded hydroxyl groups increase in number with increasing porosity of TiO_2 (i.e. with decreasing calcination temperature). Instead, the amount of isolated –OH species remains constant, since they are intrinsic to the surface chemistry of titanium dioxide and are less affected by changes in pore structure or surface area, unlike hydroxyl groups involved in hydrogen bonding or located in mesopores. These results align with the observation that a decrease in surface area leads to a reduced availability of hydroxyl groups, and consequently to a lower tendency for water to form dissociative and molecular bonds on the surface of titania.

8.2.1.3 Electro-thermal treatments of pure TiO₂

Electro-thermal treatments, such as electric field-assisted sintering, are advanced methods for processing metal oxides like titanium dioxide. These techniques use electric fields to speed up sintering in the materials, allowing them to densify and form surface defects at lower temperatures when compared to traditional methods. This is because electric fields cause localized heating, enhancing grain boundary diffusion and creating defects in the material, such as oxygen vacancies and Ti^{3+} species in the case of electro-thermal treated titanium dioxide[417]. These defects reduce the bandgap and improve visible light absorption, resulting in the 'blackening' of the

material, and possibly acting as active sites for photocatalytic and electrocatalytic reactions[418]. These treatments find applications in water-related electrocatalysis, since electro-thermally induced defects can play a role in modifying the interaction between water molecules and the oxide surface. In fact, oxygen vacancies and Ti^{3+} species enhance water adsorption, facilitating the dissociation of water molecules and the formation of surface hydroxyls, and possibly improving the transfer of electrons during catalytic reactions. These properties are particularly beneficial for processes such as water splitting, hydrogen evolution, and oxygen evolution reactions (OER)[419,420]. Therefore, in order to systematically investigate the effect of electro-thermally induced defects on titania wettability, the pure titania materials have been electro-thermally treated according to the experimental protocol reported in **Subsection 10.4.3** of the **Experimental Methods** chapter. These consisted in the application of an electric field at high temperature under low oxygen partial pressure. All materials after electro-thermal treatment all showed an effect of blackening (**Figure A19** in the Appendix), related to the formation of Ti^{3+} species and oxygen vacancies $(V_O^{\cdot\cdot})$[418,421–424], which form according to **Equations 37** and **38**, expressing the defect equations in Kröger-Vink notation:

$$O_O^x \leftrightarrow V_O^{\cdot\cdot} + 2e' + O_2 \tag{37}$$

$$O_O^x + Ti_{Ti} + e' \leftrightarrow O_O^x + Ti'_{Ti} \tag{38}$$
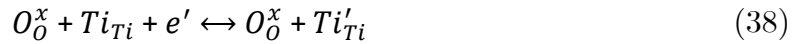
Considering the XRD results, a focus on their (101) reflections before and after electro-thermal treatments are reported in **Figure 71**, showing how for calcination temperatures greater than or equal to 500 °C the treatment was accompanied by a shift in the (101) reflection to the left, representative of an expansion of the lattice parameter. In particular, its value increases from 4.93 Å to 4.94 Å for all of the pure titanium dioxide materials, i.e. TiO_2-500, TiO_2-600 and TiO_2-700. This could be accounted for by the substitution in the Ti^{4+} sites from Ti^{3+} sites: since the Ti^{3+}

species, which are reported to form upon electrochemical reduction, have a larger ionic radius (67 pm, against the 60.5 pm of Ti^{4+} species[425]) due to a lower amount of valence electrons and therefore to the increased effective nuclear charge, their substitution in the titanium dioxide lattice determines a lattice contraction, expressed by the leftward shift of the (101) reflection of TiO_2. Moreover, the formation of oxygen vacancies may contribute to the lattice expansion of titania, since the removal of oxygen ions reduces electrostatic repulsion and alters the local electronic environment around the oxygen vacancies, increasing the effective ionic radius of nearby cations and causing the lattice to expand[426].
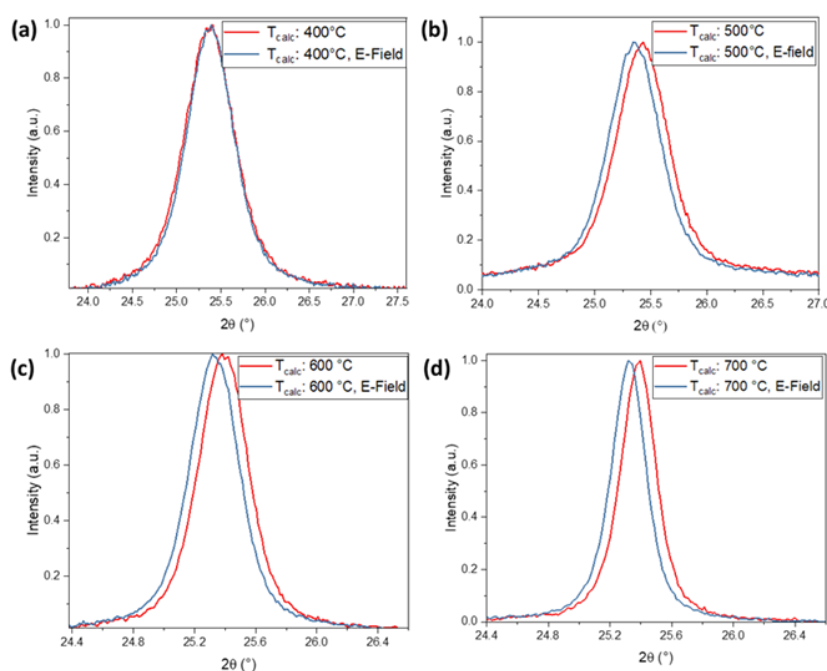
Figure 71. (101) reflection from XRD of the pure anatase materials calcined at 400 °C (a), 500 °C (b), 600 °C (c) and 700 °C (d), before and after electro-thermal treatments.

This effect is not present in the most porous of these materials, namely in TiO_2-400 after electro-thermal treatment. This result be explained by the conduction dynamics within porous ceramics such as anatase, which varies according to their porosity: since X-ray diffraction is a measurement representative of the bulk of the material, a certain crystallinity is necessary to observe a significant change in the reflection

position. Being the material in the case of TiO$_2$-400 nanostructured, and having therefore a larger surface area, surface conduction will have a greater impact than bulk conduction in the material, which translates in missed shift of the (101) reflection. Therefore, the shift in the main reflection is larger when the charge bulk conduction is larger, considering the materials post-electrothermal treatment[427]. A scheme representing the two mechanisms of conduction at different porosities is represented in **Figure A20** in the Appendix.
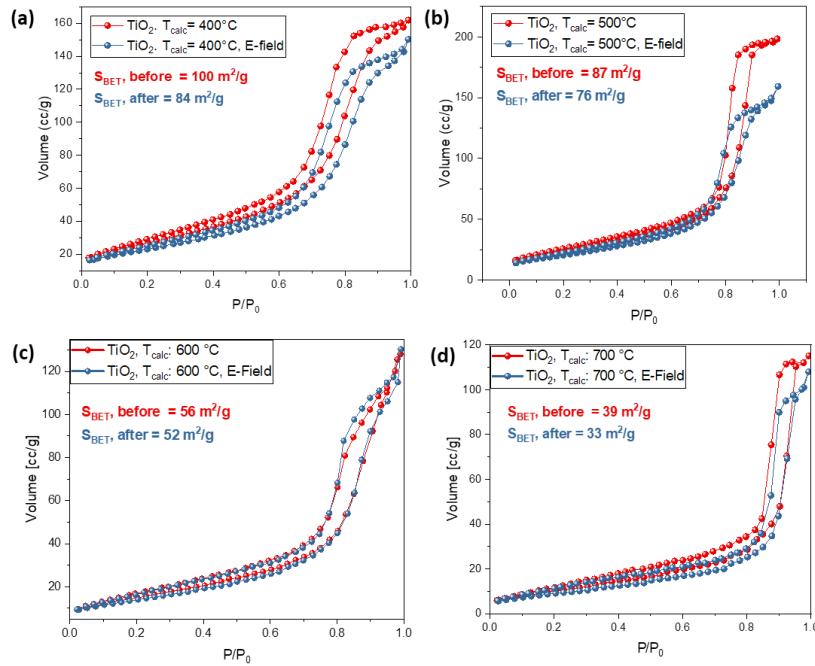
Figure 72. N$_2$-physisorption isotherms of (a) TiO$_2$-400, (b) TiO$_2$-500, (c) TiO$_2$-600 and (d) TiO$_2$-700, before and after electro-thermal treatment.

Considering the N$_2$-physisorption results reported in **Figure 72**, all materials retained type IV isotherms[223], typical of mesoporous materials, and showed a slight variation in the shape of the isotherm after the treatment. This is probably due to partial sintering of the specimen when subjected to high temperatures and in the presence of an electric field, which also determines a decrease in the SSA. This effect might be related to the larger mass transport favoring atomic diffusion, which accelerates the diffusion processes leading to faster densification and merging of neighboring titania nanocrystals[419,428], but also to the formation of defects enhancing

diffusivity because of localized high-temperature spots due to Joule heating associated with the application of the electric field[429,430]. A change is also observed in the DFT pore size distribution before and after electro-thermal treatment, as shown in **Figure 73**, where the values of the average pore size and total pore volume for each material are also reported for each material.
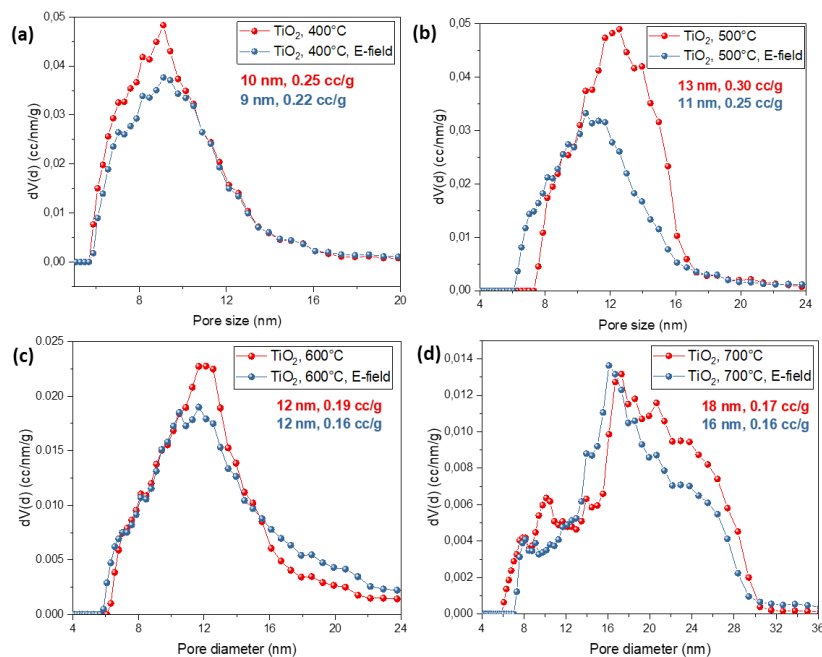
Figure 73. NLDFT pore size distributions derived from N_2-physisorption isotherms of the pure materials calcined at 400°C (a), 500°C (b), 600°C (c) and 700°C (d), before and after electro-thermal treatment.

In the case of TiO_2-600 and TiO_2-700, the PSD remained basically the same (**Figure 73c**), while TiO_2-400 and TiO_2-500 underwent a slight decrease in the average pore size. The reason for this decrease could be found in the grain growth induced by the partial sintering of the anatase crystallites because of the treatment[431], also determining a change in the shape and width of the pore size distribution, and highlighting how, during a modification of the surface with an electric field, a partial sintering of the material cannot be avoided. As in the case of pure materials and as part of the systematic analysis of the effect of these surface modification treatments on the water adsorption properties of titania, measures of water physisorption were

also conducted on the materials after electro-thermal treatment. Due to limitations in using the water physisorption apparatus caused by issues with the measuring instruments, only the gravimetric water-vapor physisorption results for TiO$_2$-500, TiO$_2$-600, and TiO$_2$-700 are reported in this chapter (**Figure 74**).
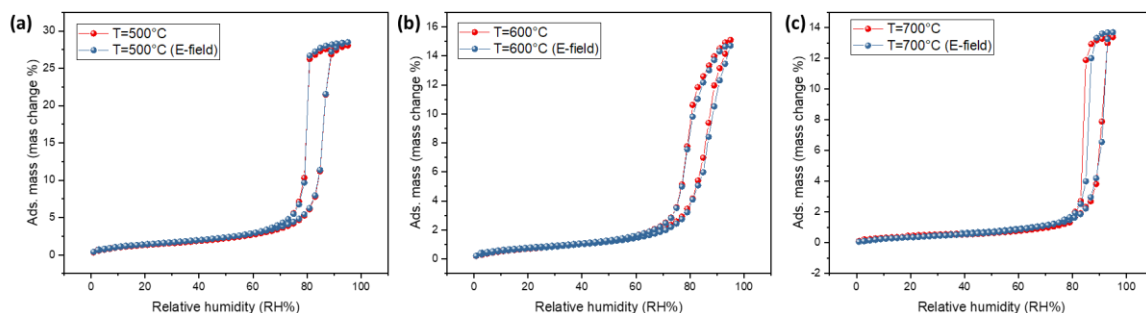
Figure 74. Gravimetric H$_2$O-physisorption isotherms measured at room temperature for TiO$_2$-500 (a), TiO$_2$-600 (b) and TiO$_2$-700 (c), before and after electro-thermal treatment.

It is noticeable how, before and after the electro-thermal treatment, no significant change in the shape of the physisorption isotherm is observed in the measured samples. This is also confirmed by the analysis of the isotherms in the region RH < 10%, which is indicative of monolayer formation on the material surface, and by the analysis of the heat of water adsorption, showing two practically overlapping or parallel adsorption branches (**Figure A21** in the Appendix), thereby suggesting that the adsorption mechanisms and surface interactions with the adsorbate are very similar before and after the treatments. The overlap of the two isotherms occurs despite some surface changes happening in the material due to defect formation, which are suggested by titania blackening, but also despite the drastic change in the material's PSD. Different reasons can be attributed to this behavior. For example, since water physisorption is a surface-specific measurement, surface modifications such as defects and vacancies at higher porosities (T$_{calc}$ < 500 °C) may not be in large enough quantity to result in a detectable difference in the water adsorption isotherms. Another possibility is that, at temperatures greater than 500 °C, SSA and porosity are too low to observe changes in the water physisorption curves.

Additionally, the possible formation of defects due to electro-thermal treatments might occur in the bulk of the material, as due to the application of an electric field the current flows through the crystallites and not on the crystallites. Another aspect to take in consideration is that, unlike nitrogen physisorption, being water a polar molecule, an increased complexity of the adsorption process has to be taken into account. These involve more complex mechanisms of surface adsorption such as hydrogen bonding and dipole-dipole interactions that lead to specific orientations of the molecules with the surface, making water adsorption behavior more intricate to predict and analyze[432,433]. Therefore, a technique such as water-vapor adsorption might not be sensitive enough to detect such slight modifications in the material surface, like the ones determined by electro-thermal treatments. A representative example of the limitations related to the sensitivity of the technique is that of the TiO_2-500 material, in which a drastic change in the pore size distribution is observed, which in addition to having a very different shape denotes a decrease in the total pore volume from 0.30 to 0.25 cc/g and an average pore size that goes from 13 to 11 nm after the treatment, but no change in the water physisorption isotherm.
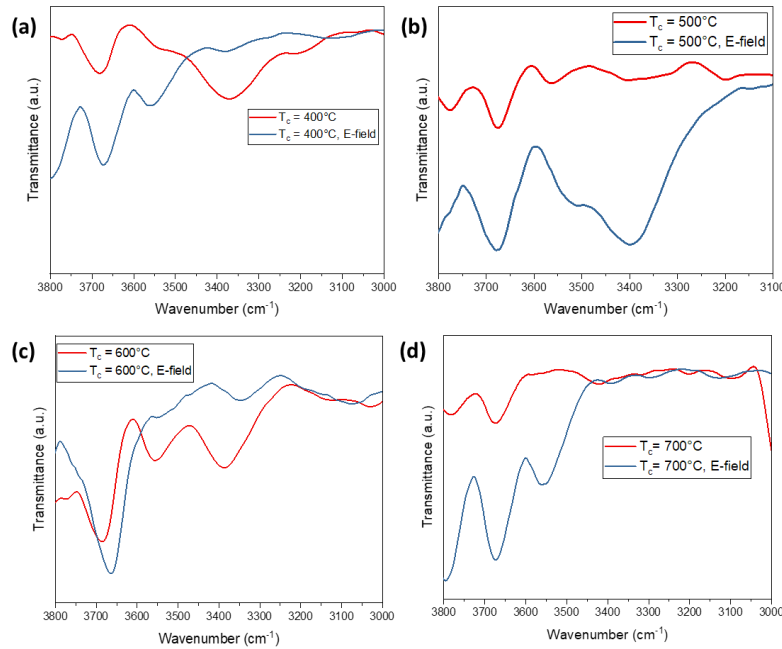
Figure 75. FT-IR spectra of TiO_2-400 (a), TiO_2-500 (b), TiO_2-600 (c) and TiO_2-700 (d), before and after electro-thermal treatment.

Therefore, as an additional technique for monitoring the amount of surface hydroxyls before and after the electro-thermal treatment, and to correlate the results with those of water-vapor physisorption, IR spectroscopy has been carried out on each of the electro-thermally treated samples. The results in **Figure 75** show a more pronounced intensity of the surface –OH stretching signal present in TiO_2-500 after the electro-thermal treatment, which should indeed coincide with improved surface wettability[414,415]. However, despite the changes recorded by nitrogen physisorption and FT-IR spectroscopy, no changes are observed in the water physisorption isotherms, either in the linear part of the curve at low relative humidity, which describe the heat of water adsorption, nor in hysteresis of the curves and in the onset of capillary condensation, leading to the conclusion that, by using water vapor physisorption as characterization technique, it is not possible to assess how electro-thermally induced surface modifications impact the water-TiO_2 interactions.

8.2.1.4 Photo-thermal treatments of pure TiO₂

The same starting materials as the previous section, i.e. the pure anatase powders calcined at different temperatures (TiO_2-400, TiO_2-500, TiO_2-600 and TiO_2-700), were subjected to photo-thermal treatments. These have gained significant attention in recent years due to their potential use in water splitting and water purification techniques, by making use of metal oxide photocatalysts such as TiO_2 for enhancing light absorption and charge recombination, exploiting the synergistic effect of thermal energy and UV-radiation[434–437]. Analyzing the effect of such treatments on the surface interactions between titania and water is therefore important for understanding how these catalysts can be optimized to address applications in sustainable energy processes and improving their catalytic efficiency. Therefore, the synthesized pure TiO_2 was subjected to photo-thermal treatments according to the experimental parameters described in **Subsection 10.4.4** of the **Experimental Methods** chapter. Studies available in the literature show these treatments to result in a

change in surface chemistry, particularly the formation of oxygen vacancies[438–441]. By way of example, Alyami[438] used X-ray Photoelectron Spectroscopy (XPS) analysis for revealing the presence of Ti^{3+} ions in the UV-treated samples, indicating the formation of oxygen vacancies. This modification led to a reduction in the bandgap from 3.20 eV to 2.95 eV, enhancing the photocatalytic activity of the TiO_2 films under natural sunlight irradiation. Another study by Hensling et. al.[439] confirmed the role of UV irradiation during pulsed laser deposition in the formation of oxygen vacancies in $SrTiO_3$ thin films. These vacancies, when present on the titania surface, lead to the formation of a greater number of surface hydroxyl groups, which form to reduce the overall surface energy[442], and thus lead to an increased hydrophilicity of the surface, as already demonstrated in past studies[443]. The mechanism that leads to their formation can be summarized according to **Figure 76**.
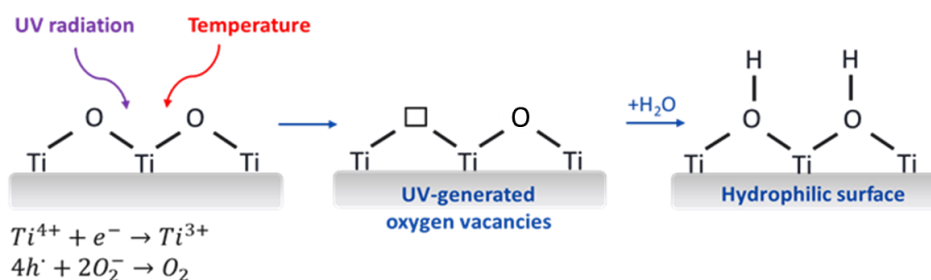
Figure 76. Mechanism of formation of surface oxygen vacancies and hydroxyl groups due to photo-thermal treatment of TiO_2.

Being TiO_2 a semiconductor with a band gap of approximately 3.2 eV[444], radiations in the UV range (meaning with $\lambda < 400$ nm) cause the formation of electron-hole pairs[83]. In fact, when titania is irradiated with UV light of energy equal to or greater than its band gap, electrons in the valence band are excited to the conduction band, leaving behind positively charged holes in the valence band and creating electron-hole pairs. The photogenerated electrons then migrate to the surface of TiO_2 and reduce Ti^{4+} to create Ti^{3+} centers[445], while the holes oxidize the lattice O^{2-} ions, leading to the oxygen release from the lattice and to the formation of oxygen vacancies[446]. As in the case of electro-thermal treatments, the formation of oxygen vacancies goes hand in hand with increased hydrophilicity of the surface, as water

molecules go to occupy the vacancies, leading to the formation of adsorbed surface hydroxyl groups (see **Figure 76**). Such increased hydrophilicity, in the case of the treatments conducted in this work, is also due to the presence of elevated temperatures during the treatments. Temperature can influence and accelerate the formation of oxygen vacancies[447]: in fact, an increased thermal energy allows for the easier diffusion of lattice oxygen atoms, and for an easier migration from their lattice positions due to the lower energy barrier to form oxygen vacancies, as well as for a more efficient formation of electron-hole pairs[448]. Therefore, the formation of such pairs can be accelerated by the presence of high temperatures, leading to a more pronounced surface modification. The results of X-ray diffraction (**Figure A22** in the Appendix) did not detect any change in the crystal structure of the materials. However, gravimetric water physisorption measurements underlined that in the case of the TiO_2-400 material (**Figure 77a**), which is the most porous sample and has the largest SSA (100 m^2/g), a clear change in the shape of the water physisorption isotherm after photo-thermal treatment is observed, with an earlier onset of capillary condensation compared to the untreated material. This change after the photo-thermal treatment is not detected in the materials with lower SSA (**Figure 77b-d**), in which all the isotherms have the same onset of capillary condensation and hysteresis cycle before and after the treatment.
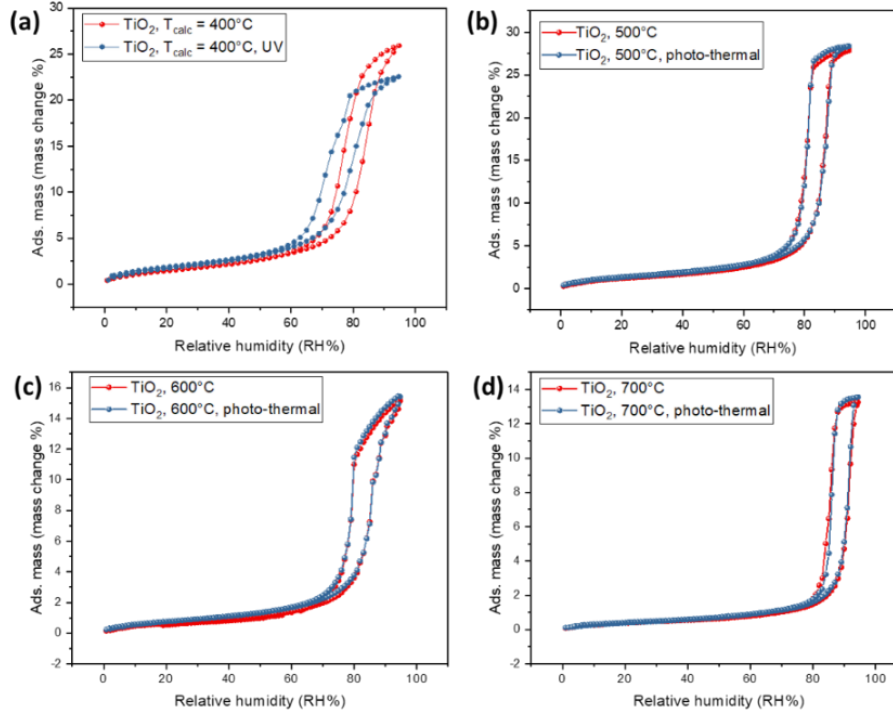
Figure 77. Gravimetric H_2O-physisorption isotherms measured at room temperature for TiO_2-400 (a), TiO_2-500 (b), TiO_2-600 (c) and TiO_2-700 (d), before and after photo-thermal treatment.

A possible reason for this could be related to the different SSA of the materials. In fact, since unlike electro-thermal treatments the UV treatments specifically involve only surface atoms, namely titanium and oxygen species, the possibility of having a surface modification, considering that the treatments were all carried out at the same temperature of 350 °C, is largely dependent on both the presence of surface oxygen species and to sufficient ion mobility, which allows for surface recombination during the treatment. Such conditions are most likely only met for the TiO_2-400 material, in which a large surface area allows for enough surface recombination and formation of an increased number of –OH groups, that will sum up to the ones initially available. Therefore, despite all the other experimental parameters being the same, the modification in the surface wettability only occurs for materials with large specific surface areas[449,450].
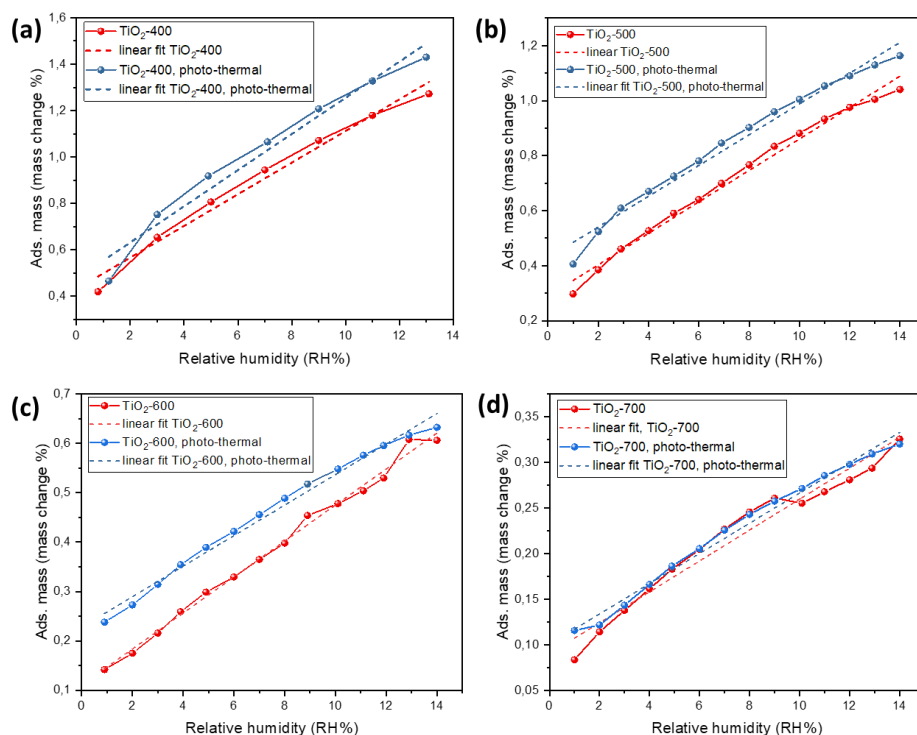
Figure 78. Water vapor adsorption isotherms with focus in the 0-12% RH region for the photo-thermally treated materials, i.e. TiO$_2$-400 (a), TiO$_2$-500 (b), TiO$_2$-600 (c) and TiO$_2$-700 (d).

Moving on to the analysis of the isotherms at low relative humidity, the results in **Figure 78** show two parallel adsorption isotherms, with a larger mass change after photo-thermal treatment observed in TiO$_2$-400 (**Figure 78a**), TiO$_2$-500 (**Figure 78b**), and TiO$_2$-600 (**Figure 78c**). This suggests a higher hydrophilicity due to hydroxils formation, while for TiO$_2$-700 no changes are observed. This is also in line with the results of FT-IR spectroscopy carried out on the materials before and after the photo-thermal treatments, shown in **Figure 79**, in which a signal attributable to surface –OH groups is present in materials calcined at 400 °C, 500 °C, and 600 °C, and not at 700 °C. These results again confirm how the SSA is a determining parameter in successfully modifying the surface chemistry of titania via photo-thermal treatments. This is due to the fact that at larger specific surface areas, i.e., at larger porosities, more radiation is absorbed and therefore more defects are formed. These defects induce the formation of a concentration of surface hydroxyl groups

that is large enough to induce a larger hydrophilicity of the TiO_2 surface, which is detected by water vapor physisorption measurements.
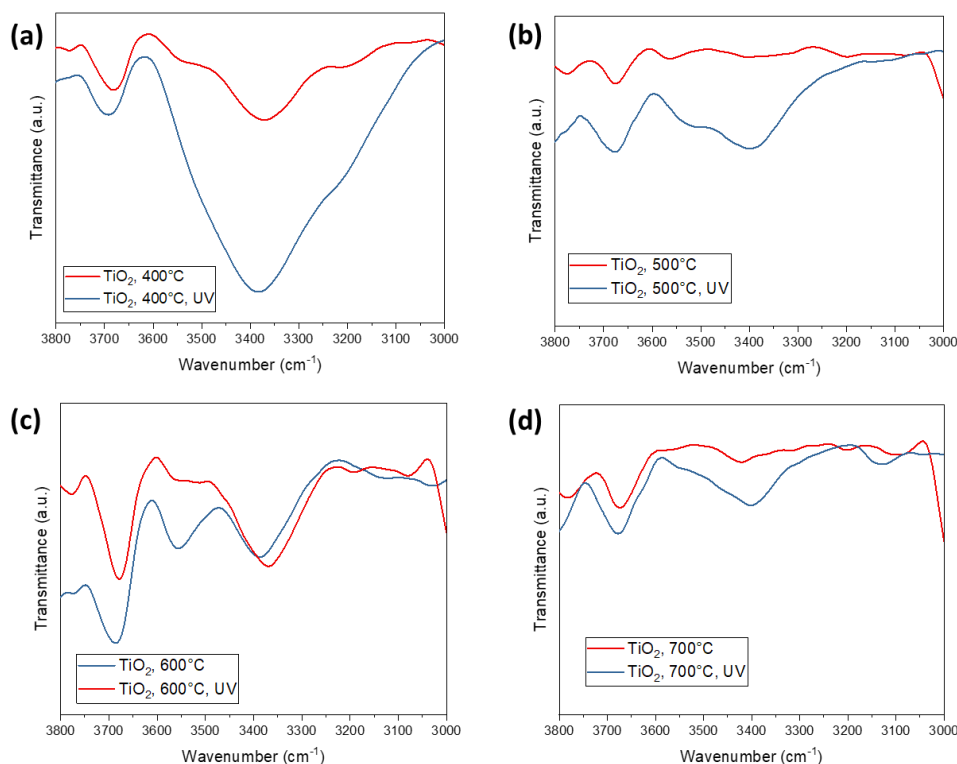
Figure 79. FT-IR spectra of TiO_2-400 (a), TiO_2-500 (b), TiO_2-600 (c) and TiO_2-700 (d), before and after photo-thermal treatment.

8.2.2 Doped mesoporous TiO_2

The surface chemistry and defect formation in the anatase powders was also modified through extrinsic doping of the materials with aliovalent transition metal ions. Doping is known to be a common technique for modifying the defect and surface chemistry of semiconductors such as titania[451–455]. Moreover, doping TiO_2 with bulk elements is a promising approach to enhance its ability to absorb visible light[455]. This improvement occurs through two main mechanisms: one is the narrowing of the band gap caused by shifts in the valence and/or conduction band edges, and the other is the creation of localized (trapped) states within the band gap[456]. Moreover, doping titania and other metal oxides such as $SrTiO_3$ with aliovalent transition metals is a well-established technique to enhance their photocatalytic performance in water

splitting, by introducing defects and modifying the electronic structure of TiO_2 in general, facilitating improved charge separation and light absorption[457–459]. In general, in the case of acceptor doping, elements with lower valency than titanium (e.g., Fe^{3+}, Co^{2+}) are inserted into the TiO_2 lattice and create charge imbalances, resulting in oxygen vacancies[460]. On the other hand, the incorporation of elements with a higher valency than titanium (e.g., Nb^{5+}, Ta^{5+}) introduces extra electrons into the TiO_2 structure that can occupy the conduction band, potentially reducing the material's band gap and enhancing its conductivity and photocatalytic activity[461].

In this work, the surface chemistry in terms of defect formation and surface acidity has been modified through doping of the starting reference material (TiO_2-400) with Nb^{5+} and Fe^{3+}. This has been carried out with an increasing nominal amount of metal doping of 1, 3 and 5%, following a synthesis procedure similar to that of pure titania. In the two different doping cases, two separate factors contribute to the change in the surface and bulk properties of the material. Nb and Fe determine a donor and acceptor doping of anatase, respectively, according to **Equations 39** and **40**, reported with Kröger-Vink notation:

$$Fe_2O_3\ (2TiO_2) \rightarrow 2Fe'_{Ti} + V_O^{\bullet\bullet} + 3O_O^X \tag{39}$$

$$2Nb_2O_5\ (5TiO_2) \rightarrow 4Nb_{Ti}^{\bullet} + V_{Ti}^{4\prime} + 10O_O^X \tag{40}$$
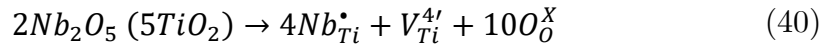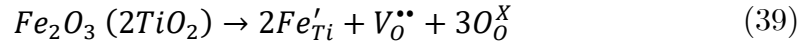
In the first case, the substitution of Ti with Nb at high oxygen partial pressures induces the formation of titanium vacancies $V_{Ti}^{4\prime}$, while in the case of iron-doping oxygen vacancies $V_O^{\bullet\bullet}$ are formed. These defects have an influence on the surface-water interaction between the terminal Ti and O groups on the titania surface and water molecules, because of the difference in surface polarity induced by modified surface charges. In the case of iron, the induction of positively charged surface oxygen vacancies typically leads to higher surface hydrophilicity in metal oxides[370,462,463]. However, because of the complexity of the mechanisms involved and due to the

discrepancy between nominal and effective doping concentrations related to the mild calcination temperatures involved, which make the incorporation of aliovalent metals in the TiO_2 more difficult, the phenomena in terms of defect formation are difficult to predict and most likely more complex, as other factors such as the overall surface acidity of the substitutional species should be taken into account. A broader perspective on the type of water-surface interaction that can take place on the titania's surface involves the focus on the presence of surface acid sites. These can be differentiated into Brønsted acid sites and Lewis acid sites. In the results discussed so far, Brønsted acidity has been taken into account when evaluating the hydrophilicity of pure titanium dioxide powders. A Brønsted acid is any species that can donate a proton to another species[464]. For a substance to act as a Brønsted acid, it must contain a hydrogen atom that can dissociate and be transferred as a proton. In the case of titanium dioxide, surface hydroxyl groups serve as potential positively charged Brønsted sites, where water molecules can adsorb through hydrogen bonding. Such sites are already present in pure, undoped titania, and their concentration – and thus the possibility of adsorption of surface water molecules – is linked to the porosity of the material, which is higher at lower calcination temperatures, because of the higher concentration of surface hydroxyl groups and thus a greater number of potential acid sites as surface interaction centers. In addition to the Brønsted sites provided by hydroxyl groups bonded to the surface oxygen atoms of titanium dioxide, Lewis acid sites are also present. These are metal sites on the surface that can accept an electron pair from a Lewis base. The Lewis acid sites on the surface of titania are provided by the coordinatively unsaturated Ti atoms present on the material's surface[465,466]. In the bulk structure of anatase, each titanium atom is coordinated to six oxygen atoms in an octahedral geometry. On the surface of titania, some titanium atoms are not fully coordinated, leading to surface unsaturation. These unsaturated titanium species can be either penta-coordinated or tetra-coordinated, and the strength of the Lewis acidity increases with the degree of titanium unsaturation. In fact, as the titanium atoms become more unsaturated, their ability to act as Lewis acids is enhanced, making them electron-deficient and more reactive towards

accepting electrons from the oxygen atoms of water. This increased reactivity leads to molecular or dissociative adsorption of water. As a result of these interactions, water molecules on the surface of titania undergo dissociation, forming hydroxyl groups (–OH) and protons (H$^+$), which are transferred to neighboring oxygen atoms[467–469]. When doping titania with aliovalent transition metals, in addition to the Brønsted acidity related to surface hydroxyl groups and the Lewis acidity of Ti atoms, the contribution to the overall Lewis acidity given by the incorporated Nb^{5+} and Fe^{3+} cations also should be taken into account, together with the consideration previously made regarding the effect of doping on the defect chemistry of TiO$_2$ (**Equations 39** and **40**). Regarding the donor and acceptor doping of titania, only a few studies are available on the impact of increasing concentrations of Fe^{3+} and Nb^{5+} as dopants in structural, optical and photocatalytic properties[461,470–473]. However, none of them address directly the dual effect of both defect chemistry and surface acidity of titania, induced with different methods, on the surface water-interaction level. In general, the doping of titania with Nb^{5+} modifies its surface Lewis acidity by increasing the number of surface Lewis acid sites, introducing electron-deficient centers. This increased Lewis acidity from Nb^{5+} doping affects titania-water interactions, enhancing the adsorption of water molecules and facilitating processes like hydrolysis and proton transfer[474,475]. Instead, the doping with Fe^{3+} induces changes in the Lewis acidity to a lesser extent than Nb^{5+}, due to its lower oxidation state. However, considering the defect **Equation 40**, the introduction of Fe as dopant in the anatase lattice leads to the subsequent formation of oxygen vacancies, which determine the formation of surface hydroxyl groups on the surface, increasing Brønsted acidity and therefore inducing more hydrophilic sites on the surface of the material[378,397,476]. All of these considerations lead to the conclusion that studying the effect of aliovalent doping with Nb^{5+} and Fe^{3+} on the interactions between water and titania is inherently complex, as it involves the interplay of multiple phenomena within the material that together influence its surface hydrophilicity.

Coming to the characterization of doped TiO$_2$, the materials synthesized are all pure and crystalline anatase phases, presenting no shift in the (101) reflection (**Figure A23** in the Appendix) and no side phases detected from X-ray diffraction measurements (**Figure 80a,b**).
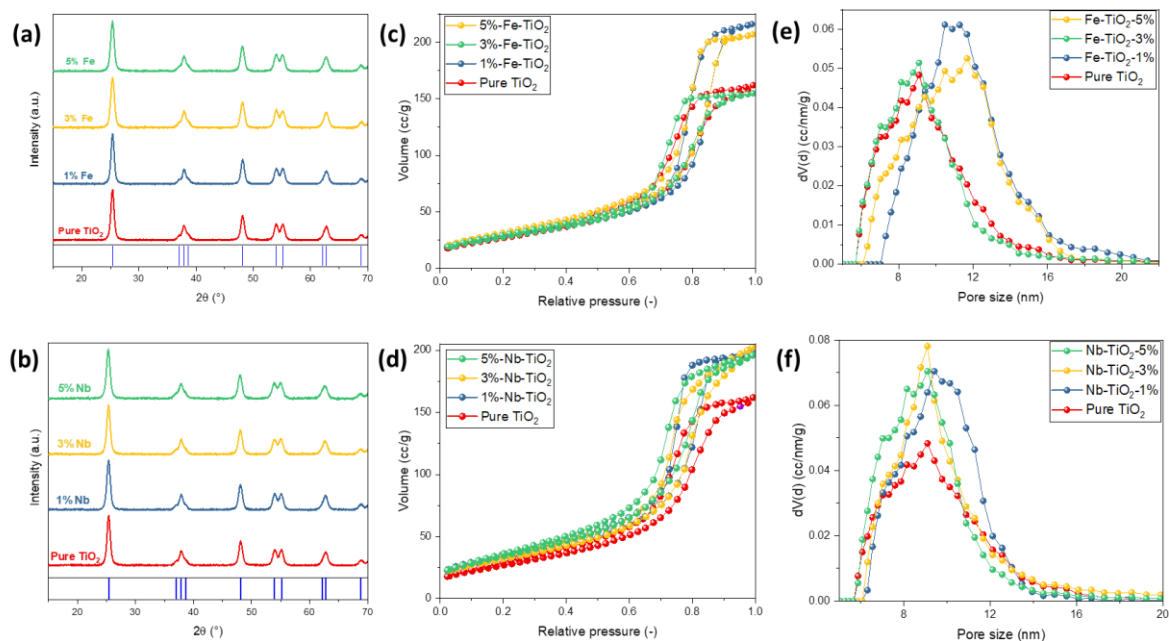

Figure 80. Powder diffractograms of the pure and (a) Fe-doped and (b) Nb-doped TiO$_2$ materials. N$_2$-physisoprtion isotherms and DFT pore size distributions of the Fe-doped (c, e) and Nb-doped (d, f) TiO$_2$ materials.

Different physisorption isotherms and DFT pore size distribution are observed, based on the type and amount of dopant inserted (**Figure 80c,f**), but without any trend observed. Because of the nanostructured nature of the materials themselves, it is not possible to make conclusions on the degree of incorporation of the dopants, since the broad reflections and the reduced peak intensity make it challenging to distinguish individual contributions from side phases[404,443]. In general, from these results it can be pointed out that, in the case of the synthesis of doped materials, the synthesis procedure does not allow for retaining control over the morphology of the same, in terms of porosity and pore size distribution.

UV-Vis analysis (**Figure 81**) for all of the doped samples and the EDX mapping (**Figure 82**) on the 3% Fe-doped and 3% Nb-doped anatase have been carried out

as complementary measurements to monitor the effect of the doping on the band-gap of the materials and whether the incorporation of metal cations was successful, respectively.
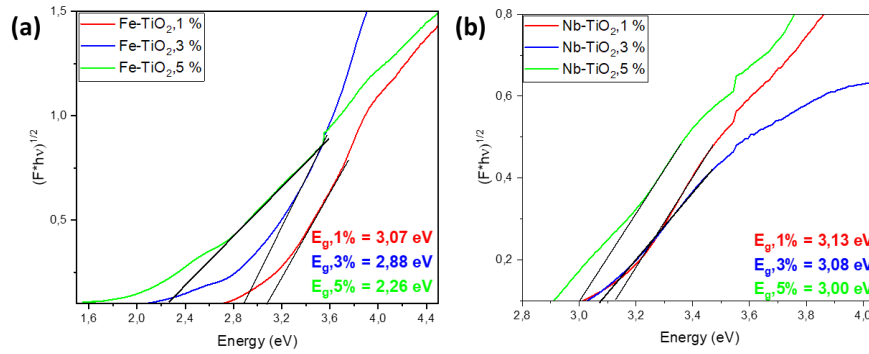
Figure 81. (a) Tauc plots of Fe-TiO$_2$ doped at 1 at.%, 3 at.% and 5 at.%. (b) Tauc plots of Nb-TiO$_2$ doped at 1 at.%, 3 at.% and 5 at.%.
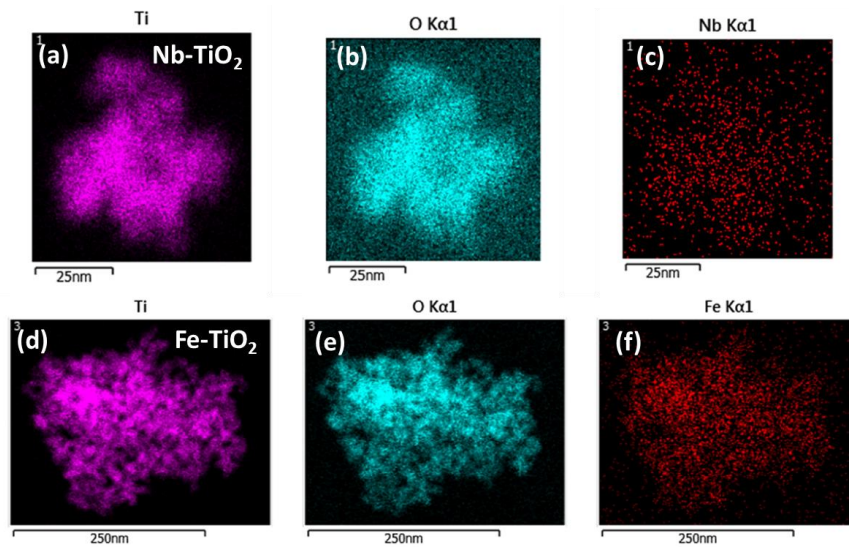
Figure 82. EDX mapping of the Nb-TiO$_2$ (a, b, c) and Fe-TiO$_2$ (d, e, f) materials.

In the case of the Fe-doped samples, the band gap value showed a gradual decrease when increasing the dopant concentration, consistent with similar experiments in the literature[477]. At the same time, it remained substantially unchanged in the case of Nb-doped materials[478]. However, it cannot be assumed that the change in the band gap is associated with an incorporation of the dopants, as the value of the band gap is also subject to changes even when the metal is not incorporated in the oxide matrix, such as in the case of the formation of side phases. The results of the EDX mapping

underlined only a partial incorporation of the metal cations within anatase TiO_2, which is around 1.10 at.% for the nominally 3% Fe-doped TiO_2 and 0.44 at.% for the Nb-doped TiO_2, and therefore a lower cation incorporation with respect to the nominal one. The reason for this discrepancy could be the small synthesis batches involved, together with the absence of a complexing agent in the sol-gel synthesis and the general difficulty in doping bulk mesoporous oxides like anatase[479], due to lattice mismatch and the general low solubility of doping metals in the metal oxide. However, as can be clearly seen from EDX, the amounts of dopants introduced within the lattice seem to be well dispersed within the material, even though additional characterization measurements such as XANES spectroscopy should be conducted to have certainty in the actual incorporation of the dopants. The 3% Fe-doped and the 3% Nb-doped titanium dioxide will henceforth be referred to as Fe-TiO_2 and Nb-TiO_2, respectively, and further characterizations were carried out on these doped titania samples. Coming to the study of water-titania interactions on the doped samples, the two Fe-TiO_2 and Nb-TiO_2 materials, together with those of the as-synthesized TiO_2 calcined at 400°C (TiO_2-400), have been taken as representative reference samples for the water physisorption measurements. In fact, the analysis of the pore size distributions obtained from nitrogen physisorption of the three samples (**Figure 83a**) shows very similar PSDs, which have the same width. This allows the materials to be compared in terms of average intercrystallite pore size, a prerequisite for comparing any changes in surface interaction with water by doping with niobium and iron. If that was not the case, any change in the early relative humidity behavior and capillary condensation onsets could not be uniquely associated with changes in the surface chemistry. Analysis of the IR spectra of the materials (**Figure 83b**) with focus in the stretching region of the –OH groups show a more pronounced signal in the case of the doped materials, which translates to a greater amount of hydroxyl groups on the surface, and thus theoretically in a greater hydrophilicity, because of the improved chance of having hydrogen bonding on the doped samples' surface. This is in agreement with what was hypothesized earlier about the effect of doping on the defect chemistry and Lewis acidity of the materials. In fact, the enhanced formation

203

of surface oxygen vacancies related to acceptor doping with Fe^{3+} and the increased Lewis acidity introduced by doping with Nb^{5+} lead to titania that is more easily protonated, and thus to an increased amount of surface hydroxyls.

So far, the water physisorption measurements have only been carried out gravimetrically. However, because of the low sensitivity pointed out earlier in detecting changes in the surface interactions observed in the case of undoped TiO_2, for the doped materials the water-vapor physisorption has been conducted both gravimetrically and volumetrically, also allowing for a comparison of the sensitivity of the two methods.
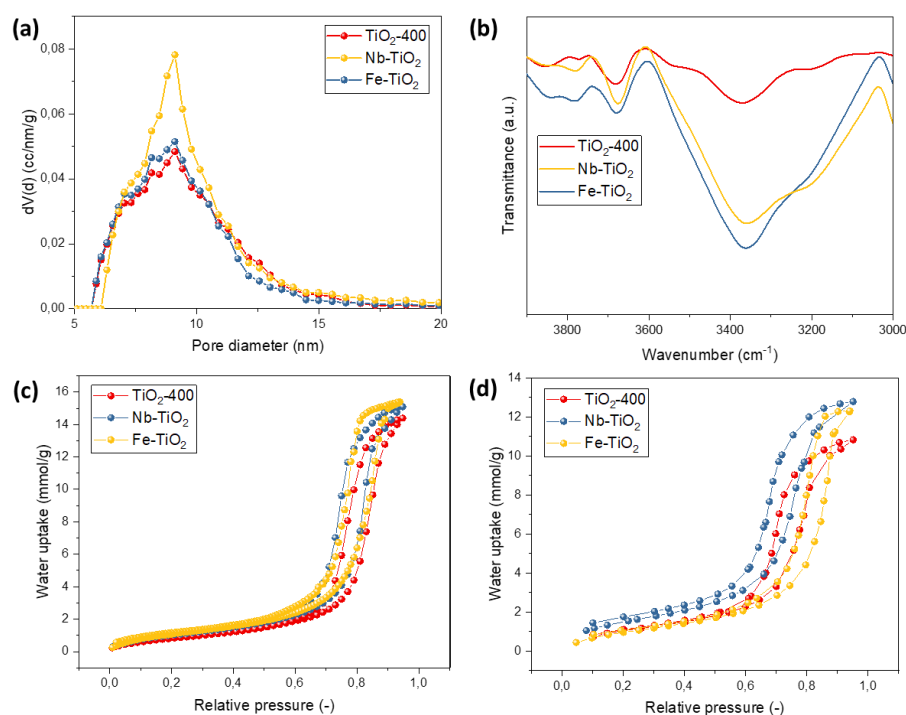
Figure 83. (a) DFT pore size distribution of the pure anatase and of the 3% Nb- and Fe-doped titania powders. (b) FT-IR spectra of the pure and doped samples. (c) Gravimetric and (d) volumetric water-vapor physisorption isotherms of the pure and doped anatase samples.

The results show a clear difference in the isotherm's trend. In the case of the gravimetric measurement (**Figure 83c**), it is observed that both materials doped with niobium and with iron demonstrate higher hydrophilicity, as evidenced by the shift of the capillary condensation region between 60 and 70 %RH, in full agreement with the IR results. Contrary to this, in the case of the volumetric measurement

(**Figure 83d**) there is a trend according to which the higher hydrophilicity of the material doped with Nb^{5+} is confirmed, with capillary condensation at approximately 65 %RH, while the material doped with Fe^{3+} shows a more pronounced hydrophobicity, indicated by the delayed capillary condensation onset (at $P/P_0 = 0.8$). The discrepancy in the outcomes of water physisorption is also supported by the isotherm adsorption analysis at low relative humidity. In fact, similarly to what was done in the case of pure titania, an analysis of the linear part of the adsorption isotherm indicates a trend in the heat of adsorption, related to the slope of the line obtained by linearizing the isotherm at low relative pressures, which agrees with that identified with the previous analysis.
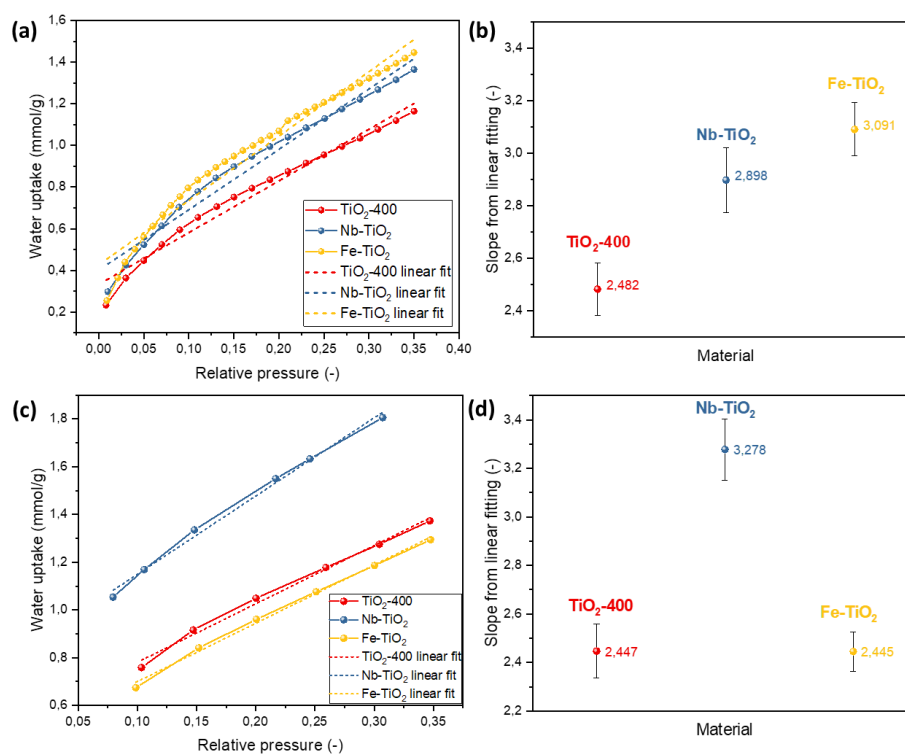
Figure 84. Gravimetric water physisorption results of the low relative pressure adsorption isotherms of TiO_2-400, Fe-TiO_2 and Nb-TiO_2 with their linear fits (a), and plot showing the slopes of the linear fitting results for each material (b). Volumetric water physisorption results of the low relative pressure adsorption isotherms of TiO_2-400, Fe-TiO_2 and Nb-TiO_2 with their linear fits (c), and plot showing the slopes of the linear fitting results for each material (d).

That is, in the case of the gravimetric measurements, a larger adsorption heat and hydrophilicity for the doped samples is evident when compared to the as-synthesized

reference pure TiO_2 (**Figure 84a,b**), while for the volumetric measurements the trend is different, with the Fe-doped material being the most hydrophobic and the Nb-doped material being significantly more hydrophilic and recording a larger heat of water physisorption (**Figure 84c,d**). In both cases the IR spectra show an increased signal for surface hydroxyl groups at 3400 cm^{-1} (**Figure 83b**), suggesting a potentially more hydrophilic behavior of both doped-materials when it comes to surface interactions with water. Discussing these results, it is evident that, since for the materials under consideration the outcome differs depending on the physical quantity being measured, the measurements are not reproducible and therefore cannot lead to unambiguous results. To explain this, a few important considerations need to be made regarding the more challenging nature of the measurements when comparing the adsorption of water with that of other gaseous adsorbents, such as N_2 or Ar. One is that the polarity of the H_2O molecules determines a possible presence on the surface of the metal oxide, in this case titanium dioxide, of a balance between water-water hydrogen bonding, $Ti-H_2O$ interactions and also $Nb-H_2O$ and $Fe-H_2O$ interactions. In fact, as mentioned previously, titania-water interactions are complex phenomena whose extent is related to several effects. These include the Brønsted acidity that increases with the concentration of surface hydroxyls, the higher Lewis acidity brought about by doping with Nb^{5+}, and enhanced oxygen vacancies formation again leading to a higher concentration of surface hydroxyls (and thus also to higher Brønsted acidity) in the case of doping with Fe^{3+}. Moreover, water tends to condense in mesopores even at low relative humidity, because of its high surface tension, and its adsorption at low temperatures could be affected by such phenomena. In particular, Viisanen *et. al.*[480] classified the typical long hysteresis that creates in the desorption branch of the physisorption isotherm in two types: a type I hysteresis, which is observed on more hydrophobic surfaces, where adsorption isotherms remain relatively linear as water approaches saturation, and type II hysteresis, which occurs on more hydrophilic surfaces, where the isotherm curves sharply near saturation (i.e. at high RH). In both cases, however, the proposed model suggests that adsorption occurs in clusters–either through contact angle hysteresis (Type I) or via film

formation near saturation (Type II)[480]. Since systematic studies on mesoporous titania anatase by water vapor physisorption are not present in the literature, the only results on a comparable system in terms of metal oxide and porosity are on porous silica[228], as discussed earlier. Therefore, considerations can only be made in terms of differences in the technical aspects of the measurements, common practices and functioning principles of the methods.

Both the gravimetric and volumetric measurements have in common the assessment of the adsorption uptake over time. Gravimetric water physisorption involves measuring the mass of water adsorbed by a powder sample before and after gradual exposure to water vapor. The increase in mass, recorded by an electronic microbalance, reflects the amount of water adsorbed. This technique is highly sensitive to small variations, making it particularly suitable for detecting low levels of water adsorption, especially at low pressures. However, it requires careful control of environmental conditions to ensure precision, as it is sensitive to external factors such as buoyancy, air drag, and vibrations, which can impact measurement accuracy[481]. In contrast, the volumetric method determines the amount of water vapor adsorbed by the sample by monitoring the pressure change in a sealed system as adsorption occurs. The pressure drop reflects the quantity of water vapor taken up by the sample, which is then calculated using an appropriate equation of state. Because this method relies on pressure measurements rather than direct mass or volume changes, it may be less sensitive to small amounts of adsorption compared to the gravimetric technique[481]. The experimental setup required for volumetric measurements is generally simpler and less affected by external factors. It can also accommodate larger sample sizes, which is particularly beneficial for materials with low adsorption capacities. While this method is easier to operate and automate, potential issues, such as water adsorption on the walls of the apparatus, can introduce inaccuracies. The choice between gravimetric and volumetric methods typically depends on various factors, including the required sensitivity, the nature and quantity of the sample, and specific experimental conditions such as temperature. In this study, however, the decision to perform gravimetric or volumetric measurements

207

– except in the case of doped materials, where both methods were employed – was dictated primarily by equipment availability. Although multiple factors may have contributed to the observed differences in results, isolating the influence of any single factor is challenging. What can be done, however, is to evaluate which of the two methods aligns more closely with the predicted increase in hydrophilicity resulting from titania doping. As mentioned earlier, the intrinsic and extrinsic defect formation of the materials contributes, together with the increased Lewis acidity in Nb-TiO_2 and the increase in oxygen vacancies formation in Fe-TiO_2, to a possible higher or lower hydrophilicity of the surface, evidenced by a larger –OH concentration in the IR spectra (**Figure 83b**). Taking into consideration the case of the gravimetric water physisorption results, considering the linearized adsorption curve at low relative humidity (**Figure 84a,b**), both the Nb-doped and the Fe-doped materials resulted to be more hydrophilic than the pure TiO_2. These results confirm that in the case of doping with Nb^{5+} the more pronounced hydrophilicity may be justified by the higher Lewis acidity, while in the case of Fe^{3+} by the larger concentration of surface –OH groups determined by the oxygen vacancies formation. Considering instead the volumetric physisorption results, the Nb-TiO_2 appears to be distinctly more hydrophilic than the pure TiO_2, while the Fe-TiO_2 is slightly more hydrophobic. This result however does not agree with that of IR spectroscopy (**Figure 83b**), which confirms the presence of bonded hydroxyls on the surface in equal amounts for Fe-TiO_2 and Nb-TiO_2, leading to the conclusion that the results of the gravimetric water physisorption better describe the expected behavior of surface hydrophilicity with respect to volumetric water physisorption. In any case, these interpretations remain largely speculative, aiming to explain the factors contributing to the discrepancies observed between volumetric and gravimetric measurements in water physisorption. The key takeaway is that, due to the inherent complexity of the materials, the intricate defect chemistry, and the experimental limitations of the techniques, water vapor physisorption alone does not appear to be sensitive enough to detect significant changes in water–surface interactions. This is despite the fact that such changes are clearly evidenced by other characterization methods used in this study.

8.2.2.1 Electro-thermal treatments of doped anatase

The electro-thermal treatments on the doped materials were carried out using the same experimental parameters as the ones performed on the pure materials (see **Experimental Methods** chapter), in order to evaluate the extent of an additional surface modification on the extrinsically doped mesoporous anatase. Powder diffractograms of the treated materials show no relevant change in the normalized reflection position for the (101) reflection of $Fe-TiO_2$ and $Nb-TiO_2$ (**Figure 85**). The larger noise in the XRD measurement, detectable by the non-smooth signal, is probably due to lower crystallinity and higher absorption due to doping with Nb and Fe in the material, leading to a higher signal-to-noise ratio.
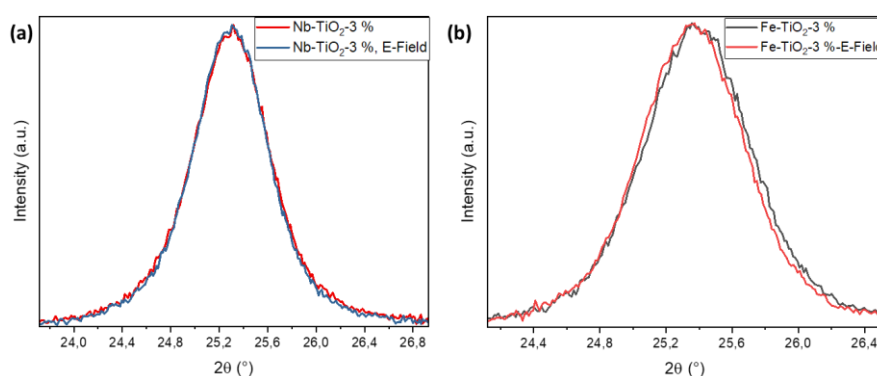
Figure 85. (101) reflection from XRD of $Nb-TiO_2$ (a) and $Fe-TiO_2$ (b), before and after electro-thermal treatment.

Since these materials were calcined at 400 °C and have a porosity larger than that of pure titania calcined at 400 °C (SSA of 116 m^2/g for the Nb-doped and 101 m^2/g for the Fe-doped materials, respectively), the fact that no significant shift is detected in the main reflection is in line with the explanation given for the electro-thermal treatments on the pure anatase, where it was concluded that a surface conduction, prevailing at higher porosities, does not bring changes to the bulk of the material in terms of crystal structure. The nitrogen adsorption isotherms (**Figure 86a,b**) reveal a reduction in porosity and partial sintering of the specimens, attributed to the combined effects of the applied electric field and elevated temperatures during the

209

treatment. A detailed analysis indicates a decrease in the SSA in both cases, from 125 m^2/g to 105 m^2/g for Nb-TiO$_2$ and from 110 m^2/g to 100 m^2/g for Fe-TiO$_2$, confirming the occurrence of partial sintering induced by the electro-thermal treatment. The average pore size of Nb-TiO$_2$ decreases from 10 nm to 9 nm, whereas that of Fe-TiO$_2$ (**Figure 86c,d**) remains largely unchanged at around 10 nm. The pore size distribution retains a similar profile, although a slight reduction in total pore volume is observed.

The unchanged DFT pore size distributions before and after electro-thermal treatment for both Fe-TiO$_2$ and Nb-TiO$_2$ suggest that any modifications observed are not due to morphological changes, but rather to alterations in surface chemistry. This consistency allows for an assessment of potential alterations in their surface chemistry, such as defect formation and variations in surface acidity, since differences in water physisorption behavior can be attributed primarily to these chemical changes rather than to shifts in pore structure.
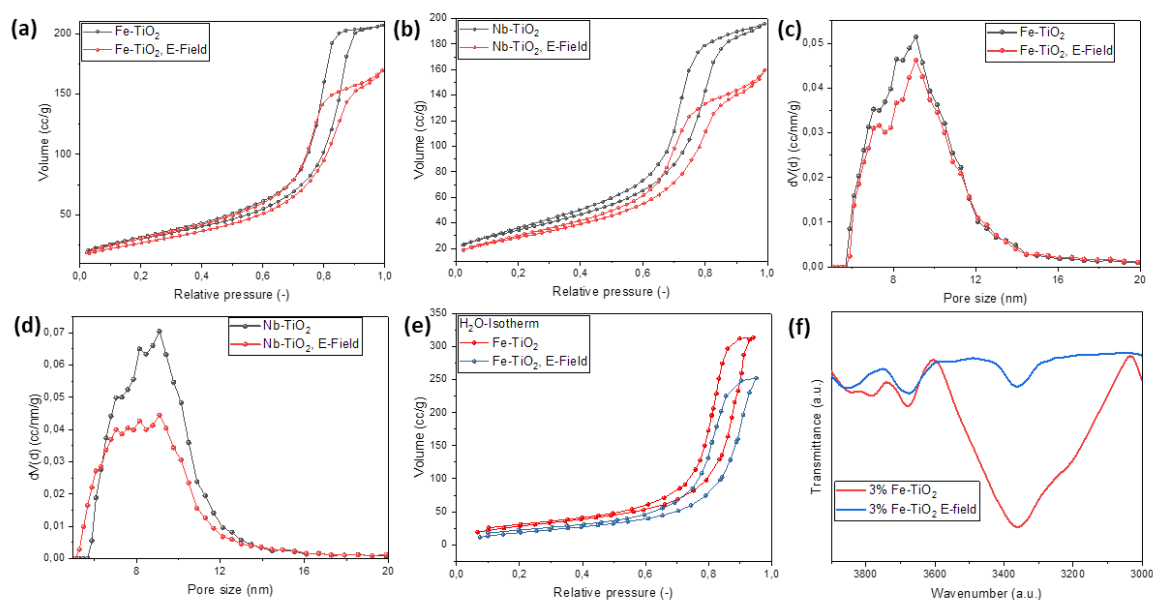
Figure 86. N$_2$-physisoprtion isotherms and DFT pore size distributions of the Fe-doped (a, b) and Nb-doped (c, d) TiO$_2$ materials. (e) Volumetric water-vapor physisorption isotherms of the Fe-doped anatase materials, before and after electro-thermal treatment. (f) IR-spectra of the Fe-doped anatase, before and after electro-thermal treatment.

The results of volumetric water physisorption (**Figure 86e**), with the same pore size distribution, indicate that the treatment preserves the type IV adsorption isotherm shape. This suggests an increase in the hydrophobicity of the titania surface, as evidenced by a shift to the right in the onset of capillary condensation and a reduction in water uptake at low relative pressures[482]. Additionally, the large hysteresis between the adsorption and desorption branches is retained.

These observations can be interpreted by considering various potential contributing factors. On one hand, doping with Fe results in a reduction in surface Lewis acidity, partly due to the electro-thermal treatment potentially leading to further reduction of Fe^{3+} to Fe^{2+}. This process also promotes the formation of oxygen vacancies, which act as active sites for water molecules to adsorb and dissociate, thereby generating additional hydroxyl groups and enhancing the Brønsted acidity. However, the observed shift toward a more hydrophobic surface in $Fe-TiO_2$ following electro-thermal treatment is likely due to a decrease in the concentration of surface hydroxyl groups, which can be attributed to a rearrangement of the electronic structure and surface species of the material[483]. A possible explanation for this behavior could be surface reconstruction due to the formation of O^- ions, reactive species that were observed in similar experiments conducted by Klauke et al.[427]. The formation of these O^- ions could lead to surface rearrangements and an increase in hydrophobicity, as they may occupy active sites that would otherwise adsorb water or form hydroxyl groups, reducing their surface availability after electro-thermal treatment. This is supported by the IR spectrum, which shows a clear decrease in the intensity of the signal associated with the stretching of surface-bound –OH groups before and after the electro-thermal treatment (**Figure 86f**). Thus, the induced hydrophobicity likely results from the rearrangement of oxygen vacancies formed by Fe doping, further enhanced by the low partial pressure (argon atmosphere) in the electro-thermal device, which promotes the surface recombination of the initially present hydroxyl groups, leading to a less hydrophilic surface.

8.3 Summary

In this chapter, the sol-gel synthesis of pure mesoporous titania powders was successfully optimized to tune their intracrystalline porosity. The availability of a larger specific surface area, related to the use of lower gel calcination temperatures, appears to have a significant effect on the concentration of hydroxyl groups on the surface of pure titania, thereby increasing its wettability. Indeed, the high porosity of pure mesoporous titania corresponds to higher hydrophilicity, indicated both by a greater slope of the adsorption curve at $P/P_0 < 0.3$, and by an onset of capillary condensation at lower relative pressures as the SSA increases, along with a gradually more intense signal of surface-bounded hydroxyls visible by FT-IR spectroscopy. Next, the effects of electro-thermal and photo-thermal treatments on water-surface interactions were also analyzed. In the case of electro-thermal treatments, although XRD, N_2-physisorption and FT-IR spectroscopy confirm surface modifications, no alterations are observed in the H_2O-physisorption isotherms. However, this result is influenced by the absence of water physisorption measurements available for pure TiO_2-400, which leaves an open question about the importance of porosity in effective surface modification by high temperature electric fields. The role of high porosity as a critical factor in surface modification of the material is also confirmed by the results of photo-thermal treatments, from which in the most porous pure material (TiO_2-400) a larger signal related to hydroxyls is noted by IR spectroscopy, demonstrating that porosity is also in the case of photo-thermal treatments the determining factor for surface modification through UV-radiation at high temperature.

Titania was then doped with Nb and Fe and after characterization subjected to water physisorption measurements, which, however, show that due to the nature of the materials, the complexity of the defect chemistry and the experimental limitations of the measurement, water vapor physisorption does not prove to be a sensitive enough technique to detect significant changes in water-surface interactions. Instead, if doping with Fe, considering the volumetric water physisorption analysis, led to an almost unchanged physisorption curve, electro-thermal treatment on the doped

material results in increased hydrophobicity, confirmed by a much less intense IR signal at 3400 cm^{-1}, which is related to surface-bonded –OH groups. Finally, photo-thermal treatment on the doped titania does not lead to significant changes in the materials hydrophilicity, probably due to limitations related to the modified surface chemistry of the doped titania compared to that of pure titania. All of these results suggest that while the materials have been successfully modified, more advanced techniques such as Diffuse Reflectance Infrared Fourier Transform Spectroscopy (DRIFTS) and Near-Ambient Pressure X-ray Photoelectron Spectroscopy (NAP-XPS) could provide further insights into how these surface modifications affect water interactions on the surface.

Chapter 9

Conclusions

In the present dissertation, the surface chemistry of different metal oxides was modified for tailoring their functional properties for sustainable catalytic applications. The research focused on three different materials. First, two Fe-based perovskite oxides systems were designed, in which iron forms a solid solution at the B-site, while the third one is mesoporous titanium dioxide (TiO_2). This choice of metals was aimed at using abundant elements on Earth, such as Fe and Ti, for designing sustainable catalyst materials.

In **Chapter 5** of this work, the focus was on studying the bimetallic exsolution process of FeNi alloy nanoparticles from a perovskite oxide with the composition $La_{0.4}Sr_{0.4}Ti_{0.60}Fe_{0.35}Ni_{0.05}O_3$ (referred to as 'LSTFN2'), where Ni is a 5 at.% dopant and Fe is present at 35 at.% as a solid solution at the B-site. The exsolution process consists of treating the perovskite material at elevated temperatures in a reducing atmosphere in order to induce the diffusion, reduction, nucleation and growth of FeNi alloy particles, which then constitute the catalytically active phase of the material when employed as a heterogeneous catalyst. To investigate the effect of temperature on the kinetics of Fe and Ni reduction, both *in-situ* XANES and *in-situ* synchrotron XRD measurements were performed to analyze the exsolution behavior at increasing temperature of 600 °C, 700 °C, 800 °C and 850 °C. This approach allowed for monitoring the reduction of the metals (via XANES) and the crystal growth (via XRD) of FeNi alloy nanoparticles. The aim was to understand the mechanism and dynamics of the bimetallic exsolution process of FeNi nanoparticles from the perovskite material, establishing a correlation between reduction and crystal growth.

In-situ XANES spectroscopy revealed that the kinetics of Ni reduction acts as the rate-determining step in the bimetallic exsolution process, driving the progression of Fe reduction, which is independent from the temperature of the treatment. The extent of reduction for both metals, specifically the maximum amounts of reduced Fe^0 and Ni^0 achievable within the material, is governed by the rate of oxygen vacancy formation in the perovskite lattice and by the stoichiometry (i.e. the composition) of the perovskite. This is due to the fact that the presence of a 20% A-site deficiency promotes oxygen vacancy generation under reducing atmospheres, thereby facilitating the reduction process. Considering the reduction of perovskite Ni^{n+} to Ni^0, two distinct behaviors were observed depending on the temperature. Faster reduction kinetics of Ni were observed at higher exsolution temperatures (800–850 °C) compared to lower temperatures (600–700 °C), as indicated by XANES results. This phenomenon was attributed to the combined influence of two factors: one kinetic and one thermodynamic. From a kinetic perspective, the increased vibrational energy of atoms at higher temperatures (i.e. 800 °C and 850 °C) resulted in faster formation of oxygen vacancies and to a more rapid oxygen release. This accelerated the attainment of the critical concentration of oxygen vacancies required to overcome the activation energy for Ni reduction, which is the rate-determining step of the process. Consequently, the reduction of Ni^{n+} (i.e., Ni cations in the perovskite matrix) to lower oxidation states, specifically Ni^{2+} and ultimately Ni^0, occurred more rapidly. This led to the rapid achievement of the maximum amount of metallic nickel dictated by the material's stoichiometry. From a thermodynamic perspective, high temperatures (800 °C and 850 °C) made Ni reduction more favorable due to the larger entropic contribution ($T\Delta S$) to the Gibbs free energy ($\Delta G = \Delta H - T\Delta S$). Additionally, the release of oxygen increased the system's entropy, and at 850 °C, the $T\Delta S$ term dominated, making ΔG more negative and further enhancing the thermodynamic favorability of Ni reduction. In contrast, at lower exsolution temperatures (600 °C and 700 °C), the slower rate of oxygen vacancy formation limited the availability of electrons required for the reduction of Ni cations to lower oxidation states. Furthermore, from a thermodynamic standpoint, the smaller

entropic contribution associated with oxygen vacancy formation at lower temperatures made ΔG less negative, thereby reducing the driving force for oxygen vacancy formation and subsequent Ni reduction. XANES spectroscopy was also employed to monitor the reduction kinetics of Fe in the material. Residual Fe^{2+} species were observed at the end of the process for all analyzed temperatures. This observation is explained by the fact that a complete reduction of Fe^{n+} to Fe^0 is not thermodynamically favored, as it would excessively destabilize the perovskite lattice. Moreover, while the reduction kinetics of Ni^0 was shown to be significantly faster at 850 °C than at 600 °C, the reduction kinetics of Fe^{n+} was found to be independent of temperature. This difference in the reduction kinetics of Ni at different temperatures, which leads to varying relative amounts of Fe^0 and Ni^0 during the reduction process, was shown to significantly influence the average composition of the exsolved FeNi alloy nanoparticles, as revealed by *in-situ* synchrotron XRD. These measurements demonstrated that a higher exsolution temperature (850 °C) results in the formation of FeNi alloys with Ni content reaching up to 50 at.%, while lower temperatures lead to reduced incorporation of Ni and a final Fe content as high as 60 at.%. Furthermore, lattice parameter calculations provided additional evidence of the temperature-dependent dynamics of crystal growth. At lower temperatures (600–700 °C), the lattice parameter evolved gradually over time, allowing for greater tunability of the alloy composition. In contrast, higher temperatures (800–850 °C) caused the rapid formation of alloys with constant lattice parameter over time, thereby reducing the compositional flexibility of the nanoparticles. This behavior perfectly matches with the reduction dynamics of Ni and Fe, representing a key finding of this chapter and serving as a foundation for the following one. In fact, the ability to influence the composition of the FeNi alloy on the material's surface by modifying the exsolution temperature opens up opportunities for the application of the $La_{0.4}Sr_{0.4}Ti_{0.60}Fe_{0.35}Ni_{0.05}O_3$ system in heterogeneous catalysis, particularly in CO_2-assisted Oxidative Dehydrogenation of Ethane (ODH) and Dry Ethane Reforming (DER).

This property of the material was explored in **Chapter 6**, whose findings are the result of a collaboration with the Korea Advanced Institute of Science and Technology (KAIST), the University of Western Macedonia and the University of Padua. In this chapter, the perovskite materials were first exsolved at increasing temperatures of 400 °C, 650 °C, and 850 °C (referred to as R400, R650, and R850, respectively) to tailor the compositions of the bimetallic FeNi alloy nanoparticles and, consequently, their catalytic selectivity. XANES spectroscopy measurements revealed that at lower temperatures (400 °C), the concentration of metallic Ni was larger than that of metallic Fe, whereas at higher temperatures (850 °C), metallic Fe became the dominant reduced species over metallic Ni. Furthermore, the bimetallic nanoparticles exsolved at 850 °C exhibited a core-shell structure, consisting of a Fe_3Ni core, a Ni skin, and an external Fe_yO_x shell. The formation of this iron oxide shell aligns with the findings of *in-situ* XANES spectroscopy of **Chapter 5**, which identified the presence of Fe^{2+} species at the end of the exsolution process. The potential mechanism responsible for this crystalline core-shell morphology was attributed to reverse oxygen spillover (ROS), wherein oxygen species migrate from an oxygen-deficient substrate to form an oxide layer on supported metal nanoparticles. Since the LSTFN2 material is 20% A-site deficient and becomes highly oxygen-deficient during exsolution, ROS is likely to occur at temperatures above 650 °C, leading to the immediate reaction of oxygen with the Fe_3Ni nanoparticle surface, resulting in the formation of a crystalline Fe_yO_x shell with metallic Ni, as Fe is more electropositive than Ni. This allowed for concluding that exsolved nanoparticles with distinct structures and compositions can be achieved by performing reduction treatments at low (400 °C) and high (850 °C) temperatures. These exsolved LSTFN2 materials were then tested as heterogeneous catalysts for the ODH and DER reactions by Anastasios Tsiotsias at the University of Western Macedonia. The results of the catalytic testing demonstrated that a modification of the exsolution temperature applied on the same LSTFN2 parent oxide allowed for precise control over reaction selectivity, directing it toward either the dehydrogenation (in the case of the Ni-richer nanoparticles of R400) or reforming pathways (for the core-shell

nanoparticles exsolved of R850), and leading to the obtainment of a functional catalyst with tailorable selectivity (**Scheme 4**).
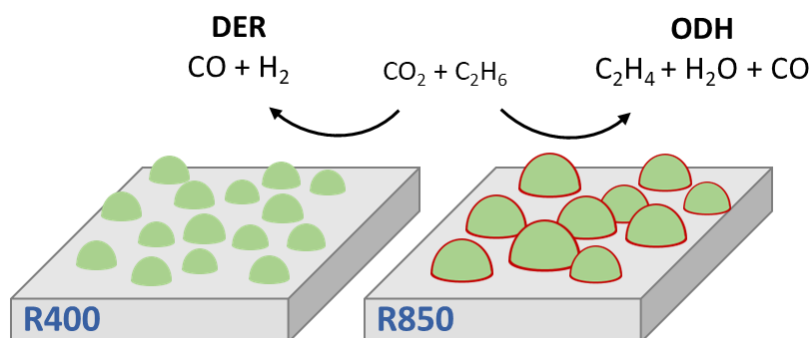
Scheme 4. Schematic sketch of the catalytic reactions taking place on R400 and R850.

Having established this, the applicability of these results was expanded to the design of a material with switchable catalytic selectivity. This was done by exploiting the unique property of perovskites to restore the original perovskite structure and partially dissolving the metal nanoparticles, when subjected to an oxidative step under air at 850 °C after the first exsolution treatment. That is, the material exsolved at 400 °C (R400) were re-oxidized (R400-O) and switched by exsolving the regenerated material at 850 °C (R400-O-R850). Likewise, R850 was also regenerated by oxidation at high temperature (R850-O) and then switched at the lower temperature examined so far, i.e. at 400 °C (R850-O-R400). A summarizing scheme of all the different exsolution steps of this study is provided in **Scheme 5**.

The analysis of the re-oxidized systems was conducted using a combination of three bulk characterization techniques: XRD, XANES, and Mössbauer spectroscopy. These methods were employed to evaluate the extent of perovskite phase restoration and the re-dissolution of metal nanoparticles back into the parent host perovskite. The complete overlap of the XANES spectra of Ni in the regenerated materials, i.e. R400-O and R850-O, demonstrated that Ni restores its pristine chemical environment to match that of the as-synthesized LSTFN2 system.
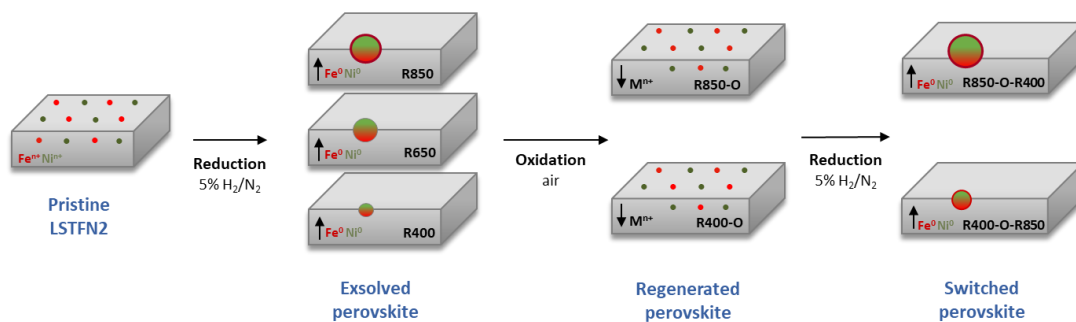
Scheme 5. Overview of the exsolution and regeneration treatments conducted in this chapter: the first reduction treatment at increasing temperatures (R400, R650 and R850); the subsequent regeneration by oxidation at 850 °C of R400 and R850 (R400-O and R850-O); and finally, the switching to the corresponding opposite temperatures (R400-O-R850 and R850-O-R400).

In contrast, a different behavior was observed for Fe: the Fe K-edge spectra of the re-oxidized samples exhibited a shape similar to those of the pristine system but with notably weaker intensity, which was attributed to the presence of residual metallic iron, as was indicated also by the XRD patterns, with formation of disordered iron oxide side-phases during re-oxidation, as revealed by Mössbauer spectroscopy. Thus, the re-oxidation of the reduced materials led to only partial reincorporation of exsolved Fe into the oxide matrix, due to its lower mobility and richer redox chemistry compared to nickel, resulting in the formation of a wide range of defective iron oxide phases. Finally, in the last step of the experimental protocol reported in **Scheme 5**, the regenerated perovskite materials were re-exsolved back to their corresponding opposite exsolution temperatures. Generally speaking, the switching process was shown to be more feasible when moving from lower exsolution temperatures (R400) to higher ones (R400-O-R850), while incomplete dissolution of bimetallic nanoparticles is observed when transitioning from high exsolution temperatures (R850) to lower ones (R850-O-R400). For the regenerated perovskites, a comparison of the XRD diffractograms of R850-O-R400 with R400 revealed that, after the switching process, the FeNi alloy nanoparticle reflection remains clearly visible. Moreover, a marked increase in the white line and pre-edge features of the Ni K-edge XANES spectra for both switched materials, R400-O-R850 and R850-O-R400, compared to the R400 and R850 systems, confirms the stronger reduction of Ni species after the switching process. In contrast, the XANES spectra of the Fe K-

edge show no significant changes before and after switching. In R850-O-R400, a higher metallic content was observed due to the incomplete dissolution of the metallic phase in R850-O, as confirmed by XRD and Mössbauer spectroscopy. At the same time, the spectrum of the R400-O-R850 material matches that of R850, indicating the presence of a large amount of Fe^0 and highly defective iron oxides. Additionally, TEM measurements of R400-O-R850 showed the recovery of the initial morphology of the alloy nanoparticles, which, as in the case of R850, are composed of an FeNi alloy surrounded by a crystalline Fe_yO_x shell. These results are also reflected in the catalytic testing of the switched materials, which demonstrated that the restoring of the original perovskite oxide structure influences the switchability of catalytic performance and selectivity. The catalytic performance of the re-exsolved materials differs from the original R400 and R850 materials due to incomplete dissolution during re-oxidation. The R400-O-R850 material exhibited catalytic performance similar to R850, with slightly lower reactant conversion and C_2H_4 selectivity, attributed to the presence of the Fe_yO_x overlay. In contrast, R850-O-R400 exhibited reduced selectivity for ethane reforming, likely due to substantial surface reconstruction during the preceding re-oxidation at 850 °C. During the subsequent re-exsolution step for R850-O-R400, these residual phases likely promoted additional particle growth, reducing the availability of active ethane reforming sites. The catalytic tests confirmed that the switching treatment of the LSTFN2 material is effective for the transition from DER to ODH, and the switch from ODH to DER proves to be more challenging due to incomplete regeneration of the perovskite matrix during re-oxidation.

These results demonstrated how switchable catalysts can be developed by making use of the regenerability properties of perovskites and by leveraging the complex redox chemistry of iron. In light of the potential of this finding, in **Chapter 7** the concept of reversibility in multimetallic exsolution was extended to another Fe-based perovskite system, again for applications as regenerable heterogeneous catalysts, as part of a collaboration with DongHwan Oh and collaboration partners at KAIST. While in Chapter 6 regeneration was understood as the re-incorporation of metal

nanoparticles into the perovskite matrix, in this case, it refers to the transition from a trimetallic alloy to a bimetallic alloy. The adopted perovskite system is a lanthanum ferrite host oxide with the general formula $La_{0.6}Ca_{0.4}Fe_{0.95}M_{0.05}O_{3-\delta}$ (M = Ni, Co, or NiCo), designed as a metal oxide oxygen carrier catalyst for Chemical Loop Reforming (CLR) coupled with CO_2 splitting. For the bimetallic-doped material ($La_{0.6}Ca_{0.4}Fe_{0.95}Co_{0.025}Ni_{0.025}O_{3-\delta}$), the exsolution of a trimetallic FeCoNi alloy nanoparticles under reducing CH_4 conditions was observed, which transitioned to NiCo bimetallic nanoparticles under oxidizing CO_2 atmospheres. This demonstrated how, by utilizing the redox chemistry of Fe, the rocking-chair-like behavior of Fe cations can be achieved, allowing them to move back and forth between the perovskite matrix and to be partially reincorporated into their original oxidation state and coordination environment. A multi-technique bulk characterization approach was employed to investigate the exsolution and re-oxidation processes, aiming at optimizing the design of regenerable heterogeneous catalysts for CLR. X-ray diffraction revealed that the Fe-alloy's exsolution coincided with the formation of a Ca-enriched $La_{1-x}Ca_xFeO_3$ phase, while CO_2-induced re-oxidation led to the disappearance of metallic reflections as Fe was reintegrated into $LaFeO_3$. This was consistent with XANES and Mössbauer spectroscopy, which confirmed the presence of metallic Fe^0 and partial re-incorporation of iron into the ferric Fe^{3+} state, with magnetite and/or maghemite detected as side phases. The combined use of XRD, XANES and Mössbauer spectroscopy provided a comprehensive understanding of the structural and chemical changes during redox cycling and highlighted the adaptability of Fe-based perovskite oxides and their exsolution and regeneration processes when extending their applicability beyond strontium titanate to lanthanum ferrite systems. To further optimize Fe exsolution for use in switchable catalysts, future investigations could explore additional process parameters, such as varying perovskite systems, material composition, and exsolution temperature.

Finally, **Chapter 8** of this dissertation explored the surface modification of mesoporous titania powders through different techniques to investigate their surface interactions with water. By utilizing water vapor physisorption measurements, this

study provided insights into the adsorption behavior and interaction mechanisms between water molecules and modified titania surfaces, aiming at evaluating their potential as catalysts for photocatalytic water splitting. The surface Brønsted acidity of mesoporous TiO_2 powders, governed by the concentration of surface hydroxyl groups capable of hydrogen bonding with water molecules, was shown to be significantly influenced by the material's specific surface area (SSA). Higher SSA enhanced surface hydrophilicity, as demonstrated by a steeper adsorption curve at $p/p_0 < 0.3$, an earlier onset of capillary condensation, and stronger signals of surface-bound hydroxyl groups observed via FT-IR spectroscopy. Moreover, the concentration of surface oxygen vacancies in the titanium dioxide materials was modified through electro- and photo-thermal treatments, as well as extrinsic doping with Fe and Nb. In all cases, the formation of oxygen vacancies, in conjunction with sufficiently high porosity, was identified as a major factor in inducing a more pronounced hydrophilicity. Electro-thermal treatments on pure TiO_2 led to increased concentration of oxygen vacancies and also resulted in a higher density of surface hydroxyl groups, as confirmed by X-ray diffraction, N_2-physisorption, and FT-IR spectroscopy. Photo-thermal treatments similarly confirmed that higher porosity enhances surface hydroxylation, as evidenced by stronger IR signals, reaffirming the critical role of SSA in water-titania interactions. However, these findings also highlight how, while the surface of the materials was successfully modified, water vapor physisorption measurements did not prove to be sensitive enough to detect significant changes in water-surface interactions. To extend the validity of these measurements, titania-water interactions could be further analyzed by using complementary techniques, such as Diffuse Reflectance Infrared Fourier Transform Spectroscopy (DRIFTS) and Near Ambient Pressure X-ray Photoelectron Spectroscopy (NAP-XPS).

Overall, the results of this dissertation showed that modifying Fe redox chemistry and surface vacancy concentrations enables the development of exsolved perovskite materials with tailorable functional properties and switchable catalytic selectivity. Moreover, concerning the defect-induced surface modifications of titania, oxygen

vacancies, together with porosity, appear to be critical parameters influencing water-oxide interactions. Complementary measurements to water vapor physisorption could provide a more comprehensive analysis of such interactions.

Chapter 10

Experimental Methods

10.1 Chemicals

Titanium(IV) isopropoxide (97%, Alfa Aesar), strontium nitrate (99%, Acros Organics), iron(III) nitrate nonahydrate (98%, Alfa Aesar), lanthanum(III) nitrate hexahydrate (99.9%, Alfa Aesar), nickel(II) nitrate hexahydrate (97%, Sigma-Aldrich), anhydrous citric acid (99.6%, Acros Organics), glycerol (99%, Alfa Aesar), calcium(II) nitrate tetrahydrate (Sigma Aldrich), cobalt(II) nitrate hexahydrate (98%, Alfa Aesar), ammonium hydroxide NH_4OH (28 v.%, Junsei), titanium(IV) tetrachloride (99.9%, Acros Organics), Pluronic P123 (pure, Sigma Aldrich), ethanol (>99.8%, Carl Roth), niobium(V) isopropoxide (99%, metal basis, 10 w/v.% in 50/50 isopropanol/hexane), aluminum(III) isopropoxide (>98%, Sigma Aldrich) and iron(III) nitrate nonahydrate (98%, Alfa Aesar) were all used as received without further purification.

10.2 Materials' synthesis

10.2.1 Synthesis of the LSTFN2 perovskite

The $La_{0.4}Sr_{0.40}Ti_{0.6}Fe_{0.35}Ni_{0.05}O_{3\pm\delta}$ (hereafter abbreviated as LSTFN2) powders of **Chapter 5** and **Chapter 6** have been synthesized via a template-free modified Pechini method[484]. In such synthesis procedure, glycerol has been selected as polyol, this choice being related to its better chelating and crosslinking properties, when compared with conventionally used ethylene glycol[485,486]. Titanium (IV) isopropoxide

($Ti(OCH(CH_3)_2)_4$) was initially combined with 11.9 mL of glycerol and stirred at room temperature for 30 minutes. Then, 40.7 mmol of citric acid were added, and the solution was heated to 60°C using an oil bath. After 45 minutes of stirring to dissolve the citric acid, stoichiometric amounts of $Sr(NO_3)_2$, $La(NO_3)_3 \cdot 6H_2O$, $Fe(NO_3)_3 \cdot 9H_2O$, and $Ni(NO_3)_2 \cdot 6H_2O$ were sequentially added at 30-minute intervals. $Sr(NO_3)_2$ was dissolved in the maximum amount of deionized H_2O possible, then added to the solution and stirred for 30 minutes. The molar ratio of glycerol to citric acid to the total metal cations was set at 30:4:1. Once all the metal precursors were added, the solution was further stirred for 2 h to ensure thorough mixing. Subsequently, the temperature was raised to 130 °C, and the solution was maintained at this temperature for another 2 h under continuous stirring. The combination of polyol (glycerol) and polycarboxylic acid (citric acid) resulted in the formation of a polyester gel through a polycondensation reaction. The polymer gel was then subjected to calcination at 400 °C for 2 h, followed by heating at 900 °C for another 2 h, using a temperature increase rate of 2 °C/min.

10.2.2 Synthesis of the LCFO perovskite

The $La_{0.6}Ca_{0.4}Fe_{0.95}M_{0.05}O_{3-\delta}$ (with M = Ni, Co, NiCo, hereafter abbreviated as LCFO) perovskite materials of **Chapter 7** were also synthesized through a sol-gel method with conventional nitrate precursors by DongHwan Oh at KAIST. $La(NO_3)_3 \cdot 6H_2O$, $Ca(NO_3)_2 \cdot 4H_2O$, $Ni(NO_3)_2 \cdot 6H_2O$, $Co(NO_3)_2 \cdot 6H_2O$, and $Fe(NO_3)_3 \cdot 9H_2O$ were completely dissolved in deionized water with citric acid as a chelating agent, at a stoichiometric ratio of metal ions:citric acid = 1:1.1. The solution was stirred at 25 °C for 30 min to form a homogeneous solution. The pH of the solution was adjusted to 7 using NH_4OH and kept at 230 °C until the solution turned into a dried gel. Then, the dried gel was heated for 3 h at 450 °C to burn any residual carbons. The calcination step was performed at 900 °C for 5 h with a ramping rate of 4 °C/min. The sample was pelletized in a uniaxial press and sintered at 1150 °C for 5 h.

10.2.3 Synthesis of mesoporous anatase TiO$_2$ powders

The sol-gel synthesis of the pure and doped mesoporous TiO$_2$ powders of **Chapter 8** has been carried out and optimized with reference to the one of Yang et. al.[125]. It consisted in mixing 20 g of ethanol with 1.854 g of poly (ethylene glycol)-block-poly (propylene glycol)-block-poly(ethylene glycol) or P123 block co-polymer for 20 min. Titanium tetrachloride (2 mL) has been used as inorganic chloride precursor and subsequently added to the mixture under gentle stirring (200 rpm). After 2 h the solution has been transferred to a large open Petri dish and subjected to 24 h drying in the oven at 40 °C for solvent removal. In order to remove the organic template, the obtained gel was then subsequently calcined with a temperature ramp of 5 °C min^{-1} at 400 °C for 5 h in a muffle oven, for the reference powder materials ('TiO$_2$-400'). In order to explore a variety of different porosities for mesoporous titania, after the first calcination step, the material was also calcined at increasing temperatures of 500, 600 and 700 °C with a temperature ramp of 5 K/min for another 2 h. This resulted in a partial sintering and grain growth of the anatase crystallites in the material, which lead to a reduction in the number and size of the pores[487,488]. The materials thus produced will henceforth be referred to as TiO$_2$-500, TiO$_2$-600 and TiO$_2$-700, respectively, and appeared after calcination as white powders. The reason for this calcination protocol is related to the necessity of starting from the same starting material calcined at 400 °C, while the two additional hours of calcination lead to a further aggregation and coalescence of the crystallites, determining a smaller intracrystalline porosity the higher is the calcination temperature.

With regards to the synthesis of the doped materials, in order to investigate the influence of the different dopants and the effects of the doping level on their porosity, increasing amounts (1 at.%, 3 at.% and 5 at.%) of metal cations have been added as isopropoxides precursors in the case of Nb^{5+}, and as nitrates in the case of Fe^{3+}. The preparation of the templated sol-gel solution was carried out as in the case of the pure titania powders. Niobium isopropoxide has been added directly to the mixture with and Eppendorf pipette after the first 2 h stirring phase and the solution was

subsequently stirred for another 2 h, before proceeding with the solvent evaporation. In the case of iron doping, $Fe(NO_3)_3 \cdot 9H_2O$ has first been dissolved in a 50:50 w.% solution of ethyl-acetyl-acetone and ethanol, and then subsequently added to the reaction mixture. In both cases, the calcination temperature has been kept at 400 °C for 5 h, allowing for the largest porosity available. The use of iron nitrate instead of other more typically used precursors, such as iron acetyl acetate, is related to the desire to obtain a more homogeneous dispersion and to maximize the number of – OH groups, which play an essential role in the physisorption of water vapor, for which the materials were designed[489]. The precise amounts of the chemicals used for each of the syntheses are summarized in **Table 9**.

Table 9. Amounts of the chemicals employed for the synthesis of the doped mesoporous TiO_2.

Doped TiO_2	Doping chemical	Chemical formula	Nominal doping (at.%)	Amount (in µl or g)
Nb-TiO_2	Niobium isopropoxide	$C_{15}H_{40}NbO_5$	1	707
			3	2124
			5	3542
Fe-TiO_2	Iron nitrate nonahydrate	$Fe(NO_3)_3 \cdot (H_2O)_9$	1	0.0735
			3	0.2208
			5	0.3686

10.3 Analytical methods

10.3.1 X-ray diffraction

Powder X-ray diffraction measurements were all carried out on an X'Pert Pro diffractometer from PANalytical Corp., using a 1.5406 Å Ni-filtered Cu-K_α radiation, operating at 45 kV and 40 mA. The average crystallite sizes of the different materials were calculated from the full width at half maximum (FWHM) of the (101) reflection by using the Scherrer equation.

10.3.2 X-ray absorption spectroscopy

The *ex-situ* X-ray absorption spectra at the Fe K-edge (7112 eV) and Ni K edge (8333 eV) of **Chapter 6** were acquired at the P64 beamline[213] of the Deutsches Elektronen Synchrotron (DESY, Hamburg, Germany) with the support of Alexandr Kalinko. A Si(111) double crystal monochromator was employed for the energy scans around the respective metal absorption edge. The XAFS spectra were collected in fluorescence geometry for both the Ni and Fe K-edges using gas ionization chambers to measure the photon intensities before and after the samples. The powders were diluted in cellulose, pressed into pellets, and then covered in Kapton tape before placing them in the beam path. Normalization of the obtained XANES data was carried out by performing pre-edge and post-edge background subtraction in the XANESA software, an open-source code software created and designed by Alexandr Kalinko of beamline P64. The same software has also been employed for the plotting and the comparison of the normalized data.

The *ex-situ* X-ray absorption spectra at the Fe K-edge (7112 eV), Co K-edge (7709 eV) and Ni K-edge (8333 eV) of **Chapter 7** were acquired at the Balder beamline of the Max IV laboratory synchrotron radiation source in Lund, Sweden. A double crystal monochromator with Si(111) and Si(311) LN2-cooled crystals[490] were employed for the energy scans around the Fe, Ni and Co metal absorption edges. The XAFS spectra were collected in fluorescence mode for both the Ni and Fe K-edges using gas ionization chambers to measure the photon intensities before and after the samples. The powders were also in this case diluted in cellulose, pressed into pellets, and then covered in Kapton tape before placing them in the beam path. Normalization of the obtained XANES data was carried out by performing pre-edge and post-edge background subtraction in the Athena software[491].

10.3.3 Nitrogen physisorption

The nitrogen physisorption isotherms were obtained at 77 K using a Quadrasorb SI-MP by Quantachrome. Outgassing was performed with a Masterprep Degasser (Quantachrome Corp.) at 120 ℃ for 12 h. The specific surface area of the as-synthesized material determined with the Brunauer-Emmett-Teller (BET) method[492] at P/P_0 = 0.07–0.3. Pore size distribution was determined with the NLDFT method[221] applying the model for silica cylindrical pores on the adsorption branch by using the Quantachrome ASiQWin software.

10.3.4 Water vapor physisorption

The water physisorption isotherms were measured with both volumetric and gravimetric instruments. The volumetric water physisorption isotherms were acquired with an Anton Paar GmbH V-star analyzer. Sample preparation involved degassing and drying of the sample at 120 °C under vacuum for 12 h. The measurement temperature was set to room temperature (25 °C). The pressure points profile has been set between 0.05 and 0.95 P/P_0, and the maximum adsorption change between two consecutive pressure points being set to 1 mmol/g, with the software adding an additional point between the predefined ones only when this limit is exceeded. The equilibrium data consisted of a total of 10 points, with an interval of 60–120 s between each measurement (depending on pressure range), and rate limit 0.005–0.1 torr/min. The gravimetric water physisorption isotherms were acquired using a Quantachrome Instruments Aquadayne DVS2 Gravimetric Sorption Analyzer. The sample preparation was done in-situ within the instrument, by bringing the sample to 80°C and subjecting to a flow of 100 mL/min of dry nitrogen for 12 h at 0% RH. The measurements were then taken at 25 °C. The pressure points profile was set between 0 and 0.95 P/P_0, with steps of 0.01. The equilibrium data were found by setting a minimum weight change on the sample that has been set to be smaller than 0.005 %/min.

10.3.5 Transmission electron microscopy

The HR-TEM analyses of **Chapter 7** were conducted using FEI Tecnai Titan cube G2 60-300 with an accelerating voltage of 300 keV at the KAIST Analysis Center for Research Advancement (KARA). For the *in-situ* TEM study of **Chapter 6**, powder samples were dispersed on a silicon nitride grid (Nanofactory, MEMS Microheater) and the TEM pictures were collected at the ultra-high vacuum level ($\approx$9.33 x 10-8 mbar) upon the temperature ramp ($\approx$900 ^{o}C). High-angle annular dark-field scanning transmission electron microscopy (HAADF-STEM) was also performed, and further energy dispersive X-ray spectroscopy (EDX) for analyzing metal cations distribution, including line-scans data, were collected together.

TEM pictures of the doped TiO_2 powders were recorded on a JEOL JEM-1011 transmission electron microscope with 100 kV acceleration voltage and SIS CCD camera system (1376x1032 px). The metal cations distribution was investigated through HR-TEM and EDX mapping on a JEOL JEM-2200FS corrected High-Resolution Transmission Electron Microscope (Cs-HRTEM), with the acceleration voltage set to 200 kV.

10.3.6 IR spectroscopy

The FT-IR spectroscopy measurements of **Chapter 8** were performed on a Bruker Vertex 70 FT-IR spectroscope in Attenuated Total Reflectance (ATR) mode. In order to avoid overlapping of the –OH stretching groups with the one of pure water on a moist sample, the materials have been treated at 130 °C for 24 h before the measurements. The spectra were collected in total reflectance and subjected to normalization and background collection. The focus has been put on the wavenumber region included between 3000 and 3600 cm^{-1}, i.e. the one of bridged surface –OH groups.

10.3.7 Mössbauer spectroscopy

Room temperature Mössbauer spectroscopy was performed on a conventional constant acceleration spectrometer mounting a Rh matrix ^{57}Co source, nominal strength 1850 MBq. The hyperfine parameters were obtained by means of standard least-squares minimization techniques. The Mössbauer parameter δ is quoted relative to α-Fe foil.

10.3.8 UV-Vis spectroscopy

UV-Vis spectroscopy for the band-gap calculations in **Chapter 8** was performed on a Cary 5000 UV-Vis-NIR spectrophotometer in the range within 200-800 nm wavelength, with the source set at 700 nm. Pure barium sulfate has been used for the baseline, mixed on a ratio of 1:5 to avoid saturation of the signal.

10.4 Surface modification of the metal oxides

10.4.1 In-situ exsolution setup

The *in-situ* XANES experiments have been carried out at the P64 beamline at Desy in Hamburg, Germany, with the support of Alexandr Kalinko and together with Benjamin Rudolph. The experiments were carried out in a specifically designed experimental setup (**Figure 87**). The powder sample was placed between quartz wool plugs inside a glass capillary with an internal diameter of 0.99 nm. This setup was heated in air using a ceramic heater until the desired experimental temperature was reached. Once the temperature stabilized, a single 120-second scan was performed in air. Subsequently, a complete X-ray Absorption Spectroscopy (XAS) scan was conducted at the Ni K-edge (8333 eV) and Fe K-edge (7112 eV), spanning from 100 eV below to 500 eV above E_0 with a resolution of 0.2 eV and a duration of 120 seconds. After this first initial scan on the pristine material, forming gas (5% H_2 in N_2) was introduced at a flow rate of 5 mL/min, and 60 additional scans were

performed under these conditions. Linear combination fitting (LCF) analysis was carried out using reference spectra from metallic Ni, $NiFe_2O_4$ and LSTFN2 (the pristine perovskite matrix) within the energy range of 8313-8413 eV for the Ni K-edge, and for the Fe K-edge with Fe^0, FeO (wüstite), $NiFe_2O_4$ and LSTFN2 iron, within the range 7092–7212 eV. The first spectrum collected after opening the valve was excluded from the LCF analysis, as it was believed that the reaction mixture had not fully entered the capillary during this initial measurement.

The *in-situ* synchrotron XRD measurements have been carried out in two separate beamtimes at the P08.1 beamline[493] at Desy in Hamburg, Germany, with the help of Dr. Chen Shen, together with Benedikt Ehrhardt. The powders were enclosed in glass capillaries with an internal diameter of 0.99 mm. These samples were exposed to monochromatic radiation at approximately 18 keV, equivalent to a wavelength of 0.68987 Å, using the Debye–Scherrer geometry. Diffraction data were collected with a Perkin Elmer XRD 1621 detector. Lanthanum hexaboride was employed as an external standard for 2ϑ range calibration. The raw diffraction data were processed into one-dimensional powder patterns. The lattice parameters of the FeNi alloy and of the perovskites have been calculated by monitoring the position of the (111) and (110) reflections, respectively, and calculated with Bragg law.
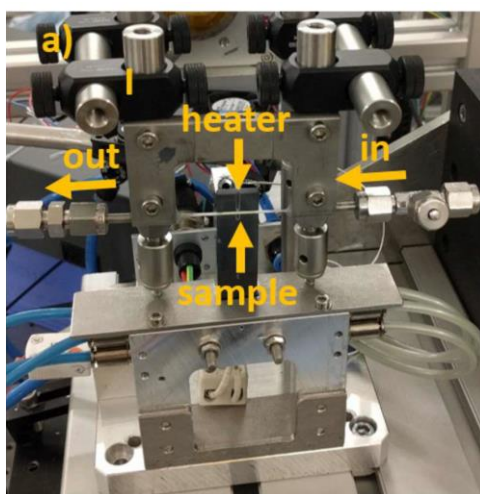
Figure 87. Picture and schematization of the experimental apparatus used for the *in-situ* synchrotron experiments, including the sample holder, the heating unit and the inlet and outlet gases.

10.4.2 Laboratory exsolution and re-oxidation setup

The *ex-situ* reduction treatments of the materials consisted in a treatment at high temperature of the catalyst powders under a 5% H_2/N_2 gas flow, with different temperatures and durations depending on the experiments. A U-shaped quartz tube was first filled with 100 mg of powder, and a heating ramp of 10 K/min was set while flushing Ar gas in the system, allowing for an inert atmosphere during the heating section. The temperature of the system was measured through a Pt-100 thermocouple mounted within the exsolution cell, for real time monitoring of the local temperature of the powder bed. Finally, once reached the target temperature, the quartz tube was then subjected to a flowrate of 20 mL/min of 5% H_2/N_2. These treatments were also carried out for all the materials in Chapter 2, but with different temperatures and duration of the treatments. In **Chapter 6**, the materials have been subjected to the reduction and oxidation treatments schematized in **Figure 88**. In the first exsolution cycle, LSTFN2 was subjected to reduction treatments at increasing temperatures of 400 °C (R400), 650 °C (R650) and 850 °C (R850) for 3 h. After that, the R400, R650 and R850 exsolved materials have been re-oxidized by filling the quartz U-tube with the exsolved (black) powders and subjected to a flowrate of 20 mL/min of air at 850 °C, flushed in the system for 5 h. Finally, the regenerated materials previously exsolved at 400 °C (R400-O) and at 850 °C (R850-O) have been again subjected to reduction at 850 °C for 3h, leading to the switched materials named R400-O-R850 and R850-O-R400.
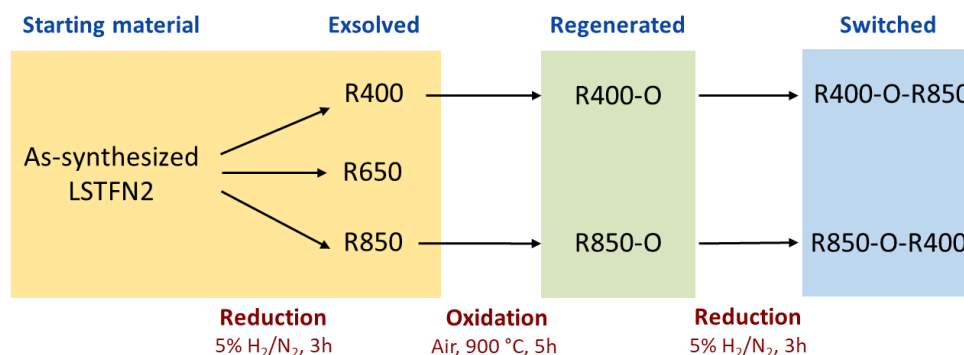
Figure 88. Scheme of the reduction and re-oxidation treatments conducted in Chapter 6.

Finally, in **Chapter 7**, the partial oxidation of CH_4 coupled with the CO_2 splitting cycle was conducted using 200 mg of LCFO perovskite. The reaction temperature was set to 850°C, with a heating rate of 10 K/min, and a gas flow rate of 20 mL/min consisting of 5% CO_2 in Ar. Following this, the CH_4 reduction step was performed under identical flow conditions (5% CH_4 in Ar) for 25 minutes to prevent coke formation. Subsequently, the CO_2 injection step was repeated for the same duration, with a 3-minute Ar purge implemented between each half-cycle of the redox process, for a total of 50 redox cycles.

10.4.3 Electro-thermal treatments of TiO_2
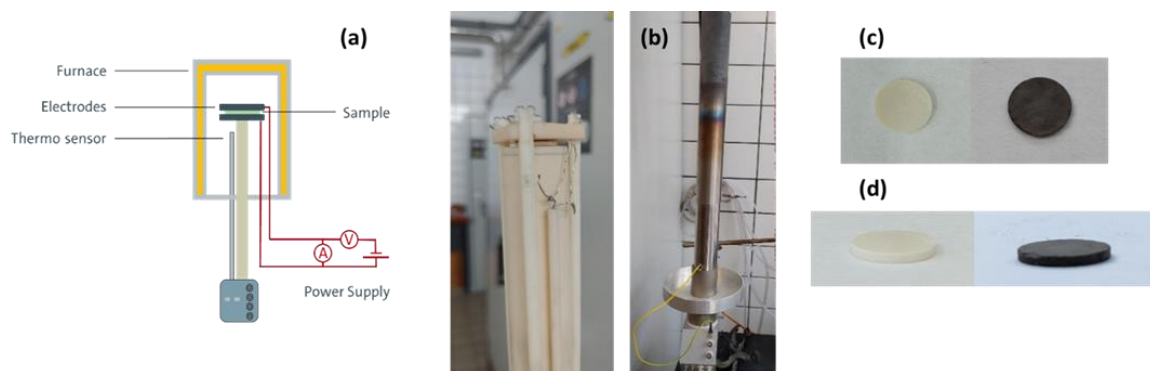
Figure 89. (a) Schematic of the electro-thermal treatments apparatus. (b) Detail of the TiO_2 pellet within the sample environment (left) and of the shielded cylinder (right). Pellets before (left) and after (right) the electro-thermal treatments for pure (c) and 3% Nb-doped (d) anatase TiO_2.

For performing the electro-thermal treatments on titanium dioxide of **Chapter 8**, the anatase powders were pressed into 13 mm diameter pellets using a hydraulic press. Both faces of the pellet were then coated with a solvent-diluted silver paste, to make them conductive, and the coated pellet has been in oven at 130 °C for 2 h. The electro-thermal treatment has been carried with the use of a NORECS Probostat, a device originally conceived for performing Electrochemical Impedance Spectroscopy (EIS)[494]. For doing so, two platinum electrodes have been connected to the pellet conductive planes, and the argon gas allowed to flow within a chamber around the sample environment, in order to lower the oxygen partial pressure of the system. The whole sample-gas chamber system was then shielded with a stainless-

steel cylinder and then placed in a cylindrical muffle oven, and the temperature brought to 300 °C. A voltage generator was used to supply a direct current to the material, setting the electric field to a value of 60 V/cm for 1 h, with the maximum current limit set to 100 mA, which was reached immediately and remained constant in all treatments. A schematic sketch of the system is shown in **Figure 89a**, while detailed pictures of the pellet within the sample environment, before and after applying the heat shield cylinder, are reported in **Figure 89b**. The electro-thermal treatments were performed on the pure materials material calcined at 400 °C, 500 °C, 600 °C and 700 °C and on both the Nb-doped and Fe-doped materials. In all cases, like in the ones of the pure TiO_2 and 3% Nb-doped TiO_2 (**Figure 89c** and **Figure 89d**, respectively), the anatase powders after the treatments showed a pronounced blackening, due to the reduction of Ti^{4+} species induced from the treatments.

10.4.4 Photo-thermal treatments of TiO₂

A dedicated setup for the photo-thermal treatments of titanium dioxide presented in **Chapter 8** has been developed and optimized for this study. A schematic sketch and a picture of the photo-thermal reactor is shown in **Figure 90**. The custom-built reactor was employed for photothermal processes, featuring a reaction space with dimensions of 35x35x40 cm (LxWxH). This chamber was made from a 1 mm thick aluminum sheet and had a 2 mm thick steel floor. The inside surfaces, except for the lower part, were lined with aluminum foil, and the entire structure was raised above the working area on a support frame. The reactor's heating mechanism consisted of four 500 W, 230 V cartridge heaters embedded in a copper block measuring 10x10x3 cm, which were centrally located at the base of the chamber. A type K NiCr-Ni thermocouple was integrated within the heating block to track its temperature. The temperature data from this thermocouple was assumed to accurately reflect the temperature of both the copper plate and its surface, as well as the sample being treated, due to copper's good thermal conductivity and the relatively small mass of

the samples in comparison to the heating block. Temperature control was managed by an ETC 7420 temperature controller from the company ENDA. The system's heating characteristics were also calibrated using an empty crucible at 350 °C to confirm the reactor's ability to maintain a stable temperature during the treatment process. For the photothermal treatment process, the samples were arranged in a flat crucible using a spatula to create a layer approximately 1-2 mm thick. This prepared crucible was then placed into the preheated reactor, positioned at the center of the light cone emitted by the UV LED lamp on the heating surface. The lamp was activated with the reactor sealed, and the sample underwent treatments at 350 °C for 4 h. Upon completion of the treatment process, the samples were promptly extracted from the reactor and allowed to cool to room temperature for subsequent characterization.
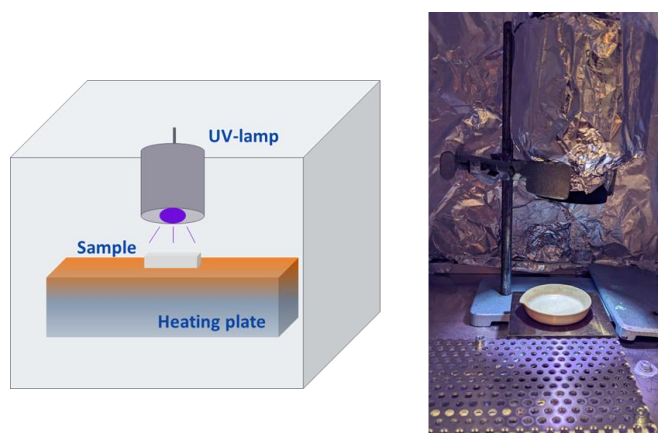
Figure 90. Schematic sketch (left) and picture (right) of the custom-made photo-thermal reactor.

10.5 Catalytic testing of LSTFN2 perovskites

The assessment of the catalytic performance of the exsolved and regenerated LSTFN2 perovskite materials for ethane oxidative dehydrogenation and dry reforming (**Chapter 6**) was performed in a quartz glass tubular reactor (9 mm I.D.) at atmospheric pressure. Initially, 100 mg of exsolved powder was each time mixed with 500 mg of quartz sand and loaded in the reactor. The total flow rate was set at 40 mL/min (10 mL/min C_2H_6, 10 mL/min CO_2 and 20 mL/min Ar), with the C_2H_6:CO_2

molar ratio being kept at 1:1. The initial reaction temperature was 400 °C, following a prior purge of the reactor and catalyst with Ar. The reaction procedure was carried out in two phases. At the first phase (activity testing), after passing the reaction mixture through the reactor at 400 °C for 30 min, the reaction temperature was slowly increased with a rate of 100 °C per hour (50 °C for every 30 min), up to 700 °C, with measurement being taken every 30 min. At the second phase (time-on-stream), after the reactor temperature reached 700 °C (3 h), the temperature was kept constant at 700 °C for another 8 h, with measurement being taken every 30 min. The approach of first introducing the two reactants at lower temperature and then ramping up the temperature before the time-on-stream operation at 700 ˚C was based on previous works dealing with dry reforming over perovskite-type catalysts [256,495,496]. In this way, the catalyst is activated under the reactant stream at lower temperature and during the temperature ramp, and can present a higher catalytic activity compared to the introduction of the two reactants directly at elevated temperature[495]. Testing of the 1% Ni/Al$_2$O$_3$ reference catalyst included a prior *in-situ* reduction step under pure H$_2$ flow at 850 °C for 1 h. The gaseous reaction products were analyzed on-line via an Agilent-7890A gas chromatograph, as described in a previous work from Tsiotsias et. al.[22]. The ethane and carbon dioxide conversions, the hydrogen, carbon monoxide, ethylene, and methane yields, as well as the selectivities (ethane basis) for ethylene (dehydrogenation), methane (cracking) and carbon monoxide (reforming), together with the H$_2$/CO molar ratio were determined by using the following equations (**Equations 41-50**):

$$X_{C_2H_6} = \frac{F_{C_2H_6,in} - F_{C_2H_6,out}}{F_{C_2H_6,in}} \times 100 \tag{41}$$

$$X_{CO_2} = \frac{F_{CO_2,in} - F_{CO_2,out}}{F_{CO_2,in}} \times 100 \tag{42}$$

$$Y_{H_2} = \frac{F_{H_2,out}}{3 \times F_{C_2H_6,in}} \times 100 \tag{43}$$

$$Y_{CO} = \frac{F_{CO,out}}{(2 \times F_{C_2H_6,in} + F_{CO_2,in})} \times 100 \tag{44}$$

$$Y_{C_2H_4} = \frac{F_{C_2H_4,out}}{F_{C_2H_6,in}} \times 100 \qquad (45)$$

$$Y_{CH_4} = \frac{F_{CH_4,out}}{2 \times F_{C_2H_6,in}} \times 100 \qquad (46)$$

$$S_{C_2H_4} = \frac{Y_{C_2H_4}}{X_{C_2H_6}} \times 100 \qquad (47)$$

$$S_{CH_4} = \frac{Y_{CH_4}}{X_{C_2H_6}} \times 100 \qquad (48)$$

$$S_{CO} = 100 - S_{CH_4} - S_{C_2H_4} \qquad (49)$$

$$H_2/CO = \frac{F_{H_2,out}}{F_{CO,out}} \qquad (50)$$

Chapter 11

Bibliography

1.   Enerdata. Global energy consumption growth accelerated in 2023 (+2.2%), much faster than its average 2010-2019 growth rate (+1.5%/year). https://yearbook.enerdata.net/total-energy/world-consumption-statistics.html

2.   World Bank Group. Total Population Trend. https://data.worldbank.org/indicator/SP.POP.TOTL

3.   IEA. World Energy Outlook 2024. https://www.iea.org/reports/world-energy-outlook-2024

4.   S&P Global. Fossil fuel use hits new highs in 2023 despite renewable energy boom. https://www.spglobal.com/commodity-insights/en/news-research/latest-news/crude-oil/062024-fossil-fuel-use-hits-new-highs-in-2023-despite-renewable-energy-boom

5.   Rapier, R. Renewable Energy Consumption Hits New Record High. *Forbes* (2024).

6.   IEA. Outlook for gaseous fuels. *World Energy Outlook 2022* https://www.iea.org/reports/world-energy-outlook-2022/outlook-for-gaseous-fuels

7.   IEA. CCUS in clean energy transition. https://www.iea.org/reports/ccus-in-clean-energy-transitions.

8.   Madejski, P., Chmiel, K., Subramanian, N. & Kuś, T. Methods and Techniques for CO_2 Capture: Review of Potential Solutions and Applications in Modern Energy Technologies. *Energies* 15, (2022).

9.   Raganati, F. & Ammendola, P. CO_2 Post-combustion Capture: A Critical Review of Current Technologies and Future Directions. *Energy and Fuels* 38, 13858–13905 (2024).

10.   Talei, S., Fozer, D., Varbanov, P. S., Szanyi, A. & Mizsey, P. Oxyfuel Combustion Makes Carbon Capture More Efficient. *ACS Omega* (2023)

11.   Alizadeh, S. M., Khalili, Y. & Ahmadi, M. Comprehensive Review of Carbon Capture and Storage Integration in Hydrogen Production: Opportunities, Challenges, and Future Perspectives. *Energies* 17, (2024).

12.   World Resoursces Institute. 7 Things to Know About Carbon Capture, Utilization and Sequestration. https://www.wri.org/insights/carbon-capture-technology.

13.   DNV. Energy Transition Outlook 2024. https://www.dnv.com/energy-transition-outlook/download/

14.   Maka, A. O. M. & Mehmood, M. Green hydrogen energy production: current status and potential. *Clean Energy* 8, 1–7 (2024).

15.   Massarweh, O., Al-khuzaei, M., Al-Shafi, M., Bicer, Y. & Abushaikha, A. S. Blue

hydrogen production from natural gas reservoirs: A review of application and feasibility. *J. CO₂ Util.* 70, 102438 (2023).

16. Ursúa, A., Gandía, L. M. & Sanchis, P. Hydrogen production from water electrolysis: Current status and future trends. *Proc. IEEE* 100, 410–426 (2012).

17. Maeda, K. & Domen, K. Photocatalytic water splitting: Recent progress and future challenges. *J. Phys. Chem. Lett.* 1, 2655–2661 (2010).

18. Aziz Aljar, M. A., Zulqarnain, M., Shah, A., Akhter, M. S. & Iftikhar, F. J. A review of renewable energy generation using modified titania for photocatalytic water splitting. *AIP Adv.* 10, (2020).

19. Wu, L. *et al.* Tuning the water-splitting mechanism on titanium dioxide surfaces through hydroxylation. *Phys. Chem. Chem. Phys.* 25, 9264–9272 (2023).

20. Catalyst Industry Data Book - Heterogeneous Catalyst and Homogeneous Catalyst Market Size, Share, Trends Analysis, And Segment Forecasts, 2023 - 2030. https://www.grandviewresearch.com/sector-report/catalyst-industry-data-book# (2023).

21. Fact.MR. Photocatalyst market. (2024) https://www.factmr.com/report/photocatalyst-market.

22. Tsiotsias, A. I. *et al.* Bimetallic Exsolved Heterostructures of Controlled Composition with Tunable Catalytic Properties. *ACS Nano* 16, 8904–8916 (2022).

23. Neagu, D., Tsekouras, G., Miller, D. N., Ménard, H. & Irvine, J. T. S. S. In situ growth of nanoparticles through control of non-stoichiometry. *Nat. Chem.* 5, 916–923 (2013).

24. Schlupp, M. V. F., Evans, A., Martynczuk, J. & Prestat, M. Micro-Solid Oxide Fuel Cell Membranes Prepared by Aerosol-Assisted Chemical Vapor Deposition. *Adv. Energy Mater.* 4, 1301383 (2014).

25. Kim, S. *et al.* Nanostructured Double Perovskite Cathode With Low Sintering Temperature For Intermediate Temperature Solid Oxide Fuel Cells. *ChemSusChem* 8, 3153–3158 (2015).

26. Neagu, D. *et al.* Nano-socketed nickel particles with enhanced coking resistance grown in situ by redox exsolution. *Nat. Commun.* 6, 8120 (2015).

27. Kwon, O., Joo, S., Choi, S., Sengodan, S. & Kim, G. Review on exsolution and its driving forces in perovskites. *JPhys Energy* 2, (2020).

28. Theofanidis, S. A., Loizidis, C., Heracleous, E. & Lemonidou, A. A. CO₂-oxidative ethane dehydrogenation over highly efficient carbon-resistant Fe-catalysts. *J. Catal.* 388, 52–65 (2020).

29. Yan, B., Yao, S. & Chen, J. G. Effect of Oxide Support on Catalytic Performance of FeNi-based Catalysts for CO₂-assisted Oxidative Dehydrogenation of Ethane. *ChemCatChem* 12, 494–503 (2020).

30. Jeong, M. H., Sun, J., Young Han, G., Lee, D. H. & Bae, J. W. Successive reduction-oxidation activity of FeOₓ/TiO₂ for dehydrogenation of ethane and subsequent CO₂ activation. *Appl. Catal. B Environ.* 270, 118887 (2020).

31. Tang, C., Kousi, K., Neagu, D. & Metcalfe, I. S. Trends and Prospects of Bimetallic

Exsolution. *Chem. - A Eur. J.* 27, 6666–6675 (2021).

32. Jiang, H.-L. & Xu, Q. Recent progress in synergistic catalysis over heterometallic nanoparticles. *J. Mater. Chem.* 21, 13705–13725 (2011).

33. Singh, A. K. & Xu, Q. Synergistic Catalysis over Bimetallic Alloy Nanoparticles. *ChemCatChem* 5, 652–676 (2013).

34. Calì, E. *et al.* Enhanced Stability of Iridium Nanocatalysts via Exsolution for the CO_2 Reforming of Methane. *ACS Appl. Nano Mater.* (2023)

35. Burnat, D. *et al.* Smart material concept: Reversible microstructural self-regeneration for catalytic applications. *J. Mater. Chem. A* 4, 11939–11948 (2016).

36. Kim, Y. H. *et al.* Nanoparticle Exsolution on Perovskite Oxides: Insights into Mechanism, Characteristics and Novel Strategies. *Nano-Micro Lett.* 16, 33 (2024).

37. A stand out family. *Nat. Mater.* 20, 1303–1303 (2021).

38. Goldschmidt, V. M. Die Gesetze der Krystallochemie. *Naturwissenschaften* 14, 477–485 (1926).

39. Zhang, M. *et al.* Recent development of perovskite oxide-based electrocatalysts and their applications in low to intermediate temperature electrochemical devices. *Mater. Today* 49, 351–377 (2021).

40. Zhu, H., Zhang, P. & Dai, S. Recent Advances of Lanthanum-Based Perovskite Oxides for Catalysis. *ACS Catal.* 5, 6370–6385 (2015).

41. Glazer, A. M. The classification of tilted octahedra in perovskites. *Acta Crystallogr. Sect. B Struct. Crystallogr. Cryst. Chem.* 28, 3384–3392 (1972).

42. Chen, H. *et al.* Activating Lattice Oxygen in Perovskite Oxide by B-Site Cation Doping for Modulated Stability and Activity at Elevated Temperatures. *Adv. Sci.* 8, 1–11 (2021).

43. Sun, Y. *et al.* A-Site Management Prompts the Dynamic Reconstructed Active Phase of Perovskite Oxide OER Catalysts. *Adv. Energy Mater.* 11, 2003755 (2021).

44. You, L. *et al.* Self-Regulated Chemical Substitution in a Highly Strained Perovskite Oxide. *Adv. Funct. Mater.* 32, 2112463 (2022).

45. Koo, B., Seo, J., Kim, J. K. & Jung, W. Isovalent doping: a new strategy to suppress surface Sr segregation of the perovskite O_2-electrode for solid oxide fuel cells. *J. Mater. Chem. A* 8, 13763–13769 (2020).

46. Stroud, D. & Ashcroft, N. W. Phase stability in binary alloys. *J. Phys. F Met. Phys.* 1, 113–124 (1971).

47. Tilley, R. J. D. Nonstoichiometry and Extrinsic Electronic Conductivity. in *Defects in Solids* 351–398 (2008).

48. Mizutani, U. & Sato, H. The Physics of the Hume-Rothery Electron Concentration Rule. *Crystals* vol. 7 (2017).

49. De Souza, R. A., Islam, M. S. & Ivers-Tiffée, E. Formation and migration of cation defects in the perovskite oxide $LaMnO_3$. *J. Mater. Chem.* 9, 1621–1627 (1999).

50. Jia, S. *et al.* Effect of oxygen vacancy concentration on the photocatalytic hydrogen evolution performance of anatase TiO_2: DFT and experimental studies. *J. Mater. Sci. Mater. Electron.* 32, 13369–13381 (2021).

51. Arandiyan, H. *et al.* Impact of Surface Defects on $LaNiO_3$ Perovskite Electrocatalysts for the Oxygen Evolution Reaction. *Chem. - A Eur. J.* 27, 14418–14426 (2021).

52. Sun, Y., Yang, J., Li, S. & Wang, D. Defect engineering in perovskite oxide thin films. *Chem. Commun.* 57, 8402–8420 (2021).

53. Phoon, B. L., Lai, C. W., Juan, J. C., Show, P. L. & Chen, W. H. A review of synthesis and morphology of $SrTiO_3$ for energy and other applications. *Int. J. Energy Res.* 43, 5151–5174 (2019).

54. Shannon, R. D. (1976). Revised effective ionic radii and systematic studies of interatomic distances in halides and chalcogenides. in *Acta Crystallographica Section A: Crystal Physics, Diffraction, Theoretical and General Crystallography* vol. 32 Vol. 32, pp. 751–767 (1976).

55. Brown, J. J., Ke, Z., Geng, W. & Page, A. J. Oxygen Vacancy Defect Migration in Titanate Perovskite Surfaces: Effect of the A-Site Cations. *J. Phys. Chem. C* 122, 14590–14597 (2018).

56. Patial, S. *et al.* Tunable photocatalytic activity of $SrTiO_3$ for water splitting: Strategies and future scenario. *J. Environ. Chem. Eng.* 8, 103791 (2020).

57. Jiang, J., Kato, K., Fujimori, H., Yamakata, A. & Sakata, Y. Investigation on the highly active $SrTiO_3$ photocatalyst toward overall H_2O splitting by doping Na ion. *J. Catal.* 390, 81–89 (2020).

58. Kawasaki, S. *et al.* Electronic Structure and Photoelectrochemical Properties of an Ir-Doped $SrTiO_3$ Photocatalyst. *J. Phys. Chem. C* 118, 20222–20228 (2014).

59. Plaza, M. *et al.* Structure of the Photo-catalytically Active Surface of $SrTiO_3$. *J. Am. Chem. Soc.* 138, 7816–7819 (2016).

60. Verbraeken, M. C. *et al.* Modified strontium titanates: From defect chemistry to SOFC anodes. *RSC Adv.* 5, 1168–1180 (2015).

61. Kopač, D., Likozar, B. & Huš, M. How Size Matters: Electronic, Cooperative, and Geometric Effect in Perovskite-Supported Copper Catalysts for CO_2 Reduction. *ACS Catal.* 10, 4092–4102 (2020).

62. Mizera, A., Kowalczyk, A., Chmielarz, L. & Drożdż, E. Catalysts based on strontium titanate doped with Ni/Co/Cu for dry reforming of methane. *Materials (Basel).* 14, (2021).

63. Jain, A. *et al.* Commentary: The materials project: A materials genome approach to accelerating materials innovation. *APL Mater.* 1, (2013).

64. Zhu, Z., Peelaers, H. & de Walle, C. G. Electronic and protonic conduction in $LaFeO_3$. *J. Mater. Chem. A* 5, 15367–15379 (2017).

65. Dumitru, R. *et al.* Lanthanum Ferrite Ceramic Powders: Synthesis, Characterization and Electrochemical Detection Application. *Mater. (Basel, Switzerland)* 13, (2020).

66. Ren, H. *et al.* Effective mineralization of p-nitrophenol by catalytic ozonation using Ce-substituted $La_{1-x}Ce_xFeO_3$ catalyst. *Chemosphere* 285, 131473 (2021).

67. Jia, L., Lloyd, M. D., Lees, M. R., Huang, L. & Walton, R. I. Limits of Solid Solution and Evolution of Crystal Morphology in $(La_{1-x}RE_x)FeO_3$ Perovskites by

Low Temperature Hydrothermal Crystallization. *Inorg. Chem.* 62, 4503–4513 (2023).

68. Lo Faro, M., Campagna Zignani, S. & Aricò, A. S. Lanthanum Ferrites-Based Exsolved Perovskites as Fuel-Flexible Anode for Solid Oxide Fuel Cells. *Materials* vol. 13 (2020).

69. Eyssler, A. *et al.* The Effect of the State of Pd on Methane Combustion in Pd-Doped $LaFeO_3$. *J. Phys. Chem. C* 114, 4584–4594 (2010).

70. Oh, D., Colombo, F. *et al.* Rocking chair-like movement of ex-solved nanoparticles on the Ni-Co doped $La_{0.6}Ca_{0.4}FeO_{3-\delta}$ oxygen carrier during chemical looping reforming coupled with CO_2 splitting. *Appl. Catal. B Environ.* 332, 122745 (2023).

71. Natali Sora, I., Felice, V., Zurlo, F., Licoccia, S. & Di Bartolomeo, E. Characterization of tantalum doped lanthanum strontium ferrite as cathode materials for solid oxide fuel cells. *J. Alloys Compd.* 648, 154–159 (2015).

72. Dai, X. *et al.* Reduction kinetics of lanthanum ferrite perovskite for the production of synthesis gas by chemical-looping methane reforming. *Chem. Eng. Sci.* 153, 236–245 (2016).

73. Marasi, M. *et al.* Ru-doped lanthanum ferrite as a stable and versatile electrode for reversible symmetric solid oxide cells (r-SSOCs). *J. Power Sources* 555, 232399 (2023).

74. Zhu, X., Li, K., Neal, L. M. & Li, F. Perovskites as Geo-inspired Oxygen Storage Materials for Chemical Looping and Three-Way Catalysis: A Perspective. *ACS Catal.* 8, 8213–8236 (2018).

75. Sastre, D., Serrano, D. P., Pizarro, P. & Coronado, J. M. Chemical insights on the activity of $La_{1-x}Sr_xFeO_3$ perovskites for chemical looping reforming of methane coupled with CO_2-splitting. *J. CO_2 Util.* 31, 16–26 (2019).

76. Taylor, D. D. *et al.* Oxygen Storage Properties of $La_{1-x}Sr_xFeO_{3-\delta}$ for Chemical-Looping Reactions–An In Situ Neutron and Synchrotron X-ray Study. *Chem. Mater.* 28, 3951–3960 (2016).

77. Neal, L. M., Shafiefarhood, A. & Li, F. Dynamic Methane Partial Oxidation Using a $Fe_2O_3@La_{0.8}Sr_{0.2}FeO_{3-\delta}$ Core–Shell Redox Catalyst in the Absence of Gaseous Oxygen. *ACS Catal.* 4, 3560–3569 (2014).

78. He, F. *et al.* The use of $La_{1-x}Sr_xFeO_3$ perovskite-type oxides as oxygen carriers in chemical-looping reforming of methane. *Fuel* 108, 465–473 (2013).

79. Shen, Z. *et al.* Increased activity in the oxygen evolution reaction by Fe^{4+}-induced hole states in perovskite $La_{1-x}Sr_xFeO_3$. *J. Mater. Chem. A* 8, 4407–4415 (2020).

80. Lee, W., Han, J. W., Chen, Y., Cai, Z. & Yildiz, B. Cation Size Mismatch and Charge Interactions Drive Dopant Segregation at the Surfaces of Manganite Perovskites. *J. Am. Chem. Soc.* 135, 7909–7925 (2013).

81. Barbero, B. P., Gamboa, J. A. & Cadús, L. E. Synthesis and characterisation of $La_{1-x}Ca_xFeO_3$ perovskite-type oxide catalysts for total oxidation of volatile organic compounds. *Appl. Catal. B Environ.* 65, 21–30 (2006).

82. Ullattil, S. G. & Periyat, P. Sol-Gel Synthesis of Titanium Dioxide. in 271–283

(2017).

83. Akira Fujishima, Tata N. Rao, D. A. T. Titanium dioxide photocatalysis. *J. Photochem. Photobiol. C Photochem. Rev.* 1, 1–21 (2010).

84. Kang, X. *et al. Titanium dioxide: From engineering to applications. Catalysts* vol. 9 (2019).

85. Gowland, D. C. A., Robertson, N. & Chatzisymeon, E. Photocatalytic Oxidation of Natural Organic Matter in Water. *Water* vol. 13 (2021).

86. Feng, X., Zhai, J. & Jiang, L. The fabrication and switchable superhydrophobicity of TiO_2 nanorod films. *Angew. Chemie - Int. Ed.* 44, 5115–5118 (2005).

87. Mragui, A. El, Logvina, Y., Luís Pinto da Silva, Zegaoui, O. & da Silva, J. C. G. E. Synthesis of Fe-and Co-doped TiO_2 with improved photocatalytic activity under visible irradiation toward carbamazepine degradation. *Materials (Basel).* 12, 4–6 (2019).

88. Bahadoran, A. *et al.* Photocatalytic Materials Obtained from E-Waste Recycling: Review, Techniques, Critique, and Update. *Journal of Manufacturing and Materials Processing* vol. 6 (2022).

89. Robert, D. & Malato, S. Solar photocatalysis: a clean process for water detoxification. *Sci. Total Environ.* 291, 85–97 (2002).

90. Kausar, F., Varghese, A., Pinheiro, D. & Devi K R, S. Recent trends in photocatalytic water splitting using titania based ternary photocatalysts-A review. *Int. J. Hydrogen Energy* 47, 22371–22402 (2022).

91. Nishioka, S., Osterloh, F. E., Wang, X., Mallouk, T. E. & Maeda, K. Photocatalytic water splitting. *Nat. Rev. Methods Prim.* 3, 1–15 (2023).

92. Agyekum, E. B., Nutakor, C., Agwa, A. M. & Kamel, S. A Critical Review of Renewable Hydrogen Production Methods: Factors Affecting Their Scale-Up and Its Role in Future Energy Generation. *Membranes (Basel).* 12, (2022).

93. Chen, X. & Mao, S. S. Titanium Dioxide Nanomaterials: Synthesis, Properties, Modifications, and Applications. *Chem. Rev.* 107, 2891–2959 (2007).

94. Sclafani, A. & Herrmann, J. M. Comparison of the photoelectronic and photocatalytic activities of various anatase and rutile forms of titania in pure liquid organic phases and in aqueous solutions. *J. Phys. Chem.* 100, 13655–13661 (1996).

95. Luttrell, T. *et al.* Why is anatase a better photocatalyst than rutile? - Model studies on epitaxial TiO_2 films. *Sci. Rep.* 4, 1–8 (2015).

96. Cardona, M. Y. P. Y. *Fundamentals of Semiconductors: Physics and Materials.* (2010).

97. Patra, S., Davoisne, C., Bouyanfif, H., Foix, D. & Sauvage, F. Phase stability frustration on ultra-nanosized anatase TiO_2. *Sci. Rep.* 5, 10928 (2015).

98. Holm, A. *et al.* Impact of rutile and anatase phase on the photocatalytic decomposition of lactic acid. *Appl. Catal. B Environ.* 253, 96–104 (2019).

99. Armaković, S. J. S., Savanović, M. M. & Armaković, S. J. S. Titanium Dioxide as the Most Used Photocatalyst for Water Purification: An Overview. *Catalysts* 13, (2023).

100. Verma, R., Gangwar, J. & Srivastava, A. K. Multiphase TiO_2 nanostructures: a review of efficient synthesis, growth mechanism, probing capabilities, and applications in bio-safety and health. *RSC Adv.* 7, 44199–44224 (2017).

101. Landmann, M., Rauls, E. & Schmidt, W. G. The electronic structure and optical response of rutile, anatase and brookite TiO_2. *J. Phys. Condens. Matter* 24, 195503 (2012).

102. Reyes-Coronado, D. *et al.* Phase-pure TiO_2 nanoparticles: anatase, brookite and rutile. *Nanotechnology* 19, 145605 (2008).

103. Horiuchi, Y., Toyao, T., Takeuchi, M., Matsuoka, M. & Anpo, M. Recent advances in visible-light-responsive photocatalysts for hydrogen production and solar energy conversion – from semiconducting TiO_2 to MOF/PCP photocatalysts. *Phys. Chem. Chem. Phys.* 15, 13243–13253 (2013).

104. Riedel, E. & Janiak, C. *Anorganische Chemie.* (de Gruyter GmbH & Co. KG, 2007).

105. Hoffmann, F. *Solid-State Chemistry.* (De Gruyter, 2023).

106. Hoppe, M. Magneto-electronic properties of ultrathin $NiFe_2O_4$ Magnetic, structural, and electronic properties of $NiFe_2O_4$ ultrathin films. (2016). ISBN 978-3-95806-122-4

107. West, A. R. *Solid state chemistry and its applications.* (John Wiley & Sons, Ltd, 2014).

108. Luksic, S. A., Riley, B. J., Schweiger, M. & Hrma, P. Incorporating technetium in minerals and other solids: A review. *J. Nucl. Mater.* 466, 526–538 (2015).

109. Tangcharoen, T. Structural, Degree of Inversion, and Magneton Number Studies on Fe^{3+}-Substituted MAl_2O_4 (M = Ni, Cu, Zn) Spinel Powders: The Evidence for Local Site Exchange of Cation and Magnetization Increment. *Phys. status solidi* 259, 2200240 (2022).

110. Hoffmann, F., Cornelius, M., Morell, J. & Fröba, M. Mesoporöse organisch-anorganische Hybridmaterialien auf Silicabasis. *Angew. Chemie* 118, 3290–3328 (2006).

111. Cornell, R. M. & Schwertmann, U. *The Iron Oxides. Synthesis* (Wiley, 2003).

112. Kozlenko, D. P. *et al.* Magnetic and electronic properties of magnetite across the high pressure anomaly. *Sci. Rep.* 9, 4464 (2019).

113. Ament, K., Wagner, D. R., Meij, F. E., Wagner, F. E. & Breu, J. High Temperature Stable Maghemite Nanoparticles Sandwiched between Hectorite Nanosheets. *Zeitschrift für Anorg. und Allg. Chemie* 646, 1110–1115 (2020).

114. Cushing, B. L., Kolesnichenko, V. L. & O'Connor, C. J. Recent advances in the liquid-phase syntheses of inorganic nanoparticles. *Chem. Rev.* 104, 3893–3946 (2004).

115. Sunde, T. O. L., Grande, T. & Einarsrud, M. Modified Pechini Synthesis of Oxide Powders and Thin Films. in *Handbook of Sol-Gel Science and Technology* 1–30 (Springer International Publishing, 2016).

116. Petrykin, V. & Kakihana, M. *Chemistry and applications of polymeric gel precursors. Handbook of Sol-Gel Science and Technology: Processing, Characterization and Applications* (2018).

117. Danks, A. E., Hall, S. R. & Schnepp, Z. The evolution of "sol-gel" chemistry as a technique for materials synthesis. *Mater. Horizons* 3, 91–112 (2016).

118. Kakihana, M. & Yoshimura, M. Synthesis and characteristics of complex multicomponent oxides prepared by polymer complex method. *Bulletin of the Chemical Society of Japan* vol. 72 1427–1443 (1999).

119. Brinker, C. J. & Scherer, G. W. *Sol-Gel Science. Materials Chemistry and Physics* (Elsevier, 1990).

120. Roy, R. Ceramics by the Solution-Sol-Gel Route. *Science (80-.).* 238, 1664–1669 (1987).

121. Pierre, A. *Introduction to Sol-Gel Processing.* (2020).

122. Hüsing, N. & Schubert, U. Porous Inorganic-Organic Hybrid Materials. in *Functional Hybrid Materials* 86–121 (Wiley, 2003).

123. Hüsing, N. & Schubert, U. *Synthesis of inorganic materials. Wiley VCH* (2005).

124. Hüsing, N. Porous Hybrid Materials. in *Hybrid Materials* 175–223 (2006).

125. Yang, P., Zhao, D., Margolese, D. I., Chmelka, B. F. & Stucky, G. D. Generalized syntheses of large-pore mesoporous metal oxides with semicrystalline frameworks. *Nature* 396, 152–155 (1998).

126. Tilley, R. J. D. *Defects in Solids. John Wiley & Sons, Inc.* (Wiley, 2008).

127. Tilley, R. J. D. Intrinsic and Extrinsic Defects in Insulators: Ionic Conductivity. in *Defects in Solids* 251–295 (2008).

128. Kröger, F. A. & Vink, H. J. Relations between the Concentrations of Imperfections in Crystalline Solids. *Solid State Phys.* 3, 307–435 (1956).

129. Tilley, R. J. D. Answers to Problems and Exercises. in *Defects in Solids* 495–505 (John Wiley & Sons, Inc., 2008).

130. De Souza, R. A. Oxygen Diffusion in $SrTiO_3$ and Related Perovskite Oxides. *Adv. Funct. Mater.* 25, 6326–6342 (2015).

131. Rudolph, B. Understanding Nickel Exsolution by Morphology And Composition Variation of the Perovskite Host Oxide. *PQDT - Global* (Universitaet Hamburg (Germany) PP - Germany, 2024).

132. Howard, S. A., Yau, J. K. & Anderson, H. U. Structural characteristics of $Sr_{1-x}La_xTi_{3+\delta}$ as a function of oxygen partial pressure at 1400 °C. 1492–1498 (1989).

133. Moos, R., Bischoff, T., Menesklou, W. & Härdtl, K. H. Solubility of lanthanum in strontium titanate in oxygen-rich atmospheres. *J. Mater. Sci.* 32, 4247–4252 (1997).

134. Calì, E. *et al.* Real-time insight into the multistage mechanism of nanoparticle exsolution from a perovskite host surface. *Nat. Commun.* 14, (2023).

135. Kang, W. *et al.* A motif for B/O-site modulation in $LaFeO_3$ towards boosted oxygen evolution. *Nanoscale* 16, 1823–1832 (2024).

136. Li, W. *et al.* High Cationic Dispersity Boosted Oxygen Reduction Reactivity in Multi-Element Doped Perovskites. *Adv. Funct. Mater.* 33, 2210496 (2023).

137. She, S. *et al.* Realizing High and Stable Electrocatalytic Oxygen Evolution for Iron-Based Perovskites by Co-Doping-Induced Structural and Electronic Modulation. *Adv. Funct. Mater.* 32, 2111091 (2022).

138. Tummino, M. L. *et al.* $Sr_{0.85}Ce_{0.15}Fe_{0.67}Co_{0.33-x}Cu_xO_3$ perovskite oxides: effect of B-site copper codoping on the physicochemical, catalytic and antibacterial properties upon UV or thermal activation. *Front. Environ. Eng.* 2, (2023).

139. Wang, J. *et al.* Fast Surface Oxygen Release Kinetics Accelerate Nanoparticle Exsolution in Perovskite Oxides. *J. Am. Chem. Soc.* 145, 1714–1727 (2023).

140. Lacz, A., Lach, R. & Drozdz, E. Effect of nickel addition on the physicochemical properties of $SrTiO_3$-based materials. *Ceram. Int.* 48, 24906–24914 (2022).

141. Zhu, Y. *et al.* Synergistically enhanced hydrogen evolution electrocatalysis by in situ exsolution of metallic nanoparticles on perovskites. *J. Mater. Chem. A* 6, 13582–13587 (2018).

142. Chien, A. C., Liao, B. Y., Chen, W. Y. & Chien, A. C. Studies of exsolution and catalytic activity of metal nanocatalysts from parent perovskite. *Catal. Sci. Technol.* 11, 4570–4580 (2021).

143. Papargyriou, D., Miller, D. N. & Irvine, J. T. S. Exsolution of Fe-Ni alloy nanoparticles from (La,Sr)(Cr,Fe,Ni)O₃ perovskites as potential oxygen transport membrane catalysts for methane reforming. *J. Mater. Chem. A* 7, 15812–15822 (2019).

144. Kim, J. *et al.* In-situ exsolution of bimetallic CoFe nanoparticles on (La,Sr)FeO₃ perovskite: Its effect on electrocatalytic oxidative coupling of methane. *Appl. Catal. B Environ.* 321, 122026 (2023).

145. Merkle, R. & Maier, J. Oxygen incorporation into Fe-doped SrTiO3: Mechanistic interpretation of the surface reaction. *Phys. Chem. Chem. Phys.* 4, 4140–4148 (2002).

146. Vračar, M. *et al.* Jahn-Teller distortion around Fe^{4+} in $Sr(Fe_xTi_{1-x})O_{3-\delta}$ from x-ray absorption spectroscopy, x-ray diffraction, and vibrational spectroscopy. *Phys. Rev. B* 76, 174107 (2007).

147. Rothschild, A., Menesklou, W., Tuller, H. L. & Ivers-Tiffée, E. Electronic Structure, Defect Chemistry, and Transport Properties of $SrTi_{1-x}Fe_xO_{3-y}$ Solid Solutions. *Chem. Mater.* 18, 3651–3659 (2006).

148. Schulze-Küppers, F. *et al.* Structural and functional properties of $SrTi_{1-x}Fe_xO_{3-\delta}$ ($0{\leqslant}x{\leqslant}1$) for the use as oxygen transport membrane. *Sep. Purif. Technol.* 147, 414–421 (2015).

149. Kim, N., Perry, N. H. & Ertekin, E. Atomic Modeling and Electronic Structure of Mixed Ionic–Electronic Conductor $SrTi_{1-x}Fe_xO_{3-x/2+\delta}$ Considered as a Mixture of $SrTiO_3$ and $Sr_2Fe_2O_5$. *Chem. Mater.* 31, 233–243 (2019).

150. Iervolino, G., Vaiano, V. & Rizzo, L. Visible light active Fe-doped TiO_2 for the oxidation of arsenite to arsenate in drinking water. *Chem. Eng. Trans.* 70, 1573–1578 (2018).

151. Wang, F., Shen, T., Fu, Z., Lu, Y. & Chen, C. Enhanced photocatalytic water-splitting performance using Fe-doped hierarchical TiO_2 ball-flowers. *Nanotechnology* 29, 35702 (2018).

152. Khan, M. A., Woo, S. I. & Yang, O.-B. Hydrothermally stabilized Fe(III) doped

titania active under visible light for water splitting reaction. *Int. J. Hydrogen Energy* 33, 5345–5351 (2008).

153. Matsubara, M., Saniz, R., Partoens, B. & Lamoen, D. Doping anatase TiO₂ with group V-b and VI-b transition metal atoms: a hybrid functional first-principles study. *Phys. Chem. Chem. Phys.* 19, 1945–1952 (2017).

154. Wu, M.-C., Lin, T.-H., Chih, J.-S., Hsiao, K.-C. & Wu, P.-Y. Niobium doping induced morphological changes and enhanced photocatalytic performance of anatase TiO₂. *Jpn. J. Appl. Phys.* 56, 04CP07 (2017).

155. Wang, H.-Y., Chen, J., Xiao, F.-X., Zheng, J. & Liu, B. Doping-induced structural evolution from rutile to anatase: formation of Nb-doped anatase TiO₂ nanosheets with high photocatalytic activity. *J. Mater. Chem. A* 4, 6926–6932 (2016).

156. Kuranov, D. *et al.* Effect of Donor Nb(V) Doping on the Surface Reactivity, Electrical, Optical and Photocatalytic Properties of Nanocrystalline TiO₂. *Materials (Basel).* 17, (2024).

157. Yue, J. *et al.* Mesoporous niobium-doped titanium dioxide films from the assembly of crystalline nanoparticles: study on the relationship between the band structure, conductivity and charge storage mechanism. *J. Mater. Chem. A* 5, 1978–1988 (2017).

158. Han, J., Cho, J., Kim, J.-C. & Ryoo, R. Confinement of Supported Metal Catalysts at High Loading in the Mesopore Network of Hierarchical Zeolites, with Access via the Microporous Windows. *ACS Catal.* 8, 876–879 (2018).

159. Jiang, S. P. Nanoscale and nano-structured electrodes of solid oxide fuel cells by infiltration: Advances and challenges. *Int. J. Hydrogen Energy* 37, 449–470 (2012).

160. Helveg, S. *et al.* Atomic-scale imaging of carbon nanofibre growth. *Nature* 427, 426–429 (2004).

161. Babucci, M., Guntida, A. & Gates, B. C. Atomically Dispersed Metals on Well-Defined Supports including Zeolites and Metal–Organic Frameworks: Structure, Bonding, Reactivity, and Catalysis. *Chem. Rev.* 120, 11956–11985 (2020).

162. Kim, J. H. *et al.* Nanoparticle Ex-solution for Supported Catalysts: Materials Design, Mechanism and Future Perspectives. *ACS Nano* 15, 81–110 (2021).

163. Sun, X. *et al.* Progress of Exsolved Metal Nanoparticles on Oxides as High Performance (Electro)Catalysts for the Conversion of Small Molecules. *Small* 17, 2005383 (2021).

164. Zhang, J., Gao, M.-R. R. & Luo, J.-L. L. In Situ Exsolved Metal Nanoparticles: A Smart Approach for Optimization of Catalysts. *Chem. Mater.* 32, 5424–5441 (2020).

165. Steiger, P., Burnat, D., Kröcher, O., Heel, A. & Ferri, D. Segregation of nickel/iron bimetallic particles from lanthanum doped strontium titanates to improve sulfur stability of solid oxide fuel cell anodes. *Catalysts* 9, (2019).

166. Kousi, K., Tang, C., Metcalfe, I. S. & Neagu, D. Emergence and Future of Exsolved Materials. *Small* 17, (2021).

167. Neagu, D. *et al.* Roadmap on exsolution for energy applications. *J. Phys. Energy* 5, 031501 (2023).

168. Gao, Y., Chen, D., Saccoccio, M., Lu, Z. & Ciucci, F. From material design to mechanism study: Nanoscale Ni exsolution on a highly active A-site deficient anode material for solid oxide fuel cells. *Nano Energy* 27, 499–508 (2016).

169. Neagu, D. & Irvine, J. T. S. Structure and properties of $La_{0.4}Sr_{0.4}TiO_3$ Ceramics for use as anode materials in solid oxide fuel cells. *Chem. Mater.* 22, 5042–5053 (2010).

170. Zhang, S. *et al.* Advances in CO2-assisted oxidative dehydrogenation of light alkanes to light alkenes. *ChemPhysChem* 202401073, (2025).

171. Kapokova, L. *et al.* Dry reforming of methane over $LnFe_{0.7}Ni_{0.3}O_{3-\delta}$ perovskites: Influence of Ln nature. *Catal. Today* 164, 227–233 (2011).

172. Papaioannou, E. I., Neagu, D., Ramli, W. K. W. W., Irvine, J. T. S. S. & Metcalfe, I. S. Sulfur-Tolerant, Exsolved Fe–Ni Alloy Nanoparticles for CO Oxidation. *Top. Catal.* 62, 1149–1156 (2019).

173. Li, G. *et al.* Bimetallic nanocrystals: Structure, controllable synthesis and applications in catalysis, energy and sensing. *Nanomaterials* 11, 1–37 (2021).

174. Kwon, O. *et al.* Self-assembled alloy nanoparticles in a layered double perovskite as a fuel oxidation catalyst for solid oxide fuel cells. *J. Mater. Chem. A* 6, 15947–15953 (2018).

175. Kwon, O. *et al.* Exsolution trends and co-segregation aspects of self-grown catalyst nanoparticles in perovskites. *Nat. Commun.* 8, 1–7 (2017).

176. Lv, Y. *et al.* High-efficiency perovskite solar cells enabled by anatase TiO_2 nanopyramid arrays with an oriented electric field. *Angew. Chemie* 132, 12067–12074 (2020).

177. Lv, H. *et al.* In Situ Investigation of Reversible Exsolution/Dissolution of CoFe Alloy Nanoparticles in a Co-Doped $Sr_2Fe_{1.5}Mo_{0.5}O_{6-\delta}$ Cathode for CO_2 Electrolysis. *Adv. Mater.* 32, 1–9 (2020).

178. Jiang, Y. *et al.* Highly Efficient B-Site Exsolution Assisted by Co Doping in Lanthanum Ferrite toward High-Performance Electrocatalysts for Oxygen Evolution and Oxygen Reduction. *ACS Sustain. Chem. Eng.* 8, 302–310 (2020).

179. Neagu, D. *et al.* Demonstration of chemistry at a point through restructuring and catalytic activation at anchored nanoparticles. *Nat. Commun.* 8, 1855 (2017).

180. Lv, H. *et al.* In situ exsolved $FeNi_3$ nanoparticles on nickel doped $Sr_2Fe_{1.5}Mo_{0.5}O_{6-\delta}$ perovskite for efficient electrochemical CO_2 reduction reaction. *J. Mater. Chem. A* 7, 11967–11975 (2019).

181. Papargyriou, D., Miller, D. N. & Sirr Irvine, J. T. Exsolution of Fe–Ni alloy nanoparticles from $(La,Sr)(Cr,Fe,Ni)O_3$ perovskites as potential oxygen transport membrane catalysts for methane reforming. *J. Mater. Chem. A* 7, 15812–15822 (2019).

182. Jiang, K., Liu, Z., Zhang, G. & Jin, W. A novel catalytic membrane reactor with homologous exsolution-based perovskite catalyst. *J. Memb. Sci.* 608, 118213 (2020).

183. Joo, S., Kwon, O., Kim, S., Jeong, H. Y. & Kim, G. Ni-Fe Bimetallic Nanocatalysts Produced by Topotactic Exsolution in Fe deposited $PrBaMn_{1.7}Ni_{0.3}O_{5+\delta}$ for Dry Reforming of Methane. *J. Electrochem. Soc.* 167, 064518 (2020).

184. Boudinar, N. *et al.* Formation of nanocrystalline Fe–Ni alloys powders by mechanical alloying method. *Adv. Mater. Process. Technol.* 1, 288–293 (2015).

185. Maulana, A., Arkundato, A., Sutisna & Trilaksana, H. Mechanical properties of Fe, Ni and Fe-Ni alloy: Strength and stiffness of materials using lammps molecular dynamics simulation. *AIP Conf. Proc.* 2314, 20008 (2020).

186. Owen, E. A., Yates, E. L. & Sully, A. H. An X-ray investigation of pure iron-nickel alloys. Part 5: the variation of lattice parameter with composition. *Proc. Phys. Soc.* 49, 323–325 (1937).

187. Lai, K. Y. & Manthiram, A. Self-Regenerating Co-Fe Nanoparticles on Perovskite Oxides as a Hydrocarbon Fuel Oxidation Catalyst in Solid Oxide Fuel Cells. *Chem. Mater.* 30, 2515–2525 (2018).

188. Liu, T. *et al.* Robust redox-reversible perovskite type steam electrolyser electrode decorated with in situ exsolved metallic nanoparticles. *J. Mater. Chem. A* 8, 582–591 (2020).

189. Lv, H. *et al.* In Situ Investigation of Reversible Exsolution/Dissolution of CoFe Alloy Nanoparticles in a Co-Doped $Sr_2Fe_{1.5}Mo_{0.5}O_{6-\delta}$ Cathode for CO_2 Electrolysis. *Adv. Mater.* 32, 1–9 (2020).

190. Zhang, C. *et al.* Influence of Oxidation Temperature on the Regeneration of a Commercial Pt-Sn/Al_2O_3 Propane Dehydrogenation Catalyst. *Catalysts* vol. 14 (2024).

191. Khouw, C. B. & Davis, M. E. Catalytic Activity of Titanium Silicates Synthesized in the Presence of Alkali-Metal and Alkaline-Earth Ions. *J. Catal.* 151, 77–86 (1995).

192. Liu, Z. & Wang, R. Contributions of Support Effect to Impregnated Cobalt CeO_2 and SiO_2 Catalysts. *Microsc. Microanal.* 23, 1890–1891 (2017).

193. Calì, E. *et al.* Enhanced Stability of Iridium Nanocatalysts via Exsolution for the CO_2 Reforming of Methane. *ACS Appl. Nano Mater.* 7, 18398–18409 (2024).

194. Joo, S. *et al.* Enhancing Thermocatalytic Activities by Upshifting the d-Band Center of Exsolved Co-Ni-Fe Ternary Alloy Nanoparticles for the Dry Reforming of Methane. *Angew. Chemie Int. Ed.* 60, 15912–15919 (2021).

195. Carrillo, A. J. & Serra, J. M. Exploring the Stability of Fe–Ni Alloy Nanoparticles Exsolved from Double-Layered Perovskites for Dry Reforming of Methane. *Catalysts* vol. 11 4–6 (2021).

196. Tsekouras, G., Neagu, D. & Irvine, J. T. S. Step-change in high temperature steam electrolysis performance of perovskite oxide cathodes with exsolution of B-site dopants. *Energy Environ. Sci.* 6, 256–266 (2013).

197. Steiger, P., Kröcher, O. & Ferri, D. Increased nickel exsolution from $LaFe_{0.8}Ni_{0.2}O_3$ perovskite-derived CO_2 methanation catalysts through strontium doping. *Appl. Catal. A Gen.* 590, 117328 (2020).

198. Komarala, E. P., Komissarov, I. & Rosen, B. A. Effect of fe and mn substitution in $LaNiO_3$ on exsolution, activity, and stability for methane dry reforming. *Catalysts* 10, (2020).

199. Lv, H. *et al.* In Situ Investigation of Reversible Exsolution/Dissolution of CoFe Alloy Nanoparticles in a Co-Doped $Sr_2Fe_{1.5}Mo_{0.5}O_{6-\delta}$ Cathode for CO_2 Electrolysis. *Adv. Mater.* 32, (2020).

200. Baena-Moreno, F. M. *et al.* Carbon capture and utilization technologies: a literature review and recent advances. *Energy Sources, Part A Recover. Util. Environ. Eff.* 41, 1403–1433 (2019).

201. Zhang, S. *et al.* Advances in CO_2-assisted oxidative dehydrogenation of light alkanes to light alkenes. *ChemPhysChem* 202401073, (2025).

202. Heracleous, E., Lee, A. F., Wilson, K. & Lemonidou, A. A. Investigation of Ni-based alumina-supported catalysts for the oxidative dehydrogenation of ethane to ethylene: structural characterization and reactivity studies. *J. Catal.* 231, 159–171 (2005).

203. Yan, B. *et al.* Dry Reforming of Ethane and Butane with CO_2 over $PtNi/CeO_2$ Bimetallic Catalysts. *ACS Catal.* 6, 7283–7292 (2016).

204. Yan, B. *et al.* Active sites for tandem reactions of CO_2 reduction and ethane dehydrogenation. *Proc. Natl. Acad. Sci. U. S. A.* 115, 8278–8283 (2018).

205. Bragg, W. H. & Bragg, W. L. The structure of some crystals as indicated by their diffraction of X-rays. *Proc. R. Soc. Lond. A* 89, 248–277 (1913).

206. Tilley, R. J. D. *Understanding Solids. Understanding Solids* (John Wiley & Sons, Ltd, 2004).

207. Suryanarayana, C. & Norton, M. G. *X-Ray Diffraction.* (Springer New York, NY, 1998).

208. Von Dreele, R. B. & Toby, B. H. X-Ray Powder Diffraction. in *Characterization of Materials* 1–23 (Wiley, 2012).

209. Holzwarth, U. & Gibson, N. The Scherrer equation versus the "Debye-Scherrer equation." *Nat. Nanotechnol.* 6, 534–534 (2011).

210. Wang, M., Árnadóttir, L., Xu, Z. J. & Feng, Z. In Situ X-ray Absorption Spectroscopy Studies of Nanoscale Electrocatalysts. *Nano-Micro Lett.* 11, 47 (2019).

211. Müller, O., Nachtegaal, M., Just, J., Lützenkirchen-Hecht, D. & Frahm, R. Quick-EXAFS setup at the SuperXAS beamline for in situ X-ray absorption spectroscopy with 10 ms time resolution. *J. Synchrotron Radiat.* 23, 260–266 (2016).

212. Fracchia, M., Ghigna, P., Vertova, A., Rondinini, S. & Minguzzi, A. Time-Resolved X-ray Absorption Spectroscopy in (Photo)Electrochemistry. *Surfaces* 1, 138–150 (2018).

213. Caliebe, W. A., Murzin, V., Kalinko, A. & Görlitz, M. High-flux XAFS-beamline P64 at PETRA III. *AIP Conf. Proc.* 2054, 60031 (2019).

214. Newville, M. Fundamentals of XAFS. *Rev. Mineral. Geochemistry* 78, 33–74 (2014).

215. Evans, J. *X-Ray Absorption Spectroscopy for the Chemical and Materials Sciences.* (Wiley, 2018).

216. Iglesias-Juez, A. *et al.* Experimental methods in chemical engineering: X-ray absorption spectroscopy–XAS, XANES, EXAFS. *Can. J. Chem. Eng.* 100, 3–22 (2022).

217. Ohnuma, T. & Kobayashi, T. X-ray absorption near edge structure simulation of

LiNi$_{0.5}$Co$_{0.2}$Mn$_{0.3}$O$_2$: Via first-principles calculation. *RSC Adv.* 9, 35655–35661 (2019).

218. Rui, N. *et al.* Highly active Ni/CeO$_2$ catalyst for CO$_2$ methanation: Preparation and characterization. *Appl. Catal. B Environ.* 282, 119581 (2021).

219. Henderson, G. S., Groot, F. M. F. De & Moulton, B. J. A. X-ray Absorption Near-Edge Structure (XANES) Spectroscopy. *Rev. Mineral. Geochemistry* 78, 75–138 (2014).

220. Baumgarten, L., Angst, M., Brückel, T., Richter, D. & Zorn, R. F04: X-ray Absorption Spectroscopy. in vol. 33 F4.1-F4.37 (2012).

221. Thommes, M. *et al.* Physisorption of gases, with special reference to the evaluation of surface area and pore size distribution (IUPAC Technical Report). *Pure Appl. Chem.* 87, 1051–1069 (2015).

222. Rouquerol, F., Rouquerol, J., Sing, K. S. W., Llewellyn, P. & Maurin, G. *Adsorption by Powders and Porous Solids. Climate Change 2013 - The Physical Science Basis* (Elsevier Ltd., 2014).

223. Thommes, M. Physical adsorption characterization of nanoporous materials. *Chemie-Ingenieur-Technik* 82, 1059–1073 (2010).

224. Emmett, P. H. & Brunauer, S. The Use of Low Temperature van der Waals Adsorption Isotherms in Determining the Surface Area of Iron Synthetic Ammonia Catalysts. *J. Am. Chem. Soc.* 59, 1553–1564 (1937).

225. Brunauer, S., Emmett, P. H. & Teller, E. Adsorption of Gases in Multimolecular Layers. *J. Am. Chem. Soc.* 60, 309–319 (1938).

226. Arena, F. *et al.* Factors Controlling the Energy of Nitrogen Monolayer Coverage on High Surface Area Catalyst Oxide Carriers. *J. Phys. Chem. C* 115, 24728–24733 (2011).

227. Lu, G. Q. & Zhao, X. S. *Nanoporous Materials: Science and Engineering.* vol. 4 (Imperial College Press, 2004).

228. Metrane, A., Delhali, A., Ouikhalfan, M., Assen, A. H. & Belmabkhout, Y. Water Vapor Adsorption by Porous Materials: From Chemistry to Practical Applications. *J. Chem. Eng. Data* 67, 1617–1653 (2022).

229. Condon, J. B. Measuring the Physisorption Isotherm. in *Surface Area and Porosity Determinations by Physisorption* (ed. Condon, J. B. B. T.-S. A. and P. D. by P.) 29–53 (Elsevier, 2006).

230. Instruments, Q. V-STAR Vapor Sorption Analyzer Operating Manual. (2014).

231. Instruments, Q. *Aquadyne Dvs operating manual^{TM}.* (2014).

232. Egerton, R. F. *Physical Principles of Electron Microscopy. An Introduction to TEM, SEM, and AEM.* (2005).

233. Fultz, B. & Howe, J. *Transmission Electron Microscopy and Diffractometry of Materials.* vol. 91.

234. Fahlman, B. D. *Materials Chemistry. Materials Chemistry* (Springer International Publishing, 2023).

235. Williams, D. B., C. Barry Carter & Carter, C. B. *Transmission Electron*

Microscopy. A Textbook for Materials Science. vol. 36 (Springer, 2009).

236. Reed, S. J. B. Electron probe microanalysis. in *Microprobe Techniques in the Earth Sciences* 49–89 (Springer US, 1995).

237. Tivol, W. F. Selected Area Electron Diffraction and its Use in Structure Determination. *Micros. Today* 18, 22–28 (2010).

238. Harris, D. C. Quantitative Chemical Analysis. in *Methods in Geochemistry and Geophysics* (2007).

239. Yadav, L. D. S. *Organic Spectroscopy. Organic Spectroscopy* (Springer-Science+Business Media, B.V., 2005).

240. Mayerhöfer, T. G., Mutschke, H. & Popp, J. Employing Theories Far beyond Their Limits–The Case of the (Boguer-) Beer–Lambert Law. *ChemPhysChem* 1948–1955 (2016).

241. Agustsson, J., Akermann, O., Barry, D. A. & Rossi, L. Non-contact assessment of COD and turbidity concentrations in water using diffuse reflectance UV-Vis spectroscopy. *Environ. Sci. Process. Impacts* 16, 1897–1902 (2014).

242. Kortüm, G. & Schreyer, G. Über die Gültigkeit der Kubelka-Munk-Funktion für Reflexionsspektren an Pulvern. *Zeitschrift fur Naturforsch. - Sect. A J. Phys. Sci.* 11, 1018–1022 (1956).

243. Myrick, M. L. *et al.* The kubelka-munk diffuse reflectance formula revisited. *Appl. Spectrosc. Rev.* 46, 140–165 (2011).

244. Kubelka, P. & Munk, F. The Kubelka-Munk Theory of Reflectance. *Zeitschrift für Tech. Phys.* 12, 593–601 (1931).

245. Tauc, J., Grigorovici, R. & Vancu, A. Optical Properties and Electronic Structure of Amorphous Germanium. *Phys. Status Solidi Basic Res.* 15, 627–637 (1966).

246. Perkins, W. D. Topics in chemical instrumentation: Fourier transform infrared spectroscopy: Part III. Applications. *J. Chem. Educ.* 64, 5–10 (1987).

247. Sun, M., Fang, Y., Zhang, Z. & Xu, H. Activated vibrational modes and Fermi resonance in tip-enhanced Raman spectroscopy. *Phys. Rev. E* 87, 20401 (2013).

248. Kayaalp, B. Design strategies towards $SrTiO_3$ based perovskite nanostructures for environmental catalysis. (2019).

249. Loutherback, K., Birarda, G., Chen, L. & N. Holman, H.-Y. Microfluidic approaches to synchrotron radiation-based Fourier transform infrared (SR-FTIR) spectral microscopy of living biosystems. *Protein Pept. Lett.* 23, 273–282 (2016).

250. Blum, M.-M. & John, H. Historical perspective and modern applications of Attenuated Total Reflectance – Fourier Transform Infrared Spectroscopy (ATR-FTIR). *Drug Test. Anal.* 4, 298–302 (2012).

251. Bianchi, C. L., Djellabi, R., Ponti, A., Patience, G. S. & Falletta, E. Experimental methods in chemical engineering: Mössbauer spectroscopy. *Can. J. Chem. Eng.* 99, 2105–2114 (2021).

252. Neagu, D. *et al.* In Situ Observation of Nanoparticle Exsolution from Perovskite Oxides: From Atomic Scale Mechanistic Insight to Nanostructure Tailoring. *ACS Nano* 13, 12996–13005 (2019).

253. Otto, S. K. *et al.* Exsolved Nickel Nanoparticles Acting as Oxygen Storage Reservoirs and Active Sites for Redox CH4 Conversion. *ACS Appl. Energy Mater.* 2, 7288–7298 (2019).

254. Chen, X., Pei, J., Guo, Y., Ning, Y. & Fu, Q. In Situ Probing Dynamic Exsolution of Fe0 from Perovskite under Graded Potentials. *J. Phys. Chem. Lett.* 2245–2253 (2025).

255. Kim, Y. H., Jeong, H., Won, B. R. & Myung, J. ha. Exsolution Modeling and Control to Improve the Catalytic Activity of Nanostructured Electrodes. *Adv. Mater.* 35, 1–10 (2023).

256. Rudolph, B. *et al.* Nanoparticle Exsolution from Nanoporous Perovskites for Highly Active and Stable Catalysts. *Adv. Sci.* 10, 1–12 (2023).

257. Arandiyan, H. *et al.* In Situ Exsolution of Bimetallic Rh–Ni Nanoalloys: a Highly Efficient Catalyst for CO_2 Methanation. *ACS Appl. Mater. Interfaces* 10, 16352–16357 (2018).

258. Ruh, T., Berkovec, D., Schrenk, F. & Rameshan, C. Exsolution on perovskite oxides: morphology and anchorage of nanoparticles. *Chem. Commun.* 59, 3948–3956 (2023).

259. Tian, Y. *et al.* Phase transition with in situ exsolution nanoparticles in the reduced $Pr_{0.5}Ba_{0.5}Fe_{0.8}Ni_{0.2}O_{3-\delta}$ electrode for symmetric solid oxide cells. *J. Mater. Chem. A* 10, 16490–16496 (2022).

260. Najimu, M., Jo, S. & Gilliard-AbdulAziz, K. L. Co-Exsolution of Ni-Based Alloy Catalysts for the Valorization of Carbon Dioxide and Methane. *Acc. Chem. Res.* 56, 3132–3141 (2023).

261. Wong, Y. J. *et al.* Development of Co Supported on Co−Al Spinel Catalysts from Exsolution of Amorphous Co−Al Oxides for Carbon Dioxide Reforming of Methane. *ChemCatChem* 11, 5593–5605 (2019).

262. Ali, S. A. *et al.* Engineering exsolved catalysts for CO_2 conversion. *Front. Energy Res.* 11, 1–9 (2023).

263. Schrenk, F. *et al.* Impact of nanoparticle exsolution on dry reforming of methane: Improving catalytic activity by reductive pre-treatment of perovskite-type catalysts. *Appl. Catal. B Environ.* 318, 121886 (2022).

264. Gao, Y. *et al.* Energetics of Nanoparticle Exsolution from Perovskite Oxides. *J. Phys. Chem. Lett.* 9, 3772–3778 (2018).

265. Li, Q., Zhu, Z., Zhou, J. & Wu, K. Exsolution of Alloyed Nanoparticles in Perovskite Oxide by Plasma. in *2024 IEEE International Conference on Plasma Science (ICOPS)* 1 (2024).

266. Guo, J. *et al.* Low-Temperature Exsolution of Ni–Ru Bimetallic Nanoparticles from A-Site Deficient Double Perovskites. *Small* 18, 2107020 (2022).

267. Cong, Y. *et al.* Cation-Exchange-Induced Metal and Alloy Dual-Exsolution in Perovskite Ferrite Oxides Boosting the Performance of Li-O_2 Battery. *Angew. Chemie Int. Ed.* 60, 23380–23387 (2021).

268. Kim, Y. H. *et al.* Nanoparticle Exsolution on Perovskite Oxides: Insights into

Mechanism, Characteristics and Novel Strategies. *Nano-Micro Letters* vol. 16 (Springer Nature Singapore, 2024).

269. Sun, Z. *et al.* Recent advances in exsolved perovskite oxide construction: exsolution theory, modulation, challenges, and prospects. *J. Mater. Chem. A* 11, 17961–17976 (2023).

270. Zhu, T., Troiani, H. E., Mogni, L. V., Han, M. & Barnett, S. A. Ni-Substituted Sr(Ti,Fe)O$_3$ SOFC Anodes: Achieving High Performance via Metal Alloy Nanoparticle Exsolution. *Joule* 2, 478–496 (2018).

271. Sun, Y. *et al.* A-site deficient perovskite: The parent for in situ exsolution of highly active, regenerable nano-particles as SOFC anodes. *J. Mater. Chem. A* 3, 11048–11056 (2015).

272. Zou, Q., Zhu, Z. & Yuan, Z. Bimetallic FeNi Alloy Nanoparticles Grown on Graphene for Efficient Removal of Congo Red From Aqueous Solution. *Adv. Sustain. Syst.* 7, 2200405 (2023).

273. Lv, H. *et al.* Promoting exsolution of RuFe alloy nanoparticles on Sr$_2$Fe$_{1.4}$Ru$_{0.1}$Mo$_{0.5}$O$_{6-\delta}$ via repeated redox manipulations for CO$_2$ electrolysis. *Nat. Commun.* 12, (2021).

274. Kim, J. *et al.* In-situ exsolution of bimetallic CoFe nanoparticles on (La,Sr)FeO$_3$ perovskite: Its effect on electrocatalytic oxidative coupling of methane. *Appl. Catal. B Environ.* 321, 122026 (2023).

275. Neagu, D. *et al.* In Situ Observation of Nanoparticle Exsolution from Perovskite Oxides: From Atomic Scale Mechanistic Insight to Nanostructure Tailoring. *ACS Nano* 13, 12996–13005 (2019).

276. Kumar, A. *et al.* Probing the electronic and local structure of Sr$_{2-x}$La$_x$CoNbO$_6$ using near-edge and extended x-ray absorption fine structures. *Phys. Rev. B* 105, 245155 (2022).

277. Vijayaraghavan, T., Sivasubramanian, R., Hussain, S. & Ashok, A. A Facile Synthesis of LaFeO$_3$-Based Perovskites and Their Application towards Sensing of Neurotransmitters. *ChemistrySelect* 2, 5570–5577 (2017).

278. Han, S., Tao, Y., Liu, Y., Lu, Y. & Pan, Z. Preparation of Monolithic LaFeO$_3$ and Catalytic Oxidation of Toluene. *Mater. (Basel, Switzerland)* 16, (2023).

279. Simon, C. *et al.* Magnetic NiFe$_2$O$_4$ Nanoparticles Prepared via Non-Aqueous Microwave-Assisted Synthesis for Application in Electrocatalytic Water Oxidation. *Chem. – A Eur. J.* 27, 16990–17001 (2021).

280. Šepelák, V. *et al.* Nanocrystalline nickel ferrite, NiFe$_2$O$_4$: Mechanosynthesis, nonequilibrium cation distribution, canted spin arrangement, and magnetic behavior. *J. Phys. Chem. C* 111, 5026–5033 (2007).

281. Kamali, S. *et al.* Extracting the cation distributions in NiFe$_{2-x}$Al$_x$O$_4$ solid solutions using magnetic Compton scattering. *J. Phys. Condens. Matter* 27, 456003 (2015).

282. Lilova, K. I., Shih, K., Pao, C. W., Lee, J. F. & Navrotsky, A. Thermodynamics of NiAl$_2$O$_4$-NiFe$_2$O$_4$ spinel solid solutions. *J. Am. Ceram. Soc.* 95, 423–430 (2012).

283. Timoshenko, J. & Roldan Cuenya, B. In Situ/ Operando Electrocatalyst

Characterization by X-ray Absorption Spectroscopy. *Chem. Rev.* 121, 882–961 (2021).

284. Blanchard, P. E. R., Grosvenor, A. P., Cavell, R. G. & Mar, A. Effects of metal substitution in transition-metal phosphides $(Ni_{1-x}M'_x)2P$ (M′ = Cr, Fe, Co) studied by X-ray photoelectron and absorption spectroscopy. *J. Mater. Chem.* 19, 6015–6022 (2009).

285. Tan, Y.-Y. *et al.* Probing temperature effects on lattice distortion and oxidation resistance of high-entropy alloys by in situ SR-XRD and XANES. *J. Mater. Res.* 36, 4413–4425 (2021).

286. Gustafsson, J. P. *et al.* A Probabilistic Approach to Phosphorus Speciation of Soils Using P K-edge XANES Spectroscopy with Linear Combination Fitting. *Soil Systems* vol. 4 (2020).

287. Grindley, N. D. F., Grindley, J. N. & Anderson, E. S. R factor compatibility groups. *Mol. Gen. Genet. MGG* 119, 287–297 (1972).

288. Hirotsu, C. Cumulative chi-squared statistic as a tool for testing goodness of fit. *Biometrika* 73, 165–173 (1986).

289. Ajiboye, B., Akinremi, O. O. & Jürgensen, A. Experimental Validation of Quantitative XANES Analysis for Phosphorus Speciation. *Soil Sci. Soc. Am. J.* 71, 1288–1291 (2007).

290. Gaur, A., Shrivastava, B. D. & Joshi, S. K. Copper K-edge XANES of Cu(I) and Cu(II) oxide mixtures. *J. Phys. Conf. Ser.* 190, 12084 (2009).

291. Yu, J. *et al.* Oxygen-Deficient Engineering for Perovskite Oxides in the Application of AOPs: Regulation, Detection, and Reduction Mechanism. *Catalysts* vol. 13 (2023).

292. Kubicek, M., Bork, A. H. & Rupp, J. L. M. Perovskite oxides-a review on a versatile material class for solar-to-fuel conversion processes. *J. Mater. Chem. A* 5, 11983–12000 (2017).

293. Managutti, P. B. *et al.* Exsolution of Ni Nanoparticles from A-Site-Deficient Layered Double Perovskites for Dry Reforming of Methane and as an Anode Material for a Solid Oxide Fuel Cell. *ACS Appl. Mater. Interfaces* 13, 35719–35728 (2021).

294. Bonkowski, A. *et al.* A Single Model for the Thermodynamics and Kinetics of Metal Exsolution from Perovskite Oxides. *J. Am. Chem. Soc.* 146, 23012–23021 (2024).

295. Guo, J., Berenov, A. & Skinner, S. J. In situ investigation of ruthenium doped lanthanum nickel titanium double perovskite and its exsolution behaviour. *Nanoscale Adv.* 6, 4394–4406 (2024).

296. Ortiz-Quiñonez, J.-L. L., Pal, U. & Villanueva, M. S. Structural, Magnetic, and Catalytic Evaluation of Spinel Co, Ni, and Co-Ni Ferrite Nanoparticles Fabricated by Low-Temperature Solution Combustion Process. *ACS Omega* 3, 14986–15001 (2018).

297. Han, L. *et al.* Interrogation of 3d Transition Bimetallic Nanocrystal Nucleation and Growth Using In Situ Electron Microscope and Synchrotron X-ray Techniques. *Nano Lett.* 24, 7645–7653 (2024).

298. Kyriakou, V. *et al.* Symmetrical Exsolution of Rh Nanoparticles in Solid Oxide Cells for Efficient Syngas Production from Greenhouse Gases. *ACS Catal.* 10, 1278–1288 (2020).

299. Owen, E. A., Yates, E. L. & Sully, A. H. An X-ray investigation of pure iron-nickel alloys. Part 5: The variation of thermal expansion with composition. *Proc. Phys. Soc.* 49, 323–325 (1937).

300. Mazlan, N. W., Murat, M. S., Tseng, C.-J., Hassan, O. H. & Osman, N. Lattice Expansion and Crystallite Size Analyses of $NiO-BaCe_{0.54}Zr_{0.36}Y_{0.1}O_{3-\delta}$ Anode Composite for Proton Ceramic Fuel Cells Application. *Energies* vol. 15 (2022).

301. Song, D. *et al.* Unraveling the atomic interdiffusion mechanism of $NiFe_2O_4$ oxygen carriers during chemical looping CO_2 conversion. *Carbon Energy* 6, 1–17 (2024).

302. Andersen, H. L. *et al.* Crystalline and magnetic structure–property relationship in spinel ferrite nanoparticles. *Nanoscale* 10, 14902–14914 (2018).

303. Hölscher, J., Andersen, H. L., Saura-Múzquiz, M., Garbus, P. G. & Christensen, M. Correlation between microstructure, cation distribution and magnetism in $Ni_{1-x}Zn_xFe_2O_4$ nanocrystallites. *CrystEngComm* 22, 515–524 (2020).

304. de Ligny, D. & Richet, P. High-temperature heat capacity and thermal expansion of $SrTiO_3$ and $SrZrO_3$ perovskites. *Phys. Rev. B* 53, 3013–3022 (1996).

305. Sahu, S. K., Maram, P. S. & Navrotsky, A. Thermodynamics of Nanoscale Calcium and Strontium Titanate Perovskites. *J. Am. Ceram. Soc.* 96, 3670–3676 (2013).

306. Lavrentiev, M. Y., Wróbel, J. S., Nguyen-Manh, D. & Dudarev, S. L. Magnetic and thermodynamic properties of face-centered cubic Fe–Ni alloys. *Phys. Chem. Chem. Phys.* 16, 16049–16059 (2014).

307. Guenzburger, D. & Terra, J. Theoretical study of magnetism and Mössbauer hyperfine interactions in ordered FeNi and disordered fcc Fe-rich Fe--Ni alloys. *Phys. Rev. B* 72, 24408 (2005).

308. Liu, S., Liu, Q. & Luo, J.-L. Highly Stable and Efficient Catalyst with In Situ Exsolved Fe–Ni Alloy Nanospheres Socketed on an Oxygen Deficient Perovskite for Direct CO_2 Electrolysis. *ACS Catal.* 6, 6219–6228 (2016).

309. Liu, S., Chuang, K. T. & Luo, J. L. Double-Layered Perovskite Anode with in Situ Exsolution of a Co-Fe Alloy to Cogenerate Ethylene and Electricity in a Proton-Conducting Ethane Fuel Cell. *ACS Catal.* 6, 760–768 (2016).

310. Zeng, D. *et al.* Enhanced hydrogen production performance through controllable redox exsolution within $CoFeAlO_x$ spinel oxygen carrier materials. *J. Mater. Chem. A* 6, 11306–11316 (2018).

311. Joo, S. *et al.* Highly active dry methane reforming catalysts with boosted in situ grown Ni-Fe nanoparticles on perovskite via atomic layer deposition. *Sci. Adv.* 6, 1–9 (2020).

312. Oh, D. *et al.* Rocking chair-like movement of ex-solved nanoparticles on the Ni-Co doped $La_{0.6}Ca_{0.4}FeO_{3-\delta}$ oxygen carrier during chemical looping reforming coupled with CO_2 splitting. *Appl. Catal. B Environ.* 332, 122745 (2023).

313. Lavrentiev, M. Y., Wróbel, J. S., Nguyen-Manh, D. & Dudarev, S. L. Magnetic and

thermodynamic properties of face-centered cubic Fe-Ni alloys. *Phys. Chem. Chem. Phys.* 16, 16049–16059 (2014).

314. Sun, Y. F. *et al.* A-site-deficiency facilitated in situ growth of bimetallic Ni-Fe nano-alloys: a novel coking-tolerant fuel cell anode catalyst. *Nanoscale* 7, 11173–11181 (2015).

315. Kayaalp, B. *et al.* Template-free mesoporous $La_{0.3}Sr_{0.7}Fe_xTi_{1-x}O_{3\pm\delta}$ with superior oxidation catalysis performance. *Appl. Catal. B Environ.* 245, 536–545 (2019).

316. Dacquin, J. P. *et al.* Influence of preparation methods of LaCoO₃ on the catalytic performances in the decomposition of N_2O. *Appl. Catal. B Environ.* 91, 596–604 (2009).

317. Conner, W. C. & Falconer, J. L. Spillover in Heterogeneous Catalysis. 759–788 (1995).

318. Chen, J. *et al.* Reverse oxygen spillover triggered by CO adsorption on Sn-doped Pt/TiO_2 for low-temperature CO oxidation. *Nat. Commun.* 14, 3477 (2023).

319. Yan, Z. *et al.* Insights into reverse oxygen spillover effect induced via CeO2 modulation to enhance the stability of CuCoOx catalysts in hydrodeoxygenation of biomass derivatives. *Appl. Catal. B Environ. Energy* 358, 124389 (2024).

320. Mao, M. *et al.* Solar-light-driven CO_2 reduction by methane on Pt nanocrystals partially embedded in mesoporous CeO_2 nanorods with high light-to-fuel efficiency. *Green Chem.* 20, 2857–2869 (2018).

321. Lykhach, Y. *et al.* Microscopic Insights into Methane Activation and Related Processes on Pt/Ceria Model Catalysts. *ChemPhysChem* 11, 1496–1504 (2010).

322. Gareev, K. G. Diversity of Iron Oxides: Mechanisms of Formation, Physical Properties and Applications. *Magnetochemistry* vol. 9 (2023).

323. Tsiotsias, A. I. *et al.* A comparative study of Ni catalysts supported on Al_2O_3, $MgO–CaO–Al_2O_3$ and $La_2O_3–Al_2O_3$ for the dry reforming of ethane. *Int. J. Hydrogen Energy* 47, 5337–5353 (2022).

324. Tsiotsias, A. I. *et al.* Towards maximizing conversion of ethane and carbon dioxide into synthesis gas using highly stable Ni-perovskite catalysts. *J. CO_2 Util.* 61, 102046 (2022).

325. Myint, M. N. Z., Yan, B., Wan, J., Zhao, S. & Chen, J. G. Reforming and oxidative dehydrogenation of ethane with CO_2 as a soft oxidant over bimetallic catalysts. *J. Catal.* 343, 168–177 (2016).

326. Georgiadis, A. G. *et al.* Biogas dry reforming over Ni/LnOx-type catalysts (Ln = La, Ce, Sm or Pr). *Int. J. Hydrogen Energy* 48, 19953–19971 (2023).

327. Theofanidis, S. A., Kasun Kalhara Gunasooriya, G. T., Itskou, I., Tasioula, M. & Lemonidou, A. A. On-purpose Ethylene Production via CO_2-assisted Ethane Oxidative Dehydrogenation: Selectivity Control of Iron Oxide Catalysts. *ChemCatChem* 14, (2022).

328. Xie, Z. *et al.* Effects of oxide supports on the CO_2 reforming of ethane over Pt-Ni bimetallic catalysts. *Appl. Catal. B Environ.* 245, 376–388 (2019).

329. Zhang, T. *et al.* Dry Reforming of Ethane over FeNi/Al–Ce–O Catalysts:

Composition-Induced Strong Metal–Support Interactions. *Engineering* 18, 173–185 (2022).

330. Xie, Z., Wang, X., Chen, X., Liu, P. & Chen, J. G. General Descriptors for CO2-Assisted Selective C-H/C-C Bond Scission in Ethane. *J. Am. Chem. Soc.* (2021).

331. Xie, Z. & Chen, J. G. Bimetallic-Derived Catalytic Structures for CO2-Assisted Ethane Activation. *Acc. Chem. Res.* 56, 2447–2458 (2023).

332. Guo, M., Feng, K., Wang, Y. & Yan, B. Unveiling the Role of Active Oxygen Species in Oxidative Dehydrogenation of Ethane with CO_2 over $NiFe/CeO_2$. *ChemCatChem* 13, 3119–3131 (2021).

333. Tasioula, M. *et al.* Tandem CO_2 Valorization and Ethane Dehydrogenation: Elucidating the Nature of Highly Selective Iron Oxide Active Sites. *ACS Catal.* 13, 2176–2189 (2023).

334. Li, Q. *et al.* Modulating the chemical environment of Ni^{2+} for the oxidative dehydrogenation of ethane: The formation of $LAS(Al^{3+}/Ga^{3+})$-Ni-OH site. *Chem. Eng. J.* 500, 156939 (2024).

335. Yu, K. & Ma, L. High-Temperature Pretreatment Effect on Co/SiO_2 Active Sites and Ethane Dehydrogenation (2023).

336. Scholz, J. *et al.* Severe Loss of Confined Sulfur in Nanoporous Carbon for Li-S Batteries under Wetting Conditions. *ACS Energy Lett.* 3, 387–392 (2018).

337. Mascotto, S. *et al.* Poly(ionic liquid)-derived nanoporous carbon analyzed by combination of gas physisorption and small-Angle neutron scattering. *Carbon N. Y.* 82, 425–435 (2015).

338. Petzold, A. *et al.* Distribution of Sulfur in Carbon/Sulfur Nanocomposites Analyzed by Small-Angle X-ray Scattering. *Langmuir* 32, 2780–2786 (2016).

339. Charisiou, N. D. *et al.* An in depth investigation of deactivation through carbon formation during the biogas dry reforming reaction for Ni supported on modified with CeO_2 and La_2O_3 zirconia catalysts. *Int. J. Hydrogen Energy* 43, 18955–18976 (2018).

340. Charisiou, N. D. *et al.* Investigating the correlation between deactivation and the carbon deposited on the surface of Ni/Al_2O_3 and Ni/La_2O_3-Al_2O_3 catalysts during the biogas reforming reaction. *Appl. Surf. Sci.* 474, 42–56 (2019).

341. Zhu, X., Li, K., Wei, Y., Wang, H. & Sun, L. Chemical-looping steam methane reforming over a CeO_2-Fe_2O_3 oxygen carrier: Evolution of its structure and reducibility. *Energy and Fuels* 28, 754–760 (2014).

342. Zheng, H., Jiang, X., Gao, Y., Tong, A. & Zeng, L. *Chemical looping reforming: process fundamentals and oxygen carriers. Discover Chemical Engineering* vol. 2 (Springer International Publishing, 2022).

343. Zhu, X., Imtiaz, Q., Donat, F., Müller, C. R. & Li, F. Chemical looping beyond combustion-a perspective. *Energy Environ. Sci.* 13, 772–804 (2020).

344. Khlifi, S., Pozzobon, V. & Lajili, M. A Comprehensive Review of Syngas Production, Fuel Properties, and Operational Parameters for Biomass Conversion. *Energies* 17, 1–17 (2024).

345. Gao, Y. *et al.* Syngas Production from Biomass Gasification: Influences of Feedstock Properties, Reactor Type, and Reaction Parameters. *ACS Omega* 8, 31620–31631 (2023).

346. Kee, R. J., Zhu, H., Sukeshini, A. M. & Jackson, G. S. Solid oxide fuel cells: Operating principles, current challenges, and the role of syngas. *Combust. Sci. Technol.* 180, 1207–1244 (2008).

347. Zhang, X., Jiang, Y., Hu, X., Sun, L. & Ling, Y. High Performance Proton-Conducting Solid Oxide Fuel Cells with a Layered Perovskite $GdBaCuCoO_{5+x}$ Cathode. *Electron. Mater. Lett.* 14, 147–153 (2018).

348. Seo, J. *et al.* Gas-Permeable Inorganic Shell Improves the Coking Stability and Electrochemical Reactivity of Pt toward Methane Oxidation. *ACS Appl. Mater. Interfaces* 12, 4405–4413 (2020).

349. Sengodan, S. *et al.* Layered oxygen-deficient double perovskite as an efficient and stable anode for direct hydrocarbon solid oxide fuel cells. *Nat. Mater.* 14, 205–209 (2015).

350. Zhang, X. *et al.* A novel $Ni–MoC_xO_y$ interfacial catalyst for syngas production via the chemical looping dry reforming of methane. *Chem* 9, 102–116 (2023).

351. Qin, L. *et al.* Impact of 1% Lanthanum Dopant on Carbonaceous Fuel Redox Reactions with an Iron-Based Oxygen Carrier in Chemical Looping Processes. *ACS Energy Lett.* 2, 70–74 (2017).

352. Löfberg, A., Guerrero-Caballero, J., Kane, T., Rubbens, A. & Jalowiecki-Duhamel, L. Ni/CeO_2 based catalysts as oxygen vectors for the chemical looping dry reforming of methane for syngas production. *Appl. Catal. B Environ.* 212, 159–174 (2017).

353. Zhu, X., Li, K., Neal, L. & Li, F. Perovskites as Geo-inspired Oxygen Storage Materials for Chemical Looping and Three-Way Catalysis: A Perspective. *ACS Catal.* 8, 8213–8236 (2018).

354. Lim, H. S., Lee, M., Kang, D. & Lee, J. W. Role of transition metal in perovskites for enhancing selectivity of methane to syngas. *Int. J. Hydrogen Energy* 43, 20580–20590 (2018).

355. Jiang, Q. *et al.* Mixed conductive composites for "Low-Temperature" thermo-chemical CO_2-splitting and syngas generation. *J. Mater. Chem. A* 8, 13173–13182 (2020).

356. Bian, Z. *et al.* A review on perovskite catalysts for reforming of methane to hydrogen production. *Renew. Sustain. Energy Rev.* 134, 110291 (2020).

357. Scheffe, J. R., Welte, M. & Steinfeld, A. Thermal Reduction of Ceria within an Aerosol Reactor for H_2O and CO_2 Splitting. *Ind. Eng. Chem. Res.* 53, 2175–2182 (2014).

358. Zhang, L. *et al.* Identifying the Role of A-Site Cations in Modulating Oxygen Capacity of Iron-Based Perovskite for Enhanced Chemical Looping Methane-to-Syngas Conversion. *ACS Catal.* 10, 9420–9430 (2020).

359. Kayaalp, B. *et al.* Template-free mesoporous $La_{0.3}Sr_{0.7}Fe_xTi_{1-x}O_{3\pm\delta}$ for CH_4 and CO oxidation catalysis. *Appl. Catal. B Environ.* 245, 536–545 (2019).

360. Jafari, T. *et al.* Photocatalytic water splitting - The untamed dream: A review of recent advances. *Molecules* 21, (2016).

361. Murat Eyvaz, Yongseung Yun, A. A. *Clean Energy Technologies - Hydrogen and Gasification Processes.* (2022).

362. Fajrina, N. & Tahir, M. A critical review in strategies to improve photocatalytic water splitting towards hydrogen production. *Int. J. Hydrogen Energy* 44, 540–577 (2019).

363. Bhom, F. & Isa, Y. M. Photocatalytic Hydrogen Production Using TiO$_2$-based Catalysts: A Review. *Glob. Challenges* 8, 2400134 (2024).

364. Eidsvåg, H., Bentouba, S., Vajeeston, P., Yohi, S. & Velauthapillai, D. TiO$_2$ as a photocatalyst for water splitting–an experimental and theoretical review. *Molecules* 26, 1–30 (2021).

365. Damkale, S. R., Arbuj, S. S., Umarji, G. G., Rane, S. B. & Kale, B. B. Highly crystalline anatase TiO$_2$ nanocuboids as an efficient photocatalyst for hydrogen generation. *RSC Adv.* 11, 7587–7599 (2021).

366. Sudrajat, H., Susanti, A. & Hartuti, S. Efficient electron extraction by CoS$_2$ loaded onto anatase TiO$_2$ for improved photocatalytic hydrogen evolution. *J. Phys. Condens. Matter* 34, (2022).

367. Sudrajat, H., Hartuti, S. & Park, J. A newly constructed photoactive system, Fe(III)-C/N-Bi$_2$O$_3$, for efficient visible light photocatalysis. *J. Alloys Compd.* 748, 390–397 (2018).

368. Foo, C. *et al.* Characterisation of oxygen defects and nitrogen impurities in TiO$_2$ photocatalysts using variable-temperature X-ray powder diffraction. *Nat. Commun.* 12, 661 (2021).

369. Wang, Z. *et al.* H-Doped Black Titania with Very High Solar Absorption and Excellent Photocatalysis Enhanced by Localized Surface Plasmon Resonance. *Adv. Funct. Mater.* 23, 5444–5450 (2013).

370. Mogal, S. I., Mishra, M., Gandhi, V. G. & Tayade, R. J. Metal Doped Titanium Dioxide: Synthesis and Effect of Metal Ions on Physico-Chemical and Photocatalytic Properties. *Mater. Sci. Forum* 734, 364–378 (2013).

371. Umezawa, N. & Ye, J. Role of complex defects in photocatalytic activities of nitrogen-doped anatase TiO$_2$. *Phys. Chem. Chem. Phys.* 14, 5924–5934 (2012).

372. Tang, J., Quan, H. & Ye, J. Photocatalytic properties and photoinduced hydrophilicity of surface-fluorinated TiO$_2$. *Chem. Mater.* 19, 116–122 (2007).

373. Dozzi, M. V., D'Andrea, C., Ohtani, B., Valentini, G. & Selli, E. Fluorine-Doped TiO$_2$ Materials: Photocatalytic Activity vs Time-Resolved Photoluminescence. *J. Phys. Chem. C* 117, 25586–25595 (2013).

374. Biedrzycki, J., Livraghi, S., Giamello, E., Agnoli, S. & Granozzi, G. Fluorine- and niobium-doped TiO$_2$: Chemical and spectroscopic properties of polycrystalline n-type-doped anatase. *J. Phys. Chem. C* 118, 8462–8473 (2014).

375. Liu, Y. *et al.* Niobium-Doped Titania Nanoparticles : *ACS Nano* 4, 5373–5381 (2010).

376. Wang, Z. *et al.* Extraordinary Hall effect and ferromagnetism in Fe-doped reduced rutile. *Appl. Phys. Lett.* 83, 518–520 (2003).

377. Erdal, S. *et al.* Hydration of rutile TiO_2: Thermodynamics and effects on n- and p-type electronic conduction. *J. Phys. Chem. C* 114, 9139–9145 (2010).

378. Khalid, A. *et al.* A practical method for incorporation of Fe (III) in Titania matrix for photocatalytic applications. *Mater. Res. Express* 8, (2021).

379. Chen, Y., Fu, X. & Peng, Z. A Review on Oxygen-Deficient Titanium Oxide for Photocatalytic Hydrogen Production. *Metals* vol. 13 (2023).

380. Foo, C., Li, Y., Lebedev, K. *et al.* Characterisation of oxygen defects and nitrogen impurities in TiO_2 photocatalysts using variable-temperature X-ray powder diffraction. *Nat Commun* 12, 661 (2021).

381. Li, Z., Zhang, X., Zhang, L., Xu, C. & Zhang, Y. Pathway Alteration of Water Splitting via Oxygen Vacancy Formation on Anatase Titanium Dioxide in Photothermal Catalysis (2020).

382. Yamazaki, S., Takaki, D., Nishiyama, N. & Yamazaki, Y. 3 - Factors affecting photocatalytic activity of TiO_2. in (eds. Wang, X., Anpo, M. & Fu, X. B. T.-C. D. in P. and P. M.) 23–38 (Elsevier, 2020).

383. Rasalingam, S., Wu, C. & Koodali, R. T. Modulation of Pore Sizes of Titanium Dioxide Photocatalysts by a Facile Template Free Hydrothermal Synthesis Method: Implications for Photocatalytic Degradation of Rhodamine B. (2015).

384. Cheng, F., Lin, G., Hu, X., Xi, S. & Xie, K. Porous single-crystalline titanium dioxide at 2 cm scale delivering enhanced photoelectrochemical performance. *Nat. Commun.* 10, 3618 (2019).

385. Liu, Y. *et al.* Radially oriented mesoporous TiO_2 microspheres with single-crystal–like anatase walls for high-efficiency optoelectronic devices. *Sci. Adv.* 1, e1500166 (2025).

386. Butburee, T. *et al.* 2D Porous TiO_2 Single-Crystalline Nanostructure Demonstrating High Photo-Electrochemical Water Splitting Performance. *Adv. Mater.* 30, 1705666 (2018).

387. Han, T. *et al.* Hydrogenated TiO_2/$SrTiO_3$ porous microspheres with tunable band structure for solar-light photocatalytic H_2 and O_2 evolution. 59, 1003–1016 (2016).

388. Liu, K. *et al.* Porous single crystalline-like titanium dioxide monolith with enhanced photoelectrochemical performance. 1–7 (2023).

389. Ismail, A. A. & Bahnemann, D. W. Mesoporous titania photocatalysts: preparation, characterization and reaction mechanisms. *J. Mater. Chem.* 21, 11686–11707 (2011).

390. Huang, L., Gubbins, K. E., Li, L. & Lu, X. Water on Titanium Dioxide Surface: A Revisiting by Reactive Molecular Dynamics Simulations. *Langmuir* 30, 14832–14840 (2014).

391. Li, R. Z., Xu, H. G., Cao, G. J., Xu, X. L. & Zheng, W. J. Interaction of TiO_2 with water: Photoelectron spectroscopy and density functional calculations. *J. Chem. Phys.* 139, (2013).

392. Miao, L., Dong, J., Yu, L. & Zhou, M. Reactions of titanium dioxides with acetylene

molecules. A matrix isolation FTIR and density functional study. *J. Phys. Chem. A* 107, 1935–1940 (2003).

393. Vittadini, A., Casarin, M. & Selloni, A. Hydroxylation of TiO₂-B: Insights from density functional calculations. *J. Mater. Chem.* 20, 5871–5877 (2010).

394. Cottre, T. *et al.* Interaction of Water with Atomic Layer Deposited Titanium Dioxide on p-Si Photocathode: Modeling of Photoelectrochemical Interfaces in Ultrahigh Vacuum with Cryo-Photoelectron Spectroscopy. *Adv. Mater. Interfaces* 8, (2021).

395. Luca, D., Mardare, D., Iacomi, F. & Teodorescu, C. M. Increasing surface hydrophilicity of titania thin films by doping. *Appl. Surf. Sci.* 252, 6122–6126 (2006).

396. Kuźmicz-Mirosław, E. *et al.* Effect of Various Surface Treatments on Wettability and Morphological Properties of Titanium Oxide Thin Films. *Materials (Basel).* 15, 1–11 (2022).

397. Mardare, D., Iacomi, F. & Luca, D. Substrate and Fe-doping effects on the hydrophilic properties of TiO₂ thin films. *Thin Solid Films* 515, 6474–6478 (2007).

398. Wang, G. *et al.* Sol–Gel Synthesis of Spherical Mesoporous High-Entropy Oxides. *ACS Appl. Mater. Interfaces* 12, 45155–45164 (2020).

399. Yuan, Q. *et al.* Homogeneously Dispersed Ceria Nanocatalyst Stabilized with Ordered Mesoporous Alumina. *Adv. Mater.* 22, 1475–1478 (2010).

400. Schwenzer, B. *et al.* Tuning the Optical Properties of Mesoporous TiO₂ Films by Nanoscale Engineering. *Langmuir* 28, 10072–10081 (2012).

401. Wang, J., Li, H., Li, H., Zuo, C. & Wang, H. Thermal Stability and Optimal Photoinduced Hydrophilicity of Mesoporous TiO₂ Thin Films. *J. Phys. Chem. C* 116, 9517–9525 (2012).

402. Ghosh, M., Lohrasbi, M., Chuang, S. S. C. & Jana, S. C. Mesoporous Titanium Dioxide Nanofibers with a Significantly Enhanced Photocatalytic Activity. *ChemCatChem* 8, 2525–2535 (2016).

403. Li, S., Yang, S., Xu, S. & Wan, Q. Influence of heat treatment on the microstructure and surface groups of Stöber silica. *Mater. Res. Express* 10, 105004 (2023).

404. Yang, Y. & Tian, C. Effects of Calcining Temperature on Photocatalytic Activity of Fe-Doped Sulfated Titania. *Photochem. Photobiol.* 88, 816–823 (2012).

405. El Seoud, O. A., Ramadan, A. R., Sato, B. M. & Pires, P. A. R. Surface Properties of Calcinated Titanium Dioxide Probed by Solvatochromic Indicators: Relevance to Catalytic Applications. *J. Phys. Chem. C* 114, 10436–10443 (2010).

406. Nanayakkara, C. E., Larish, W. A. & Grassian, V. H. Titanium dioxide nanoparticle surface reactivity with atmospheric gases, CO₂, SO₂, and NO₂: Roles of surface hydroxyl groups and adsorbed water in the formation and stability of adsorbed products. *J. Phys. Chem. C* 118, 23011–23021 (2014).

407. Shimizu, S. & Matubayasi, N. Sorption Hysteresis: A Statistical Thermodynamic Fluctuation Theory. *Langmuir* 40, 11504–11515 (2024).

408. Oh, J. S. *et al.* Adsorption Equilibrium of Water Vapor on Mesoporous Materials. 1458–1462 (2003).

409. Naono, H., Hakuman, M., Tanaka, T., Tamura, N. & Nakai, K. Porous Texture and Surface Character of Dehydroxylated and Rehydroxylated MCM-41 Mesoporous Silicas–Analysis of Adsorption Isotherms of Nitrogen Gas and Water Vapor. *J. Colloid Interface Sci.* 225, 411–420 (2000).

410. Chen, Q. *et al.* Study on Shale Adsorption Equation Based on Monolayer Adsorption, Multilayer Adsorption, and Capillary Condensation. *J. Chem.* 2017, 1496463 (2017).

411. Shaoying, Q., James, H. K., J., R. M. & P., C. M. Equilibrium and Heat of Adsorption for Water Vapor and Activated Carbon. *J. Environ. Eng.* 126, 267–271 (2000).

412. Poyet, S. & Charles, S. Temperature dependence of the sorption isotherms of cement-based materials: Heat of sorption and Clausius-Clapeyron formula. *Cem. Concr. Res.* 39, 1060–1067 (2009).

413. Athokpam, B., Ramesh, S. G. & McKenzie, R. H. Effect of hydrogen bonding on the infrared absorption intensity of OH stretch vibrations. *Chem. Phys.* 488–489, 43–54 (2017).

414. Venugopal, A., Kas, R., Hau, K. & Smith, W. A. Operando Infrared Spectroscopy Reveals the Dynamic Nature of Semiconductor-Electrolyte Interface in Multinary Metal Oxide Photoelectrodes. *J. Am. Chem. Soc.* 143, 18581–18591 (2021).

415. Dai, F., Zhuang, Q., Huang, G., Deng, H. & Zhang, X. Infrared Spectrum Characteristics and Quantification of OH Groups in Coal. *ACS omega* 8, 17064–17076 (2023).

416. Mino, L., Morales-García, Á., Bromley, S. T. & Illas, F. Understanding the nature and location of hydroxyl groups on hydrated titania nanoparticles. *Nanoscale* 13, 6577–6585 (2021).

417. Guillon, O., De Souza, R. A., Mishra, T. P. & Rheinheimer, W. Electric-field-assisted processing of ceramics: Nonthermal effects and related mechanisms. *MRS Bull.* 46, 52–58 (2021).

418. Andronic, L. & Enesca, A. Black TiO_2 Synthesis by Chemical Reduction Methods for Photocatalysis Applications. *Front. Chem.* 8, 1–8 (2020).

419. Jha, S. K. & Raj, R. The effect of electric field on sintering and electrical conductivity of Titania. *J. Am. Ceram. Soc.* 97, 527–534 (2014).

420. Guillon, O. *et al.* Field-assisted sintering technology/spark plasma sintering: Mechanisms, materials, and technology developments. *Adv. Eng. Mater.* 16, 830–849 (2014).

421. Glass, D. *et al.* Probing the Role of Atomic Defects in Photocatalytic Systems through Photoinduced Enhanced Raman Scattering. *ACS Energy Lett.* 6, 4273–4281 (2021).

422. Wang, Y. Y. *et al.* Nanocasted synthesis of mesoporous $LaCoO_3$ perovskite with extremely high surface area and excellent activity in methane combustion. *J. Phys.*

Chem. C 112, 15293–15298 (2008).

423. Liu, N. *et al.* Probe-Decorated Mesoporous Black TiO₂ Nanoplatform for the Highly Efficient Synergistic Phototherapy. *ACS Appl. Mater. Interfaces* 12, 41071–41078 (2020).

424. Feng, L. *et al.* The Development of New Catalytic Pigments Based on SiO₂ Amorphous Photonic Crystals via Adding of Dual-Functional Black TiO²⁻ˣ Nanoparticles. *ACS Omega* 7, 12089–12097 (2022).

425. http://abulafia.mt.ic.ac.uk/

426. Marrocchelli, D., Bishop, S. R. & Kilner, J. Chemical expansion and its dependence on the host cation radius. *J. Mater. Chem. A* 1, 7673–7680 (2013).

427. Klauke, K. *et al.* Enhancement of the SrTiO₃ Surface Reactivity by Exposure to Electric Fields. *ChemNanoMat* 5, 948–956 (2019).

428. Guillon, O., Rheinheimer, W. & Bram, M. A Perspective on Emerging and Future Sintering Technologies of Ceramic Materials. *Adv. Eng. Mater.* 25, (2023).

429. Wang, L., Li, Z., Itoi, T., Yoshida, H. & Lu, Y. Grain growth and phase transformation of nano-sized titanium dioxide powder during heat treatment and spark plasma sintering. *J. Mater. Res. Technol.* 20, 4409–4418 (2022).

430. Wang, S. *et al.* Electric Current-Assisted Sintering of 8YSZ: A Comparative Study of Ultrafast High-Temperature Sintering and Flash Sintering. *Adv. Eng. Mater.* 25, 1–10 (2023).

431. Yang, D. *et al.* Influences of sintering temperature on pore morphology, porosity, and mechanical behavior of porous Ti. *Mater. Res. Express* 8, (2021).

432. Campbell, C., Gomes, J. R. B., Fischer, M. & Jorge, M. New Model for Predicting Adsorption of Polar Molecules in Metal–Organic Frameworks with Unsaturated Metal Sites. *J. Phys. Chem. Lett.* 9, 3544–3553 (2018).

433. Kulkarni, G. S. *et al.* Electrical Probing and Tuning of Molecular Physisorption on Graphene. *Nano Lett.* 16, 695–700 (2016).

434. Zhang, K. *et al.* Research Progress of a Composite Metal Oxide Catalyst for VOC Degradation. *Environ. Sci. Technol.* 56, 9220–9236 (2022).

435. Rosman, N. N. *et al.* An overview of co-catalysts on metal oxides for photocatalytic water splitting. *Int. J. Energy Res.* 46, 11596–11619 (2022).

436. Ye, J.-Q., Xu, S.-Y., Liang, Q., Dai, Y.-Z. & He, M.-Y. Metal-Organic Frameworks-Derived Nanocarbon Materials and Nanometal Oxides for Photocatalytic Applications. *Chem. – An Asian J.* 19, e202400161 (2024).

437. Darko, D. A. *et al.* Photo-thermal catalysis for sustainable energy production and environmental treatment. *Front. Energy Res.* 12, (2024).

438. Alyami, M. Ultra-Violet-Assisted Scalable Method to Fabricate Oxygen-Vacancy-Rich Titanium-Dioxide Semiconductor Film for Water Decontamination under Natural Sunlight Irradiation. *Nanomaterials* vol. 13 (2023).

439. Hensling, F. V. E. *et al.* UV radiation enhanced oxygen vacancy formation caused by the PLD plasma plume. *Sci. Rep.* 8, 8846 (2018).

440. Lv, Y. *et al.* The surface oxygen vacancy induced visible activity and enhanced UV

activity of a ZnO_{1-x} photocatalyst. *Catal. Sci. Technol.* 3, 3136–3146 (2013).

441. Min, C. *et al.* Uv-light induced γ-MnO_2 nanostructures with rich oxygen vacancies for efficient low-temperature catalytic oxidation of carbon monoxide. *Chem. Eng. J.* 504, 159033 (2025).

442. Kharade, A. K. & Chang, S. Contributions of Abundant Hydroxyl Groups to Extraordinarily High Photocatalytic Activity of Amorphous Titania for CO_2 Reduction. *J. Phys. Chem. C* 124, 10981–10992 (2020).

443. Simonsen, M. E., Li, Z. & Søgaard, E. G. Influence of the OH groups on the photocatalytic activity and photoinduced hydrophilicity of microwave assisted sol-gel TiO_2 film. *Appl. Surf. Sci.* 255, 8054–8062 (2009).

444. Madelung, O. *Semiconductors: Data Handbook.* (2004).

445. Alyami, M. Ultra-Violet-Assisted Scalable Method to Fabricate Oxygen-Vacancy-Rich Titanium-Dioxide Semiconductor Film for Water Decontamination under Natural Sunlight Irradiation. *Nanomaterials* 13, (2023).

446. Dagdeviren, O. E. *et al.* The Effect of Photoinduced Surface Oxygen Vacancies on the Charge Carrier Dynamics in TiO_2 Films. *Nano Lett.* 21, 8348–8354 (2021).

447. Chen, K.-H. *et al.* Control of Oxygen Vacancies of 2D-InO_x Fabricated by Liquid Metal Printing via Temperature Modulation. *J. Phys. Chem. C* 128, 5355–5365 (2024).

448. Hirakawa, H., Hashimoto, M., Shiraishi, Y. & Hirai, T. Photocatalytic Conversion of Nitrogen to Ammonia with Water on Surface Oxygen Vacancies of Titanium Dioxide. *J. Am. Chem. Soc.* 139, 10929–10936 (2017).

449. Maeng, J. *et al.* Oxygen Vacancy-Controlled $CuOx$/N, Se Co-Doped Porous Carbon via Plasma-Treatment for Enhanced Electro-Reduction of Nitrate to Green Ammonia. *Small* 20, e2403253 (2024).

450. Ghotbi, M. Y., Nasiri, V. & Rafiee, M. A facile approach to the synthesis of non-porous and microporous sub-micron spherical zirconia and alumina-zirconia solid solution. *J. Colloid Interface Sci.* 389, 121–125 (2013).

451. Smyth, D. M. Effects of dopants on the properties of metal oxides. *Solid State Ionics* 129, 5–12 (2000).

452. Gatti, T. *et al.* Opportunities from Doping of Non-Critical Metal Oxides in Last Generation Light-Conversion Devices. *Adv. Energy Mater.* 11, (2021).

453. Amorós-Pérez, A., Cano-Casanova, L., Castillo-Deltell, A., Lillo-Ródenas, M. Á. & Román-Martínez, M. del C. TiO_2 Modification with transition metallic species (Cr, Co, Ni, and Cu) for photocatalytic abatement of acetic acid in liquid phase and propene in gas phase. *Materials (Basel).* 12, (2018).

454. Pawar, T. J., Contreras López, D., Olivares Romero, J. L. & Vallejo Montesinos, J. Surface modification of titanium dioxide. *J. Mater. Sci.* 58, 6887–6930 (2023).

455. Wach, A. *et al.* Towards understanding the TiO_2 doping at the surface and bulk. *X-Ray Spectrom.* 52, 261–268 (2023).

456. Gao, M., Zhu, L., Peh, C. K. & Ho, G. W. Solar absorber material and system designs for photothermal water vaporization towards clean water and energy

production. *Energy Environ. Sci.* 12, 841–864 (2019).

457. Nowotny, J., Bak, T., Nowotny, M. K. & Sheppard, L. R. TiO₂ Surface Active Sites for Water Splitting. *J. Phys. Chem. B* 110, 18492–18495 (2006).

458. Erfan, N. A., Mahmoud, M. S., Kim, H. Y. & Barakat, N. A. M. M. CdTiO3-NPs incorporated TiO₂ nanostructure photocatalyst for scavenger-free water splitting under visible radiation. *PLoS One* 17, e0276097 (2022).

459. Chiang, T. H. *et al.* Efficient Photocatalytic Water Splitting Using Al-Doped SrTiO₃ Coloaded with Molybdenum Oxide and Rhodium–Chromium Oxide. *ACS Catal.* 8, 2782–2788 (2018).

460. Bharti, B., Kumar, S., Lee, H.-N. & Kumar, R. Formation of oxygen vacancies and Ti³⁺ state in TiO₂ thin film and enhanced optical properties by air plasma treatment. *Sci. Rep.* 6, 32355 (2016).

461. Xu, W., Russo, P. A., Schultz, T., Koch, N. & Pinna, N. Niobium-Doped Titanium Dioxide with High Dopant Contents for Enhanced Lithium-Ion Storage. *ChemElectroChem* 7, 4016–4023 (2020).

462. Setvín, M., Wagner, M., Schmid, M., Parkinson, G. S. & Diebold, U. Surface point defects on bulk oxides: Atomically-resolved scanning probe microscopy. *Chem. Soc. Rev.* 46, 1772–1784 (2017).

463. Estrellan, C. R., Salim, C. & Hinode, H. Photocatalytic decomposition of perfluorooctanoic acid by iron and niobium co-doped titanium dioxide. *J. Hazard. Mater.* 179, 79–83 (2010).

464. Brønsted, J. N. & Lowry, T. M. Brønsted Concept of Acids and Bases Brønsted Concept of Acids and Bases The Brønsted-Lowry Theory of Acids and Bases. 1–4 (1923).

465. Martra, G. Lewis acid and base sites at the surface of microcrystalline anatase. *Appl. Catal. A Gen.* 200, 275–285 (2000).

466. Songtawee, S., Rungtaweevoranit, B., Klaysom, C. & Faungnawakij, K. Tuning Brønsted and Lewis acidity on phosphated titanium dioxides for efficient conversion of glucose to 5-hydroxymethylfurfural. *RSC Adv.* 11, 29196–29206 (2021).

467. Deiana, C., Fois, E., Coluccia, S. & Martra, G. Surface Structure of TiO₂ P25 Nanoparticles: Infrared Study of Hydroxy Groups on Coordinative Defect Sites. *J. Phys. Chem. C* 114, 21531–21538 (2010).

468. Imamura, S., Nakai, T., Kanai, H. & Ito, T. Effect of tetrahedral Ti in titania–silica mixed oxides on epoxidation activity and Lewis acidity. *J. Chem. Soc. Faraday Trans.* 91, 1261–1266 (1995).

469. Tapish Saboo. Surface organometallic chemistry on Titania. Université de Lyon; Università degli studi (Messine, Italie). (2018).

470. Hanaor, D. A. H., Assadi, M. H. N., Li, S., Yu, A. & Sorrell, C. C. Ab initio study of phase stability in doped TiO₂. *Comput. Mech.* 50, 185–194 (2012).

471. Zhao, T.-X. *et al.* Local structure and optical absorption characteristic investigation on Fe doped TiO₂ nanoparticles*. *Chinese Phys. C* 39, 28001 (2015).

472. Leedahl, B. *et al.* Structural defects induced by Fe-ion implantation in TiO₂. *J.*

Appl. Phys. 115, 53711 (2014).

473. Liu, X. *et al.* Controlling the Thermoelectric Properties of Nb-Doped TiO₂ Ceramics through Engineering Defect Structures. *ACS Appl. Mater. Interfaces* 13, 57326–57340 (2021).

474. Noguchi, S., Tokutome, T. & Iwamoto, S. Nitrification of Nb-Modified Titanias Prepared by the Solvothermal Method and their Photocatalytic Activities under Visible-Light Irradiation. *Key Eng. Mater.* 596, 43–49 (2014).

475. Guidi, V., Carotta, M. C., Ferroni, M., Martinelli, G. & Sacerdoti, M. Effect of Dopants on Grain Coalescence and Oxygen Mobility in Nanostructured Titania Anatase and Rutile. *J. Phys. Chem. B* 107, 120–124 (2003).

476. Roldán, A., Boronat, M., Corma, A. & Illas, F. Theoretical Confirmation of the Enhanced Facility to Increase Oxygen Vacancy Concentration in TiO₂ by Iron Doping. *J. Phys. Chem. C* 114, 6511–6517 (2010).

477. Rosa, D., Abbasova, N. & Di Palma, L. Titanium Dioxide Nanoparticles Doped with Iron for Water Treatment via Photocatalysis: A Review. *Nanomaterials* 14, (2024).

478. Umar, A. *et al.* Iron-Doped Titanium Dioxide Nanoparticles As Potential Scaffold for Hydrazine Chemical Sensor Applications. *Coatings* vol. 10 (2020).

479. Taneja, Y., Dube, D. & Singh, R. Recent advances in elemental doping and simulation techniques: improving structural, photophysical and electronic properties of titanium dioxide. *J. Mater. Chem. C* 12, 14774–14808 (2024).

480. Viisanen, Y. *et al.* Water Vapor Adsorption-Desorption Hysteresis Due to Clustering of Water on Nonporous Surfaces. *Langmuir* (2024).

481. Yu, J., Enzo, W., Stefano, M. & Douglas, B. A review of common practices in gravimetric and volumetric adsorption kinetic experiments. *Adsorption* 27, 295–318 (2021).

482. Miyauchi, M. Water Adsorption on Hydrophilic Fibers and Porous and Deliquescent Materials: Cellulose, Polysaccharide, Silica, Inorganic Salt, Sugar Alcohol, and Amino Acid. *ACS Omega* 8, 44212–44220 (2023).

483. Zhang, D., Yang, M. & Dong, S. Hydroxylation of the Rutile TiO₂(110) Surface Enhancing Its Reducing Power for Photocatalysis. *J. Phys. Chem. C* 119, 1451–1456 (2015).

484. Kayaalp, B. *et al.* Template-free mesoporous La₀.₃Sr₀.₇FeₓTi₁₋ₓO₃±Δ with superior oxidation catalysis performance. *Appl. Catal. B Environ.* 245, 536–545 (2019).

485. Poffe, E. *et al.* Understanding Oxygen Release from Nanoporous Perovskite Oxides and Its Effect on the Catalytic Oxidation of CH₄ and CO. *ACS Appl. Mater. Interfaces* 13, 25483–25492 (2021).

486. Kayaalp, B. *et al.* Surface Reconstruction under the Exposure of Electric Fields Enhances the Reactivity of Donor-Doped SrTiO₃. *J. Phys. Chem. C* 123, 16883–16892 (2019).

487. Zahra, S., Qaisa, S., Sheikh, A., Bukhari, H. & Amin, C. A. Effect of calcination temperature on the structure and morphology of zinc oxide nanoparticles synthesized by base-catalyzed aqueous sol-gel process. *European Journal of*

Chemistry vol. 13 162–167 (2022).

488. Jaison Jeevanandam, San Chan, Y. & Danquah, M. K. Effect of Gelling Agent and Calcination Temperature in Sol–Gel Synthesized MgO Nanoparticles. *Prot. Met. Phys. Chem. Surfaces* 55, 288–301 (2019).

489. Navío, J. A., Colón, G., Litter, M. I. & Bianco, G. N. Synthesis, characterization and photocatalytic properties of iron-doped titania semiconductors prepared from TiO_2 and iron (III) acetylacetonate. *J. Mol. Catal. A Chem.* 106, 267–276 (1996).

490. Klementiev, K., Norén, K., Carlson, S., Sigfridsson Clauss, K. G. V. & Persson, I. The BALDER Beamline at the MAX IV Laboratory. *J. Phys. Conf. Ser.* 712, 1–5 (2016).

491. Ravel, B., Newville, M. & IUCr. *ATHENA* , *ARTEMIS* , *HEPHAESTUS* : data analysis for X-ray absorption spectroscopy using *IFEFFIT*. *J. Synchrotron Radiat.* 12, 537–541 (2005).

492. Thommes, M. *et al.* Physisorption of gases, with special reference to the evaluation of surface area and pore size distribution (IUPAC Technical Report). *Pure Appl. Chem.* 87, 1051–1069 (2015).

493. Seeck, O. H. *et al.* The high-resolution diffraction beamline P08 at PETRA III. *J. Synchrotron Radiat.* 19, 30–38 (2012).

494. Norecs ProboStat Brochure.

495. Batiot-Dupeyrat, C., Gallego, G. A. S., Mondragon, F., Barrault, J. & Tatibouët, J. M. CO_2 reforming of methane over $LaNiO_3$ as precursor material. *Catal. Today* 107–108, 474–480 (2005).

496. Bonmassar, N. *et al.* In Situ-Determined Catalytically Active State of $LaNiO_3$ in Methane Dry Reforming. *ACS Catal.* 10, 1102–1112 (2020).

Chapter 12

Appendix

12.1 Figures
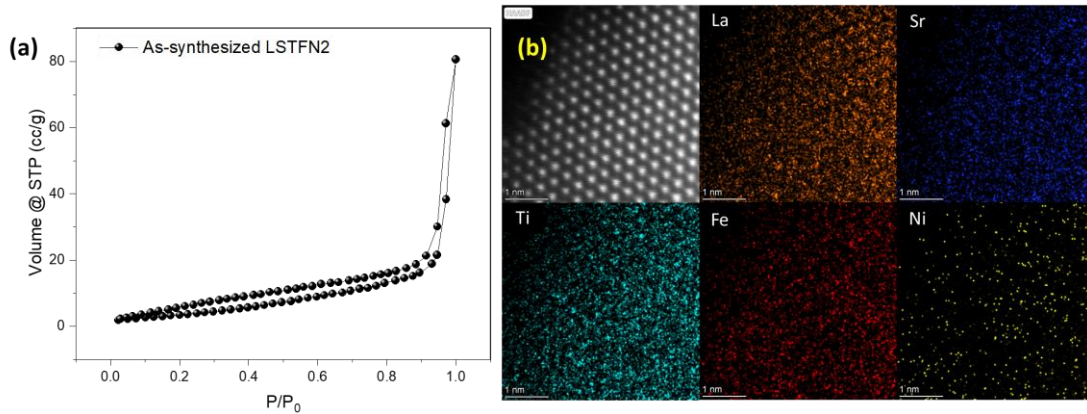
Figure A1. (a) N_2-physisorption isotherm and (b) HAADF picture with TEM-EDX mapping of the as-synthesized LSTFN2 material.
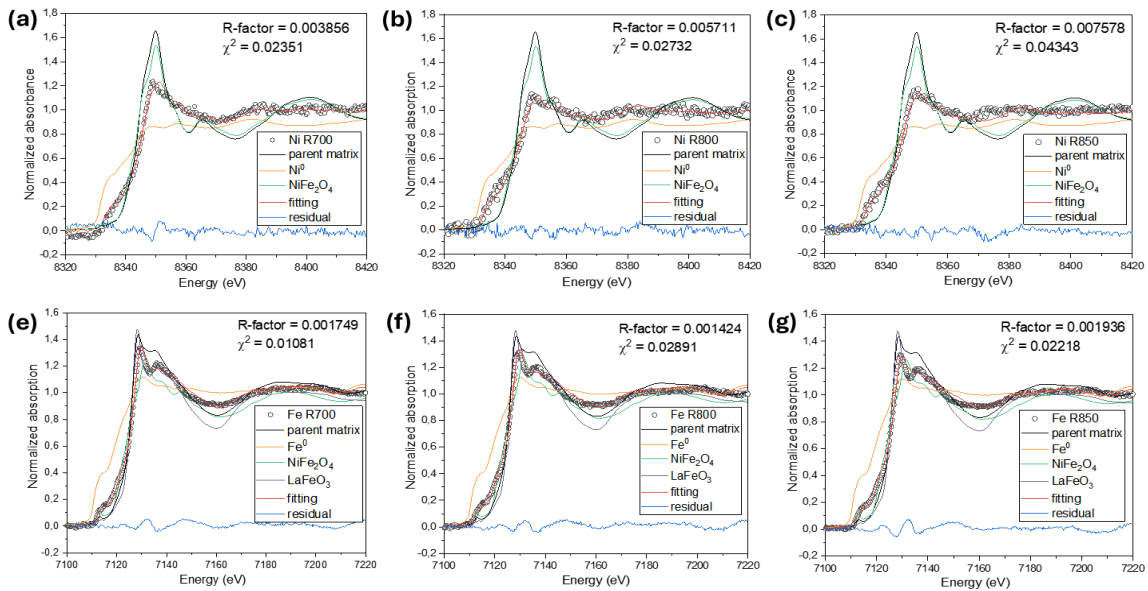
Figure A2. Ni K-edge spectra for R700 (a), R800 (b), R850 (c) and Fe K-edge spectra for R700 (d), R800 (e), and R850 (f) after the *in-situ* exsolution experiment (120 min) together with the reference spectra of parent matrix Ni, Ni^0 and $NiFe_2O_4$ for the Ni K-edge and parent matrix Fe, Fe^0, $NiFe_2O_4$ and $LaFeO_3$ for the Fe K-edge. The LCF fitting (red line), the residual plots (blue line, calculated with A^{exp}-A^{fit}, with A the normalized absorbance for the exsolved materials) and the final values of R-factor and χ^2 are reported.
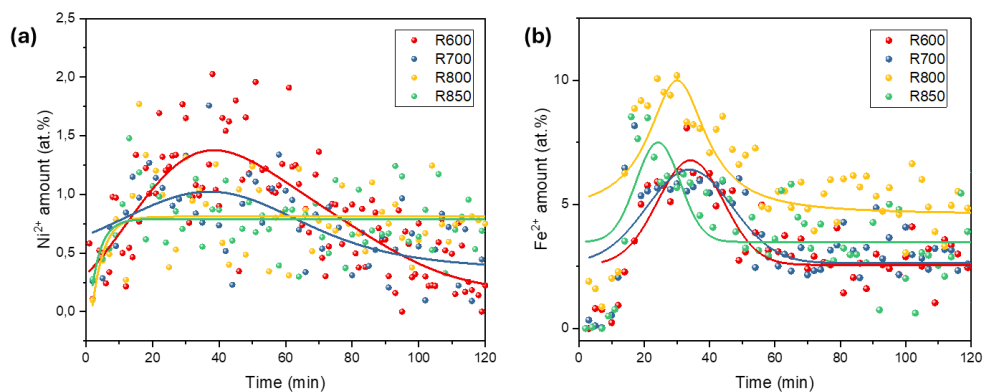
Figure A3. Overview of the reduction trend over time of the Ni^{2+} species (a) and Fe^{2+} (b) species. Solid lines in the plots have been introduced for better visualization.
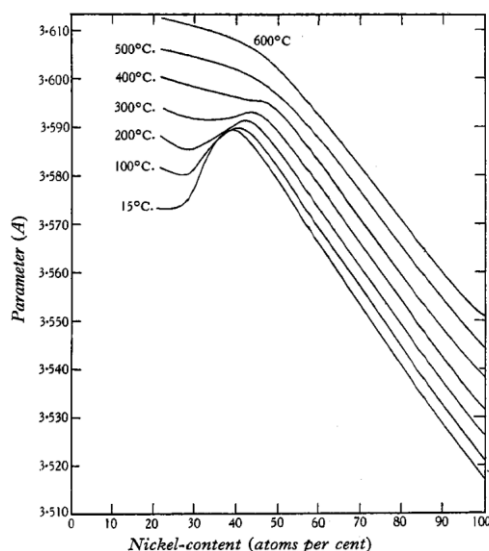
Figure A4. Lattice parameters of γ-FeNi alloys measured at different temperatures. Reported from Owen et. al.[299]
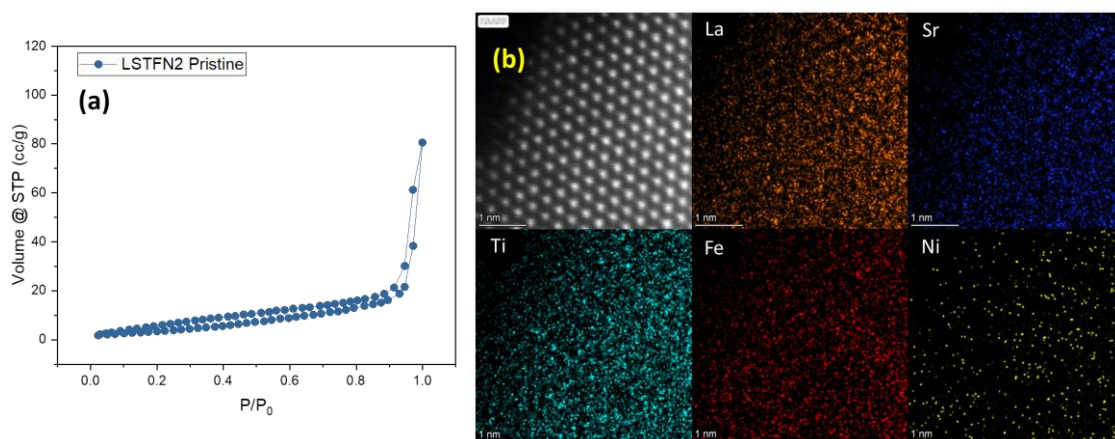
Figure A5. (a) N$_2$-physisorption isotherm of the as-synthesized LSTFN2 material. (b) HAADF picture and TEM-EDX mapping of the as-synthesized LSTFN2 material.
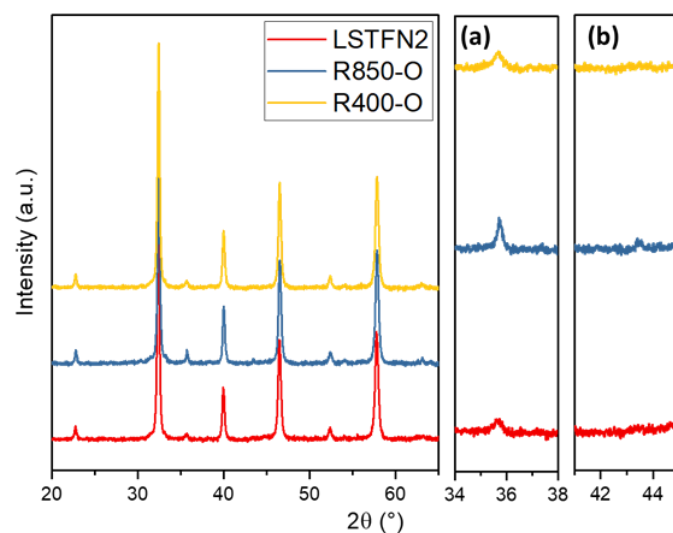
Figure A6. Powder diffractograms of the re-oxidized samples, with magnification on (a) the reflection range of the spinel oxide phase and (b) the reflection range of the metallic nanoparticles.
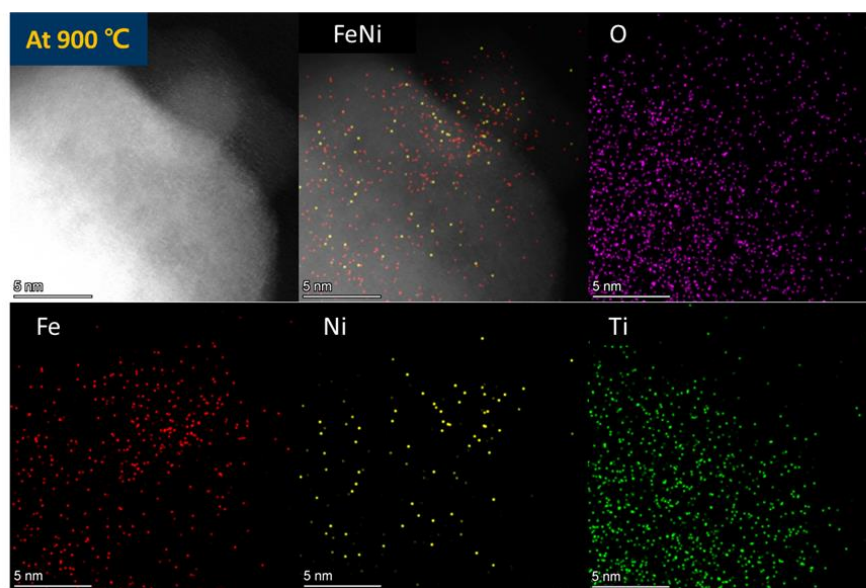
Figure A7. *In-situ* HR-TEM and EDX mapping of the LSTFN2 material at 900°C.
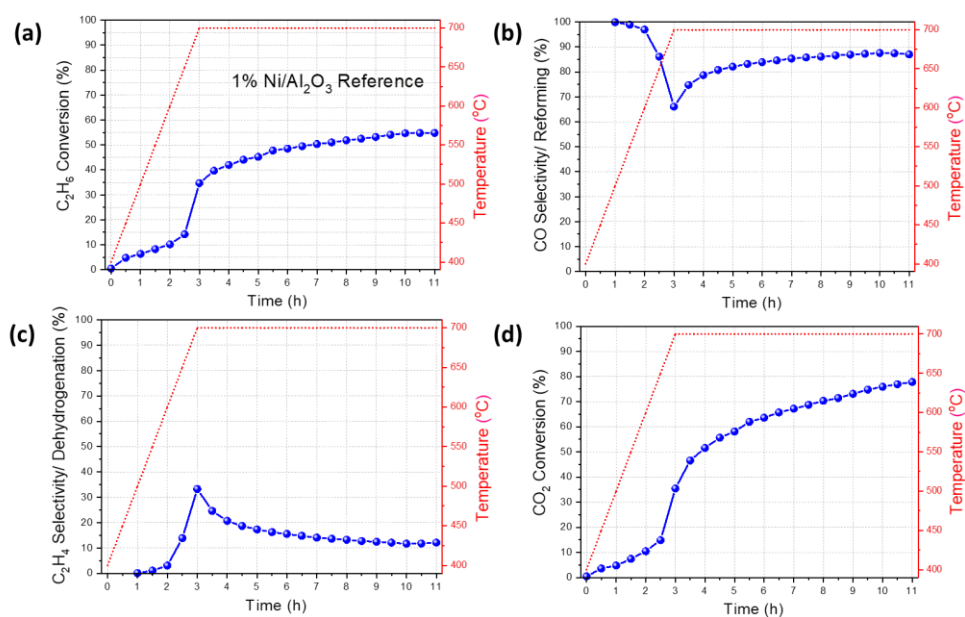
Figure A8. Trend over time of the (a) C$_2$H$_6$ conversion, (b) CO$_2$ conversion, (c) C$_2$H$_4$ selectivity (dehydrogenation) and (d) CO selectivity (reforming) during the catalytic testing for the Ni/Al$_2$O$_3$ reference.
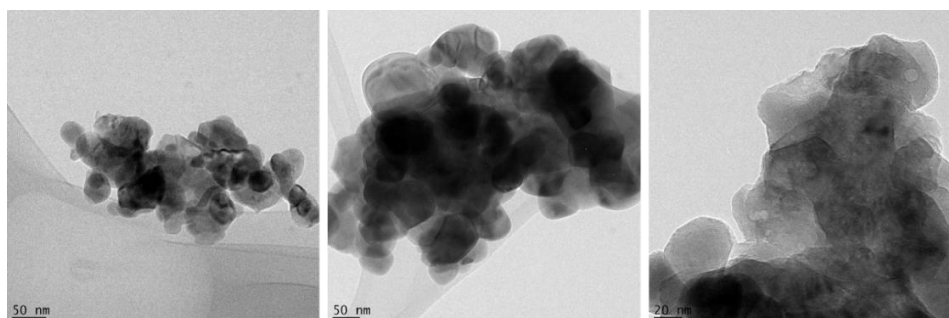
Figure A9. TEM micrographs of the R850 spent material after catalytic testing.
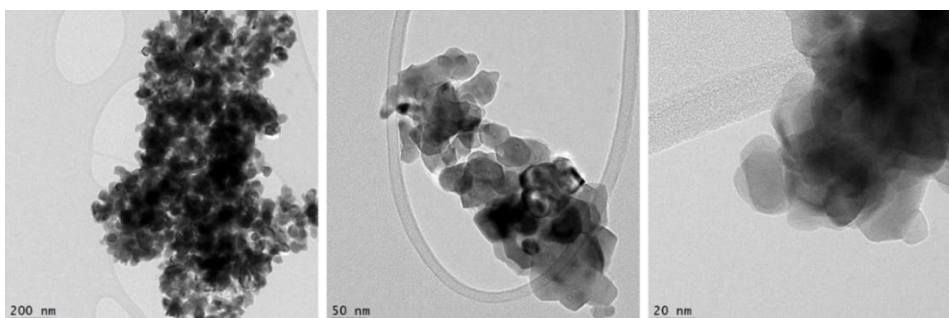
Figure A10. TEM micrographs of the R400 spent material after catalytic testing.
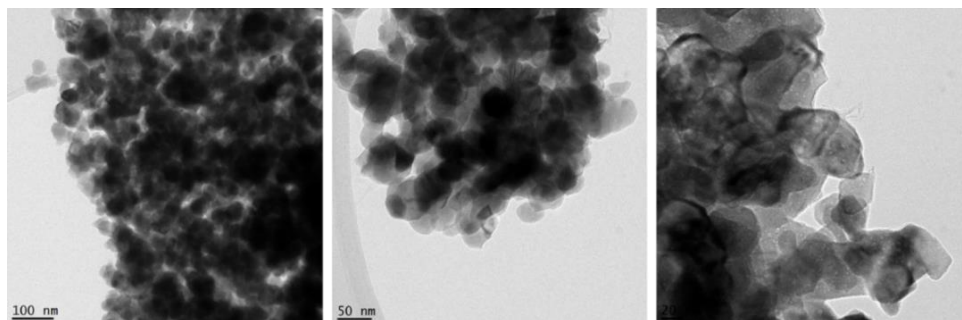
Figure A11. TEM micrographs of the R400-O-R850 spent material after catalytic testing.
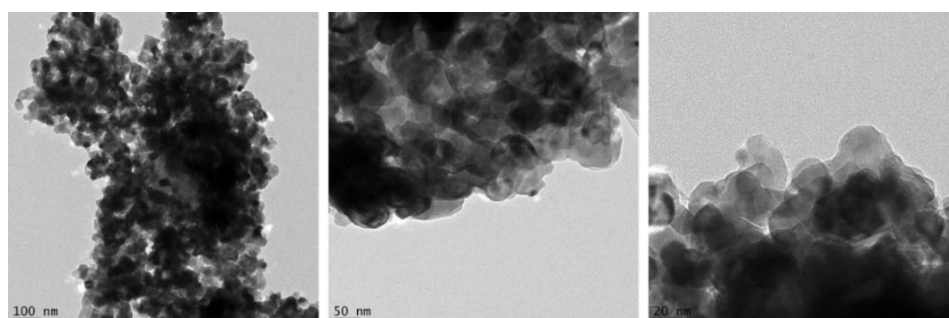
Figure A12. TEM micrographs of the R850-O-R400 spent material after catalytic testing.
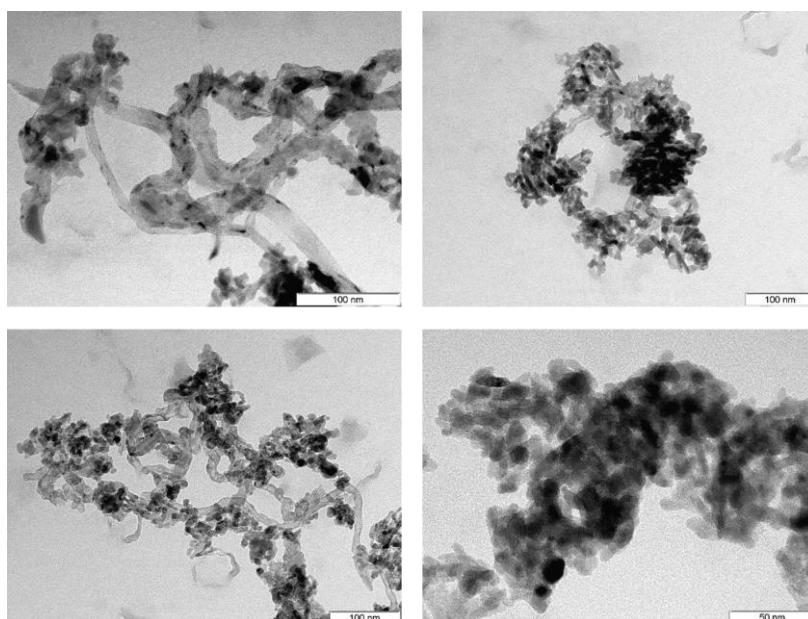
Figure A13. TEM micrographs of the Ni/Al$_2$O$_3$ spent material after the catalytic testing.
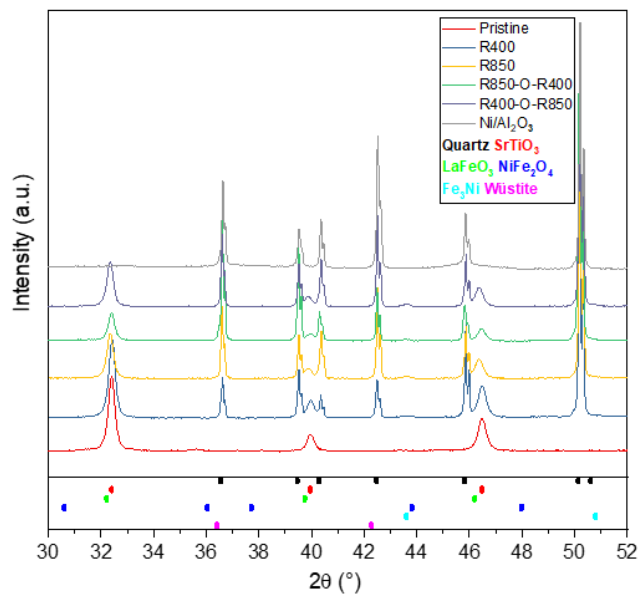
Figure A14. Post-catalysis XRD analysis of the spent catalysts. Measurements were taken in the 2ϑ range between 30° and 52°.
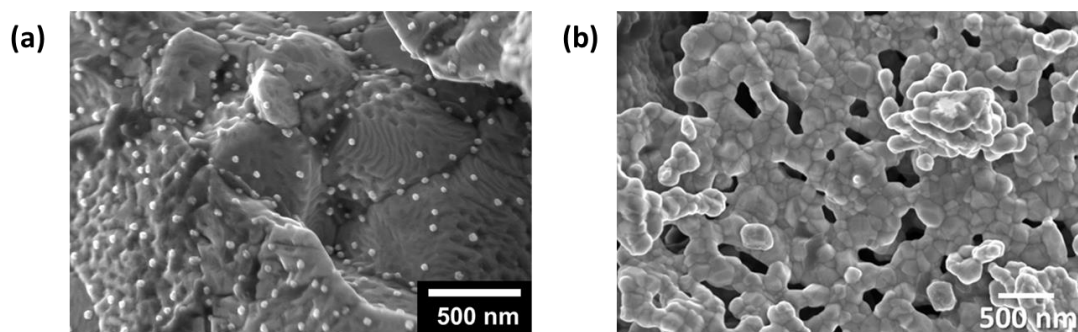
Figure A15. (a) SEM surface images of NiCo co-doped oxygen carrier after CH_4 injection step. (b) SEM images of undoped oxygen carrier after CH_4 injection step.
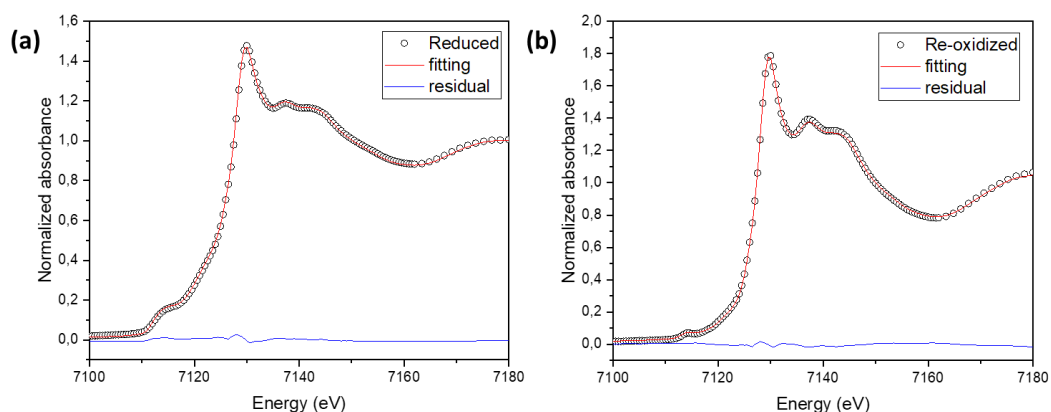
Figure A16. Fe K-edge spectra of the reduced (a) and re-oxidized (b) samples with their linear combination fittings and respective difference plots (residual) obtained from $A^{exp} - A^{fit}$, with A the normalized absorbance for the two materials.

277
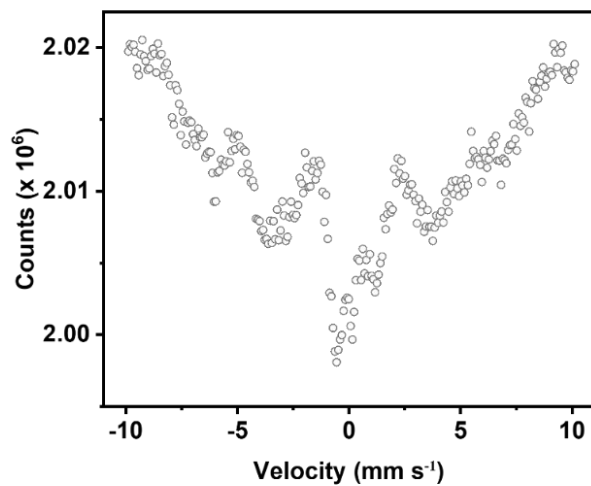
Figure A17. Mössbauer spectrum of the as-synthesized material.
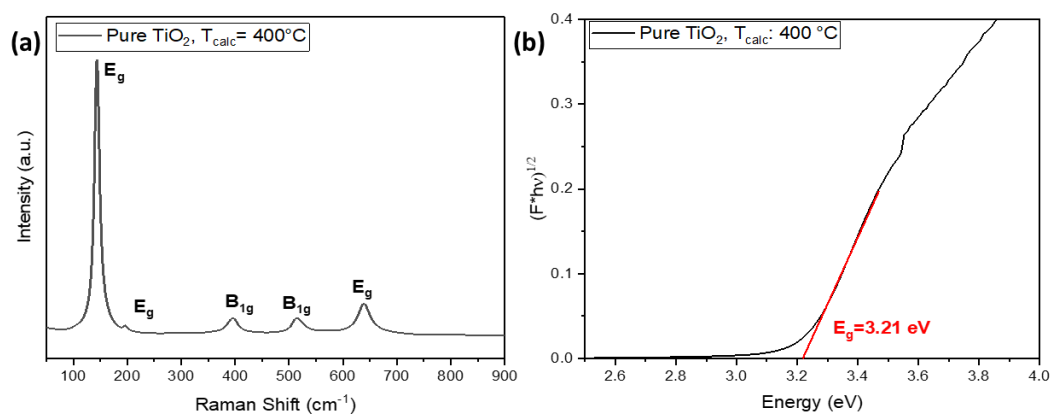
Figure A18. RAMAN spectrum and Tauc plot of the UV-Vis spectrum of TiO$_2$-400.

Figure A19. TiO$_2$-400 pellets before and after the electro-thermal treatments.
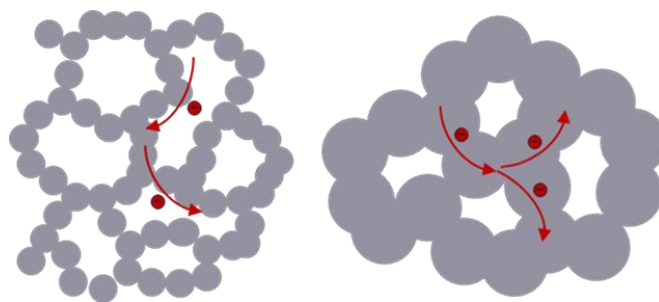
Figure A20. Schematic sketch showing the different conduction mechanisms happening in TiO$_2$ at different porosity.
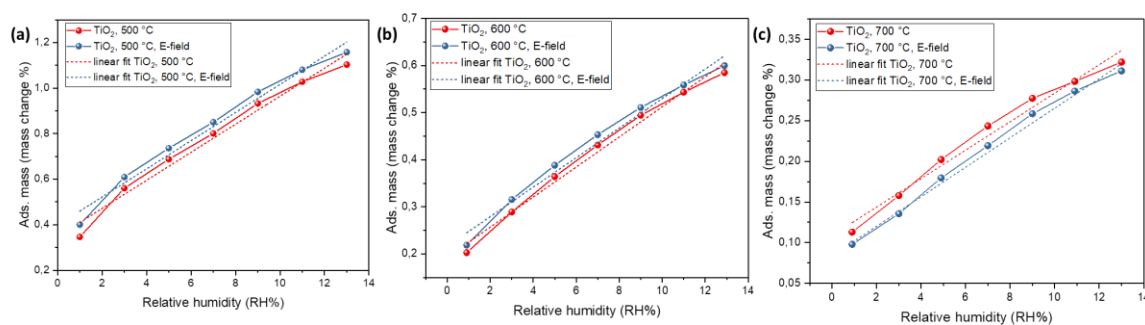
Figure A21. Water adsorption isotherms with focus in the 0-12% RH region for the electro-thermally treated materials, i.e. TiO$_2$-500 (a), TiO$_2$-600 (b) and TiO$_2$-700 (c).
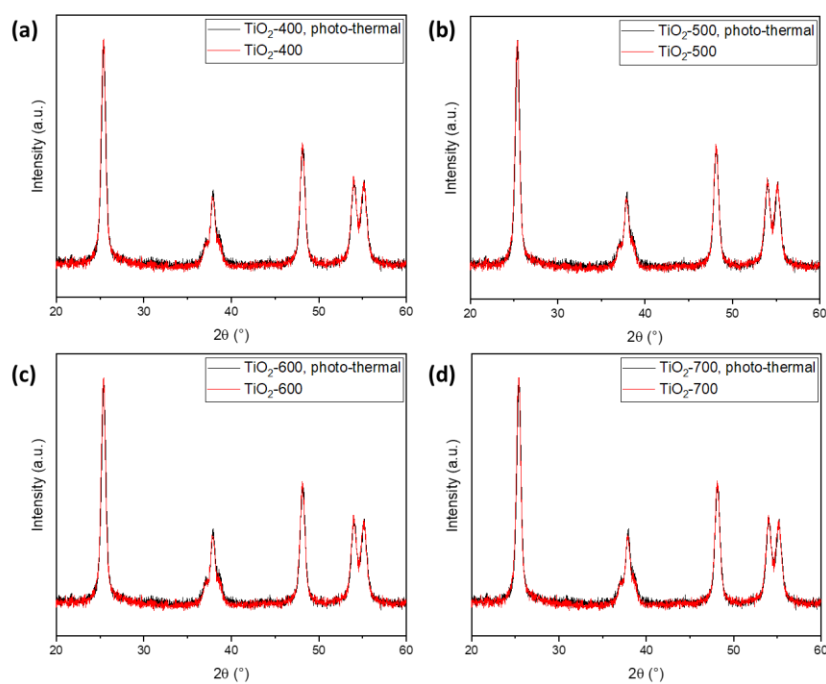
Figure A22. XRD of TiO$_2$ before and after photo-thermal treatment for TiO$_2$-400 (a), TiO$_2$-500 (b), TiO$_2$-600 (c) and TiO$_2$-700 (d).
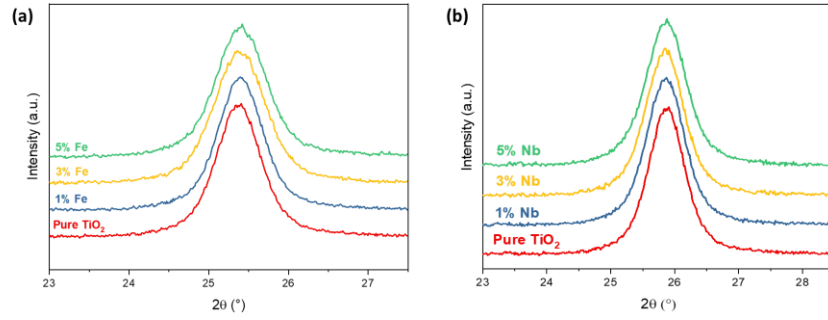
Figure A23. Focus on the (101) reflection of the X-ray diffractograms of the Fe-doped (a) and Nb-doped TiO₂ (b).
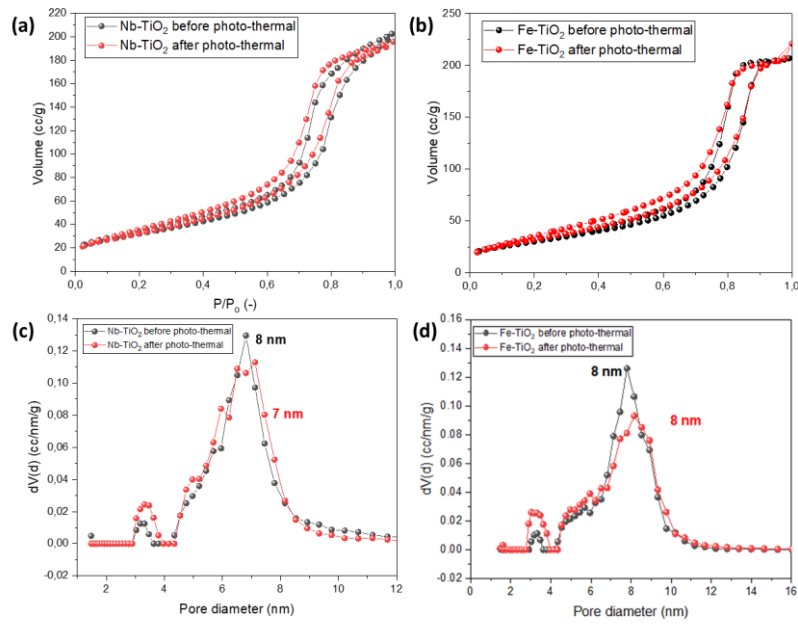
Figure A24. N$_2$-physisoprtion isotherms of the Fe-doped (a) and Nb-doped (b) anatase, before and after photo-thermal treatments. DFT pore size distribution of the (c) Fe-doped and (d) Nb-doped anatase, before and after photo-thermal treatments.

12.2 Tables

Table A1. Mössbauer hyperfine parameters of the as-synthesized LSTFN2 material, including the attributions given from the fitting of the spectrum.

Sample	d (mm/s)	Δ/e (mm/s)	Γ+ (mm/s)	Area (%)	Attribution
	0.36	0.44	0.21	58	LSTFN bulk
	0.34	0.82	0.15	10	LSTFN surface
LSTFN2	0.38	-0.01	0.23	12	6CN-Fe^{3+}
	0.28	0.04	0.32	20	4CN-Fe^{3+}

Table A2. Mössbauer hyperfine parameters of all of the materials examined in **Chapter 6**, including the attributions given from the fitting of the spectra. The ones marked with * are the magnetically coupled species.

Sample	d (mm/s)	Δ/e (mm/s)	Γ+ (mm/s)	B (T)	Area (%)	Attribution
LSTFN2	0.36	0.44	0.21	-	58	LSTFN bulk
	0.34	0.82	0.15	-	10	LSTFN surf
	0.38	-0.01	0.23	50.6	12	6CN-Fe^{3+}
	0.28	0.04	0.32	47.1	20	4CN-Fe^{3+}
R400	0.41	0.32	0.22	-	57	LSTFN bulk
	-0.04	-	0.18	-	15	NPs (Fe, FeNi alloy)
	0.29	-0.015	0.20	47.96	11	6CN-Fe^{3+}
	0.26	-0.20	0.45	45.2	17	4CN-Fe^{3+}
R650	0.13±0.01	-	0.21	-	28	Fe^0 NPs
	0.24±0.01	0.63±0.04	0.25	-	59	Bulk Fe^{3+}
	1.3±0.1	2.1±0.2	0.20	-	5	Fe^{2+}
	0	-0.02±0.09	0.20	-	7	Fe^0
R850	0.30	0.35	0.22	-	28	LSTFN bulk
	0.95	1.69	0.15	-	11	4CN-Fe^{2+}
	0.80	1.38	0.17	-	18	4CN-Fe^{2+}
	-0.11	-	0.20	-	43	NPs (Fe or FeNi)
R400-O	0.38	0.41	0.20	-	49	LSTFN bulk
	0.38	0.78	0.18	-	22	LSTFN surface
	0.43	0.11	0.38	52.2	19	LaFeO$_3$
	0.32	-0.06	0.25	49.6	10	γ-Fe$_2$O$_3$
R850-O	0.37	0.47	0.23	-	84	LSTFN bulk
	0.40	0.01	0.29	47.9	16	γ-Fe$_2$O$_3$
R400-O-R850	0.36	0.43	0.26	-	35	LSTFN2 bulk
	0.94	1.71	0.23	-	25	4CN-Fe^{2+}
	-0.04	-	0.15	-	40	Fe and Fe-Ni NPs
R850-O-R400	0.38	0.48	0.24	-	53	LSTFN2 bulk
	0.27	0.09	0.25	49.7	11	4CN-Fe^{3+} spinel
	0.41	-0.07	0.32	53.2	32	6CN-Fe^{3+} LaFeO$_3$
	0*	0*	0.2*	31.3	4	Fe^0

Table A3. Room temperature hyperfine parameters from Mössbauer spectroscopy. The hyperfine parameters isomer shift (δ), quadrupole splitting (Δ) or quadrupole shift (ε), when magnetic coupling is present, half linewidth at half maximum (Γ_+), were expressed in mm/s^{-1}, the internal magnetic field (B) in Tesla and the relative area (A) in %. δ is quoted to α-metallic Fe. SPM: superparamagnetic regime, octh.: octahedral environment, teth.: tetrahedral environment

Sample	δ (mm/s)	ε/Δ (mm/s)	Γ_+ (mm/s)	B (T)	A (%)	Attribution
	0.02±0.03	-	0.12±0.03	--	2	SPM Fe^0
	0.32±0.05	1.04±0.09	0.14±0.07	---	2	SPM Fe^{3+}
"Reduced"	0.01±0.01	0	0.23±0.01	33.85±0.05	55	Fe^0
	0.37±0.01	-0.02±0.01	0.18±0.01	51.88±0.07	31	octh. Fe^{3+} in LaFeO$_3$
	0.34±0.04	-0.03±0.04	0.25±0.08	48.9±0.4	10	octh. Fe^{3+}
	0.37±0.01	-0.05±0.01	0.16±0.01	51.88±0.04	40	octh. Fe^{3+} in LaFeO$_3$
"Re-oxidized"	0.35±0.01	-0.11±0.01	0.26±0.02	49.8±0.1	38	octh. Fe^{3+}
	0.20±0.02	0.32±0.01	0.28±0.03	42.8±0.1	22	teth. Fe^{3+}

12.3 List of used chemicals with safety information

Substance	GHS hazard pictograms	H-statements	P-statements
Citric acid		319	305+351+338
Glycerol	-	-	-
Lanthanum(III) nitrate hexahydrate		272, 315, 319, 335	302+352, 305+351+338
Nickel(II) nitrate hexahydrate		272, 302+332, 315, 317, 318, 334, 341, 350i, 360D, 372, 410	210, 273, 280, 301+312, 305+351+338, 308+313
Iron(III) nitrate nonahydrate		314	260, 264, 280 301+330+331, 303+361+353, 304+351+338+310, 363, 405, 501
Cobalt(II) nitrate nonahydrate		272, 302, 317, 318, 334, 341, 350i, 360F, 410	201, 220, 273, 280, 304+340, 342+311
Titanium(IV) isopropoxide		226, 319, 336	210, 233, 240, 241, 242, 305+351+338
Strontium nitrate		271, 318	210, 220, 280, 283 305+351+338, 306+360
Calcium(II) nitrate tetrahydrate		302, 318	270, 280, 305+351+338, 310, 330, 501
Ammonium hydroxide		314, 318, 335, 400, 410, 314, 335, 410	261, 271, 273, 280, 303+361+353, 305+351+338
Titanium(IV) tetrachloride		314, 330, 335	260, 280, 303+351+353, 304+340, 305+351+338, 310, 403+233
Pluronic® P123	-	-	-
Ethanol		225, 319	210, 233, 305+351+338

Substance	GHS hazard pictograms	H-statements	P-statements
Niobium(V) isopropoxide		225, 260, 304, 314, 336, 361f, 373, 411	210, 231+232, 280, 350+351+338, 335+334, 310
Aluminum(III) isopropoxide		228, 314, 318, 319, 336	210, 240, 241, 260, 261, 264, 264+265, 271, 280, 301+330+331, 302+361+354, 304+340, 305+351+338, 305+354+338, 316, 317, 319, 321, 337+317, 363, 370+378, 403+233, 405, 501

Acknowledgements

First and foremost, I would like to express my sincere gratitude to my doctoral supervisor Prof. Dr. Simone Mascotto for his guidance and support throughout my PhD journey, for giving me the opportunity to be part of his group, and for passing on his passion for research to me.

I am deeply grateful to Prof. Dr. Michael Fröba for his support over these years, as well as for his insightful feedback and scientific discussions regarding my research topics. I am also thankful to him for agreeing to be the first reviewer of my dissertation, to Prof. Dr. Alf Mews for accepting to be the second reviewer..

Another big thank you goes to all my colleagues from my former research group in Hamburg, as well as to the current students of the Mascotto group in Koblenz. A special thanks goes to Benny, for being a good friend and companion both in and outside the lab, and during late-night shifts making slides and working through beamtimes; to Kurt, for his patience and helpfulness in teaching me so many things in the early years of my PhD; and to Linda, for her valuable support in the final months of the writing of this dissertation, and during the preparation of my defense..

I am also thankful to all the members of the AK Fröba. Thanks to Beate, for the friendly chats and for helping me sort many things out. Thanks to Isabelle, for carrying out all my XRD measurements, and for her helpfulness and kindness. Thanks to Uta for the nice chats and for helping me out on many occasions, and to Sandra for handling my countless physisorption measurements and for the kind support during this past year and a half, something I truly appreciate. Finally, a big thanks to Frank, for the enjoyable conversations and nice travels to Denmark, and for his precious feedback on my dissertation in the last days before submission.

The scientific results presented in this thesis could not have been achieved without the collaboration of our partners in Korea, Greece, and Italy, with whom it was both a pleasure and an honor to work. I would therefore like to thank DongHwan Oh from

Finally, a special and heartfelt thank you goes to my family: to my parents, Virginia and Lorenzo, for their unwavering and unconditional support in everything I have done, and for the trust they have always placed in me; to my brothers, Giampaolo and Alberto; and to all my uncles and aunts, who are always ready to welcome me back with open arms whenever I return to Italy. And above all, thanks to my friends in Germany, in Italy, and everywhere else, and to all the people I've connected with over the past years who have shown me their support.

Again, whatever the next chapter may bring: we are just passing through!

Declaration on Oath

I hereby declare and affirm that this doctoral dissertation is my own work and that I have not used any aids and sources other than those indicated. If electronic resources based on generative artificial intelligence (gAI) were used in the course of writing this dissertation, I confirm that my own work was the main and value-adding contribution and that complete documentation of all resources used is available in accordance with good scientific practice. I am responsible for any erroneous or distorted content, incorrect references, violations of data protection and copyright law or plagiarism that may have been generated by the gAI.

Hamburg, 25th April 2025